

Cosmological Tests of Fundamental Physics

by

Alex Zucca

M.Sc., University of Trieste, University of Udine, 2014

B.Sc., University of Trieste, 2012

Thesis Submitted in Partial Fulfillment of the
Requirements for the Degree of
Doctor of Philosophy

in the
Department of Physics
Faculty of Science

© Alex Zucca 2019
SIMON FRASER UNIVERSITY
Summer 2019

Copyright in this work rests with the author. Please ensure that any reproduction or re-use is done in accordance with the relevant national copyright legislation.

Approval

Name: Alex Zucca
Degree: Doctor of Philosophy (Physics)
Title: Cosmological Tests of Fundamental Physics
Examining Committee: **Chair:** David Sivak
Assistant Professor

Levon Pogosian
Senior Supervisor
Professor

Andrei Frolov
Supervisor
Associate Professor

Igor Herbut
Supervisor
Professor

Andrew DeBenedictis
Internal Examiner
Senior Lecturer

Matthew C. Johnson
External Examiner
Associate Professor, Department of Physics and
Astronomy, York University

Date Defended: June 11, 2019

Abstract

The standard model of Cosmology, or the Λ CDM model, is able to describe remarkably well a plethora of observations with only six parameters. Nonetheless, several questions about its very nature have yet to be answered. Chief amongst them is the nature of Dark Energy, responsible for the observed acceleration of the Universe. While in the Λ CDM model Dark Energy is modelled via the cosmological constant Λ , its observed value cannot be reconciled with the predictions of quantum field theory, the framework at the basis of the standard model of particle physics. Modifications of General Relativity, known as modified gravity, offer an alternative approach to Dark Energy. The growth of large scale structure is modified in alternative gravity theories in ways that can be tested using cosmological data. We present a comprehensive analysis of a set of scalar-tensor theories of gravity that exhibit the chameleon screening mechanism. This mechanism hides the force mediated by the extra scalar from detection in local and solar system tests of gravity, while still leaving imprints in the cosmological observables.

With the increasing precision of cosmological surveys, finer effects must be included in the theoretical predictions. This is the case for the total mass of neutrinos that affect the structure formation at the percent level in a way that could be degenerate with modified gravity. Being able to break this degeneracy requires ability to account for the mass of neutrinos while constraining modified gravity theories. We thus introduce a consistent treatment of massive neutrinos in the phenomenological $\mu - \gamma$ framework and update the popular code MGCAMB used to constrain modified gravity models. We have also introduced the option for MGCAMB to work with general background histories where Dark Energy evolves with time. It has been recently shown that a dynamical Dark Energy with density that increases with time is able to alleviate the tensions between different datasets within the Λ CDM model. Modified gravity theories provide a framework to explain such behaviour of Dark Energy and we perform a reconstruction of the Lagrangian of Generalized Brans-Dicke theories from the observed expansion history of the Universe. We then study the viability of the such theories and ways of testing them with future data.

Another challenge for upcoming CMB experiments is the detection of the primordial gravitational wave background in the B-mode polarization signal. Such a background is predicted by Inflation, a period of exponential expansion in the early Universe, which is the paradigm behind the choice of the initial conditions in the Λ CDM model. CMB B-modes also offer a powerful way to test the existence of primordial magnetic fields in the early Universe. These can also arise from the inflationary mechanism or be generated during phase transitions in the early universe. We have developed a publicly available code, dubbed MagCAMB, that computes the CMB anisotropies generated by primordial magnetic fields. We also derived the tightest constrain to date on the primordial magnetic field amplitude using the CMB spectra from the Planck satellite and the B-mode measurements by the South Pole Telescope.

Keywords: Cosmology; Modified Gravity; Primordial Magnetic Fields, Cosmic Microwave Background, Large Scale Structure of the Universe

List of Publications

The results and conclusions embodied in this thesis are based on the published works:

1. J. T. Galvez Gherzi, A. Zucca and A. V. Frolov, *Observational Constraints on Constant Roll Inflation*, [arXiv:1808.01325 \[astro-ph.CO\]](#). Chapter 4 of this thesis is based on this publication. I contributed in the data analysis part, including the embedding of the power spectrum code into the parameter space grid sampler.
2. A. Zucca, Y. Li and L. Pogosian, *Constraints on Primordial Magnetic Fields from Planck combined with the South Pole Telescope CMB B-mode polarization measurements*, *Phys. Rev. D* **95**, 063506 (2017), [arXiv:1611.00757 \[astro-ph.CO\]](#). Chapter 5 is based on this publication. This publication introduced the publicly available patch **MagCAMB**. I co-developed the code MagCAMB, developed the MCMC sampler MGCosmoMC and performed the data analysis.
3. A. Hojjati, A. Plahn, A. Zucca, L. Pogosian, P. Brax, A. C. Davis and G. B. Zhao, *Searching for scalar gravitational interactions in current and future cosmological data*, *Phys. Rev. D* **93**, 043531, [arXiv:1511.05962 \[astro-ph.CO\]](#). The analysis on screened modified gravity models presented in Chapter 6 is based on this publication. I introduced the (m, β) parametrization in MGCAMB, updated the MGCosmoMC patch to include the most recent Planck data and co-developed the code for the forecast part.
4. A. Zucca, L. Pogosian, A. Silvestri and G. B. Zhao, *MGCAMB with massive neutrinos and dynamical dark energy*, [arXiv:1901.05956 \[astro-ph.CO\]](#). The new patch for **MGCAMB**, that introduces an accurate treatment of massive neutrinos and dynamical dark energy is presented in this paper. This has been recently accepted for publication on the *Journal of Cosmology and Astrophysics*. Chapter 7 is based on this paper. I re-wrote the entire MGCAMB patch, upgraded MGCosmoMC as well as CosmoMC to compute the lensing observables with the Weyl potential power spectrum.
5. Y. Wang, L. Pogosian, G. B. Zhao and A. Zucca, *Evolution of dark energy reconstructed from the latest observations*, *Astrophys. J.* **869**, L8 (2018), [arXiv:1807.03772 \[astro-ph.CO\]](#). The reconstruction of the Dark Energy density presented at the beginning of Chapter 8 is based on this publication. The remainder of Chapter 8 is based

on (still unpublished) work in collaboration with the co-authors of paper 5 above, for which I developed the designer GBD method, and introduced it in the EFTCAMB code, including the parameter space sampler.

Other works

During the course of this PhD, I published other papers that are not included in this thesis:

- A. V. Frolov, J. T. Gálvez Gherzi and A. Zucca, *Unscreening scalarons with a black hole*, *Phys. Rev. D* **95**, no. 10, 104041 (2017), [arXiv:1704.04114 \[gr-qc\]](#).
- L. Pogosian and A. Zucca, *Searching for Primordial Magnetic Fields with CMB B-modes*, *Class. Quant. Grav.* **35**, no. 12, 124004 (2018), [arXiv:1801.08936 \[astro-ph.CO\]](#).

Dedication

I would like to dedicate this thesis to all my family: my parents Susanna and Francesco. They have been providing me with loving support through all my life: without them none of this would be possible. To my brother and best friend Matteo: he is the biggest gift I had in my life. Our adventures during my research times in Europe were memorable. To my grandmother “Nonna” Carmen, who raised my brother and I, and found her own way to motivate us to study when we were younger. And to my grandfather “Nonno” Bruno, who showed me that despite the hardest challenges that the life puts on our road, it is still possible to do something great.

Acknowledgements

First of all, I would like to thank my senior supervisor Levon Pogonian. Through these four years he has been very supportive and provided me with extremely valuable help.

I would also like to thank my supervisor Andrei Frolov for the always stimulating discussions about physics and beyond; my friends and colleagues of the “Coquitlam Institute of Theoretical Physics”, Tomás and Michael. They are my first friends abroad and I am grateful for spending time with them; all the other friends that I have here, in particular to Claire, David, Joy, Igor and Camille for the support in the everyday life.

Finally, a big thanks goes to my girlfriend Helen.

Table of Contents

Approval	ii
Abstract	iii
List of Publications	v
Dedication	vii
Acknowledgements	viii
Table of Contents	ix
List of Tables	xiii
List of Figures	xv
1 Introduction	1
I Modern Cosmology	7
2 The Standard Cosmological Model	8
2.1 General Relativity	8
2.2 The expanding Universe	11
2.2.1 Matter Content of the Universe	14
2.2.2 Distances	15
2.3 Inhomogeneities in the expanding Universe	18
2.3.1 Gravitational Instability and Jeans Length	19
2.3.2 Linear Relativistic Perturbation Theory	21
2.3.3 Gauge Transformations	25
2.3.4 Evolution equations	27
2.3.5 The Boltzmann equation	29
2.3.6 Gauge Choices	31
2.3.7 Initial Conditions	32

2.4	Summary	33
3	Cosmological Observables	35
3.1	Background Observables	35
3.1.1	Type Ia Supernovae	36
3.1.2	Baryon Acoustic Oscillation	37
3.2	Perturbation Observables	39
3.2.1	Cosmic Microwave Background	43
3.2.2	Large Scale Structure	51
3.2.3	Weak Lensing	53
3.2.4	Cross-Correlations	56
II	Testing Fundamental Physics in the early Universe	60
4	Observational Constraints on Constant-Roll Inflation	61
4.1	Model and Background Dynamics	62
4.2	Perturbations	64
4.3	Deviations of n_s and r from the slow-roll expressions	68
4.4	Planck Constraints	69
4.5	Summary	72
5	Constraints on Primordial Magnetic Fields from the CMB	74
5.1	PMF as a stochastic field	76
5.2	CMB anisotropies from metric perturbations sourced by the PMF	78
5.3	MagCAMB, a patch with PMFs for CAMB	80
5.3.1	PMF Correlation functions	80
5.3.2	Implementation of the PMF Power Spectra	82
5.3.3	Results	82
5.4	Constraining PMF with Planck and SPT data	84
5.4.1	Constraints from Planck data	86
5.4.2	Constraints from Planck combined with SPT	88
5.5	Summary	90
III	Testing Fundamental Physics in the late time Universe	92
6	Phenomenology of Scalar-Tensor Gravity	93
6.1	Horndeski Action	93
6.2	Modified Gravity at cosmological scales	95
6.3	Screened Modified Gravity. The (m, β) parametrization	97

6.3.1	Evolution of linear perturbations	99
6.4	(m, β) parametrization for specific models	100
6.4.1	f(R) gravity	100
6.4.2	Dilaton model	102
6.4.3	Symmetrons	103
6.4.4	Generalized Chameleon models	104
6.4.5	Binned Model	104
6.5	Constraints from current data	104
6.5.1	The datasets used in the analysis	105
6.5.2	Constraints on $f(R)$	106
6.5.3	Constraints on the symmetron model	108
6.5.4	Constraints on the dilaton model	109
6.6	Forecasts	110
6.6.1	The data assumed in the forecast	111
6.6.2	Fisher analysis	111
6.6.3	The f(R) forecast	112
6.6.4	The symmetron forecast	113
6.6.5	The dilaton forecast	113
6.6.6	The Generalized Chameleon model	114
6.6.7	Principal Component Analysis of $m(a)$	115
6.7	Summary	118
7	MGCAMB with massive neutrinos and dynamical DE	121
7.1	Modified Growth framework	122
7.2	The new MGCAMB patch	124
7.2.1	Massive Neutrinos	127
7.2.2	The CMB source function and the weak lensing transfer function	127
7.2.3	The GR limit of MGCAMB	128
7.2.4	Other parameterizations	129
7.3	Joint constraints on modified growth, massive neutrinos and the dark energy equation of state	130
7.3.1	The datasets	130
7.3.2	The GR limit consistency check	131
7.3.3	Results	132
7.4	Discussion	134
8	Dynamical DE and Scalar-Tensor Gravity	135
8.1	The Reconstruction of the DE density	136
8.2	Dynamical DE and GBD theories	138
8.3	Designer GBD from $F(\phi)$	140

8.3.1	Parameter space	141
8.3.2	Perturbations Evolution	144
8.3.3	CMB anisotropies and Matter Power Spectra	145
8.3.4	Galaxy Number Counts and ISW effect	147
8.3.5	Physical Interpretation	148
8.4	Designer GBD from $F(a)$	149
8.4.1	Parameter Space	151
8.4.2	Results	152
8.4.3	Physical Interpretation	153
8.5	Summary	154
9	Summary and future directions	158
9.1	Early Universe	158
9.2	Late time Universe - Dark Energy	159
	Bibliography	161
	Appendix A Linear DES 1YR data	183
	Appendix B Galaxy Clustering - Weak lensing theory with Weyl potential	184
	Appendix C EFT formalism for GBD	186
	Appendix D Modifications to EFTCAMB	187
D.1	The new structure of the code	187
D.2	Implementation of the modified equations	187
D.2.1	Designer Background	187
D.3	Designer mapping EFT models	190
D.3.1	Designer $f(R)$	191
D.3.2	Designer GBD theories	192

List of Tables

Table 5.1	Priors on the nuisance parameters used in the SPT likelihood described in Sect. 5.4.2.	85
Table 5.2	Priors on the parameters varied in the MCMC analysis. We performed the analysis separately with the uniform and logarithmic priors on $B_{1\text{Mpc}}$	86
Table 5.3	Upper bounds (95% CL) for the PMF amplitude $B_{1\text{Mpc}}$ obtained from the combination of Planck data sets described in Sect. 5.4.1. The magnetic spectral index n_B and the PMF generation epoch parameter β are unconstrained.	87
Table 5.4	Upper bounds (95% CL) on the PMF amplitude $B_{1\text{Mpc}}$, the effective PMF strength B_{eff} and the magnetic density fraction $\Omega_{B\gamma}$ obtained from Planck and SPT.	89
Table 5.5	Current and forecasted 68% CL bounds on the amplitude B_λ of a scale-invariant PMF for different choices of parameters f_L and f_G quantifying the fraction of the weak lensing contribution to BB and the fraction of the galactic rotation measure, respectively. ^a Estimated 68% CL bound based on the 95% CL bound of 93 nG derived by POLARBEAR. ^b The 68% CL bound derived in this Chapter using TT, EE, TE spectra from Planck and BB from SPT. ^c Based on the B-mode spectrum alone, assuming fixed cosmological parameters.	91
Table 6.1	The 68% (95%) CL upper limits of f_{R_0} and the sum of neutrino masses using different combinations of data sets shown in the table.	107
Table 6.2	68% (95%) CL bounds on f_{R_0} , A_L and $\sum m_\nu$ using all the data sets: PLC+BAO+CMBlens+MPK+WL	108
Table 6.3	Summary of the 95% CL upper limits of the MG parameters and the sum of neutrino masses (in unit of eV) derived from current observations described in Sec. 6.5.1.	109
Table 6.4	The current 68 % C.L. uncertainties and those expected from LSST+. The blocks with “–” mean the parameter was fixed at its fiducial value. The values in parenthesis indicate those obtained for an alternative fiducial value.	118

Table 7.1 The 68 % CL uncertainties and best fit values of parameters obtained using the original CosmoMC, compared to the results from the GR limit of MGCosmoMC for two different values of a_{trans} which sets the scale factor beyond which the modified set of equations is evolved. The bound on the net mass of neutrinos is at the 95% CL. 131

Table 7.2 The 68 % CL uncertainties and best fit values of parameters constrained using MGCosmoMC. The bound on the net mass of neutrinos is at the 95% CL. Model 0 corresponds to Λ CDM with massive neutrinos. Model 1, in addition, includes modified growth on the Λ CDM background, while Model 2 adds a varying DE equation of state using the CPL parameterization. We can see that the CPL parametrization does not improve the fit of the model. 132

List of Figures

Figure 2.1	Angular diameter distance $D_A(z)$ in units of H_0/c for the Λ CDM model with $\Omega_m = 0.295$ (blue solid line) and for the Einstein-de Sitter model with $\Omega_m = 1$ (orange dashed line).	17
Figure 2.2	Luminosity distance $D_L(z)$ in units of H_0/c for the Λ CDM model with $\Omega_m = 0.295$ (blue solid line) and for the Einstein-de Sitter model with $\Omega_m = 1$ (orange dashed line).	18
Figure 3.1	Comparison of the measured distance modulus μ_{SN} from the JLA dataset with the theoretical predictions of the Λ CDM model.	37
Figure 3.2	Measurements of $D_V(z)$ from various surveys. The black solid line represent the theoretical prediction from the best-fit Λ CDM model from the Planck 2015 results.	38
Figure 3.3	Measurements of the CMB temperature anisotropies power spectrum from the Planck satellite and the South Pole Telescope. The thin black line shows the best fit model from the Planck collaboration analysis. The dashed vertical line divides the two different likelihoods for Planck. Also note that on the left the x-scale is logarithmic, while on the right is linear.	43
Figure 3.4	Measurements of the CMB E mode polarization power spectrum from the Planck satellite, the South Pole Telescope (SPT) and the Atacama Cosmology Telescope (ACT). The thin black line shows the best fit model from the Planck collaboration analysis.	45
Figure 3.5	Cross correlation power spectrum between the CMB temperature anisotropies and the E-mode polarization. The thin black line shows the best fit model from the Planck collaboration analysis. The dashed vertical line divides the two different likelihoods for Planck. Also note that on the left the x-scale is logarithmic, while on the right is linear.	47
Figure 3.6	Measurements of the B-mode CMB power spectrum performed by several surveys. The thin black line shows the best fit Λ CDM model with $r = 0.1$ from the Planck collaboration analysis.	52

Figure 3.7	Two point angular correlation function $w(\theta)$ measurements from DES. The orange line is the linear theory matter power spectrum, while the blue line represents the nonlinear power spectrum calculated with HALOFIT. The grey shaded region is an empirical cut on the nonlinear data.	54
Figure 3.8	Measurements of the cosmic shear ξ_+ angular correlation function from the Dark Energy Survey. blue and orange lines show the nonlinear and linear theory predictions respectively from the best fit Λ CDM model. The grey regions show the “soft” empirical data cut on the nonlinear scales.	57
Figure 3.9	Measurements of the cosmic shear ξ_- angular correlation function from the Dark Energy Survey. blue and orange lines show the nonlinear and linear theory predictions respectively from the best fit Λ CDM model. The grey regions show the “soft” empirical data cut on the nonlinear scales.	58
Figure 3.10	Measurement of the tangential shear γ_t from the Dark Energy Survey. As we did in the previous figures, blue and orange lines show the nonlinear and linear theory predictions respectively from the best fit Λ CDM model. The grey regions show the “soft” empirical data cut on the nonlinear scales.	59
Figure 4.1	Left panel: constant-roll inflation potential (4.4) for the model parameters $M^2 = 2.0 \times 10^{-9}m_0^2$ and different values of β . The region of interest is in the range $\phi \in (0; \phi_0]$, shown for the specific value of $\beta = 0.02$. Right panel: Map of initial conditions in the phase space for $M^2 = 2.0 \times 10^{-9}m_0^2$, $N_* = 55$ and $\beta = 0.02$. The color map represents the number of e-folds before reaching $\pm\phi_0$. Phase space trajectories converge as a power law towards the attractor (instead of exponentially, as is usually the case in slow-roll inflation) as in the case of power law inflation, which is a particular scenario of the constant-roll model.	62

Figure 4.2	Left panel: Example of the evolution of the curvature fluctuations for $\beta = 0.02$, $N_* = 0$ and $M^2 = 10^{-11}m_0^2$. Right panel: Evolution of the corresponding sum of the two tensor polarizations for the same model parameters. N is the number of e-folds from the start of numerical evolution of the background. Using the definition in (4.6), both figures also include the instant in which the CMB pivot modes leave the horizon. We show extremely long wavelength modes emerging deep from the sub-horizon scales to demonstrate that there is absolutely no evolution on super-horizon scales in all cases. . . .	64
Figure 4.3	Left panel: Power spectrum of primordial curvature fluctuations using $k_* = 2 \times 10^{-3}M_{\text{pc}}^{-1}$ as a pivot scale at $N_* = 0$. We considered the model parameters $\beta_{(1)} = 0.005$, $M_{(1)}^2 = 10^{-9}m_0^2$, $\beta_{(2)} = 0.01$, $M_{(2)}^2 = 3.82 \times 10^{-10}m_0^2$, $\beta_{(3)} = 0.02$, $M_{(3)}^2 = 7.26 \times 10^{-11}m_0^2$, $\beta_{(4)} = 0.04$ and $M_{(4)}^2 = 1.86 \times 10^{-12}m_0^2$. Right panel: Power spectrum of tensor perturbations for the same model parameters. None of the spectra show any features or running.	65
Figure 4.4	Injection scheme for the scalar and tensor modes. Evolution begins at a surface of initial conditions deep inside the horizon, with modes injected at constant k_{phys}	67
Figure 4.5	Left panel: Testing the consistency relation in (4.16) as a function of β after fixing $M^2 = 10^{-9}m_0^2$. Surprisingly, the consistency relations work well for larger values of β . Right panel: Testing (4.15) for the same value of M^2 . Here the differences are very large (up to ten orders of magnitude) for larger values of β . Both consistency relations are compared with the direct calculation of n_s and r at $N_* = 0$, right after evaluating the power spectra scalar and tensor perturbations. The shaded regions represent the ranges of β within the 68% and 95% confidence levels.	68
Figure 4.6	Scanning the parameters in the potential at $N_* = 0, 30, 60, 80$. The blue regions show the 68% C.L. (solid blue) and 95% C.L. (shaded blue) regions for the marginalized posterior probability of the scalar spectral index n_s , while the regions for the marginalized posterior of the scalar primordial amplitude A_s are plotted in different colors. On the left panel we can see the degeneracy of N_* and M^2 with respect to the amplitude. The right panel shows that the degeneracy is resolved fairly well when we use M_* defined in Eq. (4.20) instead of M	69

Figure 4.7	Different projections of the joint probability distribution from Planck 2015 likelihood evaluated at $N_* = 0$. Top panel: lateral projection of the joint distribution for β . Right panel: lateral projection of the joint distribution for $M_*/m_0 _{N_*=0}$. Left corner on the bottom: different regions of the joint posterior distribution are shown within the red stripe in orange at the 68% C.L. (solid orange) and 95% C.L. (shaded orange). The blue shaded regions correspond to the 1σ marginalized regions for the two parameters β and M_*	71
Figure 4.8	Constraints from joint Planck 2015/BKP likelihood on n_s and r . The green line shows the values of (n_s, r) from the parameter space probed in Figs. 4.6 and 4.7. For higher values of N_* , the model can cover most of the lower range of r	72
Figure 5.1	Contributions of relevant magnetic modes to the CMB temperature and polarization power spectra for a PMF with $B_{1\text{Mpc}} = 4.5$ nG and $n_B = 2.9$. For the passive modes, the time of the generation of the PMF is set at $\beta = \log_{10}(\tau_\nu/\tau_B) = 17$. The cosmological parameters are set to $\omega_b = 0.0226$, $\omega_c = 0.112$, $T_{\text{CMB}} = 2.7255$ K, $h = 0.7$, $A_s = 2.1 \times 10^{-9}$, $n_s = 0.96$, $r = 0.1$, $n_T = 1$	83
Figure 5.2	The B-mode spectrum from the PMF compensated vector mode (left panel) and tensor passive mode (right panel) with $B_{1\text{Mpc}} = 2$ nG and different values of the spectral index n_B . The black thin line shows the lensing contribution.	84
Figure 5.3	The B-mode spectrum from the PMF vector mode added to the lensing contribution (solid black line) for $B_{1\text{Mpc}} = 4.5$ nG (dashed line), $B_{1\text{Mpc}} = 3.3$ nG (dot-dashed line) and $B_{1\text{Mpc}} = 1.8$ nG (dotted line), with $n_B = -2.9$. The three SPT bandpowers are shown in orange, red and purple.	85
Figure 5.4	Left panel: the probability distribution function for the magnetic amplitude $B_{1\text{Mpc}}$ from the Planck data sets described in Sect. 5.4.1. We show only the case with $r = 0$ since varying r does not affect the results. Right panel: the marginalized PDFs for the magnetic amplitude $B_{1\text{Mpc}}$ from Planck and the combination of Planck and SPT. We only show the PDFs obtained with $r = 0$, as the case with co-varying r is essentially the same. We also show the PDFs for the nearly scale-invariant case, $n_B = -2.9$	87

Figure 5.5	Left panel: the joint probability for the magnetic amplitude $B_{1\text{Mpc}}$ and the magnetic index n_B using uniform prior on $B_{1\text{Mpc}}$. Right panel: the joint probability for $B_{1\text{Mpc}}$ and n_B using uniform prior on $\log_{10}(B_{1\text{Mpc}}/\text{nG})$. The two shaded regions represent the 68% C.L. and 95% C.L. respectively. The apparent bound on n_B in the left panel disappears when using the logarithmic prior, as shown in the right panel. Note that the 68% C.L. “islands” appearing in both panels for $B_{1\text{Mpc}}$ are numerical artifacts due to the low sensitivity of the likelihood to small values of the PMF amplitude.	88
Figure 5.6	The joint probability for the scalar to tensor ratio r and the time of generation of the PMF $\log_{10}(\tau_\nu/\tau_B)$. The two shaded regions represent the 68% CL and 95% CL, respectively.	89
Figure 6.1	Plots of CMB temperature anisotropy C_l^{TT} (left) and the matter power spectrum $P(k)$ (right) for the models studied in this paper. The parameters used for the symmetron model are: $a_\star = 0.25$, $\beta_\star = 1$ and $\xi_\star = 10^{-3}$. The parameters used for the dilaton model are: $\beta_0 = 3$ and $\xi_0 = 6 \times 10^{-3}$. The parameters used for Hu-Sawicki $f(R)$ model are $f_{R_0} = 10^{-4}$ and $n = 1$. The yellow shaded region shows the scales that are not taken into account in the data analysis.	101
Figure 6.2	The marginalized posterior distribution for the f_{R_0} parameter in the Hu-Sawicki model ($n = 1$) for different combinations of datasets. The solid lines show the PDF in case of massive neutrinos with a fixed mass $\sum m_\nu = 0.06$ eV, while the dashed lines show the PDF for the case when the neutrino mass was varying. Due to the degeneracy between f_{R_0} and $\sum m_\nu$, we see that the constraint on f_{R_0} become weaker when the neutrino mass is varied. The datasets are labeled according to the notation introduced in Sec. 6.5.1. The symbol + means that we add data on top of the PLC+BAO dataset. For example, +lensing means PLC+BAO+lensing.	106
Figure 6.3	Left panel: joint contours for f_{R_0} and $\sum m_\nu$ in the Hu-Sawicki model ($n = 1$) after marginalizing over all other cosmological parameters. The darker and lighter shades correspond respectively to the 68% C.L. and the 95% C.L. Right panel: joint contours for f_{R_0} and A_L in the Hu-Sawicki model. The darker and lighter shades correspond respectively to the 68% C.L. and the 95% C.L. Using PLC+BAO data sets only it is possible to detect high values of f_{R_0} that can cure the tension in lensing amplitude A_L . However such high values are ruled out once we add lensing and LSS data sets.	107

Figure 6.4	The marginalized posterior distribution for ξ_\star in symmetron model with $\beta_\star = 1$ and $a_\star = 0.25$ considering neutrinos with $\sum m_\nu = 0.06$ eV (red solid line) and marginalizing over a varying $\sum m_\nu$ (blue dashed line). The data sets used in this analysis are PLC+BAO+lensing+MPK+WL as described in section 6.5.1.	109
Figure 6.5	Marginalized posterior distribution for ξ_0 in the dilaton model with $\beta_0 = 5$. The datasets used in the analysis are PLC+BAO+lensing+MPK+WL as described in section 6.5.1. The red solid line shows the case with massive neutrinos with a fixed mass of $\sum m_\nu = 0.06$ eV, while the blue solid lines shows the PDF after marginalizing over a varying $\sum m_\nu$	110
Figure 6.6	Expected 1σ bounds on the parameters of the Hu-Sawicki model. The assumed fiducial model is marked with a star. The importance of using the“Full” set of observables (WL, GC and their cross-correlation) is clearly demonstrated. The Planck CMB data is included in all cases and is important for constraining the standard cosmological parameters.	112
Figure 6.7	Comparison of the uncertainties expected from LSST+ vs those from DES+ for the f_{R_0} parameter of the $n = 1$ Hu-Sawicki model and the total mass of neutrinos. The assumed fiducial model is marked with a star. The effect of fixing n , as opposed to marginalizing over it, is also shown.	113
Figure 6.8	Expected 1σ constrains from LSST+ on the parameters of the symmetron model. The assumed fiducial models are marked with a star. Unlike current data, LSST+ can simultaneously constrain β_\star and a_\star to a few percent level, and will improve the current bounds on ξ_\star . See Table 6.4 for a quantitative comparison.	114
Figure 6.9	Expected 1σ bounds on the ξ_\star parameter of the symmetron model and the mass of neutrinos, $\sum m_\nu$. The assumed fiducial model is marked with a star. Fixing the other MG parameters in this model, as opposed to marginalizing over them, does not change the degree of degeneracy, neither it improves the constraints.	115
Figure 6.10	1σ bounds on the neutrino masses and parameters of the dilaton model expected from LSST+. The fiducial values are marked with stars.	116
Figure 6.11	Expected 1σ constrains on the the Generalized Chameleon parameters for a fiducial model with $r = 3$ (top) and $r = 1$ (bottom) as a fiducial model. In each case, the value of r is varied and marginalized over.	117

Figure 6.12	Left panel: the uncertainties (square roots of eigenvalues) associated with the eigenmodes of $m(a)$ for the case when the coupling is fixed at $\beta = 0.4$ (solid line), and when it is marginalized over (dashed line). Right panel: the first four best constrained eigenmodes of $m(a)$ after marginalizing over β	118
Figure 7.1	Maximum relative difference in C_ℓ^{TT} and $P(k)$ between the GR limit ($\mu = \gamma = 1$) of MGCAMB and standard CAMB for several values of the sum of the neutrino masses and different values of the scale factor at which the modified equations are turned on.	127
Figure 7.2	The marginalized joint posterior distribution of the Model 1 and Model 2 parameters. The plots along the diagonal show the marginalized posterior distribution of each parameter. The grey dashed lines indicate the Λ CDM limit values of the additional parameters. The darker and lighter shades correspond to the 68% and the 95% CL, respectively.	133
Figure 8.1	Reconstructions of the DE fractional density $X(a)$. The green line (and its shaded regions) denote our “standard” reconstruction using a prior $\sigma_{\bar{X}} = 0.04$ and a correlation scale $a_c = 0.06$. The blue reconstruction denote the evidence weighted reconstruction. In both cases the shaded regions denote the 1σ (68% C.L.) intervals. Finally, for comparison, we highlighted the Λ CDM scenario with the black dashed line.	138
Figure 8.2	Hyperbolic tangent fits to the reconstructions of $X(a)$. On the left panel we show the weighted reconstruction with its 1σ confidence level and its tanh fitting function in black (hereafter X1). On the right panel we show the standard reconstruction with and in the dashed black line its tanh fitting function. The solid black line on the right panel denotes an alternative form of $X(a)$ (hereafter X2) used in the reconstruction of the GBD theories.	141
Figure 8.3	DE equation of state w_{DE} for the two fitting functions X1 and X2 introduced in Fig. 8.2.	143
Figure 8.4	The EFT $\Omega = F(\phi) - 1$ function for the reconstructed GBD theories using an exponential $F(\phi)$. The “confidence levels” regions denote the prior distribution on the parameters ϕ'_{ini}, ξ and $\log_{10} a_{\text{ini}}$ projected on the Ω function.	143

Figure 8.5	CMB anisotropies from the reconstructed GBD theories from the X1 (left panel) and X2 (right panel) DE densities. As expected the GBD theories affect mainly the ISW effect at low ℓ . The lower panels show the difference in power w.r.t. the Λ CDM best fit model.	145
Figure 8.6	Linear matter power spectrum (at redshift $z = 0$) for the reconstructed GBD theories from X1 (left panel) and X2 (right panel). The lower panels show the relative differences w.r.t. the Λ CDM best fit model.	146
Figure 8.7	Comparison of the CMB temperature and Galaxy Number Counts cross correlation spectra between the Planck best-fit Λ CDM model and the designed GBD theory from the X1 (upper panels) and X2 (lower panels) DE densities. As we can see, the CMB temperature - GNC cross correlations for the GBD theories can be either positive or negative.	147
Figure 8.8	Reconstructed potential for four of the sampled GBD theories with coupling $\xi = 0.5, 1.5, 3$ and 10 respectively.	149
Figure 8.9	Cosmological observables for the models reconstructed in Fig. 8.8 compared to the best fit Λ CDM model.	150
Figure 8.10	Power law EFT Ω functions reconstructed from the DE density X1.	152
Figure 8.11	Polynomial EFT Ω functions reconstructed from the weighted $X(a)$ (upper left), standard $X(a)$ (upper right) and their respective tanh fits (lower panels).	153
Figure 8.12	Cosmological observables from the reconstructed power law $\Omega(a)$ using the X1 DE density.	154
Figure 8.13	Cosmological observables from the reconstructed polynomial $\Omega(a)$	155
Figure 8.14	Reconstructed coupling and potential from the DE density X1 for the power law time dependence of $\Omega(a)$	156
Figure 8.15a	Cosmological observables from the theory reconstructed in Fig. 8.14.	156
Figure 8.15b	Reconstructed coupling and potential from the standard and weighted DE density reconstructions (and their tanh fit) using a fifth order polynomial coupling $F(a)$	157
Figure 8.15c	Cosmological observables from GBD theories reconstructed from polynomial $\Omega(a)$	157
Figure 8.15a	188
Figure 8.15b	190

Chapter 1

Introduction

We are living in a golden era for Cosmology. Ongoing and future observational collaborations are relentlessly working to map cosmic structures with unprecedented accuracy. The standard cosmological model, known as the Λ -*Cold-Dark Matter* (Λ CDM) model, that emerged from the observations of the last two decades has been put under thorough scrutiny and its six parameters are now known with percent level accuracy. The detection of gravitational waves by LIGO/Virgo [1, 2, 3, 4] has recently opened a very promising observational window for probing new physics and has so far shown good consistency with Λ CDM. Nonetheless, several questions about the very nature of the model still need to be answered and the hope is that future observations will shed light on some of them.

This may be the case for Dark Energy (DE), which dominates the energy amount of the Universe and is postulated to drive the observed cosmic accelerated expansion. In 1998, measurements of the Type Ia supernovae by the Supernova Cosmology Project [5] and the High-Z Supernovae Search Team [6] reported strong evidence that the Universe recently entered a phase of accelerated expansion. Independent probes also confirmed this scenario. The accurate measurements of the cosmic microwave background (CMB) anisotropies over the full sky performed by the Wilkinson Microwave Probe (WMAP) satellite [7, 8], and later improved by the Planck satellite [9, 10, 11], confirmed the cosmological picture emerged from the supernovae measurements, and provided evidence for DE from CMB data alone. Also, cosmological surveys such as SDSS, WiggleZ, CFHTLenS and DES performed precise measurements of the distribution of structure in the Universe. The agreement among all these observations confirmed the standard cosmological model, making cosmic acceleration, and hence the presence of a form of Dark Energy, an established fact.

Yet, from a theoretical viewpoint, we struggle to find an explanation for the accelerated expansion. In Λ CDM DE is modelled by the cosmological constant Λ . Its small measured value however requires an extreme fine-tuning of the vacuum energy in the context of the present understanding of particle interactions [12]. Alternatives to the vacuum energy nature of DE are provided by quintessence fields, and modified gravity (MG) theories. Both cases imply the existence of extra degrees of freedom. For quintessence, it is a scalar field

minimally coupled to matter, whose energy density can mimic the cosmological constant. However, the current cosmological data shows a preference for an *increasing* DE density [13], which would imply a ghost instability in the context of a minimally coupled quintessence field. If such “phantom” [14, 15, 16] behaviour of DE was confirmed by the next generation observations, the quintessence field scenarios would be ruled out.

Another potential explanation for DE would be through the modification of gravity laws on cosmological scales. General Relativity (GR) is one of the most theoretically appealing theories, being the only interacting theory of a Lorentz-invariant massless spin-2 particle with second order equations of motion [17, 18, 19, 20, 21]¹. Thus, extensions to GR would have to sacrifice one of those assumptions. Experimentally, GR is known to work remarkably well within the solar system. Time-delays of the radio waves emitted by the Cassini spacecraft constrain the Post-Parametrized-Newtonian (PPN) parameters to be consistent with GR in one part to 10^5 [22]. Other probes such as light rays deflections [23] and the precession of the perihelion of Mercury [24] also agree remarkably well with the predictions of GR. Furthermore, the recent detection of gravitational waves from black-hole mergers [1] strongly agree with the GR predictions of the waveform. Also, the gravitational wave detection from neutron stars mergers [2] accompanied by its electromagnetic counterpart [3, 4] constrained the speed of gravitational waves to be the same as the speed of light to one part in 10^{15} . Nevertheless, deviations from GR are still possible at cosmological scales. The most common approach is to add extra degrees of freedom in the gravitational sector of the action [25]. These extra fields could lead to different patterns in structure formation and hence current and future large scale structure probes such as DES, LSST and Euclid have the potential to test gravity on cosmological scales.

From an Effective Field Theory (EFT) perspective, scalar-tensor theories of gravity are well motivated. The effective degrees of freedom of an ultra-violet (UV) completion of GR could emerge as an extra propagating scalar field. Although with different motivations, Horndeski derived the most general Lagrangian for a scalar-tensor theory of gravity in the 70s [26]. These class of theories, now known as *Horndeski theories*, were later rediscovered and further investigated in a cosmological context [27, 28, 29] less than a decade ago. The phenomenology of these theories is extremely rich and complex, due to the large number of free functions present in the theory. The extra scalar field would mediate an extra force, usually referred to as *fifth force*, that could range from cosmological scales down to sub-millimetre scales. Laboratory experiments such as the one performed by the Eöt-Wash group [30, 31, 32] ruled out extra degrees of freedom down to a scale of $\lambda = 56 \mu m$. For scalar-tensor theories of gravity acting at larger scales, ideally at cosmological scales, there must be a *screening mechanism* hiding these extra forces that, otherwise, would have already been observed in the laboratory and solar system tests [25]. Constraining scalar-tensor

¹To be precise, it is the only *low energy* limit of an interacting Lorentz-invariant spin-2 field.

theories on cosmological scales however becomes quickly a prohibitive task due to the large parameter space to probe. In this context, a phenomenological approach to testing gravity on cosmological scales would be more desirable. This has been performed in two different complementary approaches. The authors of [33, 34] proposed an EFT approach to writing the action for background evolution and linear cosmological perturbations in a general scalar-tensor theory of gravity. In this framework, dubbed EFT of DE, there are 6 free functions of time appearing in the action. Recently, an attempt to constrain them was performed in [35], showing no detectable deviation from GR, although the uncertainties are still quite large and will improve with data from the future surveys. Another approach is to look at the modifications of the equations of motion induced by deviations from GR [36, 37]. This approach has the advantage of having only two functions of time and scale describing the deviations from GR at the perturbative level and one function of time describing the background expansion.

The nature of DE is not the only puzzle faced in Cosmology. Another important question is deeply connected to the origin of the structure in the Universe. The general idea is that structure, such as stars and galaxies, originated from the gravitational collapse of regions of initially small overdensities. These small perturbations are observed in the CMB, as anisotropies in its temperature. But what causes these small fluctuations remain somewhat of a mystery. Their origin is usually attributed to the amplifications of quantum fluctuations in the light degrees of freedom that become classical fluctuations of the metric during a period of exponentially fast expansion of the Universe at very early times. This period, called cosmological *inflation* was initially postulated in the eighties to explain the observed isotropic temperature of the CMB [38, 39, 40, 41, 42]. Indeed, photons coming from patches of the sky that were not in causal contact at the time of recombination were observed with the same temperature, indicating that somehow, they were in thermal equilibrium. This dilemma, known as the *homogeneity problem* could be solved assuming that at very early times, the patches of observed sky were actually in causal contact but were subsequently separated by a violent rapid expansion of the Universe. It was soon realized that the inflationary mechanism could also solve the *flatness problem*, that is why the observed Universe has spatial curvature consistent to be zero [42]. More importantly, quantum fluctuations of the field driving inflation, usually dubbed *the inflaton*, can seed the primordial inhomogeneities that later evolve and are observed in the CMB. In its most common form, inflation is modelled by a scalar field slowly rolling down a shallow potential. Since the first results of the Planck Satellite there has been a renewed interest in the field of inflation. Indeed, the plethora of inflationary models emerged in these last years have been put under scrutiny confirming that, so far, the observations of the CMB anisotropies are in good agreement with the inflationary mechanism [43, 44]. Yet, we still lack concrete evidence of its existence. The signature of inflations might be imprinted in the CMB B-mode polarization signal. The B-mode anisotropies are generated by primordial gravitational waves resulting from the in-

flationary mechanism. However, the measurement of the CMB B-mode is technically very challenging as the B-mode signal is contaminated by the foreground dust emission. To date, the upper bound of the amplitude the primordial gravitational waves - expressed as the ratio between tensor and density fluctuations and denoted as r - is set to $r \lesssim 0.1$ [45]. However, the future CMB B-mode polarization surveys such as the Simons Array [46] and CMB-S4 [47] will be able to probe a regime down to $r \approx 10^{-3}$, shedding light upon the inflationary scenario.

Cosmological measurements also offer an exquisite way to probe physics outside the realm of cosmology. For instance, large scale structure measurements are very sensitive to the number and the total mass of neutrinos [48]. Cosmological bounds on the mass of neutrinos are very powerful and constrain the sum of the neutrino masses to be $\lesssim 0.1$ eV.

Furthermore, cosmological observations offer the possibility to answer some important questions in astrophysics. For example, the origin of the magnetic fields observed in almost all gravitationally bound cosmic structures is still not fully understood. Magnetic fields of a few μG are observed in galaxies and galaxy clusters [49]. While the alignment of the magnetic fields with the galactic disk plane suggests that they could be originated by amplification of a seed through the dynamo effect, the efficiency of the dynamo and the required strength of seed are still debated. In particular, observations of galactic magnetic fields in galaxies at high redshift ($z > 2$) [50] imply that the dynamo would have short time to operate and would have required a seed as large as $10^{-11} G$ [51]. Moreover, preliminary observations of nG magnetic fields in the intercluster space [52, 53] add to the problem, as no dynamo could operate in these regions. An interesting possibility is that these observed magnetic fields could be the remnants of fields originated in the pre-recombination epoch. The generation of these primordial magnetic field (PMF) is predicted to occur in certain early-Universe scenarios including inflation [54, 55] and phase transitions [56]. The PMF would subsequently survive in a frozen-in state [49] until structure formation when it would collapse with the matter to seed the galactic fields, or survive in the void regions. PMFs affect CMB anisotropies by sourcing metric and matter fluctuations through the Lorentz force on the baryons of the primeval plasma. Measurements of the CMB temperature and polarization anisotropies can offer a powerful tool to constrain the strength of the PMF. The 7-years results from WMAP [57] and the Planck satellite collaboration placed an upper bounds on the amplitude of the PMF at the $\lesssim 4nG$ level [58]. The nG threshold is of fundamental importance. In fact a PMF with strength of $1nG$ coherent on a scale of 1 Mpc, would naturally be compressed to a μG strength field during galaxy formation. Of particular interest are the measurements of the CMB B-mode polarization. Indeed, the rotational component of the Lorentz force would produce B-mode polarization anisotropies that survive the small scale damping well past the Silk scale [59, 60, 61]. The South Pole Telescope (SPT) and the POLARBEAR measurements of the small scale B-mode polarization of the CMB offered competitive upper bounds [62, 63] on the same order as the constraints from the

WMAP and Planck satellites measurements. The latest measurements from SPT [64] and future B-mode polarization surveys such as the Simons Array [46] and CMB-S4 [47] of CMB observations can offer a potential improvement on the upper bounds of the PMF amplitude. However, because the amplitude of the CMB spectra scales as the fourth power of the PMF amplitude, they will likely not offer constraints below the critical nG level. PMF also generates CMB B-modes through Faraday rotation (FR) [65, 66, 67]. This magnetic B-mode scales linearly with the PMF amplitude and thus can potentially be used to efficiently constrain PMF in the next generation of B-modes surveys.

There are other puzzles in Cosmology that will not be discussed in this thesis. Chief amongst them is the nature of Dark Matter (DM), which constitutes a fundamental brick of the Λ CDM model. Evidence for its existence ranges from rotational curves of galaxies, CMB observations and large scale structures. However, a direct detection of DM particles is still lacking to date.

The goal of this thesis is to use the current cosmological data to provide, if possible, a quantitative answer to some of the questions mentioned so far. Part I of this thesis is devoted to review the standard cosmological model and serves as a reference for the core of this thesis presented in the following Parts, II and III. In Chapter 2 we review the framework on which the Λ CDM model is based. In particular we will show how an expanding Universe naturally arises in GR, and how the various components in the Universe affect the expansion history. The first evidence for DE was indeed obtained by fitting the luminosity distance of Type Ia supernovae hosted in high-redshift galaxies, and depends on how the Universe expanded since then. We also review the perturbation theory framework. The evolution of small perturbations evolving on the smooth expanding background is used to analyse the inhomogeneities that we observe in the CMB as well as in the large scale of the Universe. All these tools are used in Chapter 3 to analyse the main cosmological observables, distinguishing those that probe the background expansion history and those that probe perturbations.

Cosmic history provides a logical structure for this work. We will present our work starting from the very first instants of the Universe, to present times. In Part II we investigate the pre-recombination Universe. In Chapter 4 we use the CMB measurements from the Planck satellite and B-mode polarization measurements from the BICEP/Keck array to constrain the constant roll models of inflation. While the most common inflationary models assume that the field is slowly rolling down its shallow potential, constant roll inflation is a phenomenological way to parametrize small deviations from it. Most importantly, as the slow roll condition is not assumed a priori, it offers a framework to assess the consistency of the slow roll hypothesis. In Chapter 5 we move a little forward in time and search for signs of PMF in the CMB anisotropies. Specifically, we perform a comprehensive analysis of the CMB anisotropies sourced by PMF and, using the latest Planck CMB measurements along with the latest high- ℓ B-mode measurements from SPT, we set the tightest upper bounds

on the PMF amplitude to date. We also discuss other possible ways to constrain PMFs with the next generation surveys.

We then move on to the post recombination era with Part III devoted to explore Dark Energy and related issues. In Chapter 6 we perform a systematic analysis of the most common modified gravity models that exhibit a viable screening mechanism. Specifically, we consider the symmetron, dilaton and chameleon models - the latter in the $f(R)$ gravity case. We first investigate their constraints using some of the latest observations and then forecast how the constraints will evolve in the next generation surveys. While in this Chapter we focus on modified gravity models that have the same expansion history as the Λ CDM model, in Chapter 7 we relax the Λ CDM hypothesis and we introduce a dynamical DE into the popular code MGCAMB. This code is used to compute cosmological predictions in phenomenological parametrizations of MG and can be used along with its Markov Chain Monte Carlo (MCMC) suite MGCosmoMC, to constrain MG models using the latest data. We also revised and updated the entire code and we introduce an accurate treatment of massive neutrinos in the modified growth scenario.

In Chapter 8 we investigate the time evolution of the DE density. There have been many studies that considered the equation of state (EOS) of DE (w_{DE}) and tried to detect deviations from the Λ CDM limit $w_{\text{DE}} = -1$. In [13], it was shown that current data seem to prefer $w_{\text{DE}} < -1$. This would rule out minimally coupled quintessence models as they would necessarily have negative kinetic energies (*ghost* instabilities). In this chapter we will argue that instead of using the DE EOS, constraining the DE density is a more suitable quantity to investigate MG theories. We perform a reconstruction of the DE fractional density and find that there is minimal Bayesian evidence that supports a deviation from the cosmological constant. We also discuss the consequences of the reconstructed DE density on scalar-tensor theories of gravity.

Finally, we conclude with a summary in Chapter 9.

Part I

Modern Cosmology

Chapter 2

The Standard Cosmological Model

The aim of this chapter is to introduce the theoretical framework of the standard model of cosmology. We will progressively build the Λ CDM model first starting from GR, and then showing how it naturally accommodates an expanding solution for a homogeneous and isotropic Universe. The expansion of the Universe then accelerates when the cosmological constant (CC) becomes relevant, at redshifts $z \lesssim 1$.

We then introduce the perturbation theory framework. This allows us to study how small perturbations in the metric and the energy-momentum evolve on the background. We will restrict to linear perturbation theory for two main reasons. First, the observed isotropy of the CMB, with fluctuations at the order of 10^{-5} suggests that a linear description can be very accurate. Also, on large cosmological scales linear theory works remarkably well, breaking down at smaller scales. Second, nonlinear scales are hard to treat in MG models, especially if MG exhibits a screening mechanism. Furthermore, smaller scales are more sensitive to astrophysical effects and do not offer a clean window to cosmological tests of gravity.

2.1 General Relativity

Since most of the composite objects that constitute the Universe are not electrically charged, the only interaction that we expect acting on cosmological scales is gravity. Also, because General Relativity (GR) is the most successful theory of gravity to date - being able to explain the precession of Mercury's perihelion [68], the deflection of light rays [69, 70], and the gravitational redshift that affects clocks in the Global Positioning System (GPS) - it is logical that the Λ CDM model is built upon GR. According to GR, physical events take place in a four-dimensional spacetime, usually denoted as \mathcal{M} (from *manifold*), and the gravitational interactions are just the result of particles responding to the local curvature of the spacetime. The geometrical properties of the spacetime are encoded in the metric

tensor $g_{\mu\nu}$, so that the line element on \mathcal{M} is given by

$$ds^2 = g_{\mu\nu} dx^\mu dx^\nu, \quad (2.1)$$

where x^μ are coordinates in some coordinate system.

The metric tensor $g_{\mu\nu}$ is treated as a classical field, like the matter fields “living” on the spacetime \mathcal{M} , and its dynamics is given by the Einstein-Hilbert action [71],

$$S_{\text{EH}} = \int d^4x \sqrt{-g} \frac{m_0^2}{2} (R - 2\Lambda) + \int d^4x \sqrt{-g} \mathcal{L}_m(\psi, g_{\mu\nu}), \quad (2.2)$$

where we adopted the “natural units” with $\hbar = c = k_B = 1$, $m_0^2 \equiv 1/8\pi G$ is the reduced Planck mass with G being the Newton constant, g is the determinant of the metric tensor, R is the Ricci scalar, Λ is the cosmological constant and $\mathcal{L}_m(\psi, g_{\mu\nu})$ is the Lagrangian of the matter fields, collectively denoted as ψ , that also depends on the metric tensor $g_{\mu\nu}$. The first term in the action (2.2) is usually referred to as the gravitational sector of the action, while the second term is called, for obvious reasons, the matter sector. The dynamics of the metric tensor is described by the Einstein equations. These can be obtained from the principle of least action, $\delta S_{\text{EH}} = 0$, and are given by

$$G_{\mu\nu} \equiv R_{\mu\nu} - \frac{1}{2} g_{\mu\nu} R = \frac{1}{m_0^2} T_{\mu\nu} - g_{\mu\nu} \Lambda, \quad (2.3)$$

where $G_{\mu\nu}$ is the Einstein tensor, $R_{\mu\nu}$ is the Ricci tensor and $T_{\mu\nu}$ is the energy-momentum tensor of the matter fields defined as

$$\frac{1}{2} \sqrt{-g} T_{\mu\nu} = \frac{\partial \sqrt{-g} \mathcal{L}_m}{\partial g^{\mu\nu}} - \partial_\alpha \frac{\partial \sqrt{-g} \mathcal{L}_m}{\partial (\partial_\alpha g^{\mu\nu})}. \quad (2.4)$$

The energy-momentum tensor is covariantly conserved, that means

$$\nabla_\mu T^{\mu\nu} \equiv \partial_\mu T^{\mu\nu} + \Gamma_{\alpha\mu}^\mu T^{\alpha\nu} + \Gamma_{\mu\alpha}^\nu T^{\mu\alpha} = 0, \quad (2.5)$$

where $\Gamma_{\beta\gamma}^\alpha$ are the Christoffel symbols defined as

$$\Gamma_{\beta\gamma}^\alpha = \frac{1}{2} g^{\alpha\lambda} (-\partial_\lambda g_{\beta\gamma} + \partial_\beta g_{\gamma\lambda} + \partial_\gamma g_{\lambda\beta}). \quad (2.6)$$

It is worth noticing that a covariant derivative defined through the Christoffel symbols above is said to be *compatible* with the metric tensor $g_{\mu\nu}$. This implies that $\nabla_\alpha g_{\mu\nu} = 0$.

Eq. (2.5) is a covariant generalization of the special relativity equation

$$\partial_\mu T^{\mu\nu} = 0, \quad (2.7)$$

and is a direct consequence of the Bianchi identity, $\nabla_\mu G^{\mu\nu} = 0$. Ideally, by solving the Eqs. (2.3) and (2.5) for the metric tensor $g_{\mu\nu}$ and the energy-momentum tensor of the matter content in the Universe, we can understand its evolution. Of course, having at hand $g_{\mu\nu}$ and $T_{\mu\nu}$ for the entire Universe is unrealistic without some assumptions. In the next section we will review the assumptions, or the symmetries, underlying the standard cosmological model, but before that, we shall focus on some other important facts in GR. Test particles move according to the *geodesic equation*,

$$P^\mu \nabla_\mu P^\nu = 0, \quad (2.8)$$

where P^μ is the 4-momentum defined as $P^\mu \equiv mu^\mu$ for particles of mass m and $P^\mu \equiv k^\mu$ for massless particles. Here $u^\mu \equiv dx^\mu/d\lambda$ is the four velocity of the particle with λ being an affine parameter that parametrizes the particle trajectory $x^\mu(\lambda)$ and k^μ is the wave vector for the massless particles. The geodesic equation is a direct consequence of the *weak equivalence principle* (WEP). The WEP is based on the observation that, in Newtonian mechanics, the inertial and gravitational masses, although being conceptually distinct things, have the same values. This means that the behaviour of freely falling particles is universal, independent of their mass. Mathematically, the weak equivalence principle is encoded in the minimal coupling between matter fields ψ and the metric tensor $g_{\mu\nu}$. In fact, there is no interaction Lagrangian between ψ and $g_{\mu\nu}$. The interaction is only included in the invariant 4-volume element $d^4x\sqrt{-g}$.

A consequence of the geodesic equation is that the massless particles trajectories, like the light rays, also bend in proximity of large mass distributions, a result initially shown by Einstein [69, 70] and confirmed by many observations. It is worth noticing that also Newtonian gravity predicts that light would bend in proximity of gravitational fields, but only half of the value predicted in GR [72].

The deflection of light rays gives rise to a *lensing* effect of the background objects by mass distributions positioned along the line of sight. This has important consequences in cosmology. In principle, being able to detect the distortions of background galaxies in proximity - on the projected plane - of foreground galaxies can be used to reconstruct the mass distribution on the line of sight. As we will see later, mapping the mass distribution in the Universe is of fundamental importance to test GR on cosmological scales.

GR has been thoroughly tested since its formulation and is so far our best theory to describe gravitational interactions. GR is also very robust from a theoretical viewpoint. Its uniqueness has been proven in many ways. At the low energy limit, GR is the only theory of a self-interacting Lorentz-invariant spin-2 massless particle [17, 18, 19, 20, 21]. Furthermore, Lovelock proved [73] that the only second-order, local gravitational field equations derivable from an action containing solely the four-dimensional metric tensor (and its related tensors) are the Einstein equations with the cosmological constant (2.3).

These above results guarantee that if we were to consider other theories of gravity, we would need to choose one of the following ways out:

- Adding new degrees of freedom. This can be obtained by adding, for example, a scalar degree of freedom in the gravitational sector of the action, or make the Christoffel symbols independent variables: this means that the connection is not the one compatible with the metric any longer. The latter is usually known as the Palatini approach. It is still remarkable how actually GR is still very unique even in the Palatini approach. Namely, the Lagrangian density

$$\mathcal{L} = \sqrt{-g} \frac{m_0^2}{2} R, \quad (2.9)$$

gives the same Einstein equations using either variation of the metric $g_{\mu\nu}$ or using the Palatini approach.

- Considering extra dimensions. For example, the observed four-dimensional spacetime could be embedded in a higher dimensional manifold. This is at the basis of the gravity model by Dvali, Gabadadze and Porrati (DGP) [74], for example.
- Breaking the non-locality assumption.
- Considering higher-order equations of motion, providing that the Ostrogradsky theorem is not violated. For example, $f(R)$ gravity, where the Lagrangian (2.9) is replaced by the following,

$$\mathcal{L} = \sqrt{-g} \frac{m_0^2}{2} f(R), \quad (2.10)$$

yields fourth-order equations of motion. However, with a proper choice of the function f it is possible to avoid Ostrogradsky instabilities (*ghost-like* extra fields).

In Part III we will actually use one, or rather a combination, of the above possibilities and test their cosmological viability. For the remaining of this and the following Chapters we will only consider GR and specifically the Λ CDM model. In later chapters, we will consider theories of gravity in which an extra scalar degree of freedom is present in the gravitational sector of the action.

2.2 The expanding Universe

The standard cosmological model is based on two fundamental assumptions:

- The *cosmological principle*, stating that the Universe is *isotropic* and *homogeneous*. The isotropy of the Universe, meaning that the Universe looks, on average, the same in all directions, is a very well tested fact. The Cosmic Microwave Backgrounds (CMB) has the same temperature, up to 10^{-5} order fluctuations, across the entire sky [8, 10,

11, 75]. The homogeneity of the Universe means that different observers across the Universe see the same average properties of the sky, regardless of their position. Of course, this does not mean that *all* observers in the Universe see the same average properties. In a more precise way, the homogeneity of the Universe implies that there exists a family of freely falling observers (called *comoving observers*) moving along with the average motion of their neighbouring galaxies, whose view of the Universe will be, on average, the same. Measuring the homogeneity of the Universe is however much more complicated - we are effectively unable to move away in cosmic time or distance from here-and-now and hence cannot probe spatial variations on constant time slices; effectively, our observations only access the past lightcone of here-and-now. Direct observation thus cannot distinguish between an evolving homogeneous distribution of matter and inhomogeneity with a different time evolution [76]. However, future measurements and observations of the time dependence of the CMB polarization in proximity of massive galaxy clusters [77].

- GR holds at all scales. As we mentioned in the previous section, GR is both theoretically and experimentally robust. It is therefore logical that the standard model of cosmology relies on a general relativistic description of the Universe.

We shall now see how the two assumptions above lead naturally to an expanding Universe solution. Let us begin by considering the metric tensor $g_{\mu\nu}$. The cosmological principle leads to a very simple form of the metric tensor. The isotropy assumption requires the spatial part of the metric tensor to be spherically symmetric while the homogeneity implies that this spatial spherical symmetry has to be the same for different comoving observers. There are three types of spatial curvatures that respect the homogeneity principle: a spatially flat Universe, a hyper-spherical closed Universe and a hyperbolic open Universe. The line element with a metric tensor with the above properties takes the Friedmann-Robertson-Walker (FRW) form,

$$ds^2 = -dt^2 + a(t)^2 \left[dr^2 + S_\kappa^2(r, R) d\Omega \right], \quad (2.11)$$

where a is the scale factor, t is the cosmic time, r is the radial, co-moving distance around the observer, R is the curvature radius of the Universe, and the function $S_\kappa(r, R)$ depends on the geometry of the Universe. We have

$$\begin{aligned} S_\kappa(r, R) &= r && \text{if } \kappa = 0 && \text{(flat geometry),} \\ S_\kappa(r, R) &= R \sin(r/R) && \text{if } \kappa = +1 && \text{(closed geometry),} \\ S_\kappa(r, R) &= R \sinh(r/R) && \text{if } \kappa = -1 && \text{(open geometry).} \end{aligned}$$

The scale factor $a(t)$ controls how the physical distance between different comoving observers evolves with time. For two observers at two different comoving coordinates \mathbf{x}_1 and \mathbf{x}_2 , the

physical distance separating them (at the same cosmic time t) is given by

$$d_{\text{phys}} = a(t)|\mathbf{x}_1 - \mathbf{x}_2|. \quad (2.12)$$

Being able to detect $\dot{a} > 0$ is hence an important proof of the expanding Universe.

Throughout this work we will mainly focus on the flat Universe. The flatness is experimentally well tested. For a flat Universe the line element (2.11) assumes the simple form

$$ds^2 = -dt^2 + a^2(t)\delta_{ij}dx^i dx^j. \quad (2.13)$$

This line element can also be written as

$$ds^2 = a^2(\tau) \left[-d\tau^2 + \delta_{ij}dx^i dx^j \right], \quad (2.14)$$

by introducing the conformal time τ defined through

$$d\tau = \frac{dt}{a(t)}. \quad (2.15)$$

The conformal time is useful to follow photons geodesics, for which $ds = 0$, and helps us to introduce the concept of cosmological *redshift*. Let us suppose that two photons were emitted at time t_{em} and $t_{\text{em}} + dt_{\text{em}}$ from a source at comoving position x and reached us at t_0 and $t_0 + dt_0$. Since photons are travelling along the lightcone lines, the conformal time separation between the two photons at emission and detection will be the same: $d\tau_{\text{em}} = d\tau_0$. This means that the emitted and observed frequency are different by a factor of

$$\frac{\nu_{\text{em}}}{\nu_0} \sim \frac{dt_0}{dt_{\text{em}}} = \frac{1}{a_{\text{em}}}, \quad (2.16)$$

where we set $a_0 \equiv 1$. The observed wavelength λ_0 is then related to the emitted wavelength λ_{em} by

$$1 + z \equiv \frac{\lambda_0}{\lambda_{\text{em}}} = \frac{1}{a_{\text{em}}}, \quad (2.17)$$

where z is the redshift parameter. This is exactly what Hubble observed [78]. The spectral lines of the abundant elements in distant galaxies are shifted to higher wavelengths *i.e.* towards more red colors. Since $\lambda_0 > \lambda_{\text{em}}$, this means that the scale factor at the emission time was smaller than the scale factor today, hence the Universe is expanding! This relation also implies that, if the scale factor is a monotonic function of time, we can refer to times in the Universe using the scale factor a or, equivalently, the redshift z .

2.2.1 Matter Content of the Universe

Because of the symmetries of a homogeneous and isotropic Universe, its matter content can only be described as a perfect fluid whose energy-momentum tensor is given by

$$T_{\mu\nu} = (\rho + P)u_\mu u_\nu + P g_{\mu\nu}, \quad (2.18)$$

where ρ is the energy density, P is the pressure and u^μ is the four-velocity of the fluid. For the FRW background the 4-velocity of the comoving observers is simply $u^\mu \equiv (-1, 0, 0, 0)$. The evolution of the matter fields is obtained from the conservation of the energy-momentum tensor equation (2.5). Taking $\nu = 0$ in Eq. (2.5) leads to the energy conservation equation,

$$\dot{\rho} + 3\mathcal{H}(\rho + P) = 0, \quad (2.19)$$

where overdots represent derivatives with respect to the conformal time τ and $\mathcal{H} \equiv \dot{a}/a$ is the conformal time Hubble parameter. The Hubble parameter with respect to cosmic time is usually denoted as

$$H = \frac{1}{a} \frac{da}{dt} = \frac{\mathcal{H}}{a}. \quad (2.20)$$

The energy conservation equation can be solved once we know the Equation of State (EoS) of the fluid $w = P/\rho$. For non-relativistic uncoupled fluids, $w = 0$ and $\rho \sim a^{-3}$. This pressure-less fluid models non-relativistic matter such as the homogeneous distribution of Cold Dark Matter (CDM) and baryons. Relativistic species such as photons and massless neutrinos have the equation of state $w = 1/3$ and their energy density scales as $\rho \sim a^{-4}$. For species with a time dependent equation of state, such as massive neutrinos that transition from being a relativistic component in the early Universe to a pressure-less components in the late-time Universe, the energy density evolves as

$$\rho(a) = \rho^0 \exp \left[-3 \int_a^1 d \ln a (1 + w(a)) \right], \quad (2.21)$$

where we defined the energy density at present time as $\rho^0 \equiv \rho(a_0)$ and we set the present time scale factor as $a_0 \equiv 1$.

The evolution of the scale factor can be obtained by plugging the metric (2.11) and the energy momentum tensor of the components of the Universe into the Einstein equations (2.3). For the $\mu = \nu = 0$ equation we obtain the Friedmann equation

$$\mathcal{H}^2 = \frac{\rho a^2}{3m_0^2} + \frac{\Lambda}{3} - \kappa, \quad (2.22)$$

which connects the expansion rate, \dot{a}/a , with the energy density in the Universe, its curvature κ and the cosmological constant (CC) Λ . The CC represents a constant term in the Friedmann equation and can be treated as a perfect fluid with constant energy den-

sity $\rho_\Lambda = m_0^2 \Lambda$. By requiring $\dot{\rho}_\Lambda = 0$ we obtain from the conservation equation (2.5) that $P_\Lambda = -\rho_\Lambda$. Hence the EoS of the cosmological constant is that of vacuum energy, *i.e.* $w_\Lambda = -1$. The overall fluid of the Universe is made up of several components, so by denoting its the total energy density as ρ_{tot} and its total pressure as P_{tot} we can define an effective EoS as

$$w_{\text{eff}} = \frac{P_{\text{tot}}}{\rho_{\text{tot}}}. \quad (2.23)$$

It is also useful to define the concept of *critical density*, *i.e.* the present time density of a flat Universe, $\kappa = 0$,

$$\rho_{\text{crit}}^0 = 3m_0^2 H_0^2. \quad (2.24)$$

The Friedmann equation can then be rewritten as

$$H^2(a) = H_0^2 \left[\Omega_m a^{-3} + \Omega_r a^{-4} + \Omega_\kappa a^{-2} + \Omega_\Lambda \right] \quad (2.25)$$

where we introduced the matter density parameters $\Omega_i \equiv \rho_i^0 / \rho_{\text{crit}}^0$ for matter radiation and the cosmological constant, while for curvature we have $\Omega_\kappa \equiv \kappa / \rho_{\text{crit}}^0$.

By combining the 00 and *ii* Einstein equations, we can also obtain the second Friedmann equation, or the *acceleration equation*,

$$\frac{\ddot{a}}{a} = -\frac{1}{6m_0^2} \sum_i (\rho + 3P) + \frac{1}{3m_0^2} \rho_\Lambda, \quad (2.26)$$

2.2.2 Distances

In an expanding Universe, the physical distance between two objects located at two fixed co-moving points changes with time. If their co-moving distance is χ , then the physical distance D_{phys} between them scales as

$$D_{\text{phys}}(t) = a(t)\chi. \quad (2.27)$$

If we consider the change in the physical distance, we obtain the Hubble law

$$\dot{D}_{\text{phys}} = \frac{\dot{a}}{a} a \chi = H D_{\text{phys}}, \quad (2.28)$$

stating that the recessional velocity of nearby galaxies is proportional to their distance to us. Therefore, light emitted with wavelength λ_{em} by a source moving away from us will be redshifted, *i.e.* its wavelength will be stretched according to

$$1 + z = \frac{\lambda_{\text{obs}}}{\lambda_{\text{em}}}, \quad (2.29)$$

where λ_{obs} is the observed wavelength and z is the redshift.

When observing galaxies, usually we typically detect their size, their brightness and their redshifts. In an expanding Universe, the concept of distance depends on the observable we use to define it. For example we could infer the *angular distance* to a galaxy, by looking at the angle subtended by the galaxy on the sky, while from the detected flux of photons we could infer the *luminosity distance*. In a flat spacetime, the two distances are equivalent but as we will shortly show they are different in an expanding background. We first define the comoving distance from a source at scale factor a to us. It is defined as the distance travelled by a light on the comoving grid and it is given by

$$\chi(a) = \int_{t(a)}^{t_0} \frac{dt'}{a(t')} = \int_a^1 \frac{da'}{a'^2 H(a')} = \int_0^z \frac{dz'}{H(z')}. \quad (2.30)$$

From this definition the *comoving horizon* is defined as the distance travelled by light from the initial time $t = 0$ until now and it reads

$$\chi_0 = \int_0^{t_0} \frac{dt'}{a(t')}. \quad (2.31)$$

Angular diameter distance For an object of known physical length ℓ that subtends an angle θ in the sky, the *angular diameter distance* is defined as

$$D_A \equiv \frac{\ell}{\theta}. \quad (2.32)$$

In an expanding Universe, the distance to the source (galaxy) is given by its comoving distance, multiplied by the scale factor, so that we can write the subtended angle as

$$\theta = \frac{\ell/a}{\chi(a)}. \quad (2.33)$$

Plugging the above equation in the definition for the angular distance we find

$$D_A = a\chi(a), \quad (2.34)$$

or, converting the scale factor to redshift,

$$D_A = \frac{\chi(z)}{1+z}. \quad (2.35)$$

In Fig. 2.1 we show the angular diameter distance D_A for the Λ CDM model and the Einstein-de Sitter model (with $\Omega_m = 1$).

Luminosity distance. The luminosity distance is defined by comparing the luminosity L_s of a source with its observed brightness, or *flux* F . For a source emitting photons at a

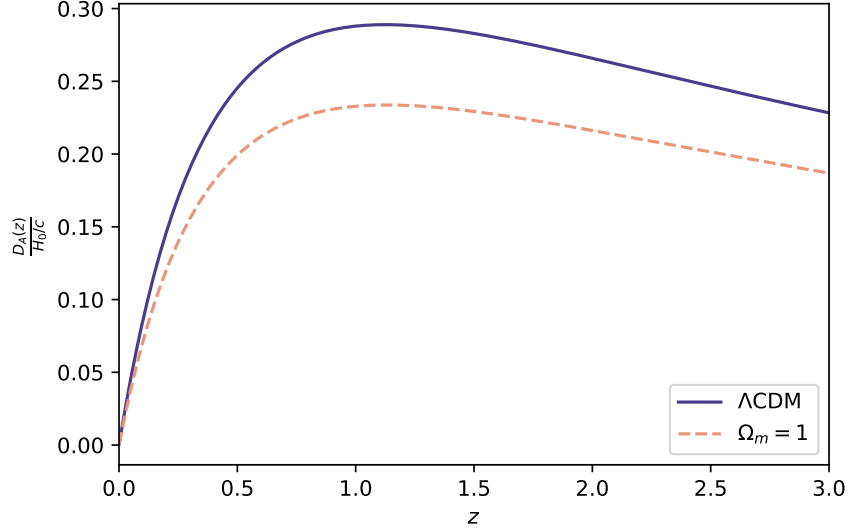


Figure 2.1: Angular diameter distance $D_A(z)$ in units of H_0/c for the Λ CDM model with $\Omega_m = 0.295$ (blue solid line) and for the Einstein-de Sitter model with $\Omega_m = 1$ (orange dashed line).

single energy, its luminosity is given by

$$L_s = \frac{N_\gamma E_{\gamma \text{ em}}}{\Delta t_{\text{em}}}, \quad (2.36)$$

where N_γ is the number of photons of energy $E_{\gamma \text{ em}}$ emitted in the time Δt_{em} . To get the luminosity distance we have to take into account first that in an expanding background the photon's energy decreases due to the cosmological redshift,

$$a_{\text{em}} E_{\gamma \text{ em}} = a_{\text{obs}} E_{\gamma \text{ obs}} \quad (2.37)$$

and second, that the number of photons received in the interval Δt_{obs} also decreases according to Eq. (2.16),

$$\frac{\Delta t_{\text{em}}}{\Delta t_{\text{obs}}} = \frac{a_{\text{em}}}{a_{\text{obs}}} \quad (2.38)$$

The *flux* measured by an observer at comoving distance $\chi(a_{\text{em}})$ is given by the number N_γ of photons with energy $E_{\gamma \text{ obs}} = a_{\text{em}} E_{\gamma \text{ em}}$ observed in the interval Δt_{obs} that cross the spherical shell of comoving distance $\chi(a_{\text{em}})$,

$$F = \frac{N_\gamma E_{\gamma \text{ obs}}}{\Delta t_{\text{obs}}} \frac{1}{4\pi\chi(a_{\text{em}})^2} = \frac{N_\gamma E_{\gamma \text{ em}}}{\Delta t_{\text{em}}} \frac{a_{\text{em}}^2}{4\pi\chi(a_{\text{em}})^2} = \frac{L_s a_{\text{em}}^2}{4\pi\chi(a_{\text{em}})^2} = \frac{L_s}{4\pi D_L^2}, \quad (2.39)$$

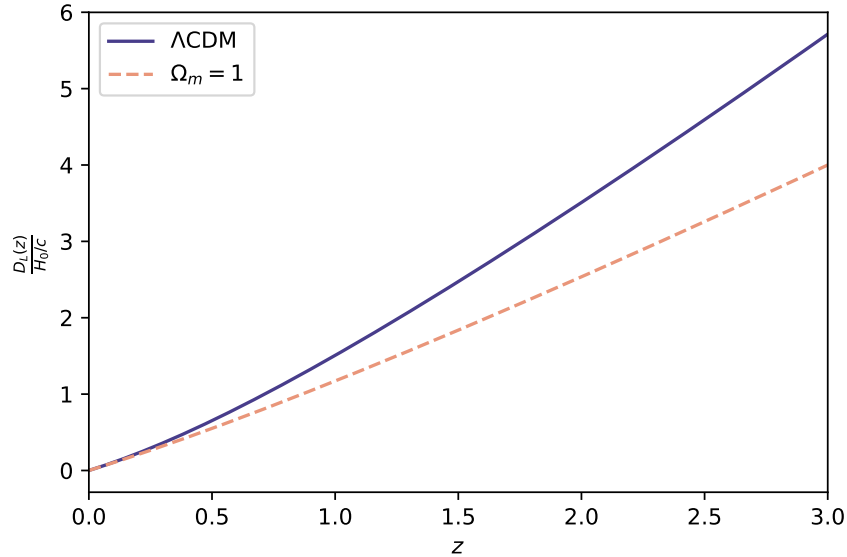


Figure 2.2: Luminosity distance $D_L(z)$ in units of H_0/c for the Λ CDM model with $\Omega_m = 0.295$ (blue solid line) and for the Einstein-de Sitter model with $\Omega_m = 1$ (orange dashed line).

where D_L is defined through the last equality. The luminosity distance to a source at redshift z is thus given by

$$D_L(z) = \frac{\chi(a)}{a} = (1+z)\chi(z). \quad (2.40)$$

Observations of standard candles, *i.e.* objects with a known luminosity, provide us with the luminosity distance as a function of redshift. The shape of $D_L(z)$ depends on how the Hubble parameter $H(z)$ changes as a function of redshift and hence depends on the matter content of the Universe. In Fig. 2.2 we compare the luminosity distance for the flat Λ CDM model with $\Omega_m = 0.295$ (blue solid line) and the Einstein-de Sitter matter dominated Universe with $\Omega_m = 1$ (orange dashed line). In the late 1990s, observations of the luminosity distance of Type Ia Supernovae, revealed that the Universe is in the phase of accelerated expansion. In Sect. 3.1.1 we will give the details of the Supernovae analysis that will be later used in other parts of the thesis.

2.3 Inhomogeneities in the expanding Universe

The Universe described in the previous section is smooth and homogeneous. We call it the background, or “zero order” description of the Universe. Indeed, observations of the CMB show a very smooth, homogeneous Universe at redshift $z \sim 1090$. However, at lower redshifts, $z \lesssim 10$, the observed Universe looks rather inhomogeneous, filled with galaxies, galaxy clusters and vast void regions. Studying how these observed structures formed start-

ing from a nearly homogeneous distribution provides a powerful tool for testing gravity on cosmological scales.

The goal of this section is to provide a brief introduction of the cosmological perturbation theory. The idea is to start from a nearly homogeneous distribution of matter in the Universe and see how small perturbations in the metric and energy-momentum tensors evolve under the gravitational interaction.

Intuitively we can think of structure formation in the following way. Let us imagine that in a small patch of the Universe the mass density is slightly larger than in the rest of the Universe. This little patch will start attracting more and more matter from the neighbouring regions, finally becoming very massive. This idea is at the basis of the growth of structure through *gravitational instability*. The gravitational pull into this region will then stop when the pressure forces of the matter inside this region become comparable to the gravitational forces. To grasp the idea of gravitational instability in a slightly more mathematical way, in the next subsection we discuss a simple Newtonian case, with a fluid moving under the influence of gravity. This model allows us to introduce the concept of gravitational instability and *Jeans length*, that are also present in the general relativistic scenario. Then in the following subsections we will review the relativistic perturbation theory.

2.3.1 Gravitational Instability and Jeans Length

Let us consider a fluid with density ρ and pressure P moving with velocity v under the influence of the Newtonian gravitational potential Φ . As briefly mentioned above, there are two types of forces acting in opposite ways in this scenario. Gravity attracts matter into overdense regions, while pressure repels them. As we will shortly see, the gravitational instability arises when the force exerted by pressure cannot overcome the gravitational force. The dynamics of the fluid we consider is governed by the continuity, Euler and Poisson equations,

$$\frac{D\rho}{Dt} + \rho\nabla\mathbf{v} = 0, \quad (2.41)$$

$$\frac{D\mathbf{v}}{Dt} = -\frac{\nabla P}{\rho} - \nabla\Phi, \quad (2.42)$$

$$\nabla^2\Phi = 4\pi G\rho, \quad (2.43)$$

where

$$\frac{D}{Dt} \equiv \frac{\partial}{\partial t} + \mathbf{v} \cdot \nabla, \quad (2.44)$$

is the convective time derivative and express the variation of a quantity as it moves with the fluid. To close the system of equations, one needs to express the pressure P in terms of the density ρ and the entropy S . Here, for simplicity, we assume that the fluid pressure

depends only on its density, $P = P(\rho)$ so that one can write the gradient of the pressure as

$$\vec{\nabla}P = \left(\frac{\partial P}{\partial \rho}\right)_S \vec{\nabla}\rho = c_s^2 \vec{\nabla}\rho, \quad (2.45)$$

where we defined the speed of sound c_s^2 as

$$c_s^2 \equiv \left(\frac{\partial P}{\partial \rho}\right)_S^{1/2}. \quad (2.46)$$

The subscript S denotes the variation performed keeping the entropy constant. Let us assume that the fluid configuration can be described as small perturbations around the static background values of density and pressure. Let us introduce the small parameter ϵ to keep track of the perturbation order. We will restrict to small perturbations, so that quantities $\mathcal{O}(\epsilon^2)$ can be ignored. The quantities entering the continuity, Euler and Poisson equations can then be written as

$$\rho = \bar{\rho}[1 + \epsilon\delta(t, \mathbf{r})], \quad (2.47)$$

$$\mathbf{v} \rightarrow \epsilon\mathbf{v}(t, \mathbf{r}), \quad (2.48)$$

$$\Phi \rightarrow \epsilon\Phi(t, \mathbf{r}), \quad (2.49)$$

$$\vec{\nabla}P \rightarrow \epsilon\bar{\rho}c_s^2\vec{\nabla}\delta \quad (2.50)$$

Neglecting $\mathcal{O}(\epsilon^2)$ terms, and working in Fourier space, the fluid equations read

$$\dot{\delta} + i\mathbf{k} \cdot \mathbf{v} = 0, \quad (2.51)$$

$$\dot{\mathbf{v}} + c_s^2 i\mathbf{k}\delta + i\mathbf{k}\Phi, \quad (2.52)$$

$$k^2\Phi = -4\pi G\bar{\rho}\delta. \quad (2.53)$$

The three equations above can be combined in the gravitational collapse equation that reads,

$$\ddot{\delta} + [k^2c_s^2 - 4\pi G\bar{\rho}] \delta = 0. \quad (2.54)$$

This equation can be simply solved by considering an exponential solution for the density perturbation, i.e. $\delta \sim \exp(\lambda t)$. Let us first define the *Jeans* wavevector k_J such that

$$k_J^2c_s^2 = 4\pi G\bar{\rho}. \quad (2.55)$$

From k_J we can then define the *Jeans length*, as $\lambda_J = 2\pi/k_J$. The physical meaning of the Jeans length is to define the wavelengths of the perturbations for which the pressure force exactly cancels the gravitational force. For scales smaller than the Jeans length, $k > k_J$,

the parenthesis in Eq. (2.54) is positive and the solution is a propagating acoustic wave,

$$\delta \sim \exp \left[\pm i \sqrt{k^2 c_s^2 - 4\pi G \bar{\rho}} t \right]. \quad (2.56)$$

However, for scales larger than the Jeans length, $k < k_J$, the pressure does not support the gravitational force and the perturbation becomes an exponentially growing solution,

$$\delta \sim \exp \left[\sqrt{4\pi G \bar{\rho} - k^2 c_s^2} t \right]. \quad (2.57)$$

The simple model described in this subsection is very powerful and with the proper modifications can be even extended to an expanding background. As we will see shortly, the expanding background will provide a friction term in the gravitational collapse equation that will dampen the amplitude of the perturbations. This simple model can still be employed as a starting point to study structure formation in the late-time Universe, when radiations and horizon effects are negligible.

2.3.2 Linear Relativistic Perturbation Theory

When describing the evolution of perturbations in the early Universe, when radiation is relevant, or on scales that are close to the horizon, it becomes necessary to use the general relativistic machinery for structure formation that we are about to introduce. General relativity is also needed to describe late time effects involving neutrinos and the lensing of photons by the matter distribution. Because of the observed isotropy of the CMB, we expect that linear perturbation theory will describe fairly well the early Universe, breaking down only at later times below the scales of galaxy clusters.

We consider small perturbations around the flat FRW metric (2.14),

$$g_{\mu\nu} = \bar{g}_{\mu\nu} + \delta g_{\mu\nu}, \quad (2.58)$$

where $\bar{g}_{\mu\nu}$ is the flat FRW background metric and $\delta g_{\mu\nu}$ are the perturbations to the background metric. Perturbation theory is valid as long as the perturbations $\delta g_{\mu\nu}$ are small, which in this context means

$$|\delta g_{\mu\nu}| \ll \max_{\mu,\nu} \bar{g}_{\mu\nu}. \quad (2.59)$$

We also consider small perturbations in the energy-momentum tensor,

$$T_{\mu\nu} = \bar{T}_{\mu\nu} + \delta T_{\mu\nu}, \quad (2.60)$$

where a condition analogous to the equation (2.59) has to hold for the quantities $\delta T_{\mu\nu}$. Using the metric (2.58) we can then derive all the other perturbed geometrical quantities, such as the Cristoffel symbols, the Ricci tensor and the Ricci scalar, and write the Einstein

equations

$$\bar{G}_{\mu\nu} + \delta G_{\mu\nu} = \frac{1}{m_0^2} (\bar{T}_{\mu\nu} + \delta T_{\mu\nu}). \quad (2.61)$$

Because the background quantities satisfy the background Einstein equations $\bar{G}_{\mu\nu} = m_0^{-2} \bar{T}_{\mu\nu}$ (the Friedmann equations if $\bar{g}_{\mu\nu}$ is the FRW metric), then the metric perturbations evolve according to the perturbed Einstein equations,

$$\delta G_{\mu\nu} = \frac{1}{m_0^2} \delta T_{\mu\nu}. \quad (2.62)$$

Matter perturbations evolve then according to the perturbed conservation equation

$$\partial_\mu (\delta T_\nu^\mu) + \bar{\Gamma}_{\mu\alpha}^\mu \delta T_\nu^\alpha + \delta \Gamma_{\mu\alpha}^\mu \bar{T}_\nu^\alpha - \bar{\Gamma}_{\mu\nu}^\alpha \delta T_\alpha^\mu - \delta \Gamma_{\mu\nu}^\alpha \bar{T}_\alpha^\mu = 0. \quad (2.63)$$

In the following we will develop in detail the equations above. The complications in GR arise from the fact that one has the freedom to choose the coordinate systems. In perturbation theory these choices are known as *gauges*, and historically have created some confusion in understanding the evolution of the perturbations. One can in principle work with Gauge invariant quantities, as pioneered by Bardeen [79] and later developed by Durrer [80]. In this thesis we will mainly work by choosing the proper gauge when describing the physics we wish to investigate. Because we will use different gauges, in this section we present the general formalism without fixing the gauge, leaving the specific choice to the following chapters.

For a general metric perturbation, the line element can be written as

$$ds^2 = -a^2(\tau) [1 + 2A] d\tau^2 - 2a^2(\tau) B_i d\tau dx^i + a^2(\tau) (\delta_{ij} + 2H_{ij}) dx^i dx^j, \quad (2.64)$$

where the quantities A , B_i and H_{ij} are the perturbation quantities. As we have seen above, the cosmological principle implies that the background metric is symmetric under spatial rotations and spatial translations. It is then reasonable to decompose the perturbation quantities into the irreducible representations of the rotations, *i.e.* scalar, vector and tensor components. Also, because of the translational symmetry, it is useful to perform a harmonic analysis, that means we should work in Fourier space. Scalar, vector and tensor components evolve independently, as well as different Fourier modes. In a spatially flat background we can expand a scalar function f in terms of its Fourier transforms as

$$f(\tau, \mathbf{x}) = \frac{1}{\sqrt{(2\pi)^3}} \int d^3 \mathbf{k} e^{i\mathbf{k}\cdot\mathbf{x}} f(\tau, \mathbf{k}). \quad (2.65)$$

We can re-write the expansion above as

$$f(\tau, \mathbf{x}) = \sum_{\mathbf{k}} Q_{\mathbf{k}}^{(0)}(\mathbf{x}) f(\tau, \mathbf{k}), \quad (2.66)$$

where the function $Q_{\mathbf{k}}^{(0)}(\mathbf{x}) \equiv \exp[i\mathbf{k} \cdot \mathbf{x}]$ is an eigenfunction of the Laplacian operator, *i.e.*

$$\square Q_{\mathbf{k}}^{(0)} = -k^2 Q_{\mathbf{k}}^{(0)}, \quad (2.67)$$

that transforms as a scalar under the group of spatial rotations SO(3). Irrotational (*i.e.* curl-free or “scalar”) components of a vector field, can be expanded in terms of the quantities $Q_i^{(0)}$ obtained by simply taking a derivative of the quantities $Q^{(0)}$,

$$Q_i^{(0)} \equiv -\frac{1}{k} \nabla_i Q^{(0)} = -i \hat{k}_i e^{i\mathbf{k} \cdot \mathbf{x}}, \quad (2.68)$$

while the “scalar” component of a tensor field can be expanded in terms of the functions $Q_{ij}^{(0)}$ defined as

$$Q_{ij}^{(0)} \equiv \frac{1}{k^2} \nabla_i \nabla_j Q^{(0)} + \frac{1}{3} \delta_{ij} Q^{(0)} = -\left(\hat{k}_i \hat{k}_j - \frac{1}{3} \delta_{ij} \right) e^{i\mathbf{k} \cdot \mathbf{x}}. \quad (2.69)$$

Vector (or divergence-free) components of a field are expanded in terms of the spin-1 eigenfunctions of the Laplacian,

$$\square Q_i^{(\pm 1)} = -k^2 Q_i^{(\pm 1)}, \quad (2.70)$$

where the sign (± 1) denotes that there are two independent solutions corresponding to two different helicity states of the functions. The two vector harmonics are written as

$$Q_i^{(\pm 1)} = e_i^{(\pm)} e^{i\mathbf{k} \cdot \mathbf{x}}, \quad (2.71)$$

where $\mathbf{e}^{(\pm)}$ are the helicity basis vectors,

$$e_i^{(\pm)} = -\frac{i}{\sqrt{2}} (e_i^1 \pm i e_i^2), \quad (2.72)$$

and \mathbf{e}^1 and \mathbf{e}^2 are two unit vectors orthogonal to $\hat{\mathbf{k}}$. The functions $Q_i^{(\pm 1)}$ satisfy the divergence-less condition

$$\delta^{ij} \nabla_j Q_i^{(\pm 1)} = 0. \quad (2.73)$$

The “vector” components of a tensor field can be constructed out of the functions

$$Q_{ij}^{(\pm 1)} = -\frac{1}{2k} \left(\nabla_i Q_j^{(\pm 1)} + \nabla_j Q_i^{(\pm 1)} \right) = -\frac{i}{2} \left(e_i^{(\pm)} \hat{k}_j + e_j^{(\pm)} \hat{k}_i \right) e^{i\mathbf{k} \cdot \mathbf{x}}. \quad (2.74)$$

Finally, the “intrinsically” tensorial quantities are expanded in terms of the 2 independent spin-2 eigenfunctions of the Laplacian operator,

$$\square Q_{ij}^{(\pm 2)} = -k^2 Q_{ij}^{(\pm 2)}, \quad (2.75)$$

that satisfy the divergence-free condition

$$\delta^{ik}\nabla_k Q_{ij}^{(\pm 2)} = 0, \quad (2.76)$$

and the trace-free condition,

$$\delta^{ij}Q_{ij}^{(\pm 2)} = 0. \quad (2.77)$$

The tensor harmonics $Q_{ij}^{(\pm 2)}$ are written in terms of the tensors $e_{ij}^{(\pm 2)}$,

$$Q_{ij}^{(\pm 2)} = e_{ij}^{(\pm 2)} e^{i\mathbf{k}\cdot\mathbf{x}}, \quad (2.78)$$

where $e_{ij}^{(\pm 2)}$ are defined as

$$e_{ij}^{(\pm 2)} = \sqrt{\frac{3}{2}} e_i^{(\pm 1)} e_j^{(\pm 1)}. \quad (2.79)$$

With the quantities introduced above, we can decompose the metric perturbations A , B_i and H_{ij} as

$$A = A^{(0)}Q^{(0)}, \quad (2.80)$$

$$B_i = B^{(0)}Q_i^{(0)} + B^{(\pm 1)}Q_i^{(\pm 1)}, \quad (2.81)$$

$$H_{ij} = H_L Q^{(0)}\delta_{ij} + H_T Q_{ij}^{(0)} + H^{(\pm 1)}Q_{ij}^{(\pm 1)} + H^{(\pm 2)}Q_{ij}^{(\pm 2)}. \quad (2.82)$$

It is understood that for vector and tensor components, we are summing over the independent helicity modes,

$$B^{(\pm 1)}Q_i^{(\pm 1)} = B^{(+1)}Q_i^{(+1)} + B^{(-1)}Q_i^{(-1)}. \quad (2.83)$$

The 10 functions $A^{(0)}$, $B^{(0)}$, $B^{(\pm 1)}$, H_L , H_T , $H^{(\pm 1)}$ and $H^{(\pm 2)}$ constitute all the perturbations of the metric tensor.

Similarly, we introduce small perturbations on the energy-momentum tensor of a perfect fluid,

$$T_{\mu\nu} = \bar{T}_{\mu\nu} + \delta T_{\mu\nu}, \quad (2.84)$$

where the perturbations of the energy momentum tensor are

$$\delta T_0^0 = -\bar{\rho}\delta, \quad (2.85)$$

$$\delta T_0^i = -(\bar{\rho} + \bar{P})v^i, \quad (2.86)$$

$$\delta T_i^0 = (\bar{\rho} + \bar{P})(v_i - B_i), \quad (2.87)$$

$$\delta T_j^i = \bar{P}\pi_j^i. \quad (2.88)$$

We can expand the perturbations above as

$$\delta = \delta^{(0)}Q^{(0)}, \quad (2.89)$$

$$v_i = v^{(0)}Q_i^{(0)} + v^{(\pm 1)}Q_i^{(\pm 1)}, \quad (2.90)$$

$$\pi_j^i = \pi_L Q^{(0)}\delta_j^i + \pi_T Q_{ij}^{(0)} + \pi^{(\pm 1)}Q_{ij}^{(\pm 1)} + \pi^{(\pm 2)}Q_{ij}^{(\pm 2)}. \quad (2.91)$$

2.3.3 Gauge Transformations

When describing perturbations of the metric tensor $g_{\mu\nu}$, we can choose any coordinate system. Of course, perturbations in different frames are going to be different. However, since we are considering perturbations around a fixed background metric, we are going to restrict to “small” coordinate transformations that leave the background metric invariant,

$$g \rightarrow \tilde{g} = g + \epsilon L_X g, \quad (2.92)$$

where ϵ is a small parameter and L_X is the Lie derivative of the metric tensor g along the vector field X that generates the infinitesimal coordinate transformation. These infinitesimal coordinates transformations are usually referred to as *gauge transformations*. We shall now see how the gauge transformations change the metric tensor. To be specific, let us pick a vector field X of the following form

$$X^\mu = (T, L^i), \quad (2.93)$$

where the spatial component can be decomposed as

$$L_i = L^{(0)}Q_i^{(0)} + L^{(\pm 1)}Q_i^{(\pm 1)}. \quad (2.94)$$

The Lie derivative of the metric tensor is given by

$$(L_X g)_{\mu\nu} = X^\alpha (\partial_\alpha g_{\mu\nu}) + (\partial_\mu X^\alpha) g_{\alpha\nu} + (\partial_\nu X^\alpha) g_{\mu\alpha}, \quad (2.95)$$

and the Lie derivative of the energy-momentum tensor is, similarly,

$$(L_X T)_{\mu\nu} = X^\alpha (\partial_\alpha T_{\mu\nu}) + (\partial_\mu X^\alpha) T_{\alpha\nu} + (\partial_\nu X^\alpha) T_{\mu\alpha}. \quad (2.96)$$

The perturbation components of the metric tensor then transform as

$$\tilde{A} = A + \mathcal{H}T + \dot{T}, \quad (2.97)$$

$$\tilde{B}^{(0)} = B^{(0)} - \dot{L}^{(0)} - kT^{(0)}, \quad (2.98)$$

$$\tilde{B}^{(\pm 1)} = B^{(\pm 1)} - \dot{L}^{(\pm 1)}, \quad (2.99)$$

$$\tilde{H}_L = H_L + \mathcal{H}T^{(0)} + \frac{k}{3}L^{(0)}, \quad (2.100)$$

$$\tilde{H}_T = H_T - kL^{(0)}, \quad (2.101)$$

$$\tilde{H}^{(\pm 1)} = H^{(\pm 1)} - kL^{(\pm 1)}, \quad (2.102)$$

$$\tilde{H}^{(\pm 2)} = H^{(\pm 2)}, \quad (2.103)$$

while the components of the energy-momentum tensor similarly transform as

$$\tilde{\delta}^{(0)} = \delta^{(0)} - 3\mathcal{H}(1+w)T^{(0)}, \quad (2.104)$$

$$\tilde{v}^{(0)} = v^{(0)} - \dot{L}^{(0)}, \quad (2.105)$$

$$\tilde{v}^{(\pm 1)} = v^{(\pm 1)} - \dot{L}^{(\pm 1)}, \quad (2.106)$$

$$\tilde{\pi}_L = \pi_L - 3\frac{c_s^2}{w}(1+w)\mathcal{H}T, \quad (2.107)$$

$$\tilde{\pi}_T = \pi_T, \quad (2.108)$$

$$\tilde{\pi}^{(\pm 1)} = \pi^{(\pm 1)}, \quad (2.109)$$

$$\tilde{\pi}^{(\pm 2)} = \pi^{(\pm 2)}. \quad (2.110)$$

There are at least three remarks at this point.

- *Gauge dependence.* Quite obviously from the above discussion, perturbations of the metric and the energy-momentum tensor depend on the frame used to describe the perturbations. Let us first consider the scalar perturbations. There are four functions for the metric tensor perturbations, A , $B^{(0)}$, H_L and H_T and four functions for the energy-momentum tensor perturbations, $\delta^{(0)}$, $v^{(0)}$, π_L and π_T . Among these, up to two functions can be set to zero using the two scalar components of the gauge vector field X , i.e. T and $L^{(0)}$.
- Another important remark regards the *gauge independence*. We have just seen that in general one can set to zero up to four perturbations by proper choice of gauge. However, there is not enough freedom to set all the perturbations to zero: remember that a symmetric tensor (such as the perturbed $g_{\mu\nu}$) has 10 degrees of freedom, while the gauge choice allows to set to zero up to four components, the same as the number of coordinates we can choose. Therefore, if a tensor is perturbed in a frame it is, in general, perturbed in all the frames, i.e. the perturbations are a gauge-independent concept.

- *Gauge-invariance.* While quantities are in general gauge-dependent, it is possible to define quantities that are gauge-invariant. This led to the development of the gauge-invariant perturbation theory by Bardeen [79] and later by Durrer [80]. For example, one can introduce the gauge-invariant scalar metric potentials, Φ and Ψ as

$$\Phi = -H_L - \frac{1}{3}H_T - \frac{\mathcal{H}}{k}B^{(0)} + \frac{\mathcal{H}}{k^2}\dot{H}_T, \quad (2.111)$$

$$\Psi = A^{(0)} + \frac{1}{k}\left(\dot{B}^{(0)} + \mathcal{H}B^{(0)}\right) - \frac{1}{k^2}\left(\ddot{H}_T + \mathcal{H}\dot{H}_T\right). \quad (2.112)$$

2.3.4 Evolution equations

Now that we have developed the essential tools to deal with the inhomogeneities in the Universe, we shall derive the evolution equations for each perturbation. The idea is quite simple, although the calculations are usually lengthy. From the perturbations of the metric tensor, $\delta g_{\mu\nu}$ we can derive the perturbations of the Christoffel symbols, $\delta\Gamma_{\beta\lambda}^\alpha$, and all the geometrical quantities entering the Einstein tensor, $\delta G_{\mu\nu}$ to write, at the end the perturbed Einstein equations

$$\delta G_{\mu\nu} = \frac{1}{m_0^2}\delta T_{\mu\nu}. \quad (2.113)$$

The Einstein equations are usually accompanied by the perturbed conservation equations,

$$\partial_\mu\delta T_\nu^\mu + \delta\Gamma_{\mu\alpha}^\mu\bar{T}_\nu^\alpha + \bar{\Gamma}_{\mu\alpha}^\mu\delta T_\nu^\alpha - \delta\Gamma_{\mu\nu}^\alpha\bar{T}_\alpha^\mu - \bar{\Gamma}_{\mu\nu}^\alpha\delta T_\alpha^\mu = 0. \quad (2.114)$$

We are now at a fork, meaning that we can choose two different approaches equally valid. Either we write down the Einstein equations and the conservation equations in terms of the gauge invariant quantities such as the Bardeen potentials seen above, or we can simply pick a gauge and write down the equations in that gauge. Since in the next chapters we will discuss different observables in the Universe, and since each of them has a gauge in which the equations are simpler, we choose here to write down the Einstein and the conservation equations in terms of all the gauge-dependent quantities. Then in the following chapters, as we will need to choose a gauge we will simply do all the necessary substitutions. Let us begin with the Einstein equations. The scalar components provide four equations, the (00),

(0*i*), (i*i*) and (i*j*) equations. They are written as

$$3\mathcal{H}^2 A - k\mathcal{H}B - 3\mathcal{H}\dot{H}_L - k^2 \left(H_L + \frac{H_T}{3} \right) = -\frac{a^2}{2m_0^2} \bar{\rho} \delta, \quad (2.115)$$

$$k\mathcal{H}A - k\dot{H}_L - \frac{k}{3}\dot{H}_T = \frac{a^2}{2m_0^2} (\bar{\rho} + \bar{P}) (v^{(0)} - B^{(0)}), \quad (2.116)$$

$$\left[\left(2\frac{\ddot{a}}{a} - \mathcal{H}^2 \right) A + \mathcal{H}\dot{A} - \frac{k^2}{3}A - \frac{k}{3}(\dot{B} + \mathcal{H}B) \right. \\ \left. - \frac{k}{3}\mathcal{H}B - \frac{(a\dot{H}_L)^\cdot}{a} - \mathcal{H}\dot{H}_L - \frac{k^2}{3} \left(H_L + \frac{H_T}{3} \right) \right] = \frac{a^2}{2m_0^2} \bar{P} \pi_L, \quad (2.117)$$

$$-k^2 A - k(\dot{B} + \mathcal{H}B) + \frac{(a\dot{H}_T)^\cdot}{a} + \mathcal{H}(\dot{H}_T - kB) - k^2 \left(H_L + \frac{H_T}{3} \right) = \frac{a^2}{m_0^2} \bar{P} \pi_T. \quad (2.118)$$

Next we can write the vector components of the Einstein equations, where we write the helicity modes superscripts as (1) to have a lighter notation. They provide two equations corresponding the (0*i*) and the (i*j*) components:

$$-\frac{k}{2a^2} (H^{(1)} - kB^{(1)}) = \frac{1}{m_0^2} (\bar{\rho} + \bar{P}) (v^{(1)} - B^{(1)}), \quad (2.119)$$

$$-k^2 (\dot{B}^{(1)} + \mathcal{H}B^{(1)}) + \frac{(a\dot{H}^{(1)})^\cdot}{a} + \mathcal{H}(\dot{H}^{(1)} - kB^{(1)}) = \frac{a^2}{m_0^2} \bar{P} \pi^{(1)}. \quad (2.120)$$

Finally, the tensor mode of the Einstein equations provide one single equation for the two modes (here again we denote both helicity modes symbols as (2)),

$$\frac{(a\dot{H}^{(2)})^\cdot}{a} + \mathcal{H}\dot{H}^{(2)} + k^2 H^{(2)} = \frac{a^2}{m_0^2} \bar{P} \pi^{(2)}. \quad (2.121)$$

As mentioned above, the above equations have to accompanied by the conservation equations of the energy-momentum tensor. For the scalar components they read,

$$\dot{\delta} + (1+w) (kv + 3\dot{H}_L) + 3\mathcal{H} (c_s^2 - w) \delta + 3\mathcal{H}w\Gamma = 0, \quad (2.122)$$

$$\left(\dot{v} - \dot{B} \right) + \mathcal{H}(1-3w)(v-B) + \frac{\dot{w}}{1+w}(v-B) \\ - \frac{w}{1+w}k\Gamma - \frac{c_s^2}{1+w}k\delta + \frac{2}{3}\frac{w}{1+w}k\pi_T - kA = 0, \quad (2.123)$$

where we used the gauge-invariant variable $\Gamma \equiv \pi_L - c_s^2 \delta / w$ proportional to the entropy flux. For the vector component we have

$$\left(\dot{v}^{(1)} - \dot{B}^{(1)} \right) + \mathcal{H}(1-3w)(v^{(1)} - B^{(1)}) + \frac{\dot{w}}{1+w}(v^{(1)} - B^{(1)}) + \frac{1}{2}\frac{w}{1+w}k\pi^{(1)} = 0. \quad (2.124)$$

2.3.5 The Boltzmann equation

When we need to describe interacting species in the early Universe, such as the photon-baryon fluid, the equations (2.122), (2.123) and (2.124) are not enough. Specifically, we need to take into account the energy-momentum transfer between the species and the *Boltzmann* equation formalism provides the tools to deal with this. The idea is to follow the evolution of the interacting fluids through their phase-space distribution function defined, on a spatial hypersurface, as

$$dN = f(x^i, P^j, \tau) d^3x d^3P \quad (2.125)$$

Here P^j is the spatial part of the contravariant 4-momentum P^μ . From the phase-space distribution function we can write the energy-momentum tensor as

$$T_\nu^\mu = \int \frac{d^3P}{\sqrt{-g}} \frac{P^\mu P_\nu}{P^0} f(x^i, P^j, \tau). \quad (2.126)$$

To specify the distribution function we want to express it in terms of the measured quantities in the frame of the co-moving observer. To do so, let us consider the ortho-normal tetrad $(E_\delta)^\mu$, $(E_{\hat{i}})^\mu$, where $(E_\delta)^\mu$ is time-like and it is pointing along the 4-velocity of the observer at rest. In terms of the coordinate basis we have

$$E_\delta = a^{-1}(1 - A)\partial_0 - a^{-1}B^i\partial_i, \quad (2.127)$$

$$E_{\hat{i}} = a^{-1}(1 - H_L)\partial_i - a^{-1}H_i^j\partial_j, \quad (2.128)$$

with B^i , H_i^j containing the scalar, vector and tensor (for the latter) components. In this frame we can write the four-momentum of the particles as

$$P^\mu = E(E_\delta)^\mu + p^{\hat{i}}(E_{\hat{i}})^\mu, \quad (2.129)$$

where E is the energy and $p^{\hat{i}}$ is the 3-momentum measured by the observer. In an expanding background it is useful to define the comoving energy $\epsilon \equiv aE$ and momentum $q = ap$ such that they are conserved in the background. The three-momentum can then be written as

$$p^{\hat{i}} = \frac{q}{a} e^{\hat{i}}, \quad (2.130)$$

where \mathbf{e} is the unit vector in the direction of the momentum. The on-shell condition with these variables then becomes

$$\epsilon^2 = q^2 + a^2 m^2, \quad (2.131)$$

with m being the rest mass of the particles. We can now write the phase-space distribution function in terms of these new variables, $f(\tau, \mathbf{x}, \epsilon, \mathbf{e})$. To follow the evolution of the perturbations of the particles we need to calculate the evolution of the time derivative of their

distribution function. This reads

$$\frac{df}{d\tau} = \frac{\partial f}{\partial \tau} + \frac{\partial f}{\partial \mathbf{e}} \frac{\partial \mathbf{e}}{\partial \tau} + \frac{\partial f}{\partial(\log \epsilon)} \frac{\partial(\log \epsilon)}{\partial \tau} + \frac{\partial f}{\partial x^i} \frac{\partial x^i}{\partial \tau} = C[f] \quad (2.132)$$

where $C[f]$ is the collisional integral and depends on the details of the interaction. Working with only linear perturbations makes the second term above vanish as it is a second order term: the direction of the momentum changes at first order since with no perturbations, momentum would be constant. Also, the dependence of the distribution function on the direction is a first order term, otherwise it would spoil the isotropy of the background distribution \bar{f} . The final Boltzmann equation of linear perturbation theory is then,

$$\frac{\partial f}{\partial \tau} + \frac{\partial \bar{f}}{\partial(\log \epsilon)} \frac{\partial(\log \epsilon)}{\partial \tau} + \frac{\partial f}{\partial x^i} \frac{\partial x^i}{\partial \tau} = C[f], \quad (2.133)$$

where \bar{f} is the background distribution function. At the background level the unperturbed (background) function has to respect the homogeneity and isotropy symmetries and thus, for massless particles, it assumes the Bose-Einstein (or Fermi-Dirac) form,

$$\bar{f}(\epsilon, \tau) = \frac{1}{e^{(E-\mu_c)/T} \pm 1} = \frac{1}{e^{(\epsilon/a-\mu_c)/T} \pm 1}, \quad (2.134)$$

where μ_c is the chemical potential that vanishes for photons. Perturbations of the distribution function are defined as

$$f(\tau, \mathbf{x}, \epsilon, \mathbf{e}) = \bar{f}(\epsilon, \tau) [1 + \psi(\tau, \mathbf{x}, \epsilon, \mathbf{e})], \quad (2.135)$$

with ψ containing the scalar, vector and tensor components. The Boltzmann equation for the perturbation ψ becomes

$$\frac{\partial \psi}{\partial \tau} + \psi \frac{\partial(\log \bar{f})}{\partial \tau} + \frac{\partial(\log \bar{f})}{\partial(\log \epsilon)} \frac{\partial(\log \epsilon)}{\partial \tau} + \frac{\partial \psi}{\partial x^i} \frac{q e^i}{\epsilon} = C[f]. \quad (2.136)$$

We can extract the scalar, vector and tensor components of the equation above by using the 0 component of geodesic equation,

$$P^0 \frac{dP^0}{d\tau} = -\Gamma_{\alpha\beta}^0 P^\alpha P^\beta, \quad (2.137)$$

to write $\partial(\log \epsilon)/\partial \tau$ in terms of the components of the metric perturbations. We shall not derive this equations in details as it is beyond the scope of this thesis. Finally, it is worth noticing that in the case of a thermal distribution, for examples for CMB photons of cosmic neutrinos, the perturbation of the distribution function is written in terms of the

temperature anisotropy Θ defined as

$$f = \bar{f} \left[1 - \frac{d \log \bar{f}}{d \log \epsilon} \Theta(\tau, \mathbf{x}, \mathbf{e}) \right]. \quad (2.138)$$

By plugging this definition in equation (2.136) one can write the Boltzmann equations for the temperature anisotropies of the CMB. We will review this in Chapter 3 when we will describe both temperature and polarization anisotropies of the CMB.

2.3.6 Gauge Choices

In principle, we have almost all the tools necessary to solve the equations for the perturbations of the metric and the energy-momentum tensor. The last thing are the initial conditions. Since solving the equations is the last step of the analysis, it is the perfect time to choose a gauge. Here we review the two most commonly used gauges, the conformal Newtonian gauge and the synchronous gauge. They are both restricted to describe scalar perturbations only for the following reason. Scalar perturbations are the only one affecting the large scale structure of the Universe since vector and tensor modes do not couple to pressure-less matter, such as (decoupled) baryons and dark matter. Also, the temperature anisotropies of the CMB are dominated by the scalar modes, although vector and tensor modes are important for extracting some interesting physics as we will discuss in the next chapters.

Newtonian gauge. This gauge is commonly used when studying structure formation and it is also used to formulate most of the phenomenology of modified gravity models. It is called “Newtonian” because the two scalar functions of the metric can be interpreted as the large scale Newtonian gravitational potential. This gauge is fixed by the following choices of the metric,

$$A = \Psi, \quad B^{(0)} = 0, \quad H_L = -\Phi, \quad H_T = 0. \quad (2.139)$$

The advantage of using this gauge is that the equations assume a Newtonian-like form, making it easy to understand the phenomenology.

Synchronous gauge In the synchronous gauge, commonly used in numerical codes such as CAMB [81] and CLASS [82, 83], the variables are chosen as

$$A = 0, \quad B^{(0)} = 0, \quad H_L = \frac{h}{6}, \quad H_T = -3 \left(\eta + \frac{h}{6} \right). \quad (2.140)$$

The synchronous gauge however does not fully fix the gauge, leaving room for spurious gauge modes, so that the equations that fix the gauge do not yield unique solutions. Numerical codes avoid this ambiguity by solving the equations in the synchronous gauge in which the CDM velocity is zero.

2.3.7 Initial Conditions

In order to solve the set of equations that we set up through this section we need to set the initial conditions. These are usually set at very early times, when the modes are far outside the horizon. In this case the cosmological perturbations are algebraically related among themselves, so one only needs to set one constant to evolve all perturbations. Setting the initial conditions for cosmological perturbations in the Λ CDM model is deeply connected to the cosmological inflation. It was realized that the inflationary mechanism, developed to solve the horizon and flatness problems could also provide a natural framework to seed the primordial fluctuations.

Inflation, in its most common form is driven by a scalar field ϕ rolling slowly down its potential. The scalar field, usually referred to as *inflaton*, is minimally coupled to gravity and its Lagrangian is given by

$$\mathcal{L}_\phi = -\frac{1}{2}(\partial\phi)^2 - V(\phi) \quad (2.141)$$

The equation of state for the inflaton field is given by

$$w_\phi \equiv \frac{P_\phi}{\rho_\phi} = \frac{\frac{1}{2}a^2\dot{\phi}^2 - V(\phi)}{\frac{1}{2}a^2\dot{\phi}^2 + V(\phi)}, \quad (2.142)$$

and in the case of $\dot{\phi}^2 \ll V(\phi)$ - which is the slow roll condition - it is $w_\phi \simeq -1$. This means that the energy density of the inflaton is approximately constant and through the Friedmann equation (2.22), also the Hubble parameter is almost constant. A sufficiently long period of inflation with an almost constant Hubble parameter, which yields an exponentially fast expansion of the Universe, is able to stretch the scales outside the horizon, providing an elegant solution to the horizon problem. Inflation also provides a mechanism to source the primordial perturbations. At the beginning of inflation, the metric perturbations are inside the horizon and coupled to the inflaton field. The tensor modes $H^{(2)}$ evolve freely under the background influence of the inflaton ϕ and freeze when they exit the horizon. Outside the horizon, tensor modes are effectively correlated according to

$$\langle H^{(2)}(\mathbf{k})H^{(2)}(\mathbf{k}') \rangle = (2\pi)^3\delta^{(3)}(\mathbf{k} - \mathbf{k}')P_H(k), \quad (2.143)$$

where the tensor power spectrum is related to the Hubble rate at the end of inflation through

$$P_H(k) = \frac{H^2}{m_0^2 k^3}. \quad (2.144)$$

Since these parameters are usually unknown the tensor power spectrum is usually parametrized as

$$k^3 P_H(k) = A_T \left(\frac{k}{k_T} \right)^{n_t} \quad (2.145)$$

where A_T is the tensor amplitude, n_T is the tensor spectral index and k_T is the arbitrary tensor pivot scale.

Likewise, scalar metric perturbations are sourced by the inflaton, although the scenario is slightly more complex than in the tensor case, since the perturbations in the scalar field ϕ couple to the metric perturbations directly¹.

In the Newtonian gauge (2.139), the comoving curvature perturbation ζ defined as

$$\zeta = -\Psi + \frac{vH}{k^2(\bar{\rho} + \bar{P})}, \quad (2.146)$$

is conserved outside the horizon and is related to the Newtonian potential Ψ after inflation as

$$\zeta = -\frac{3}{2}\Psi. \quad (2.147)$$

The primordial scalar power spectrum can then be written in terms of the inflation parameters as [84]

$$P_\Psi(k) = \frac{2H^2}{\epsilon m_0^2 k^3} \quad (2.148)$$

with the Hubble factor H evaluated at horizon crossing and with the slow-roll parameter ϵ defined as

$$\epsilon \equiv -\frac{d}{dt} \left(\frac{1}{H} \right). \quad (2.149)$$

Similarly to the tensor case, the scalar power spectrum is parametrized in term of

$$k^3 P_\Psi(k) = A_s \left(\frac{k}{k_s} \right)^{1-n_s}, \quad (2.150)$$

where A_s is the scalar amplitude, n_s is the scalar spectral index and k_s the arbitrary scalar pivot scale.

Usually the tensor amplitude A_T is parametrized in terms of the scalar amplitude A_s through the tensor-to-scalar ratio r defined as

$$A_T = rA_s. \quad (2.151)$$

2.4 Summary

In this Chapter we provided an introduction to the standard Model of cosmology, the Λ CDM model. This model is described by the six parameters,

$$\Omega_m, \quad H_0, \quad \Omega_b, \quad A_s, \quad n_s, \quad \kappa, \quad (2.152)$$

¹See for example the discussion about inflation in [84]

where here κ denotes the optical depth at reionization that we define in the next Chapter. The first two parameters describe the background expansion history of the Universe, while the others describe structure formation and in general how perturbations evolve in the background. The tensor fluctuations parameter n_T and r are not included in the minimal Λ CDM model as they have not been observed yet. In the next Chapter we will describe the cosmological observables that are able to probe these parameters.

Chapter 3

Cosmological Observables

In the previous Chapter we introduced the machinery used in GR to treat the standard model of Cosmology. The goal of this Chapter is to provide a short theoretical description of the the observables and the measurements performed in modern cosmology along with the introduction of the main datasets used in this thesis.

The dynamics of the Λ CDM model is divided into the background and perturbations components, so it is logical to divide the cosmological observables according to what they can actually probe. First, the background observables are the ones that directly probe the Hubble expansion of the Universe. They can be the measurements of the luminosity distance of Type Ia Supernovae, or measurements of the angular-diameter distance from the baryon acoustic oscillations (BAOs). We review these observables in Sect. 3.1.

The other types of observables probe how the anisotropies and inhomogeneities are distributed in the Universe. They can probe the background evolution indirectly, by studying how perturbations evolve on the background. Typical observables probing the perturbations distribution are the measurements of the CMB temperature and polarization anisotropies, and other observables probing the distribution of matter such as galaxy clustering, redshift space distortions and weak lensing. We review this type of observables and the statistical tools used to analyse them in Sect. 3.2.

3.1 Background Observables

As we saw in the Chapter 2, in the standard model of cosmology the expansion of the Universe is modelled through a homogeneous and isotropic FRW Universe. The dynamics of the expanding Universe is determined by the two Friedmann equations (2.22)-(2.26) with the parameters

$$H_0, \Omega_m, \Omega_r, \Omega_\Lambda, \Omega_\kappa. \tag{3.1}$$

The background observables probe specifically these parameters, or at least a subset of them. Below we review the observations of the type Ia supernovae and the baryon acoustic oscillations.

3.1.1 Type Ia Supernovae

Type Ia Supernovae (SN Ia) are identified by their spectra which has no hydrogen lines, but a strong ionized Silicon (Si) II line at maximum brightness. They are also characterized by their light curve shape, their luminosity and their color. Although the SN Ia family is not exactly homogeneous there are several approaches to make them *standard candles*, *i.e.* objects whose intrinsic luminosity can be inferred by observing their physical properties.

A commonly used model is the *Spectral Adaptive Lightcurve Template 2* (SALT2) [85, 86], wherein the SN Ia are standardized by fitting their lightcurve to an empirical template and the fit parameters are then used in the cosmological analysis. For each SN Ia, three parameters are retrieved from its light curve: one is the apparent magnitude at maximum (in the rest frame B-band) denoted as m_B^* , one describes the light curve shape, x_1 (also known as *stretch*) and finally the last is the color correction c . The distance modulus of each SN Ia is then taken as

$$\mu_{\text{SN}} = m_B^* - M + \alpha x_1 - \beta c, \quad (3.2)$$

where the absolute magnitude M , and the two empirical parameters α and β are the same for all supernovae and are fitted along the cosmological parameters by minimizing the Hubble diagram residuals.

The distance modulus μ_{SN} is then compared with the Λ CDM predictions

$$\mu \equiv 5 \log_{10} \left(\frac{D_L}{10 \text{ pc}} \right), \quad (3.3)$$

where D_L is the luminosity distance given in equation (2.40).

In Fig. 3.1 we show the comparison of the measured distance modulus μ from the *Joint Lightcurve Analysis* (JLA) dataset [87] and the theoretical prediction from the Λ CDM model. The parameters of the Λ CDM model in Fig. 3.1 are derived from the analysis in [88]. JLA is a joint analysis using combination of SN Ia observations at low redshift, $z < 0.1$, (denoted as low- z) performed by several collaborations [89, 90, 91, 92], intermediate redshifts measurements $0.05 < z < 0.4$ covered by the *Sloan Digital Sky Survey* (SDSS), high-redshift measurements up to $z \sim 1$ by the Supernova Legacy Search (SNLS) and the high redshift range $z > 1$ covered by the *Hubble Space Telescope* (HST) supernovae search.

It is worth mentioning that not all the background parameters can be simultaneously fit using the SN Ia observations. Specifically, there is a degeneracy between the Hubble constant H_0 and the absolute magnitude M , so usually the Hubble parameter is fixed to some fiducial value inferred from other observables. The same is true for the curvature Ω_κ . CMB anisotropies measurements are consistent with a spatially flat Universe $\Omega_\kappa = 0$, so that the DE density parameter Ω_Λ can be inferred by setting $\Omega_\Lambda = 1 - \Omega_m$.

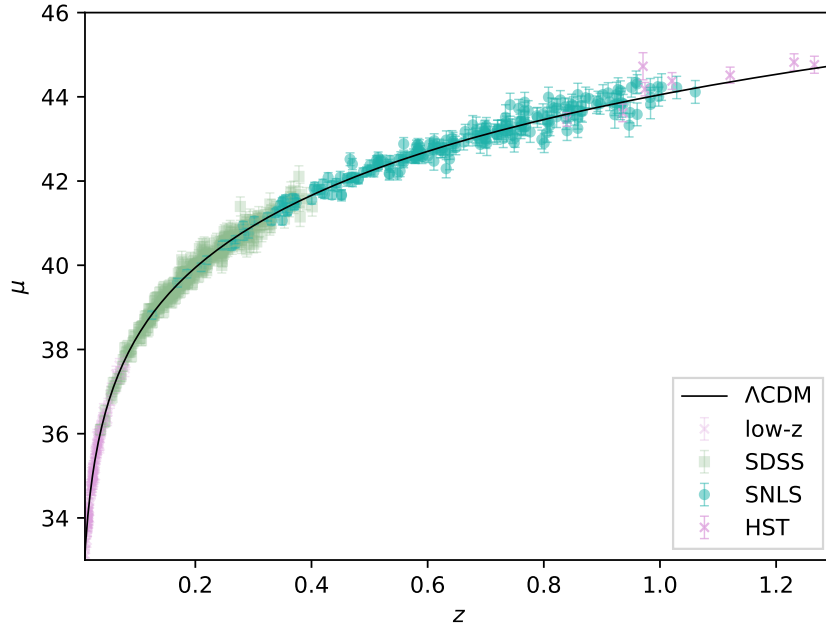


Figure 3.1: Comparison of the measured distance modulus μ_{SN} from the JLA dataset with the theoretical predictions of the ΛCDM model.

3.1.2 Baryon Acoustic Oscillation

Another powerful low-redshift probe is the measurement of the position of the baryon acoustic oscillation (BAO) feature in the correlation function of large scale structures (LSS). In Sect. 2.3.1 we saw how below the Jeans scale, density fluctuations propagate like acoustic waves. Such acoustic waves were also present in the baryon-photon plasma before recombination, sourced by the density fluctuations generated before the hot big bang (for example by the inflationary mechanism). A characteristic scale, roughly given by the distance these waves could propagate in the plasma prior to recombination and typically called the *sound horizon*, is then imprinted in the matter correlation function when baryons and photons decouple. The sound horizon is given by [93, 94]

$$r_s = \int_{z_{\text{drag}}}^{\infty} \frac{c_s(z) dz}{H(z)}, \quad (3.4)$$

where z_{drag} is the redshift at which baryons stopped being influenced by the Compton drag from photons and c_s is the speed of sound given by

$$c_s = \frac{1}{\sqrt{3(1+R)}}, \quad (3.5)$$

with $R = 3\rho_b/\rho_\gamma$. After recombination this scale is stretched by the Hubble expansion and its location can be observed in the LSS correlation function as a little bump. The sound

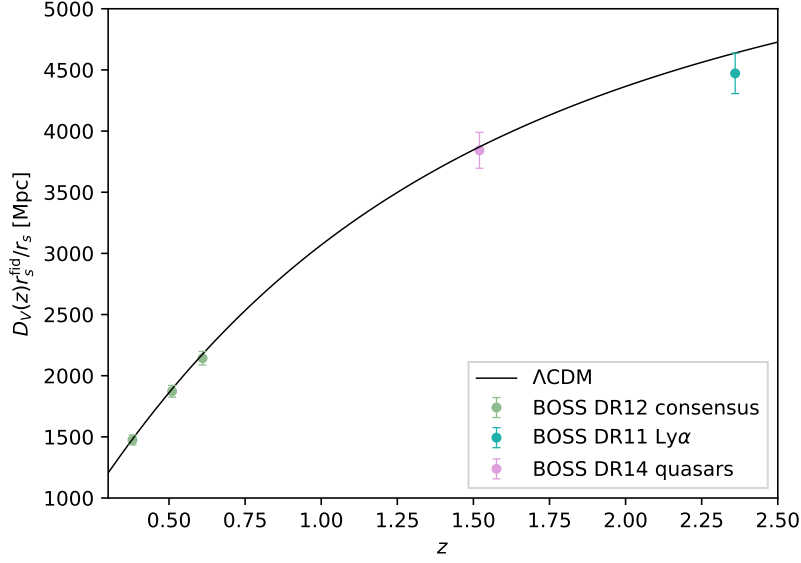


Figure 3.2: Measurements of $D_V(z)$ from various surveys. The black solid line represent the theoretical prediction from the best-fit Λ CDM model from the Planck 2015 results.

horizon at recombination is very large, $r_s \approx 150$ Mpc, due to the relativistic speed at which acoustic waves propagates. Its large scale and the the subsequent Hubble stretch, protects the BAO feature in the correlation function against contamination by nonlinear clustering happening at late-times, making the BAO scale an excellent *standard ruler* [95]. Although the BAO scale is pretty robust against systematic effects, its measurements are limited by statistics. In fact, in order to detect the BAO feature in the LSS correlation function with sufficient signal to noise ratio, surveys need to observe very large volumes. The observables corresponding to the BAO scale are typically separated in its radial (line-of-sight) and transverse (angular) components, and are given by

$$\Delta z = H(z)r_s, \quad (3.6)$$

$$\Delta\theta = r_s/(1+z)D_A, \quad (3.7)$$

respectively, where D_A is the comoving angular-diameter distance. Results are typically reported in terms of these quantities or also in terms of D_V/r_s where

$$D_V = \left[(1+z)^2 D_A^2(z) \frac{cz}{H(z)} \right]^{1/3}. \quad (3.8)$$

Usually, observations which extracted the BAO from the monopole of the LSS correlations are only able to constrain a combination of the parallel and transverse BAO scale and hence report their results in terms of the parameter D_V . This is the case for example for

the 6dF Galaxy Survey [96] and the SDSS Main Galaxy Sample (MGS) [97] that provided the measurement of D_V at the redshift $z = 0.106$ and $z = 0.15$ respectively. More recent measurements of the BAO scale were performed by the SDSS Baryon Oscillation Spectroscopic Survey (BOSS). The recent Data Release (DR) 12 [98] reported the measurement of the parallel and transverse components of BAO scale at three different redshift bins, $z_i = \{0.38, 0.51, 0.61\}$. These type of measurement were also performed by cross-correlating the Lyman- α forest absorption of quasars from the BOSS DR 11 [99], yielding a BAO scale measurement at the effective redshift $z = 2.36$. Recently, the BAO measurement from the clustering of quasars sample of BOSS DR 14 also provided a measurement of D_V at an intermediate redshift $z = 1.52$ [100]. In Fig. 3.2 we show the measurements of $D_V(z)r_s^{\text{fid}}/r_s$ from the BOSS DR 12 from large scale structure, from the Lyman- α forest cross correlation and from the quasars sample. The black solid line represents $D_V(z)$ from the best fit Λ CDM model from the Planck 2015 results while the sound horizon scale from the fiducial Λ CDM model is $r_s^{\text{fid}} = 147.78$ Mpc. Alternatively, results are also presented in terms of the two dimensionless parameters α_{\parallel} and α_{\perp} defined as

$$\alpha_{\parallel} = \frac{H^{\text{fid}}(z)r_s^{\text{fid}}}{H(z)r_s}, \quad (3.9)$$

$$\alpha_{\perp} = \frac{d_A(z)r_s^{\text{fid}}}{d_A^{\text{fid}}r_s}, \quad (3.10)$$

where $H^{\text{fid}}(z)$ and r_s^{fid} are the Hubble parameter and the sound horizon in a fiducial cosmological model.

3.2 Perturbation Observables

In this Section we introduce the cosmological observables that probe the anisotropies and inhomogeneities that we observe in the Universe. We will restrict to large scales observables, so that nonlinear effects can be ignored and the linear perturbation theory introduced in Chapter 2 is able to describe the observations accurately. Observables that belong to this category are able to probe the cosmological parameters with very high accuracy and are very powerful tools that we will use in this thesis. While in Chapter 2 we introduced the general dynamics of the perturbations, here we shall explore its statistical properties, that are what we eventually observe in the sky. This reflects the fact that we are not able to predict where in the sky over-densities and eventually galaxies formed, but rather we can predict how they are distributed in the Universe. A limitation in Cosmology arises from the fact that we observe only one Universe and thus cannot perform ensemble averages or expectation values. We can however observe fluctuations over a scale λ and average them over many distinct regions of size $\sim \lambda$. Cosmologists usually adopt an *ergodic*-like hypothesis

according to which the Universe is statistically homogeneous and isotropic, so that ensemble averages can be replaced by spatial averages in our Universe.

Let $\mathcal{O}_\alpha(\hat{\mathbf{n}})$ be the value of a scalar field observed in the direction $\hat{\mathbf{n}}$ in the sky. This field could be the CMB temperature, the galaxy number or other cosmological observables. We treat $\mathcal{O}_\alpha(\hat{\mathbf{n}})$ as a random field with mean zero, *i.e.* $\langle \mathcal{O}_\alpha(\hat{\mathbf{n}}) \rangle = 0$, where $\langle \cdot \rangle$ denotes averages across the sky. As mentioned earlier we replace ensemble averages with spatial averages. In general we are interested in the probability distribution function of the observable $\mathcal{O}_\alpha(\hat{\mathbf{n}})$. For instance we could be interested in testing whether the distribution is Gaussian or not. This is of interest since the simplest inflationary mechanisms predict Gaussian initial conditions, and this Gaussianity is preserved by the linear perturbation theory, breaking down only at smaller scales where nonlinear effects become important. This is usually done by looking at the correlation function

$$\langle \mathcal{O}_\alpha(\hat{\mathbf{n}})\mathcal{O}_\alpha(\hat{\mathbf{n}}') \rangle = C(\hat{\mathbf{n}} \cdot \hat{\mathbf{n}}') = C(\theta), \quad (3.11)$$

where θ is the angle separation of the two directions. The fact that the correlation function depends only on the angle separation between the two directions, and not on the specific directions, is a consequence of the isotropy of the background model. In general we can look at higher moments (also known as n -point correlation functions,

$$\langle \mathcal{O}_\alpha(\hat{\mathbf{n}})\mathcal{O}_\alpha(\hat{\mathbf{n}}')\mathcal{O}_\alpha(\hat{\mathbf{n}}'') \dots \mathcal{O}_\alpha(\hat{\mathbf{n}}^{(n)}) \rangle, \quad (3.12)$$

that can be related to the two point correlation function through Isserlis' theorem (also known, in particle physics, as Wick's theorem),

$$\langle x_1 x_2 \dots x_{2n} \rangle = \langle x_1 x_2 \rangle \langle x_3 x_4 \rangle \dots \langle x_{2n-1} x_{2n} \rangle + \text{permutations}. \quad (3.13)$$

For a Gaussian field odd moments vanish, so one check of Gaussianity is verifying that observations are in agreement with $\langle xxx \rangle = 0$. The Fourier transform of the three-point correlation function $\langle xxx \rangle$ is called bi-spectrum. Because we are looking at observables projected on the celestial sphere it is useful to expand the field $\Delta(\hat{\mathbf{n}})$ in spherical harmonics,

$$\mathcal{O}_\alpha(\hat{\mathbf{n}}) = \sum_{\ell m} a_{\ell m}^\alpha Y_{\ell m}(\hat{\mathbf{n}}), \quad (3.14)$$

where the $Y_{\ell m}$ are the spherical harmonics and $m = -\ell, \dots, \ell$. By plugging the expansion above in the correlation function we obtain

$$\langle \mathcal{O}_\alpha(\hat{\mathbf{n}})\mathcal{O}_\alpha(\hat{\mathbf{n}}') \rangle = \sum_{\ell, \ell', m, m'} \langle a_{\ell m} a_{\ell' m'} \rangle Y_{\ell m}(\hat{\mathbf{n}}) Y_{\ell' m'}(\hat{\mathbf{n}}'). \quad (3.15)$$

From statistical isotropy it is possible to prove that

$$\langle a_{\ell m} a_{\ell' m'}^* \rangle = \delta_{\ell\ell'} \delta_{mm'} C_\ell^{\alpha\alpha}, \quad (3.16)$$

so if we have a map of our observable \mathcal{O}_α over the sky - which consists of the measurement of $a_{\ell m}^\alpha$ - we can compute the power spectrum C_ℓ by

$$C_\ell^{\alpha\alpha} = \frac{1}{2\ell+1} \sum_m \langle a_{\ell m}^\alpha a_{\ell m}^{\alpha*} \rangle. \quad (3.17)$$

Also, a useful property of property of the spherical harmonics is that

$$\sum_{m=-\ell}^{\ell} Y_{\ell m}^*(\hat{\mathbf{n}}) Y_{\ell m}(\hat{\mathbf{n}}') = \frac{2\ell+1}{4\pi} \mathcal{P}_\ell(\hat{\mathbf{n}} \cdot \hat{\mathbf{n}}'), \quad (3.18)$$

where \mathcal{P}_ℓ is the Legendre polynomial of order ℓ , so that Eq. (3.15) becomes

$$\langle \mathcal{O}_\alpha(\hat{\mathbf{n}}) \mathcal{O}_\alpha(\hat{\mathbf{n}}') \rangle = \sum_\ell \left(\frac{2\ell+1}{4\pi} \right) C_\ell^{\alpha\alpha} \mathcal{P}_\ell(\theta). \quad (3.19)$$

The information we usually extract is, especially for the CMB, the power spectrum $C_\ell^{\alpha\alpha(\text{meas.})}$. In order to test the measured power spectrum against theory we need to compute the theoretical power spectrum $C_\ell^{\alpha\alpha(\text{theory})}$.

We shall now see how this computation is performed for a general scalar observable \mathcal{O}_α . In the following subsections we will outline the calculation for specific observables. The key quantities are the coefficients $a_{\ell m}^\alpha$, and the power spectrum is then computed using Eq. (3.17). First, let us note that the observable \mathcal{O}_α is usually given by a weighted integral along the line of sight,

$$\mathcal{O}_\alpha(\hat{\mathbf{n}}) = \int_0^{\tau_0} d\tau W(\tau) \mathcal{O}_\alpha(\hat{\mathbf{n}}(\tau_0 - \tau), \tau), \quad (3.20)$$

where the *window function* $W(\tau)$ is normalized,

$$\int_0^{\tau_0} d\tau W(\tau) = 1. \quad (3.21)$$

Now let us expand the observable $\mathcal{O}_\alpha(\hat{\mathbf{n}}(\tau_0 - \tau), \tau)$ in spherical harmonics, so that that Eq. (3.20) becomes

$$\mathcal{O}_\alpha(\hat{\mathbf{n}}) = \int_0^{\tau_0} d\tau W(\tau) \sum_{\ell m} a_{\ell m}^\alpha(\tau) Y_{\ell m}^*(\hat{\mathbf{n}}), \quad (3.22)$$

where the coefficients $a_{\ell m}^\alpha(\tau)$ are given by

$$a_{\ell m}^\alpha(\tau) = \int d\Omega_{\hat{\mathbf{n}}} \mathcal{O}_\alpha(\hat{\mathbf{n}}(\tau_0 - \tau), \tau) Y_{\ell m}^*(\hat{\mathbf{n}}). \quad (3.23)$$

Comparing equations (3.22) and (3.14) we find that the theoretical predictions of $a_{\ell m}^\alpha$ are given by

$$a_{\ell m}^\alpha = \int_0^{\tau_0} d\tau W(\tau) \int d\Omega_{\hat{\mathbf{n}}} O_\alpha(\hat{\mathbf{n}}(\tau_0 - \tau), \tau) Y_{\ell m}^*(\hat{\mathbf{n}}). \quad (3.24)$$

In order to connect the observable $O_\alpha(\hat{\mathbf{n}}(\tau_0 - \tau), \tau)$ to the perturbation theory framework developed in Chapter 2, let us expand its values in Fourier modes,

$$a_{\ell m}^\alpha = \int_0^{\tau_0} d\tau W(\tau) \int d\Omega_{\hat{\mathbf{n}}} \int \frac{d^3 k}{(2\pi)^3} \mathcal{O}_\alpha(\mathbf{k}, \tau) e^{i\mathbf{k} \cdot \hat{\mathbf{n}}(\tau_0 - \tau)} Y_{\ell m}^*(\hat{\mathbf{n}}). \quad (3.25)$$

Now the exponential can be expanded in Legendre polynomials,

$$e^{i\mathbf{k} \cdot \hat{\mathbf{n}}(\tau_0 - \tau)} = \sum_{\ell'} (i)^{\ell'} (2\ell' + 1) j_{\ell'} [k(\tau_0 - \tau)] \mathcal{P}_{\ell'}(\hat{\mathbf{k}} \cdot \hat{\mathbf{n}}), \quad (3.26)$$

and be further expanded in spherical harmonics using Eq. (3.18). Furthermore, we can write $\mathcal{O}_\alpha(\mathbf{k}, \tau) \equiv \tilde{\mathcal{O}}_\alpha(k, \tau) \mathcal{R}(\mathbf{k})$, where $\tilde{\mathcal{O}}$ is the *transfer function* and \mathcal{R} is the primordial curvature perturbation. In doing this, we assumed that at very early times, when $k\tau \ll 1$, all the perturbations are algebraically related to the curvature perturbation \mathcal{R} emerging from the inflationary mechanism.

Plugging equations (3.18) and (3.26) into equation (3.25), and using the fact that spherical harmonics are normalized, yields

$$a_{\ell m}^\alpha = 4\pi i^\ell \int_0^{\tau_0} d\tau W(\tau) \int \frac{d^3 k}{(2\pi)^3} j_\ell [k(\tau_0 - \tau)] \tilde{\mathcal{O}}_\alpha(k, \tau) \mathcal{R}(\mathbf{k}) Y_{\ell m}^*(\hat{\mathbf{k}}). \quad (3.27)$$

Then, squaring the above equation yields the following equation for the theoretical power spectrum,

$$C_\ell^{\alpha\alpha} = \frac{2}{\pi} \int dk k^2 P_{\mathcal{R}}(k) I_\ell^\alpha(k) I_\ell^\alpha(k), \quad (3.28)$$

where $P_{\mathcal{R}}(k)$ is the primordial power spectrum defined as

$$\langle \mathcal{R}(\mathbf{k}) \mathcal{R}^*(\mathbf{k}') \rangle = (2\pi)^3 P_{\mathcal{R}}(k) \delta^{(3)}(\mathbf{k} - \mathbf{k}'), \quad (3.29)$$

and the transfer functions $I_\ell^\alpha(k)$ assume the form

$$I_\ell^\alpha(k) = \int_0^{\tau_0} d\tau W(\tau) \tilde{\mathcal{O}}_\alpha(k, \tau) j_\ell [k(\tau_0 - \tau)]. \quad (3.30)$$

The procedure above can also be generalized to cross-correlations of different observables \mathcal{O}_α and \mathcal{O}_β , and obtain

$$C_\ell^{\alpha,\beta} = \frac{2}{\pi} \int dk k^2 P_{\mathcal{R}}(k) I_\ell^{(\alpha)}(k) I_\ell^\beta(k). \quad (3.31)$$

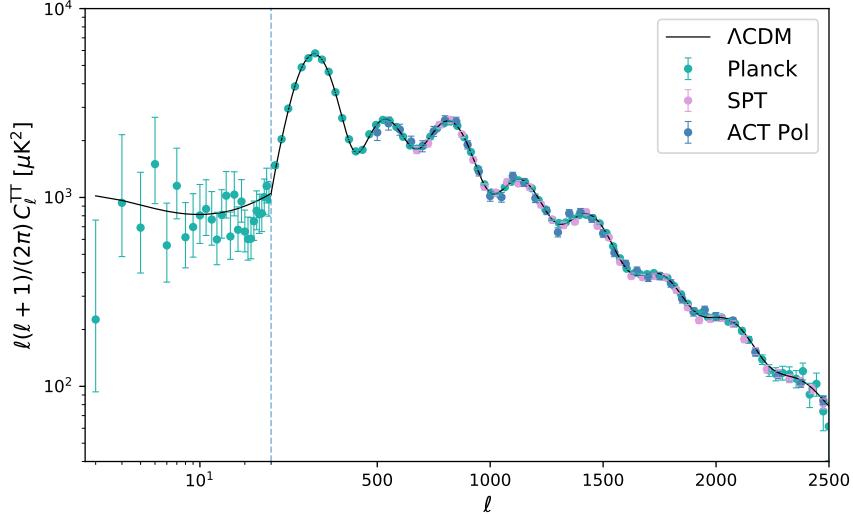


Figure 3.3: Measurements of the CMB temperature anisotropies power spectrum from the Planck satellite and the South Pole Telescope. The thin black line shows the best fit model from the Planck collaboration analysis. The dashed vertical line divides the two different likelihoods for Planck. Also note that on the left the x-scale is logarithmic, while on the right is linear.

Usually, numerical codes that solve the Boltzmann equations and the perturbation equations are designed to efficiently compute theoretical predictions given by equation (3.31). They are usually divided in a “physics” part and in a “geometry part”. The physics part solves the equations of motions and store the solutions $\tilde{\mathcal{O}}_\alpha(k, \tau)$ on a grid of k and τ values. The geometry part then performs the integral (3.30) on a grid of ℓ and k values and eventually does the integration over the wave vector k (3.31). Examples of such codes are CMBFAST[101], later replaced by CAMB [81] and CLASS [82]. In the next two parts of the thesis we will extensively modify CAMB to test physics beyond Λ CDM with cosmological observables.

3.2.1 Cosmic Microwave Background

The aim of this section is to outline the calculation of the CMB temperature and polarization anisotropies. Polarization is an extremely powerful source of information about the underlying physics and we will extensively use it in Part II of this thesis. The CMB radiation observed in the direction $\hat{\mathbf{n}}$ is described by the intensity matrix, built from the time average of the electric field tensor $E_i^* E_j$ and is usually decomposed in terms of the Stokes’ parameters I, Q, U and V ,

$$I_{ij} = \begin{pmatrix} \langle E_1^* E_1 \rangle & \langle E_1^* E_2 \rangle \\ \langle E_2^* E_1 \rangle & \langle E_2^* E_2 \rangle \end{pmatrix} = \begin{pmatrix} I + Q & U - iV \\ U + iV & I - Q \end{pmatrix}. \quad (3.32)$$

Here the indices 1 and 2 refer to the local orthonormal basis formed by the vectors $\hat{\mathbf{n}}, \varepsilon_1, \varepsilon_2$ and $\langle \cdot \rangle$ denotes averages over times much larger than the characteristic time of the oscillations of the field. The intensity I is related to the temperature anisotropies, Q and U are related to linear polarization, while V is the Stokes' parameter quantifying the circular polarization that is expected to vanish for CMB as it is not generated by Thomson scattering.

The temperature anisotropy $\Theta \equiv \delta T^{\text{CMB}} / \bar{T}^{\text{CMB}}$ is expanded in spherical harmonics as we did in equation (3.14) for a general observable Δ ,

$$\Theta(\hat{\mathbf{n}}) = \sum_{\ell, m} a_{\ell m}^{(T)} Y_{\ell m}(\hat{\mathbf{n}}). \quad (3.33)$$

The Stokes' parameters Q and U are then combined in two other variables that transform, under rotations, as spin-2 functions and are expanded as,

$$(Q + iU)(\hat{\mathbf{n}}) = \sum_{\ell, m} a_{\ell m}^{(+2)} Y_{\ell m}(\hat{\mathbf{n}}), \quad (3.34)$$

$$(Q - iU)(\hat{\mathbf{n}}) = \sum_{\ell, m} a_{\ell m}^{(-2)} Y_{\ell m}(\hat{\mathbf{n}}), \quad (3.35)$$

where ${}_{\pm s} Y_{\ell m}(\hat{\mathbf{n}})$ are the spin- s weighted spherical harmonics. The polarization variables $Q \pm iU$ are then transformed in spin-0 functions, acting with the raising and lowering spin operators twice, thus avoiding the ambiguities of change of polarization basis when considering separate patches of the sky.

$$\bar{\partial}^2(Q + iU)(\hat{\mathbf{n}}) = \sum_{\ell, m} \sqrt{\frac{(\ell + 2)!}{(\ell - 2)!}} a_{\ell m}^{(+2)} Y_{\ell m}(\hat{\mathbf{n}}), \quad (3.36)$$

$$\partial^2(Q - iU)(\hat{\mathbf{n}}) = \sum_{\ell, m} \sqrt{\frac{(\ell + 2)!}{(\ell - 2)!}} a_{\ell m}^{(-2)} Y_{\ell m}(\hat{\mathbf{n}}). \quad (3.37)$$

Here $\bar{\partial}$ and ∂ are the spin raising and lowering operator respectively. The two quantities above can be further combined to form two quantities that remain unchanged or change sign, respectively, under parity transformations, and they are

$$E(\hat{\mathbf{n}}) = -\frac{1}{2} \left[\bar{\partial}^2(Q + iU)(\hat{\mathbf{n}}) + \partial^2(Q - iU)(\hat{\mathbf{n}}) \right] = -\frac{1}{2} \sum_{\ell, m} \sqrt{\frac{(\ell + 2)!}{(\ell - 2)!}} \left[a_{\ell m}^{(+2)} + a_{\ell m}^{(-2)} \right] Y_{\ell m}(\hat{\mathbf{n}}) \quad (3.38)$$

$$B(\hat{\mathbf{n}}) = \frac{i}{2} \left[\bar{\partial}^2(Q + iU)(\hat{\mathbf{n}}) - \partial^2(Q - iU)(\hat{\mathbf{n}}) \right] = \frac{i}{2} \sum_{\ell, m} \sqrt{\frac{(\ell + 2)!}{(\ell - 2)!}} \left[a_{\ell m}^{(+2)} - a_{\ell m}^{(-2)} \right] Y_{\ell m}(\hat{\mathbf{n}}) \quad (3.39)$$

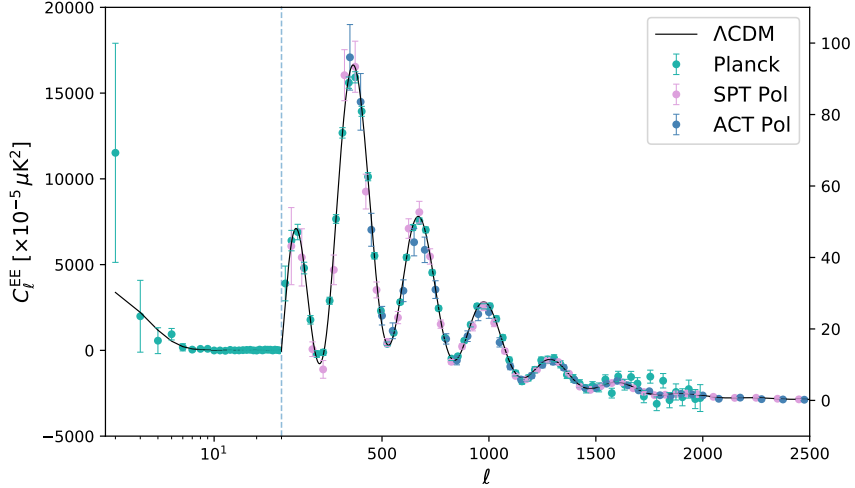


Figure 3.4: Measurements of the CMB E mode polarization power spectrum from the Planck satellite, the South Pole Telescope (SPT) and the Atacama Cosmology Telescope (ACT). The thin black line shows the best fit model from the Planck collaboration analysis.

The temperature anisotropy Θ and the two quantities above have the same expansion as the one in equation (3.14) and thus, given the temperature and polarization maps $a_{\ell m}^{\text{T},(\pm 2)}$, we can compute the power spectra C_{ℓ}^{TT} , C_{ℓ}^{EE} , C_{ℓ}^{BB} and the cross correlation C_{ℓ}^{TE} , according to equation (3.17).

We now need to turn on the theoretical predictions of these power spectra. They are obtained from Eqs. (3.28), (3.31) provided we have first calculated the transfer functions (3.30). To do so, we have to use the machinery of the Boltzmann equations developed in Sect. 2.3.5 applied to the photons distribution function. When considering polarization, the phase space distribution function assumes the form of a 2×2 matrix, $f_{\lambda\lambda'}$, where λ and λ' are the polarization indices. The photon distribution function can then be written as

$$f_{\lambda\lambda'} = f^{(0)} \left(\mathbf{I} + \mathbf{T}^{(1)} \right), \quad (3.40)$$

where $f^{(0)}$ is the background level distribution function of the Bose-Einstein form (2.134), \mathbf{I} is the 2×2 identity matrix and $\mathbf{T}^{(1)}$ is the perturbation matrix. We can further decompose the perturbation matrix as

$$\mathbf{T}^{(1)} = -\frac{\partial \log f^{(0)}}{\partial \log \epsilon} \left[\Theta \mathbf{I} + \frac{Q + iU}{T} \mathbf{M}_+ + \frac{Q - iU}{T} \mathbf{M}_- \right], \quad (3.41)$$

where ϵ is the photon energy, $\mathbf{M}_{\pm} \equiv (\sigma_3 \mp i\sigma_1)/2$ and $\sigma_{1,2,3}$ are the Pauli matrices. The Boltzmann equation for the perturbation matrix $\mathbf{T}^{(1)}$ is then a matrix generalization of equation (2.136). Encapsulating the temperature and polarization perturbations into the

vector $\tilde{\mathbf{T}} \equiv [\Theta, (Q + iU), (Q - iU)]$, the Boltzmann equation for $\mathbf{T}^{(1)}$ reads

$$\frac{\partial \tilde{\mathbf{T}}}{\partial \tau} + \frac{\partial \tilde{\mathbf{T}}}{\partial x^i} \frac{qe^i}{\epsilon} + \tilde{\mathbf{G}} = \mathbf{C}[\tilde{\mathbf{T}}], \quad (3.42)$$

where $\mathbf{C}[\tilde{\mathbf{T}}]$ is the collisional term due to Thomson scattering and $\tilde{\mathbf{G}}$ is the gravitational redshift term (the second and third terms in Eq. (2.136)). Deriving the collisional term is beyond the scope of this thesis, and the literature is quite rich in this regard, for example see [102, 103, 104]. Following [104] we can expand the perturbations $\tilde{\mathbf{T}}$ in normal modes G_ℓ^m ,

$$\Theta(\tau, \mathbf{x}, \hat{\mathbf{n}}) = \int \frac{d^3 k}{(2\pi)^3} \sum_\ell \sum_{m=-2}^2 \Theta_\ell^{(m)}(\tau, \mathbf{k}) G_\ell^m, \quad (3.43)$$

$$(Q \pm iU)(\tau, \mathbf{x}, \hat{\mathbf{n}}) = \int \frac{d^3 k}{(2\pi)^3} \sum_\ell \sum_{m=-2}^2 \left(E_\ell^{(m)}(\tau, \mathbf{k}) \pm i B_\ell^{(m)}(\tau, \mathbf{k}) \right)_{\pm 2} G_\ell^m. \quad (3.44)$$

The normal modes are intuitively obtained in the following way. Given a quantity $\mathcal{O}(\tau, r\hat{\mathbf{n}}, \hat{\mathbf{n}})$ in the sky, in a coordinate system where the observer at τ_0 is at the origin, its angular dependence can be expanded first in spherical harmonics (spin-weighted spherical harmonics if \mathcal{O} transforms as a spin function) as we did in equation (3.14),

$$\mathcal{O}(\tau, r\hat{\mathbf{n}}, \hat{\mathbf{n}}) = \sum_{\ell m} \mathcal{O}_\ell^m(\tau, \hat{\mathbf{n}}r)_s Y_\ell^m(\hat{\mathbf{n}}). \quad (3.45)$$

The space dependence of the coefficients $\mathcal{O}_\ell^m(\tau, \hat{\mathbf{n}}r)$ can be further expanded in plane waves,

$$\mathcal{O}(\tau, r\hat{\mathbf{n}}, \hat{\mathbf{n}}) = \int \frac{d^3 k}{(2\pi)^3} \sum_{\ell m} \mathcal{O}_\ell^m(\tau, \mathbf{k})_s Y_\ell^m(\hat{\mathbf{n}}) e^{i\mathbf{k}\cdot\hat{\mathbf{n}}r}. \quad (3.46)$$

Plane waves then bring their own angular dependence as they can be expanded in Legendre polynomials, *i.e.* spherical harmonics Y_ℓ^0 ,

$$e^{i\mathbf{k}\cdot\hat{\mathbf{n}}r} = \sum_{\ell'} (-i)^{\ell'} \sqrt{4\pi(2\ell'+1)} j_{\ell'}(kr) Y_{\ell'}^0(\hat{\mathbf{n}}), \quad (3.47)$$

so that $\mathcal{O}(\tau, r\hat{\mathbf{n}}, \hat{\mathbf{n}})$ is, in the end, expanded on functions of the form

$$j_{\ell'}(kr)_s Y_\ell^m(\hat{\mathbf{n}}) Y_{\ell'}^0(\hat{\mathbf{n}}). \quad (3.48)$$

Note that in equation (3.47) we chose a coordinate system such that \mathbf{k} is aligned along the z axis. The product of the two spherical harmonics can be thought as the sum of orbital (from the plane wave) and intrinsic angular momenta, and using the Clebsch-Gordan relations, can be transformed in the spherical harmonics of total angular momentum $L = |\ell - \ell'|, \dots, \ell + \ell'$

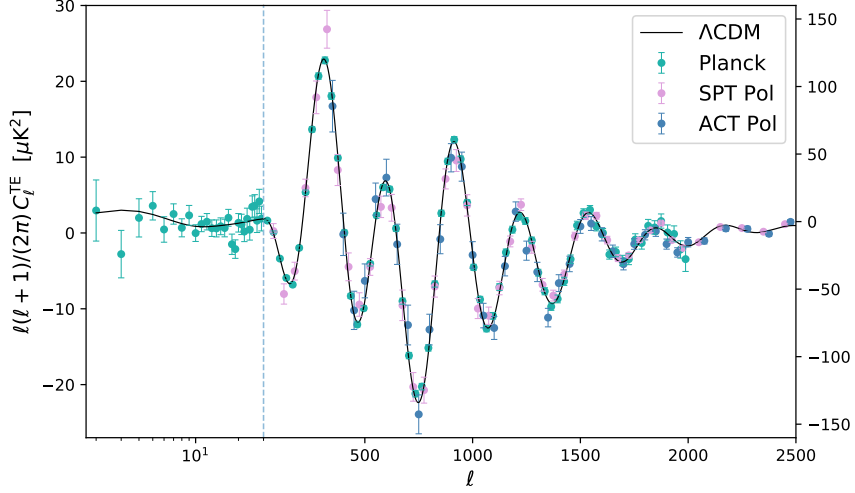


Figure 3.5: Cross correlation power spectrum between the CMB temperature anisotropies and the E-mode polarization. The thin black line shows the best fit model from the Planck collaboration analysis. The dashed vertical line divides the two different likelihoods for Planck. Also note that on the left the x-scale is logarithmic, while on the right is linear.

and total spin $S = 0, \dots, s$. According to the selection rules - the same used in quantum mechanics - the sum over the total angular momentum spherical harmonics will be weighted by different ℓ' contributions of the orbital spherical Bessel functions entering Eq. (3.47). These can be re-expressed in terms of the j_ℓ functions using the recursion relations. The normal modes (for spin-0 functions) are then written as

$$G_\ell^m(\hat{\mathbf{n}}, r) = \sum_{\ell'} (-i)^{\ell'} \sqrt{4\pi(2\ell' + 1)} j_{\ell'}^{(\ell m)}(kr) Y_{\ell'}^m, \quad (3.49)$$

where the radial functions $j_{\ell'}^{(\ell m)}(kr)$ are the ones obtained by using the recursion relations. Likewise, the spin-2 normal modes are expanded in a similar fashion,

$$\pm_2 G_\ell^m = \sum_{\ell} (-i)^\ell \sqrt{4\pi(2\ell + 1)} \left[\epsilon_\ell^{(m)}(kr) \pm i\beta_\ell^{(m)}(kr) \right] \pm_2 Y_\ell^m(\hat{\mathbf{n}}). \quad (3.50)$$

The advantage of this approach is that the normal modes isolate the scalar, vector and tensor contributions according to the value of m . In fact, it turns out that the normal modes $G_{0,1,2}^{(0)}$ are related to the scalar eigenfunctions $Q^{(0)}, Q_i^{(0)}$ and $Q_{ij}^{(0)}$ that we introduced in Sect. 2.3.2. Likewise, the normal modes $G_{1,2}^{(\pm 1)}$ are related to the eigenfunctions $Q_i^{(\pm 1)}, Q_{ij}^{(\pm 1)}$ and $G_2^{(\pm 2)}$ to $Q_{ij}^{(\pm 2)}$. Since metric perturbations that source the anisotropies Θ, E, B through the Boltzmann equations (3.42) only contain scalar, vector and tensor modes, the expansions (3.43) and (3.44) contain only terms with $m = -2, \dots, 2$. Plugging these expansions into

the Boltzmann equation (3.42) yields equations for the multipoles,

$$\dot{\Theta}_\ell^{(m)} = k \left[\frac{0\kappa_\ell^m}{(2\ell-1)} \Theta_{\ell-1}^{(m)} - \frac{0\kappa_{\ell+1}^m}{(2\ell+3)} \Theta_{\ell+1}^{(m)} \right] + \dot{\kappa} \Theta_\ell^{(m)} + S_\ell^{(m)}, \quad (3.51)$$

$$\dot{E}_\ell^{(m)} = k \left[\frac{2\kappa_\ell^m}{(2\ell-1)} E_{\ell-1}^{(m)} - \frac{2m}{\ell(\ell+1)} B_\ell^{(m)} - \frac{2\kappa_{\ell+1}^m}{(2\ell+3)} E_{\ell+1}^{(m)} \right] + \dot{\kappa} \left[E_\ell^{(m)} + \sqrt{6} P^{(m)} \delta_{\ell,2} \right], \quad (3.52)$$

$$\dot{B}_\ell^{(m)} = k \left[\frac{2\kappa_\ell^m}{(2\ell-1)} B_{\ell-1}^{(m)} + \frac{2m}{\ell(\ell+1)} E_\ell^{(m)} - \frac{2\kappa_{\ell+1}^m}{(2\ell+3)} B_{\ell+1}^{(m)} \right] + \dot{\kappa} B_\ell^{(m)}, \quad (3.53)$$

where ${}_s\kappa_\ell^m = \sqrt{(\ell^2 - m^2)(\ell^2 - s^2)}/\ell^2$, $\dot{\kappa} = -n_e \sigma_T a$ is the differential optical depth with n_e being the density of free electrons and σ_T the Thomson cross section. The source functions $S_\ell^{(m)}$ and $P^{(m)}$ are given by

$$S_0^{(0)} = -\dot{\kappa} \Theta_0^{(0)} + \dot{\Phi}, \quad S_1^{(0)} = -\dot{\kappa} v_B^{(0)} + k \Psi, \quad S_2^{(0)} = -\dot{\kappa} P^{(0)}, \quad (3.54)$$

$$S_1^{(1)} = -\dot{\kappa} v_B^{(1)} + \dot{V}, \quad S_2^{(1)} = -\dot{\kappa} P^{(1)}, \quad (3.55)$$

$$S_2^{(2)} = -\dot{\kappa} P^{(2)} - \dot{H}, \quad (3.56)$$

$$P^{(m)} = \frac{1}{10} \left[\Theta_2^{(m)} - \sqrt{6} E_2^{(m)} \right]. \quad (3.57)$$

The Boltzmann equations are then integrated along the line of sight [101] to provide the formal solutions

$$\frac{\Theta_\ell^{(m)}(\tau_0, k)}{2\ell+1} = \int_0^{\tau_0} d\tau e^{-\kappa} \sum_{\ell'} S_{\ell'}^{(m)}(\tau) j_\ell^{(\ell'm)}(k(\tau_0 - \tau)), \quad (3.58)$$

$$\frac{E_\ell^{(m)}(\tau_0, k)}{2\ell+1} = \sqrt{6} \int_0^{\tau_0} d\tau \dot{\kappa} e^{-\kappa} P_\ell^{(m)}(\tau) \epsilon_\ell^{(m)}(k(\tau_0 - \tau)), \quad (3.59)$$

$$\frac{B_\ell^{(m)}(\tau_0, k)}{2\ell+1} = \sqrt{6} \int_0^{\tau_0} d\tau \dot{\kappa} e^{-\kappa} P_\ell^{(m)}(\tau) \beta_\ell^{(m)}(k(\tau_0 - \tau)), \quad (3.60)$$

where

$$\kappa = \int_\tau^{\tau_0} d\tau' n_e(\tau') \sigma_T a(\tau'). \quad (3.61)$$

We can then take into account the initial conditions by writing the solutions $X_\ell^{(m)}(\tau_0, k)$, where $X = \Theta, E, B$, as $X_\ell^{(m)}(\tau_0, k) = \xi^{(m)}(k, \tau_{\text{in}}) \tilde{X}_\ell^{(m)}(\tau_0, k)$, where \tilde{X} is the *transfer function* and $\xi^{(m)}$ is the scalar, vector or tensor primordial metric perturbation at initial time. Finally, the theoretical power spectra C_ℓ^{TT} , C_ℓ^{EE} , C_ℓ^{TE} and C_ℓ^{BB} , can be computed using

$$(2\ell+1)^2 C_\ell^{XY} = \frac{2}{\pi} \int dk k^2 \sum_{m=-2}^2 \tilde{X}_\ell^{(m)*}(\tau_0, k) \tilde{Y}_\ell^{(m)}(\tau_0, k) \mathcal{P}_\xi^{(m)}(k), \quad (3.62)$$

where the primordial power spectrum $\mathcal{P}_\xi^{(m)}(k)$ is defined through

$$\langle \xi^{(m)}(\mathbf{k}, \tau_{\text{in}}) \xi^{(m)}(\mathbf{k}', \tau_{\text{in}}) \rangle = (2\pi)^2 \mathcal{P}_\xi^{(m)}(k) \delta^{(3)}(\mathbf{k} + \mathbf{k}'). \quad (3.63)$$

The advantage of integrating along the line of sight is the following. In computing the power spectra C_ℓ , we need to know the multipoles $X_\ell^{(m)}$ at τ_0 . Without using the line of sight approximation, that would require evolving a considerable amount of equations, making the computations very inefficient. With the line of sight approach however, we only need to evolve the sources which require at maximum the quadrupoles Θ_2 and E_2 . In order to have accurate solutions of the quadrupoles we can evolve the Boltzmann hierarchy up to some ℓ_{max} , and neglect the higher order multipoles. The numerical codes we mentioned earlier use the line of sight integration method to compute the CMB anisotropies. At this point we would like to make a few more remarks.

- First, one only needs to evolve the modes $m = 0, 1, 2$. The negative modes can be obtained by using the parity properties,

$$\Theta_\ell^{-|m|} = \Theta_\ell^{|m|}, \quad E_\ell^{-|m|} = E_\ell^{|m|}, \quad B_\ell^{-|m|} = -B_\ell^{|m|}. \quad (3.64)$$

The last relation also tells that $B_\ell^{(0)} = 0$, which reflects the fact that the B-mode polarization pattern cannot be generated by scalar sources. Also, because of the parity relations above, it is evident that in the power spectra (3.62) the B-modes do not couple to the temperature anisotropies and the E-mode polarization.

- Let us consider the temperature anisotropy integral solution (3.58) (the scalar component only) and ignore for a moment the polarization term which is usually small ($< 10\%$). We can write the integral solution as

$$\begin{aligned} \frac{\Theta_\ell(\tau_0, k)}{(2\ell + 1)} &= \int_0^{\tau_0} d\tau g(\tau) [\Theta_0 + \Psi] j_\ell[k(\tau_0 - \tau)] + \int_0^{\tau_0} d\tau e^{-\kappa} (\dot{\Psi} + \dot{\Phi}) j_\ell[k(\tau_0 - \tau)] \\ &+ \int_0^{\tau_0} d\tau \frac{d}{d\tau} \left[g(\tau) \frac{v_B^{(0)}}{k} \right] j_\ell[k(\tau_0 - \tau)], \end{aligned} \quad (3.65)$$

where $g(\tau) = -\dot{\kappa} \exp(-\kappa)$ is the *visibility function* that represents the probability that a photon last scattered with an electron at time τ and is peaked at $z \simeq 1100$. The second term in the equation above is known as the *integrated Sachs-Wolfe* (ISW) term. Physically it corresponds to a change in the temperature anisotropy given by photons passing through a time-evolving potential well. In matter dominated era, $\Phi = \Psi = \text{const}$, so the ISW term vanishes. However, when DE starts to dominate the energy density of the Universe, the (opposite of the) potentials Φ and Ψ start to

decay, so that the ISW term

$$I_\ell^{\text{ISW}}(k) = \int_0^{\tau_0} d\tau e^{-\kappa} (\dot{\Psi} + \dot{\Phi}) j_\ell[k(\tau_0 - \tau)] \quad (3.66)$$

is positive and boosts the temperature of the photons. The ISW term is a very powerful probe of DE [105], important to constrain models of DE, but it is sub-dominant in the CMB power spectrum C_ℓ and it requires other techniques to be detected. We will see this in Sect. 3.2.4.

- Another important signal on the CMB that we have not mentioned so far is the *weak lensing* signal [106]. When photons coming from the last scattering surface pass through a potential well, their trajectory is deflected (or *lensed*) by the gradient of the potential. Lensing has a quantitatively important effect in the CMB temperature, in the polarization signal and it also induces non-gaussianities. In Newtonian gauge photons are deflected by the gradient of the Weyl potential $\Phi_+ \equiv (\Psi + \Phi)/2$ such that the deflection angle α is given by

$$\alpha(\hat{\mathbf{n}}) = -2 \int_0^{\chi_*} d\chi \frac{\chi_* - \chi}{\chi_*} \nabla_\perp \Phi_+(\hat{\mathbf{n}}\chi, \chi), \quad (3.67)$$

so that one can usually define the lensing potential

$$\psi(\hat{\mathbf{n}}) = -2 \int_0^{\chi_*} d\chi \frac{\chi_* - \chi}{\chi_* \chi} \Phi_+(\hat{\mathbf{n}}\chi, \chi), \quad (3.68)$$

such that the deflection angle is given by $\alpha(\hat{\mathbf{n}}) = \nabla_\perp \psi(\hat{\mathbf{n}})$. This means that the observed polarization matrix $\mathbf{T}^{(1)}$ is actually transported away according to

$$\mathbf{T}^{(1)}(\hat{\mathbf{n}}) = \mathbf{T}^{(1)}(\hat{\mathbf{n}} + \nabla_\perp \psi), \quad (3.69)$$

effectively rotating the polarization matrix and generating a B-mode signal. The impacts of lensing on the temperature and E-mode polarization are similar and arise as a convolution of the temperature, or the E-mode polarization, with the lensing potential effectively, dampening the peaks and troughs. In metric gravity theories, in which the matter Lagrangian is minimally coupled to gravity, the CMB lensing works exactly in the same way as in GR. However, the way the Weyl potential evolves usually changes with different theories.

- Perturbations in the CMB arising at the last scattering surface are usually referred to as *primary anisotropies*, while perturbations generated when photons travel from the last scattering surface to us are called *secondary perturbations*. Examples of the latter are the ISW effect and the CMB lensing discussed above. There are other secondary anisotropies in the CMB that we just mention here. *Reionization* happens when ion-

izing sources start forming and neutral hydrogen and helium in the Universe begin to reionize. CMB photons can then re-scatter on the newly produced free electrons, effectively dampening the CMB temperature on scales inside the horizon at the time of reionization. It can also produce a large scale polarization signal. Other secondary perturbations include the *thermal Sunyaev-Zeldovich* (tSZ) effect [107] due to CMB photons scattering with electrons in hot-ionized gas around galaxy clusters, and other Doppler effects due to photons scattering off electrons in bulk-motion such as the *Ostriker-Vishniac* [108] (on linear scales) and the *kinetic Sunyaev-Zeldovich* [107] (on nonlinear scales) effects.

We now illustrate some of the measurements of the CMB anisotropies along with the theoretical predictions from the fiducial model from [11]. In Fig. 3.3 we show the CMB temperature anisotropies power spectrum measured by the Planck satellite [11], the South Pole Telescope (SPT) [109, 110] and the Atacama Cosmology Telescope (ACT) [111, 112]. The thin black line represents the best-fit Λ CDM model from [11], while the vertical dashed line divides the range of the two Planck likelihoods. Likewise, in Figs. 3.4 and 3.5 we show the power spectrum of the CMB E-mode polarization and the TE cross correlations from the same surveys. Finally, in Fig. 3.6 we show the measurements of the CMB B-mode pattern from the BICEP2/Keck array and Planck cross correlation analysis [45], SPT [64] and POLARBEAR [64]. Here the black line represents the weak lensing signal in the B-mode polarization pattern. We also assumed that the inflationary mechanism produce tensor modes with tensor to scalar ratio $r = 0.1$ that induce B-mode polarization at larger scales (small ℓ).

3.2.2 Large Scale Structure

We now move on in cosmic time and we jump at much later times, when structure has already formed. Analyzing the statistical distribution of the clustering of matter is of fundamental importance in cosmology and can provide useful insights into gravity theories.

Galaxies are trackers of the matter distribution and one can use the galaxy distribution correlation function to infer important properties of the total matter distribution. The simplest statistics is the galaxy-galaxy angular correlation function, defined as the two point function,

$$w(\theta) \equiv \langle \delta N_g(\hat{\mathbf{n}}, z) \delta N_g(\hat{\mathbf{n}}', z) \rangle, \quad (3.70)$$

where θ is the separation angle between the directions $\hat{\mathbf{n}}$ and $\hat{\mathbf{n}}'$, and $\delta N_g(\hat{\mathbf{n}}, z)$ is the overabundance of galaxies at redshift z in the direction $\hat{\mathbf{n}}$, defined as

$$\delta N_g(\hat{\mathbf{n}}, z) = N_g(\hat{\mathbf{n}}, z) - \bar{N}_g(z). \quad (3.71)$$

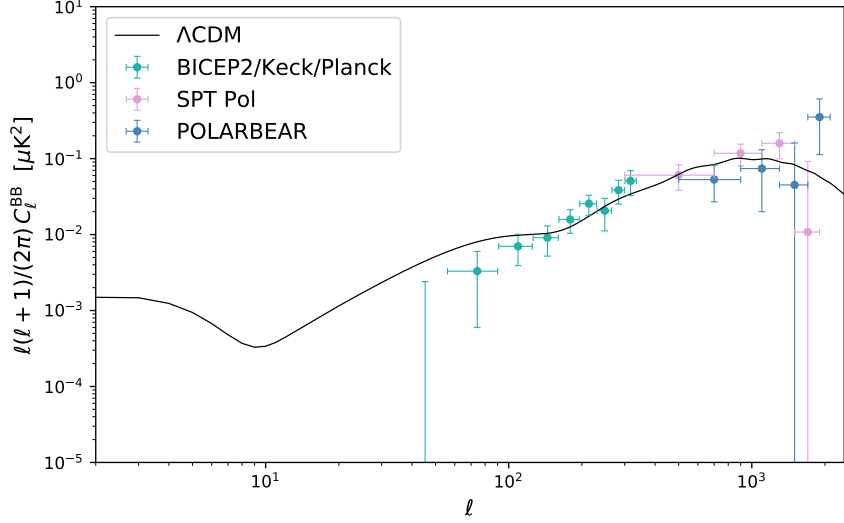


Figure 3.6: Measurements of the B-mode CMB power spectrum performed by several surveys. The thin black line shows the best fit Λ CDM model with $r = 0.1$ from the Planck collaboration analysis.

Here $N_g(\hat{\mathbf{n}}, z)$ is the number of galaxies observed, while $\bar{N}_g(z)$ is the average number of galaxies at redshift z . We are interested in how to compute the theoretical predictions of such quantity. We assume that galaxies track matter overdensity according to

$$\delta N_g(\mathbf{k}, z) = b_g(k, z) \delta_m(\mathbf{k}, z), \quad (3.72)$$

where $b_g(k, z)$ is the galaxy *bias* that might depend on the scale k and the redshift z . In order to compute the angular correlation function (3.70) we can use the formalism developed at the beginning of Sect. 3.2 and use Eq. (3.28) to compute the galaxy-galaxy angular power spectrum. The transfer function $I_\ell(k)$ is given by

$$I_\ell^g(k) = \int_0^{\tau_0} d\tau W(\tau) b_g(k, \tau) \tilde{\delta}(k, \tau) j_\ell[k(\tau_0 - \tau)]. \quad (3.73)$$

As pointed out in [113], other relativistic corrections can enter the transfer function (3.73). For simplicity, here we ignore them, as they are usually not very big.

On small scales, the transfer functions (3.73) are time consuming to compute due to the rapid oscillation of the spherical Bessel functions at large ℓ . For this reason, many analyses use the Limber approximation that consists (at first order) in replacing the integral over the spherical Bessel function with an integral over a Dirac delta function [114],

$$\int dx j_\ell(x) \cdots \rightarrow \sqrt{\frac{\pi}{2\nu}} \int dx \delta(\nu - x) \cdots, \quad (3.74)$$

where $\nu = \ell + 1/2$. The transfer function then becomes

$$I_\ell^g(k) = \frac{1}{k} W\left(\tau_0 - \frac{\ell + 1/2}{k}\right) b_g\left(k, \tau_0 - \frac{\ell + 1/2}{k}\right) \tilde{\delta}\left(k, \tau_0 - \frac{\ell + 1/2}{k}\right), \quad (3.75)$$

where the pre-factor $1/k$ comes from the change of variables in the Dirac delta function. Plugging the above transfer function, in the correlation function (3.19) and using the fact that, for large ℓ , $\mathcal{P}_\ell(\cos\theta) \approx J_0(\ell\theta)$, we obtain

$$w(\theta) = \int \frac{d\ell \ell J_0(\ell\theta)}{2\pi} \int \frac{d\chi}{\chi^2} W^2(\chi) b_g^2\left(\frac{\ell + 1/2}{\chi}, \chi\right) \tilde{\delta}^2\left(\frac{\ell + 1/2}{\chi}, \chi\right) P_{\mathcal{R}}\left(\frac{\ell + 1/2}{\chi}\right), \quad (3.76)$$

where J_0 is the zero order Bessel function of the first kind. There is however a caveat in the derivation above. When considering the small scales limit, we are approaching the regime of nonlinear scales, so that the perturbation theory developed in Chapter 2 breaks down. To fix this, the linear transfer functions $\tilde{\delta}^2$, along with the primordial power spectrum $P_{\mathcal{R}}$, should be replaced by the nonlinear matter power spectrum P_{NL} , so that the correlation function becomes

$$w(\theta) = \int \frac{d\ell \ell J_0(\ell\theta)}{2\pi} \int \frac{d\chi}{\chi^2} W^2(\chi) b_g^2 P_{\text{NL}}\left(\frac{\ell + 1/2}{\chi}, \chi\right). \quad (3.77)$$

In GR, there are several empirical prescriptions to compute the nonlinear matter power spectrum. Some of them are based on phenomenological fitting formulas (halo models) for the power spectrum derived from N-body simulations [115, 116, 117], with more recent extensions provided in [118, 119, 120]. In Part III, we will investigate phenomenological deviations from GR for which there is no nonlinear prescription for the matter power spectrum, so we will truncate the data sets to linear scales only.

In Fig. 3.7 we show the measurements of the angular correlation function $w(\theta)$ from the Dark Energy Survey (DES) [121] for the 5 redshift bins used in the survey. The orange lines represent the Λ CDM linear theory predictions, while the blue ones are the nonlinear corrections obtained with HALOFIT [118]. The grey shaded region is an empirical cut on the nonlinear scales, as explained in Appendix A.

3.2.3 Weak Lensing

In Sect. 3.2.1 we mentioned that CMB photons passing in the vicinity of a potential well are deflected. Likewise, photons coming from distant galaxies are deflected when passing through gravitational potentials between the observer (us) and the source galaxies. The lensing potential is related to angle deflection of the photons trajectory, and for sources at a comoving distance χ is the same as in equation (3.68),

$$\psi(\hat{\mathbf{n}}, \chi) = -2 \int_0^\chi \frac{d\chi'}{\chi'} \frac{\chi - \chi'}{\chi} \Phi_+(\chi' \hat{\mathbf{n}}, \chi'). \quad (3.78)$$

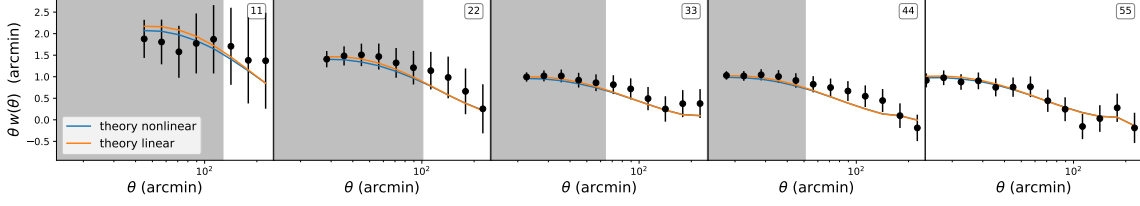


Figure 3.7: Two point angular correlation function $w(\theta)$ measurements from DES. The orange line is the linear theory matter power spectrum, while the blue line represents the nonlinear power spectrum calculated with HALOFIT. The grey shaded region is an empirical cut on the nonlinear data.

The lensing potential is averaged over sources with a distribution $n(\chi)$,

$$\begin{aligned}\psi(\hat{\mathbf{n}}) &= -2 \int_0^{\chi_\infty} d\chi n(\chi) \int_0^\chi \frac{d\chi'}{\chi'} \frac{\chi - \chi'}{\chi} \Phi_+(\chi' \hat{\mathbf{n}}, \chi') \\ &= -2 \int_0^{\chi_\infty} \frac{d\chi}{\chi} q(\chi) \Phi_+(\chi \hat{\mathbf{n}}, \chi),\end{aligned}\quad (3.79)$$

where the *lensing efficiency function* $q(\chi)$ is given by

$$q(\chi) = \int_\chi^{\chi_\infty} d\chi' n(\chi') \frac{\chi' - \chi}{\chi'}.\quad (3.80)$$

As we did at the beginning, we can expand the lensing potential in spherical harmonics and compute its angular power spectrum $C_\ell^{\psi\psi}$ using equations (3.28) and (3.30),

$$C_\ell^{\psi\psi} = \frac{8}{\pi} \int dk k^2 I_\ell^{\text{WL}}(k) I_\ell^{\text{WL}}(k) P_{\mathcal{R}}(k),\quad (3.81)$$

where the weak lensing transfer functions are given by

$$I_\ell^{\text{WL}}(k) = \int_0^{\chi_\infty} \frac{d\chi}{\chi} q(\chi) \Phi_+(k, \chi) j_\ell(k\chi).\quad (3.82)$$

As mentioned for the CMB, the effect of gravitational lensing is to remap the observed position of the sources, from $\hat{\mathbf{n}}$ to $\hat{\mathbf{n}}'$, and the transformation depends on the gradient of the lensing potential ψ . The Jacobian of the transformation is hence described by the second derivatives of the lensing potential ψ and, being a matrix, can be expanded in the same manner as we did for the CMB polarization,

$$\nabla_i \nabla_j \psi = \kappa \mathbf{I} + (\gamma_1 + i\gamma_2) \mathbf{M}_+ + (\gamma_1 - i\gamma_2) \mathbf{M}_-, \quad (3.83)$$

where the *convergence* κ is related to the magnification of the image and the *shear* $\gamma \equiv \gamma_1 + i\gamma_2$ describes how images change shape but still maintaining the same size. The convergence

and the shear can then be decomposed in (spin-weighted) spherical harmonics and behave like the temperature and polarization components of the CMB,

$$\kappa(\hat{\mathbf{n}}) = -\frac{1}{2} \sum_{\ell,m} \ell(\ell+1) \psi_{\ell,m} Y_{\ell,m}(\hat{\mathbf{n}}), \quad (3.84)$$

$$(\gamma_1 \pm i\gamma_2)(\hat{\mathbf{n}}) = \frac{1}{2} \sum_{\ell,m} \sqrt{\frac{(\ell+2)!}{(\ell-2)!}} \psi_{\ell,m \pm 2} Y_{\ell,m}(\hat{\mathbf{n}}), \quad (3.85)$$

where $\psi_{\ell,m}$ are the coefficients of the decomposition in spherical harmonics of the lensing potential ψ . The shear can also be expanded in E and B modes, as

$$(\gamma_1 \pm i\gamma_2)(\hat{\mathbf{n}}) = \sum_{\ell,m} (\epsilon_{\ell,m} \pm i\beta_{\ell,m})_{\pm 2} Y_{\ell,m}(\hat{\mathbf{n}}). \quad (3.86)$$

In the Born approximation, the lensing potential ψ has a vanishing B-mode contribution, so we can write,

$$\epsilon_{\ell,m} = \frac{1}{2} \sqrt{\frac{(\ell+2)!}{(\ell-2)!}} \psi_{\ell,m}, \quad (3.87)$$

which turns to a relation for the angular power spectra,

$$C_{\ell}^{\epsilon\epsilon} = \frac{1}{4} \frac{(\ell+2)!}{(\ell-2)!} C_{\ell}^{\psi\psi}. \quad (3.88)$$

Similarly, for the convergence power spectrum we have

$$C_{\ell}^{\kappa\kappa} = \frac{1}{4} \ell^2 (\ell+1)^2 C_{\ell}^{\psi\psi}. \quad (3.89)$$

Since the shear components are defined by the direction $\hat{\mathbf{n}}$, taking the correlation functions between shear at different directions $\hat{\mathbf{n}}_1$ and $\hat{\mathbf{n}}_2$ requires rotating the basis onto the circle connecting the two directions [122, 123]. Denoting the rotated shear with $\bar{\gamma}$, the correlation functions can be expressed as The angular correlation function can then be expressed as

$$\xi_+(\theta) \equiv \langle \bar{\gamma}^*(\hat{\mathbf{n}}_1) \bar{\gamma}(\hat{\mathbf{n}}_2) \rangle = \sum_{\ell} \frac{2\ell+1}{4\pi} C_{\ell}^{\epsilon\epsilon} d_{22}^{\ell}(\theta), \quad (3.90)$$

$$\xi_-(\theta) \equiv \langle \bar{\gamma}(\hat{\mathbf{n}}_1) \bar{\gamma}(\hat{\mathbf{n}}_2) \rangle = \sum_{\ell} \frac{2\ell+1}{4\pi} C_{\ell}^{\epsilon\epsilon} d_{2-2}^{\ell}(\theta), \quad (3.91)$$

where θ is the angle between $\hat{\mathbf{n}}_1$ and $\hat{\mathbf{n}}_2$, and $d_{2\pm 2}^{\ell}$ are the reduced Wigner D-matrices. In the flat-sky limit, valid for small patches of sky, the Wigner D-matrices can be approximated with Bessel functions of the first kind,

$$d_{2\pm 2}^{\ell} \approx J_{0/4}(\ell\theta), \quad (3.92)$$

and, using the Limber approximation, the correlation functions can be written as

$$\xi_{\pm}(\theta) = \int \frac{d\ell \ell^5 J_{0/4}(\ell\theta)}{2\pi} \int \frac{d\chi}{\chi^4} q^2(\chi) \Phi_+^2\left(\frac{\ell+1/2}{\chi}, \chi\right) P_{\mathcal{R}}\left(\frac{\ell+1/2}{\chi}\right), \quad (3.93)$$

Unlike in most of the literature about weak lensing, here we did not replace the Weyl potential Φ_+ with the total matter density function. To do so one should use the fact that in GR, at late times $\Phi \simeq \Psi$, and then use the Poisson equation to replace Φ with δ . This is in general not the case for modified gravity theories and hence we kept the dependence on the Weyl potential. This also suggest that in general weak lensing is sensitive to the growth of structure and through Φ_+ and hence is potentially a powerful tool for investigating deviations from GR.

Weak lensing is also sensitive to DE, through both the lensing efficiency function and Φ_+ . The most recent measurements of the cosmic shear angular correlation function has been performed by DES [121]. In Figs. 3.8 and 3.9 we show the DES measurements of the angular correlation function of the cosmic shear $\xi_{\pm}(\theta)$ in the 5 redshift bins used in the survey. We also show the best fit Λ CDM linear and nonlinear theoretical predictions in orange and blue respectively. The grey regions are the empirical cutoffs of the nonlinear sector of the datasets, which are suitable for model-independent tests of modified gravity.

3.2.4 Cross-Correlations

Finally, it is possible to consider cross-correlations between the observables presented above. In particular we will be interested in the cross correlations between the CMB temperature and the galaxy number count,

$$C_{\ell}^{\text{T,g}} = \frac{2}{\pi} \int dk k^2 I_{\ell}^{\text{T}}(k) I_{\ell}^{\text{g}}(k) P_{\mathcal{R}}(k), \quad (3.94)$$

where $I_{\ell}^{\text{T}}(k)$ is the ISW transfer function. The cross correlation above is able to pick up the weak ISW signal expected to arise from the decay of the gravitational potentials during the accelerated phase of the expansion of the Universe. We hence expect a positive correlation between CMB temperature and galaxy clustering. However, the signal-to-noise ratio is intrinsically very small for the CMB-galaxy cross correlation [124], and obtaining high significance measurements of the ISW signal is rather challenging. Nevertheless, cross-correlations between the CMB temperature provided by the WMAP and Planck satellites and other galaxy catalogues produced a $3-4\sigma$ detection of a positive ISW effect [125, 126, 127, 128, 129], in agreement with the Λ CDM model.

Another potentially significant measurement arise from the cross correlation between background galaxies lensing and foreground galaxies position. The shapes of the background source galaxies are tangentially distorted by the gravitational potentials of the foreground

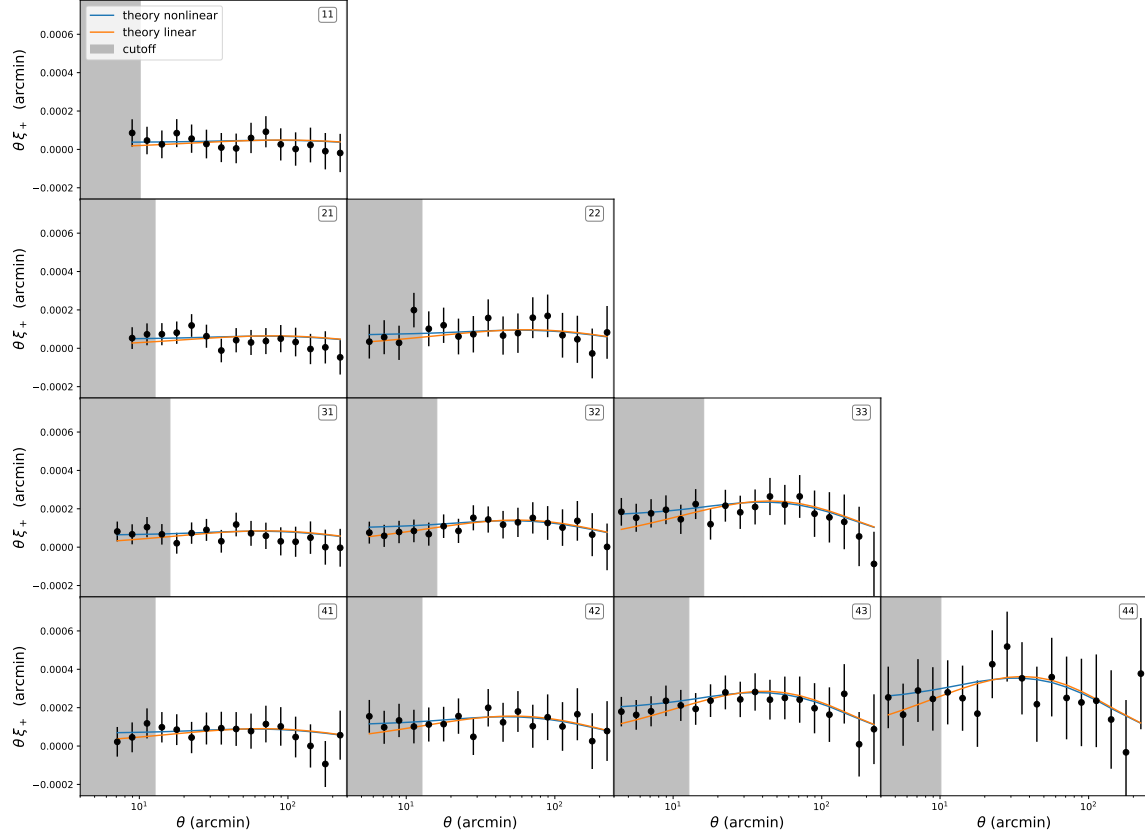


Figure 3.8: Measurements of the cosmic shear ξ_+ angular correlation function from the Dark Energy Survey. blue and orange lines show the nonlinear and linear theory predictions respectively from the best fit Λ CDM model. The grey regions show the “soft” empirical data cut on the nonlinear scales.

galaxies. The theoretical prediction is a cross correlation of the form,

$$C_\ell^{\gamma^t} = \frac{2}{\pi} \int dk k^2 I_\ell^g(k) I_\ell^{\text{WL}}(k) P_{\mathcal{R}}(k), \quad (3.95)$$

usually calculated in the flat-sky limit and using the Limber approximation. In Fig. 3.10 we show the recent measurements of the tangential shear $\gamma_t(\theta)$ by DES. As we did before we show the best fit linear and nonlinear theoretical predictions along with the empirical nonlinear data cutoff.

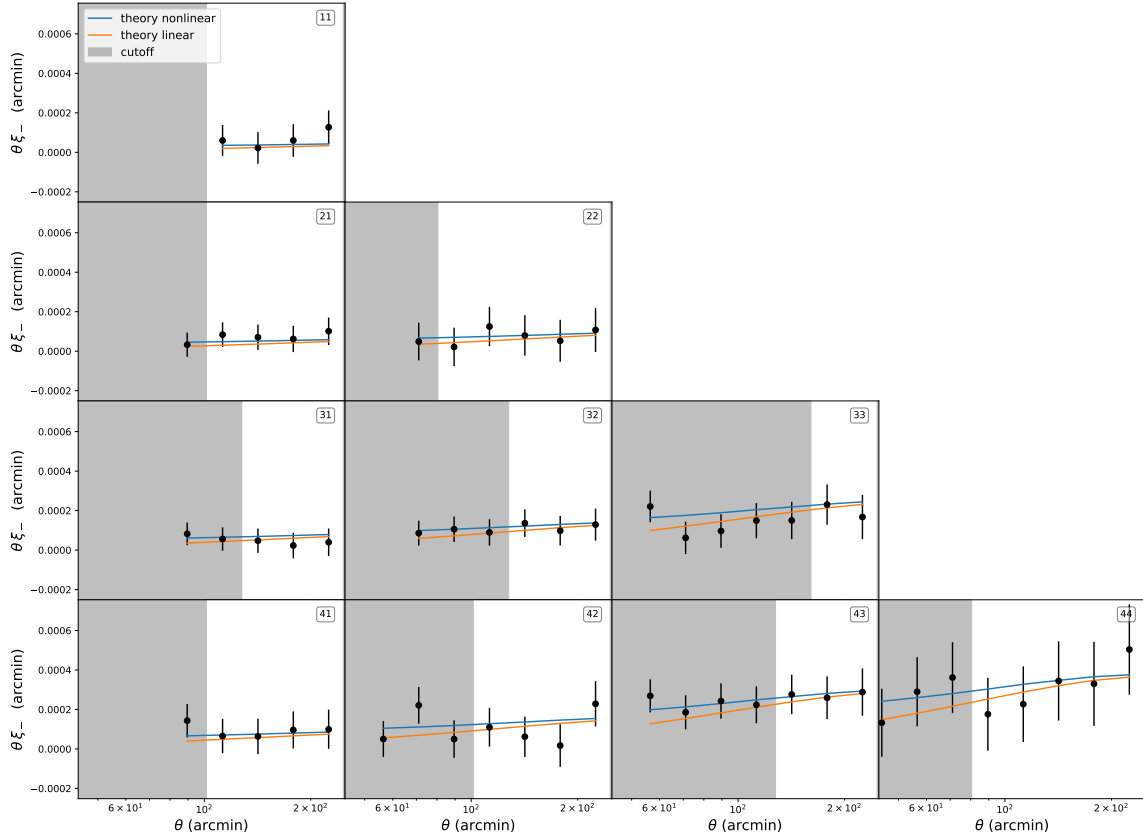


Figure 3.9: Measurements of the cosmic shear ξ_{-} angular correlation function from the Dark Energy Survey. blue and orange lines show the nonlinear and linear theory predictions respectively from the best fit Λ CDM model. The grey regions show the “soft” empirical data cut on the nonlinear scales.

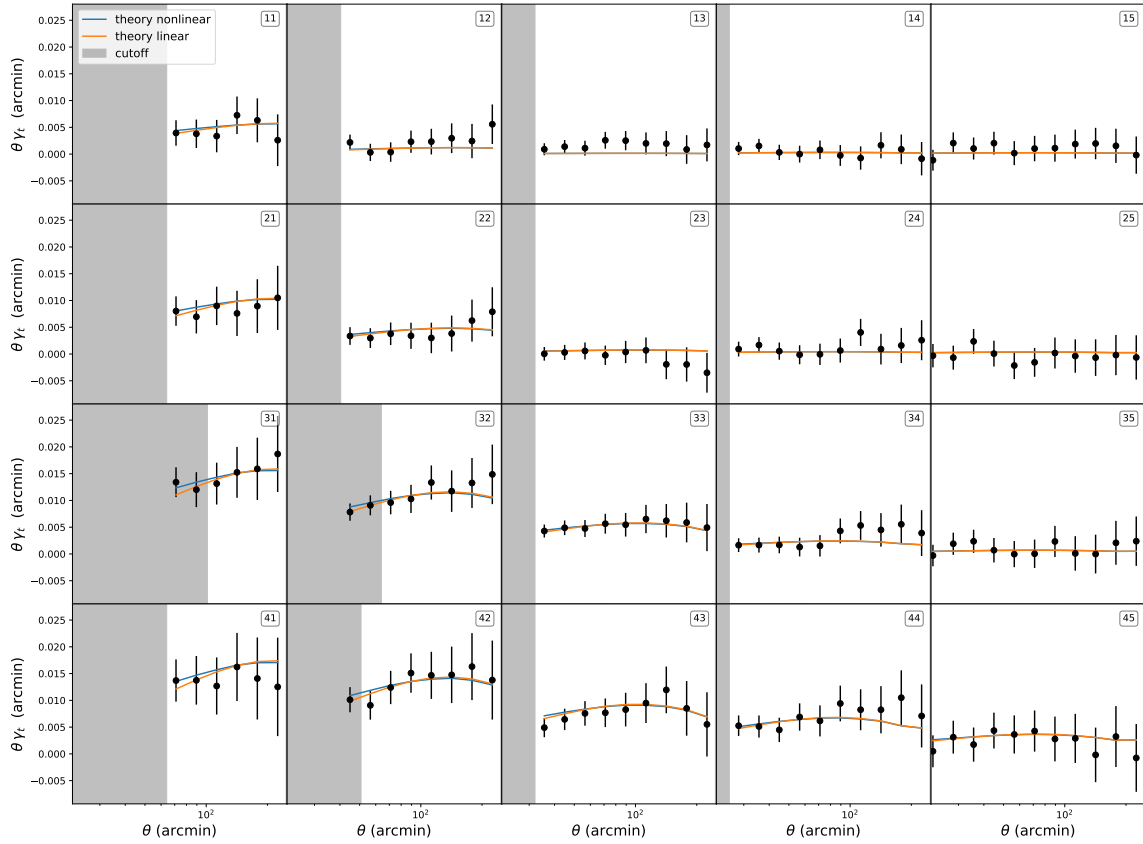


Figure 3.10: Measurement of the tangential shear γ_t from the Dark Energy Survey. As we did in the previous figures, blue and orange lines show the nonlinear and linear theory predictions respectively from the best fit Λ CDM model. The grey regions show the “soft” empirical data cut on the nonlinear scales.

Part II

Testing Fundamental Physics in the early Universe

Chapter 4

Observational Constraints on Constant-Roll Inflation

We begin this part with an observational test on constant-roll inflation models. Throughout the years, a multitude of inflationary models were proposed where the dynamics of the background field is highly overdamped, and the production of scalar and tensor fluctuations can be completely characterized by the so-called slow-roll parameters. Slow roll by itself is not a necessary condition for an inflationary model to be viable, and it is interesting to also explore models which break away from the slow-roll restrictions.

As a way to parametrize deviations from the slow roll condition, Motohashi *et. al.* recently introduced a constant-roll inflation [130, 131] where the scalar driving the inflation is assumed to roll down its potential at a constant rate, be it slow or not. The model is rather interesting as it characterizes the deviation from a slow roll by a single parameter and allows analytic integration of the expansion history and the full scalar field potential reconstruction. The potential driving constant-roll inflation only differs from the one in natural inflation [132] by the addition of a negative cosmological constant (with specially chosen value). The constant-roll rate can be tuned by the period of the potential, which corresponds to the global symmetry breaking scale in natural inflation.

In this Chapter, we show how it is possible to use the current data CMB data to derive constraints on the constant roll model of inflation. Although this was already performed in [131], the confrontation of this model with observational data used the well-known consistency relations between slow-roll and fluctuation spectra parameters [133, 134], which assumes that using the exact background solutions, one can describe certain features of the perturbations spectra by using slow-roll approximation while this holds accurately in the parameter range to be explored.

Here we adopt a fully numerical approach and do not impose any slow roll conditions, but rather we evaluate directly the scalar and tensor power spectra of primordial fluctuations. This procedure allows us to evaluate deviations from the standard slow-roll approximation of the spectral index n_s and the tensor-to-scalar ratio r .

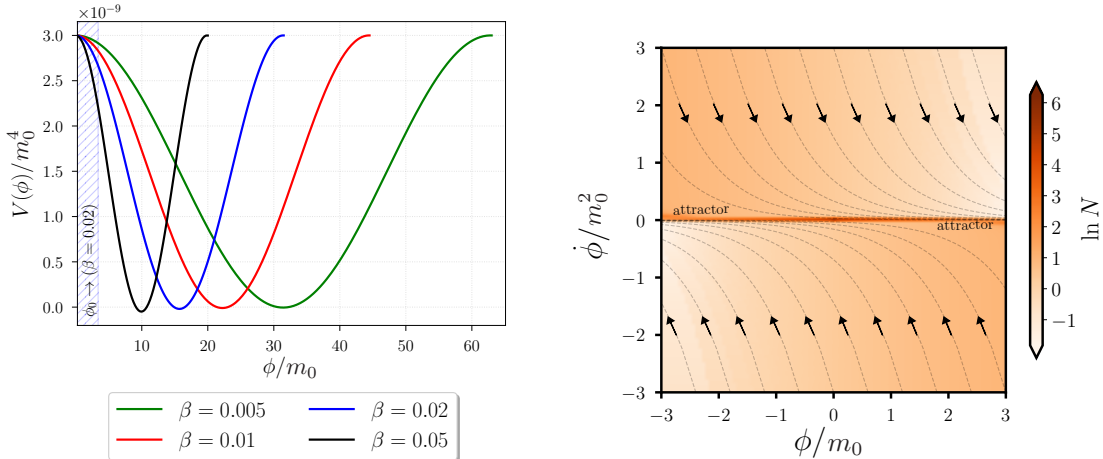


Figure 4.1: Left panel: constant-roll inflation potential (4.4) for the model parameters $M^2 = 2.0 \times 10^{-9} m_0^2$ and different values of β . The region of interest is in the range $\phi \in (0; \phi_0]$, shown for the specific value of $\beta = 0.02$. Right panel: Map of initial conditions in the phase space for $M^2 = 2.0 \times 10^{-9} m_0^2$, $N_* = 55$ and $\beta = 0.02$. The color map represents the number of e-folds before reaching $\pm\phi_0$. Phase space trajectories converge as a power law towards the attractor (instead of exponentially, as is usually the case in slow-roll inflation) as in the case of power law inflation, which is a particular scenario of the constant-roll model.

The numerical integrations are performed with a single-field version of a general method developed in [135] which separates the fast and slow scales in the mode evolution to exponentially increase efficiency of sub-horizon integration. This computational method allows us to scan a significant portion of the parameter space quickly and extremely accurately even on a personal computer with minimal specifications.

Constant-roll inflation has an uncertainty on the field value where inflation ends, as the potential needs to be cut at some value ϕ_0 to get an exit from inflation. This introduces a third parameter to the model in addition to the mass scale and the roll rate, which fortunately turns out to be entirely degenerate as far as fluctuation spectra are concerned. This allows us to set tight constraints on two combinations of the model parameters for constant-roll inflation: one that determines the amplitude of scalar and tensor perturbations (along with the characteristic energy scale where inflation occurs), and the second one which sets the roll rate (and quantifies the deviations from the slow-roll approximation). We also compare constant-roll inflation with other models by comparing the allowed regions on the r versus n_s diagram, where each point can be identified with (at least) one choice of the model parameters after the spectrum is evaluated at the pivot scale.

4.1 Model and Background Dynamics

In this section, we review the constant-roll inflation model and its background evolution [130]. The dynamics of the inflaton field minimally coupled to gravity is governed by the

effective action

$$S = \int d^4x \sqrt{-g} \left[\frac{m_0^2}{2} R - \frac{1}{2} g^{\mu\nu} \partial_\mu \phi \partial_\nu \phi - V(\phi) \right], \quad (4.1)$$

where ϕ is the inflaton field with a canonical kinetic term. Here we use the signature $(-, +, +, +)$ and assume the spatially flat Friedmann-Lemaître-Robertson-Walker metric for background. The constant-roll inflation potential $V(\phi)$ we use throughout this Chapter was derived in [131, 136] after reducing the order of the standard background equation of motion

$$\ddot{\phi} + 3H\dot{\phi} + V'(\phi) = 0 \quad (4.2)$$

by the constant-roll *ansatz* $\ddot{\phi} = \beta H \dot{\phi}$. Here overdots represent derivatives w.r.t. the cosmic time t . The role of β is to parametrize the magnitude of the second time derivative and thus, the deviations from the slow-roll approximation. Using the two Friedmann equations

$$\begin{aligned} 3m_0^2 H^2 &= \frac{1}{2} \dot{\phi}^2 + V(\phi), \\ -2m_0^2 \dot{H} &= \dot{\phi}^2, \end{aligned} \quad (4.3)$$

it is possible to find a particular solution for the background evolution and reconstruct the constant-roll inflation potential $V(\phi)$, which turns out to be

$$V(\phi) = 3m_0^2 M^2 \left[1 - \frac{3 + \beta}{6} \left\{ 1 - \cos \left(\frac{\sqrt{2\beta}\phi}{m_0} \right) \right\} \right]. \quad (4.4)$$

The shape of the potential is illustrated in the left panel of Fig. 4.1 and evaluated at different values of β . The mass M determines both the energy scale at which inflation occurs and the amplitude of the primordial fluctuations. The potential (4.4) can become negative, and must be cut off somewhere before that to end inflation gracefully.

In the absence of an inherent point on the potential where inflation ends, it is important to explicitly specify the field range where we will evaluate the curvature and tensor fluctuations. The background field evolution proceeds from arbitrarily small values to some upper bound ϕ_0 where the potential is modified and inflation ends, which we parametrize by setting to be N_* e-folds away from reaching the critical point where $V = 0$ in the unmodified potential (4.4). This range depends on the model parameters and is illustrated in the left panel of Fig. 4.1, where ϕ_0 can be calculated as

$$\frac{\phi_0}{m_0} = \sqrt{\frac{2}{\beta}} \sin^{-1} \left\{ e^{-N_*\beta} \sin \left[\frac{1}{2} \cos^{-1} \left(\frac{\beta - 3}{\beta + 3} \right) \right] \right\}. \quad (4.5)$$

We note that ϕ_0 is independent of M . Thus, the model has three parameters, namely M , β and N_* . It is clear that N_* and M are degenerate since amplitude of scalar fluctuations can be changed by either a shift in the energy scale of the potential, or by moving the endpoint

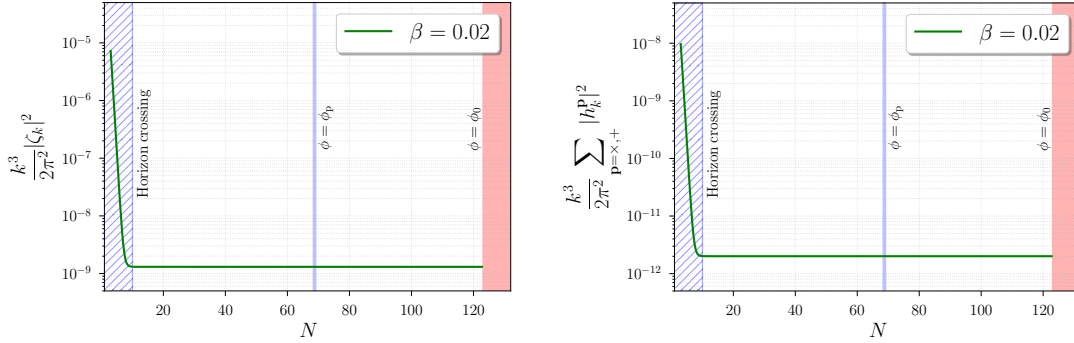


Figure 4.2: Left panel: Example of the evolution of the curvature fluctuations for $\beta = 0.02$, $N_* = 0$ and $M^2 = 10^{-11}m_0^2$. Right panel: Evolution of the corresponding sum of the two tensor polarizations for the same model parameters. N is the number of e-folds from the start of numerical evolution of the background. Using the definition in (4.6), both figures also include the instant in which the CMB pivot modes leave the horizon. We show extremely long wavelength modes emerging deep from the sub-horizon scales to demonstrate that there is absolutely no evolution on super-horizon scales in all cases.

ϕ_0 closer or further from $\phi = 0$ where potential is flat, up to the value where $V = 0$. In a similar way, it is necessary to define the field value ϕ_p in which the scalar/tensor CMB pivot modes exit the horizon

$$\frac{\phi_p}{m_0} = \sqrt{\frac{2}{\beta}} \sin^{-1} \left[e^{-55\beta} \sin \left(\sqrt{\frac{\beta}{2}} \frac{\phi_0}{m_0} \right) \right], \quad (4.6)$$

this is located 55 e-folds before the end of inflation. Using the equations of motion for the field (4.2) and the Hubble scale (4.3), we scan the phase space in order to find the number of e-folds for every choice of initial conditions inside the interval $\phi/m_0 \in [-3; 3]$ and $\dot{\phi}/m_0^2 \in [-3; 3]$. Our results are shown in the right panel of Fig. 4.1 for $M^2 = 2.0 \times 10^{-9}m_0^2$, $N_* = 55$ and $\beta = 0.02$, where $\phi_0 = 3.38$ corresponds to our choice for β . A few phase space trajectories are also plotted in the same figure. A choice of initial conditions close to the attractor (with $\dot{\phi}$ small in this case) generates more expansion before reaching $\pm\phi_0$ due to a slow convergence to the attractor of the trajectories starting away from it. We take $\dot{\phi} = 0$ as a suitable initial condition for the background field velocity that always reaches the attractor, and start numerical evolution of the background sufficiently far in the past for trajectory to settle to the attractor before considering fluctuations.

4.2 Perturbations

In this section, we recount the standard treatment of scalar and tensor perturbations required to obtain the power spectra of primordial fluctuations, and describe an extremely effective way to do so numerically. Let us first recall the expansion of the action (4.1) up to

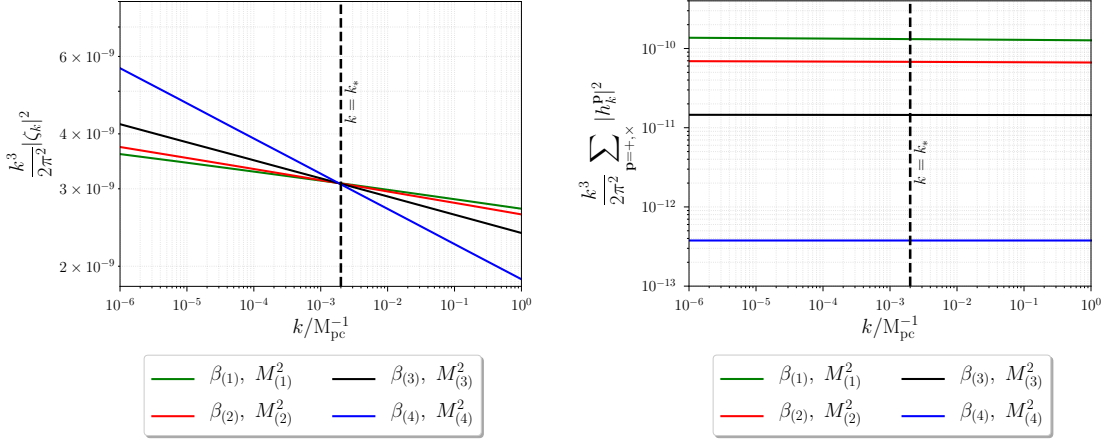


Figure 4.3: Left panel: Power spectrum of primordial curvature fluctuations using $k_* = 2 \times 10^{-3} M_{\text{pc}}^{-1}$ as a pivot scale at $N_* = 0$. We considered the model parameters $\beta_{(1)} = 0.005$, $M_{(1)}^2 = 10^{-9} m_0^2$, $\beta_{(2)} = 0.01$, $M_{(2)}^2 = 3.82 \times 10^{-10} m_0^2$, $\beta_{(3)} = 0.02$, $M_{(3)}^2 = 7.26 \times 10^{-11} m_0^2$, $\beta_{(4)} = 0.04$ and $M_{(4)}^2 = 1.86 \times 10^{-12} m_0^2$. Right panel: Power spectrum of tensor perturbations for the same model parameters. None of the spectra show any features or running.

second order in perturbations

$$\begin{aligned}
S_2 &= \frac{m_0^2}{8} \int a^2 d\eta d^3x \left[h'_{ij} h'^{ij} - (\nabla_k h_{ij})(\nabla^k h^{ij}) \right] \\
&\quad + \frac{1}{2} \int \left(\frac{\phi'^2}{H^2} \right) d\eta d^3x \left[\zeta'^2 - (\nabla_i \zeta)(\nabla^i \zeta) \right], \tag{4.7}
\end{aligned}$$

which is written in the gauge $\delta\phi = 0$ and in conformal time η . Latin indices are raised and lowered by the Kronecker delta and primes denote derivatives w.r.t. η . In terms of the polarization modes $h_{ij} \equiv \sum_{\mathbf{p}=+,\times} h^{\mathbf{p}} \sigma_{ij}^{\mathbf{p}}$, the last expression is equivalent to

$$\begin{aligned}
S_2 &= \frac{m_0^2}{8} \sum_{\mathbf{p}=+,\times} \int a^2 d\eta d^3x \left[(h^{\mathbf{p}'})^2 - (\nabla_k h^{\mathbf{p}})(\nabla^k h^{\mathbf{p}}) \right] \\
&\quad + \frac{1}{2} \int \left(\frac{\phi'^2}{H^2} \right) d\eta d^3x \left[\zeta'^2 - (\nabla_i \zeta)(\nabla^i \zeta) \right], \tag{4.8}
\end{aligned}$$

where we used the fact that $\text{tr}(\sigma^+)^2 = \text{tr}(\sigma^\times)^2 = 1$ and $\text{tr}(\sigma^+ \sigma^\times) = 0$. Now, we introduce the Mukhanov-Sasaki variables $v \equiv \phi'/H\zeta$ and $v^{\mathbf{p}} \equiv am_0 h^{\mathbf{p}}/2$ [137, 138, 139] to rewrite the action as

$$\begin{aligned}
S_2 &= \frac{1}{2} \sum_{\mathbf{p}=+,\times} \int d\eta d^3x \left[(v^{\mathbf{p}'})^2 - (\nabla_k h^{\mathbf{p}})(\nabla^k h^{\mathbf{p}}) \right. \\
&\quad \left. + \frac{a''}{a} (v^{\mathbf{p}})^2 \right] + \frac{1}{2} \int d\eta d^3x \left[v'^2 - (\nabla_i v)(\nabla^i v) + \frac{z''}{z} v^2 \right],
\end{aligned}$$

where $z = \phi'/\sqrt{2}m_0H$. Hence, the action for perturbations is now canonically normalized. In Fourier space, the equations of motion for fluctuations are given by

$$v_k'' + \left(k^2 - \frac{z''}{z}\right)v_k = 0, \quad (4.9)$$

$$(v_k^{\mathbf{P}})'' + \left(k^2 - \frac{a''}{a}\right)v_k^{\mathbf{P}} = 0, \quad (4.10)$$

where the Fourier transformed Mukhanov-Sasaki variables are $v_k \equiv \phi'/H \zeta_k$ and $v_k^{\mathbf{P}} \equiv am_0 h_k^{\mathbf{P}}/2$. Both (4.9) and (4.10) have the form a harmonic oscillator with time-dependent frequency

$$\xi_k'' + \omega_{\text{eff}}^2(\eta)\xi_k = 0. \quad (4.11)$$

We will now apply a very simple trick which is incredibly effective for numerical evaluation of the perturbation spectra, which is the single-field version of the general method [135]. The fluctuation variable ξ_k can be redefined in terms of real amplitude L_k and phase Θ_k as $\xi_k \equiv L_k \exp(i\Theta_k)$. Substituting this ansatz into (4.11) splits the differential equation into real and imaginary parts

$$L_k'' + [\omega_{\text{eff}}^2(\eta) - (\Theta_k')^2] L_k = 0, \quad (4.12)$$

$$\Theta_k'' + 2\frac{L_k'}{L_k} \Theta_k' = 0, \quad (4.13)$$

where the imaginary part (4.13) is separable and has a simple analytic solution $\Theta_k'(\eta) = \Theta_k'(\eta_0)L_k^2(\eta_0)/L_k^2(\eta)$. Once the phase is eliminated from (4.12), we obtain

$$L_k'' + \left[\omega_{\text{eff}}^2(\eta) - \omega_{\text{eff}}^2(\eta_0)\frac{L_k^4(\eta_0)}{L_k^4(\eta)}\right] L_k = 0, \quad (4.14)$$

where the Bunch-Davies vacuum deep inside horizon at $\eta = \eta_0$ sets $\Theta_k'(\eta_0) = \omega_{\text{eff}}(\eta_0)$, $L_k = 1/\sqrt{2\omega_{\text{eff}}}$, and $L_k'(\eta_0) = 0$ as initial conditions for mode evolution. The key observation is that the last term in (4.14) cancels the effective mode oscillation frequency, allowing numerical evolution to keep track of changes in amplitude only, with precision increasing deep inside the horizon where the vacuum state is more accurate. One no longer needs to resolve exponentially large physical oscillation scale (k/a) inside horizon, and can use a time step merely a fraction of the Hubble scale to resolve the evolution of the amplitudes without compromising the precision of the evolution routine. The latter expression is also known as the Ermakov-Pinney equation [140, 141, 142]. The implementation of this simple technique in equations (4.9) and (4.10) allowed us to calculate the evolution of the scalar curvature and the tensor fluctuations to extremely high precision, as shown in the two panels of Fig. 4.2.

We can evaluate the power spectra of scalar and tensor perturbations once we compute the evolution of the scalar and tensor modes for relevant wavenumbers. As an illustration, we

calculated the spectra for several sets of the model parameters choosing $k_* = 2 \times 10^{-3} M_{\text{pc}}^{-1}$ as a pivot scale in Fig. 4.3. The most striking fact to observe in both panels is the absence of any features or running in the spectra including $\beta = 0.02$, as it was argued in [131]. This can be checked for any number of the modes used to produce each of the spectra. Thus, the estimations made in that paper about the shape of the spectrum, in analogy with the approximate treatment for natural inflation (see [143] for further details) are perfectly valid. Nevertheless, we can increase accuracy of the parameter estimation (especially away from the slow-roll regime) by calculating the power spectra directly for each of the model realizations.

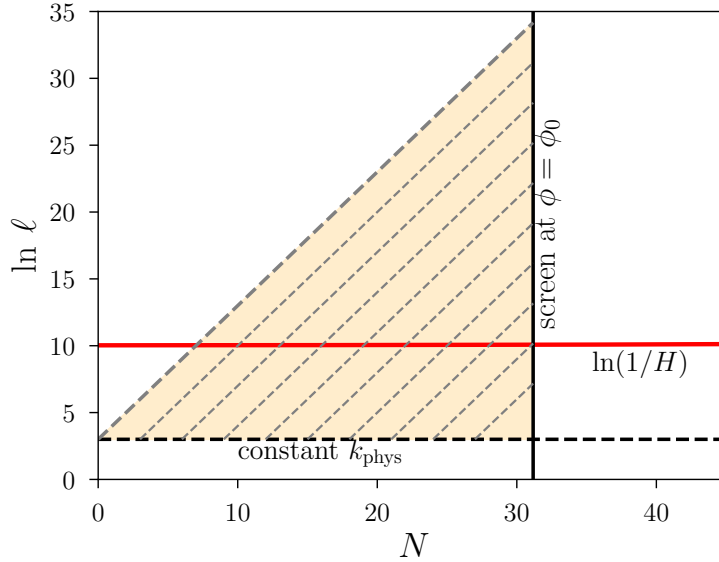


Figure 4.4: Injection scheme for the scalar and tensor modes. Evolution begins at a surface of initial conditions deep inside the horizon, with modes injected at constant k_{phys} .

To further improve the efficiency of our calculations in Fig. 4.3, we use the approximate time-translational symmetry of the Bunch-Davies vacuum deep inside the horizon, and only keep track of the physical wavelengths we are interested in. Scalar and tensor modes are evolved from a constant physical length scale 10^3 times smaller than the horizon and then collected at moment of time when $\phi = \phi_0$ as shown in the mode injection scheme depicted in Fig 4.4. The length scale $1/H$ where the modes freeze out is plotted in red. Comoving modes evolve from $\lambda_{\text{phys}} = 10^{-3}/H$ across the physical length scale ℓ following the lines of constant comoving wavenumber (which have a slope of 1) until they reach the screen at $\phi = \phi_0$, where the mode amplitudes and the power spectra are evaluated. We can safely omit the evolution of the modes at physical scales shorter than injection point k_{phys} (below the orange triangle) as the vacuum is essentially stationary there.

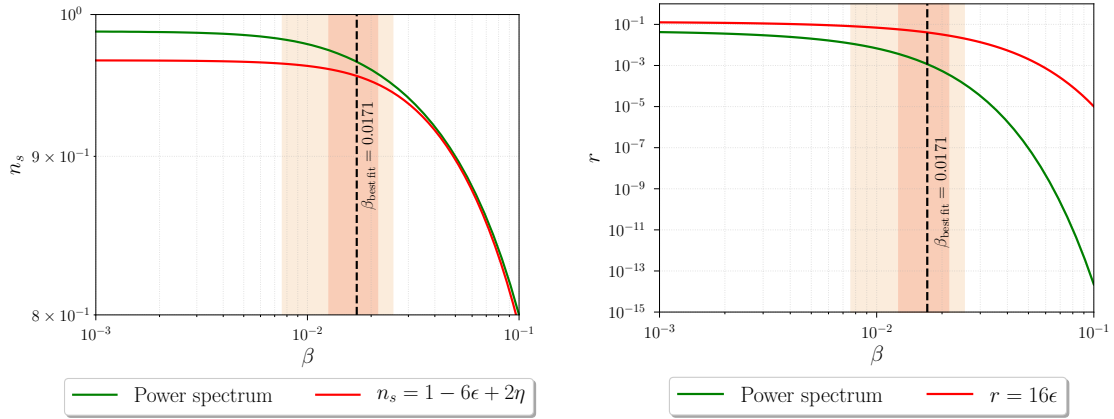


Figure 4.5: Left panel: Testing the consistency relation in (4.16) as a function of β after fixing $M^2 = 10^{-9}m_0^2$. Surprisingly, the consistency relations work well for larger values of β . Right panel: Testing (4.15) for the same value of M^2 . Here the differences are very large (up to ten orders of magnitude) for larger values of β . Both consistency relations are compared with the direct calculation of n_s and r at $N_* = 0$, right after evaluating the power spectra scalar and tensor perturbations. The shaded regions represent the ranges of β within the 68% and 95% confidence levels.

4.3 Deviations of n_s and r from the slow-roll expressions

To begin with, we first compare the two consistency relations [133, 134]

$$r = 16\epsilon, \quad (4.15)$$

$$n_s = 1 - 6\epsilon + 2\eta, \quad (4.16)$$

with the values of n_s and r obtained from the scalar and tensor power spectra, as shown in Fig. 4.5. These relations are the basis of the confrontation with Planck data made in [131]. The slow-roll parameters ϵ and η appearing in (4.15) and (4.16) are calculated there to be

$$\epsilon = \frac{\beta(3 + \beta)^2 \sin^2(\sqrt{2\beta}\phi/m_0)}{[-3 + \beta - (3 + \beta) \cos(\sqrt{2\beta}\phi/m_0)]^2}, \quad (4.17)$$

$$\eta = \frac{2\beta(3 + \beta) \cos(\sqrt{2\beta}\phi/m_0)}{-3 + \beta - (3 + \beta) \cos(\sqrt{2\beta}\phi/m_0)}. \quad (4.18)$$

Fig. 4.5 shows comparison of the slow-roll approximations (4.15) and (4.16) to the values inferred from the direct spectrum computation. Both slow-roll parameters are evaluated at $\phi = \phi_0$, which makes them independent of M . Our procedure allows us to evaluate both power spectra well beyond the slow-roll approximation, we show $\beta \in [0.001; 0.1]$ which contains the reliability interval suggested in [131]. $M^2 = 10^{-9}m_0^2$ is fixed as an arbitrary constant, which has no difference with its best-fit value at any other value of N_* . From Fig. 4.5, it is interesting to notice that the deviations from the slow-roll definition in (4.15)

are always non-negligible, especially in the range of large values of β . The magnitude of scalar perturbations is of $\mathcal{O}(1)$ at $\beta \geq 0.05$ and grows continuously as β increases, implying that the perturbative approach is no longer valid in this regime for β . The opposite occurs with the deviations from (4.16) as we can observe in the left panel. In either of these cases, it is beneficial to avoid the approximation derived from the slow-roll approximation in order to calculate n_s and r since (i) this imposes restrictions on the valid range of β and (ii) as shown in Fig. 4.5, the calculation of both parameters from the power spectra shows noticeable deviations from the approximate expressions in (4.15) and (4.16) in both the original reliability range $\beta \in [0.005; 0.025]$ and within the 95% C.L. range, as depicted in both panels of the last figure. One possible cause is the spurious running of n_s seen in the slow-roll consistency relations, which makes (4.15) and (4.16) depend slightly on the exact field value they are evaluated at. If one wants high precision, it is easier to just calculate the spectra directly rather than dealing with intricacies of the slow-roll expansion [144] to get to the required expansion order.

4.4 Planck Constraints

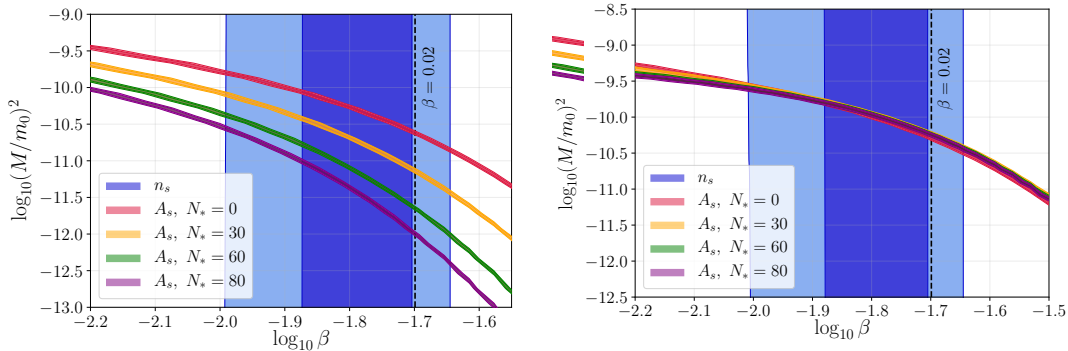


Figure 4.6: Scanning the parameters in the potential at $N_* = 0, 30, 60, 80$. The blue regions show the 68% C.L. (solid blue) and 95% C.L. (shaded blue) regions for the marginalized posterior probability of the scalar spectral index n_s , while the regions for the marginalized posterior of the scalar primordial amplitude A_s are plotted in different colors. On the left panel we can see the degeneracy of N_* and M^2 with respect to the amplitude. The right panel shows that the degeneracy is resolved fairly well when we use M_* defined in Eq. (4.20) instead of M .

In this section we use the CMB anisotropies measurements from the Planck satellite [9, 10, 43] and their joint analysis with the BICEP2/Keck Array [45] to derive the constraints on the model parameters of the constant roll inflation. On the left panel of Fig. 4.6 we show the constraints on the parameters M^2 and β from the Planck constraints on the scalar amplitude A_s and spectral index n_s . The blue band corresponds to the region constrained

by the scalar spectral index, n_s , while the other colored bands corresponds to the constrained regions from the scalar amplitude for different N_* values. Here the degeneracy between the parameters M and N_* mentioned in Sect.4.1 is evident: for a fixed value of β one can raise or lower the value of M and keep A_s constant by adjusting N_* . To deal with this degeneracy one can proceed in two ways. Either we fix N_* to some arbitrary value and we constrain M for that choice, or we can combine the two variables M and N_* into one that parametrizes the degeneracy. We choose the latter and to find the combination of the two parameters we work in the following way. In the exact slow roll approximation we have, for N_* adequately large,

$$A_s \propto \frac{H^2}{\epsilon} \simeq \frac{M^2 \sinh^2(\beta N_*)}{\beta} \sim \frac{M^2}{\beta} e^{2N_*\beta}, \quad (4.19)$$

where H^2 is the Hubble parameter at the end of inflation evaluated analytically in [131] and the slow-roll parameter ϵ is defined in (4.17). Thus we can constrain the combination

$$M_*^2 \equiv M^2 \exp(2N_*\beta) \quad (4.20)$$

for which A_s is constant for a fixed β . We evaluate the choice of this parameter graphically in the right panel of Fig. 4.6. We can see that for different N_* values, the constrained area lies in the same range of M_* .

As mentioned earlier, observational constraints on the constant-roll inflation parameters were already derived in [131] although by means of the slow-roll approximation. Here we improve on those earlier results as we are able to very accurately compute the power spectra of the scalar and tensor fluctuations using the evolution scheme presented in Sect. 8.3.2. Also, as discussed in Appendix 4.3, deviations from the slow-roll conditions might be noticeable even in the best fit range of β given the precision of the present day observational data.

In a Bayesian framework the posterior probability for the model parameters is usually sampled through Markov Chain Monte Carlo (MCMC) engines such as CosmoMC [145] or MontePython [146] coupled to a Boltzmann solver such as CAMB [81] or CLASS [147]. The constraints on the model parameters are then derived by marginalization of the posterior probability. In this work however, we derived the constraints on constant-roll inflation by simply mapping the posterior probability on the parameters (n_s, A_s, r) to two of the constant-roll inflation parameters (β, M^2) at a fixed N_* . To do so, we evaluated the scalar and tensor power spectra on the logarithmic grid $\log_{10} \beta \in [-3, -1.5]$, $\log_{10}(M/m_0)^2 \in [-15, -7]$ for different values of $N_* = 0, 30, 60, 80$, and computed the parameters n_s, A_s, r, n_T for each sample. The absence of features in the power spectra, as shown in Fig. 4.3, allowed us to quickly obtain the scalar and tensor spectral indexes by a simple linear regression in more than 8000 different model realizations.

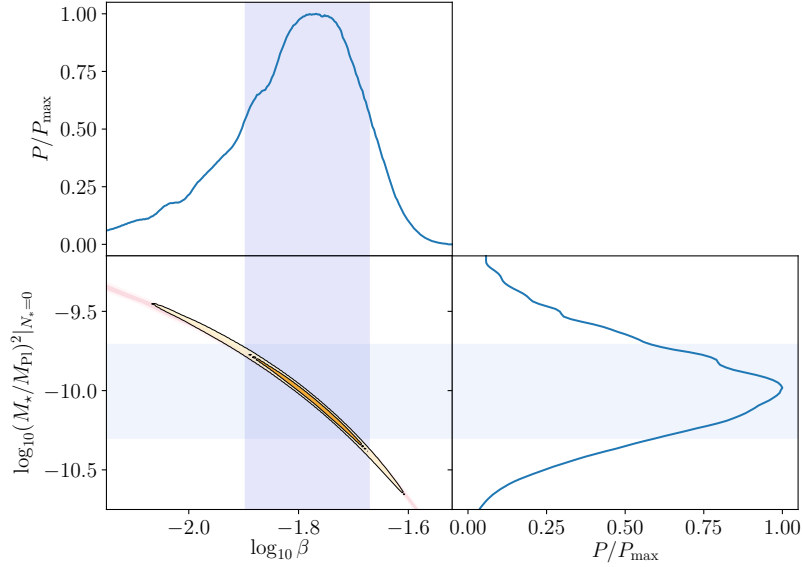


Figure 4.7: Different projections of the joint probability distribution from Planck 2015 likelihood evaluated at $N_* = 0$. Top panel: lateral projection of the joint distribution for β . Right panel: lateral projection of the joint distribution for $M_*/m_0|_{N_*=0}$. Left corner on the bottom: different regions of the joint posterior distribution are shown within the red stripe in orange at the 68% C.L. (solid orange) and 95% C.L. (shaded orange). The blue shaded regions correspond to the 1σ marginalized regions for the two parameters β and M_* .

The joint-posterior distribution over the parameters β and the new parameter, M_* , was then computed according to

$$\mathcal{P} \left[\log_{10} \beta, \log_{10} \left(\frac{M_*}{m_0} \right)^2 \right] = \mathcal{P}(n_s, \ln A_s) J, \quad (4.21)$$

where the Jacobian J was computed numerically from the results

$$n_s = n_s \left[\log_{10} \beta, \log_{10} \left(\frac{M_*}{m_0} \right)^2 \right], \quad (4.22)$$

$$\ln A_s = \ln A_s \left[\log_{10} \beta, \log_{10} \left(\frac{M_*}{m_0} \right)^2 \right]. \quad (4.23)$$

The posterior joint distribution $\mathcal{P}(n_s, \ln A)$ was generated from the MCMC chains provided by the Planck collaboration¹². The results are shown in Fig. 4.7. The orange shaded regions represent the joint posterior probability $\mathcal{P}(\log_{10} \beta, \log_{10}(M_*/m_0)^2)$, while the blue shaded regions represent respectively the marginalized 1σ regions for the parameters $\log_{10} \beta$

¹<https://pla.esac.esa.int/pla/>

²https://wiki.cosmos.esa.int/planckpla2015/index.php/Cosmological_Parameters

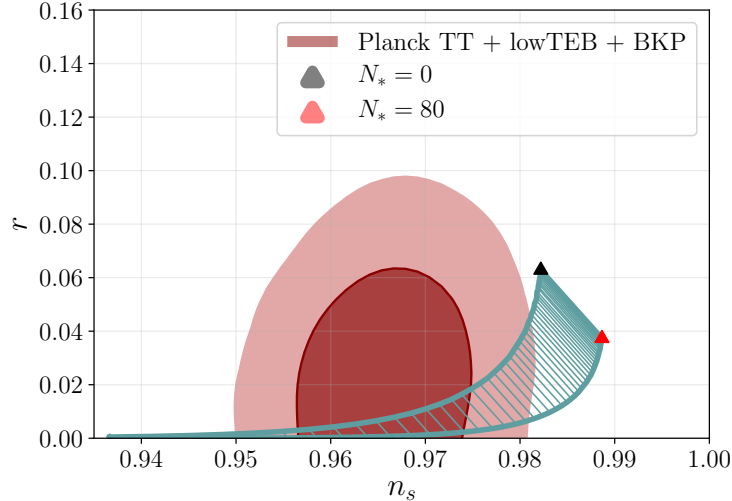


Figure 4.8: Constraints from joint Planck 2015/BKP likelihood on n_s and r . The green line shows the values of (n_s, r) from the parameter space probed in Figs. 4.6 and 4.7. For higher values of N_* , the model can cover most of the lower range of r .

and $\log_{10}(M_*/m_0)^2$). From the definition in (4.20), the constraints on the constant-roll inflation parameters are obtained by marginalizing the posterior probability (4.21) and are $\log_{10} \beta = -1.77^{+0.17}_{-0.35}$ and $\log_{10}(M_*/m_0)^2 = -9.98^{+0.7}_{-0.6}$ at 95% C.L.

In Fig. 4.8, we illustrate the region of constant-roll model parameters we probed in the r versus n_s diagram overlaying the joint likelihood distribution provided by Planck 2015. The hatched region corresponds to the variation of N_* spanning values from 0 to 80, while the M and β range as in Fig. 4.6. If one is willing to increase N_* further (corresponding to hill-top inflation) very small values of r can be achieved. Interestingly, the parameter region of the constant-roll inflation does not overlap with any of the existing regions constrained by other models shown in [45], which makes constant-roll inflation a testable alternative for future observations.

4.5 Summary

In this Chapter, we provided constraints of the model parameters in constant-roll inflation, as proposed in [130, 131]. These are not the only efforts regarding models with similar features, for instance see [144, 148, 149, 150, 151, 152, 153, 154, 155] for further examples. Our numerical procedure is optimized for an efficient evaluation of the scalar and tensor power spectra of primordial fluctuations, and can scan more than 8000 different choices of model parameters in a reasonable time on minimal computing hardware. It does not require assuming the slow-roll approximation as it is based on the direct computation of the cosmological parameters (n_s, r, A_s, n_T) from the featureless power spectra shown in

Fig. 4.3. The code passed numerous accuracy tests and long-time integration of the mode evolution confirms that there is no spurious evolution on super-horizon scales.

In order to provide tight constraints of the model parameters, we needed to address the degeneracy between M and N_* . We found M_* defined in (4.20) to be a good auxiliary parameter that leaves the spectra almost invariant under different choices of N_* for any fixed value of M_* . After using the CMB measurements from the Planck Collaboration [9, 10, 43] and their joint likelihood with the BICEP2/Keck Array [45], we estimated $\log_{10} \beta = -1.77^{+0.17}_{-0.35}$ and $\log_{10}(M_*/m_0)^2 = -9.98^{+0.7}_{-0.6}$ at 95% C.L. for $N_* = 0$, as shown in Fig. 4.7. The constraints for β are not significantly modified by any different choice of N_* , however, due to the parameter degeneracy the same cannot be said about the constraints for M . The parameter range on r versus n_s diagram covered by constant-roll inflation in Fig. 4.8 does not appear to overlap with any of the regions covered by the other inflationary models considered in [10, 43], making this model observationally interesting for the next generations of CMB experiments.

Chapter 5

Constraints on Primordial Magnetic Fields from the CMB

In this Chapter, we move forward in cosmic time, and investigate the cosmological consequences of a primordial magnetic field (PMF) in the early Universe. A frozen-in magnetic field configuration could in fact be sustained during the pre-recombination epoch, when the Universe was fully ionized [49]. There are many reasons that favour the existence of such PMF and are of both theoretical and experimental nature [156]. Chief amongst them is the unexplained origin of the galactic magnetic fields, typically of a few micro-Gauss (μG) strength and coherent over the extent of the galaxy. Such magnetic fields could be generated through a dynamo mechanism, but it would still require a seed field of a certain minimum strength [51]. Moreover, μG strength fields are observed in high redshift galaxies that are too young to have gone through the number of revolutions necessary for the dynamo to work [50]. Alternatively, the galactic fields could trace their origin to turbulent magnetic field amplification during structure formation at high redshift [157, 158, 159, 160, 161], with the small-scale dynamo converting turbulent energy into magnetic energy. Another possibility is that the supernova explosions in protogalaxies provided the magnetic seed fields that were later amplified by compression, shearing and stochastic motions [162, 163]. A PMF of sufficient strength on appropriate scales could provide the seed, or eliminate the need for dynamical amplification altogether. For a typical galactic halo of a few kilo-parsec (kpc) size that forms in a collapse of a few Mega-parsec (Mpc) sized region, the latter possibility requires a PMF of ~ 0.1 nano-Gauss (nG) present day strength¹ coherent over a comoving Mpc scale in order to compress into a μG level galactic field [156]. Observed galactic fields with almost 10 nG strengths would require a PMF of about 1 nG present day strength to eliminate the need for the dynamo, making the 1 nG strength of the PMF an important threshold.

¹It is conventional to use comoving units to describe the strength of cosmological magnetic fields, *i.e.* $\mathbf{B} = \mathbf{B}_{\text{today}} = a^2 \mathbf{B}(a)$.

PMFs are expected to have been produced at some level in the electroweak (EW) and the QCD phase transitions [164]. Detailed studies of hydromagnetic and magnetohydrodynamic (MHD) turbulence [165, 166, 167, 168] have demonstrated that magnetic power can transfer from smaller to larger scales through both *inverse transfer* and *inverse cascade*, but it is challenging to obtain a coherence scale and the amplitude of the field large enough to explain the galactic fields. For instance, simulations performed in [168] show that the PMF generated in the EW phase transition can at best reach a strength of 0.3 nG at a scale of 30 kpc if the initial field is maximally helical [169] and if its initial amplitude is the largest allowed by the big bang nucleosynthesis (BBN) bound [170, 171, 172, 173]. Another possibility is for the PMF to have been generated during [54, 55] and at the end of Inflation [56, 174, 175], although there it is also challenging to generate a PMF of nG strength. As there are still significant gaps in our understanding of the early universe phase transitions and connecting inflation with particle physics, the possibility of an observationally relevant PMF cannot be ruled out [176]. In fact, constraints on the PMF can help us select among different theories of the early universe [177, 178].

The goal of this Chapter is to study the impact of a PMF on the CMB and use the recent measurements of the CMB temperature and polarization anisotropies to constrain the PMF strength. As we will show in Sect. 5.2, PMFs source CMB anisotropies through metric perturbations and through the Lorentz force felt by baryons in the pre-recombination plasma [179, 180, 181, 182, 183]. Of particular importance are the vortical perturbations, which lead to B-mode polarization patterns [59, 60, 61, 184, 185]. As they contribute to anisotropies on smaller angular scales ($\ell \sim 1000$), the magnetic vector modes are not as obscured by the galactic foregrounds as the inflationary B-mode. B-modes are then expected to play a fundamental role in the search for PMFs and the recent measurements of the B-mode polarization by POLARBEAR [186], BICEP/Keck [187, 188] and SPT [64] have opened a new opportunity for probing the PMF [189]. Prior to these measurements, the strongest CMB bounds on the PMF strength were derived by the Planck Collaboration [58] using the 2015 Planck data [9]. They placed a limit on the PMF strength of $B_{1\text{Mpc}} < 4.4$ nG at the 95% confidence level (CL). Comparable bounds were obtained in [190] using the 7-year WMAP data [191] combined with the high- ℓ temperature anisotropy spectrum from SPT [62]. After that, the POLARBEAR collaboration placed a bound of $B_{1\text{Mpc}} < 3.9$ nG [63] using only their B-mode spectrum, with the cosmological parameters fixed to the best fit Λ CDM values.

In Sect. 5.4 we present a comprehensive analysis using the CMB measurements performed by the Planck satellite, combined with the recent B-mode polarization measurements by SPT and co-varying the PMF parameters along with the Λ CDM ones. We show indeed the B-modes play an important role in the search of PMFs and we derive the tightest bound on the PMF strength to date.

Over the next few years, Stage III CMB experiments, such as SPT-3G [192] and the Simons Observatory (SO) [193], will measure the B-mode spectrum with a significantly better accuracy. However, while they will reduce the uncertainty in the PMF contribution to BB by more than an order of magnitude [194], it will translate into only a minor improvement in the bound on the PMF strength thanks to the quartic dependence of the spectrum on B_λ . It will remain at or just below 1 nG even after the data from a future Stage IV ground based experiment [47] or a future space mission become available. Other probes, such as Faraday Rotation, can be used to bring the bound further down [65, 195, 196, 197].

5.1 PMF as a stochastic field

In this Chapter we consider CMB anisotropies sourced by a PMF generated in the early Universe at a time τ_B before the neutrino decoupling τ_ν . Under the ideal MHD approximation, which is known to hold well in the highly conducting primeval plasma of the early universe and on cosmological scales at smaller redshifts, the PMF configuration remains frozen in the plasma. Its strength evolves with time according to $\mathbf{B}(\mathbf{x}, \tau) = \mathbf{B}(\mathbf{x}, \tau_0)/a^2(\tau)$ (see [198] for a review), where τ_0 denotes the present conformal time and a is the scale factor normalized to $a(\tau_0) = 1$. Following the convention, we will refer to the amplitude of the PMF in terms of the “comoving” field strength $\mathbf{B}(\mathbf{x}, \tau_0)$.

We assume that the PMF does not have a homogeneous component, as it would break the isotropy of the Universe and has already been strongly constrained by CMB [199, 200]. Instead, we model the PMF as a statistically, isotropic, Gaussian-distributed random field described by a power spectrum

$$\langle B_i(\mathbf{k})B_j^*(\mathbf{k}') \rangle = (2\pi)^3 \delta^{(3)}(\mathbf{k} - \mathbf{k}') P_{ij} P_B(k), \quad (5.1)$$

where $P_{ij} = \delta_{ij} - \hat{k}_i \hat{k}_j$. In the equation above, we have neglected the parity-odd contribution from the helical component of the PMF. Including the helical component requires introducing additional free parameters and is largely degenerate with the overall normalization, weakening the bounds on the PMF strength by about 25% [58]. Given this, for the sake of simplicity, we omit the helical contribution in the remaining of this and the next Chapters. However, future data can, in principle, measure it through parity-odd CMB polarization spectra [201, 202, 203].

The magnetic power spectrum is commonly taken to be a power law parametrized as

$$P_B(k) = \begin{cases} S_0 k^{n_B}, & k < k_D \\ 0, & k \geq k_D \end{cases} \quad (5.2)$$

where n_B is the spectral index and $2\pi/k_D$ is the damping scale below which magnetic fields dissipate due to radiation viscosity [59, 204]. The spectral index depends on the

generation mechanism of the PMF. The originally proposed simple inflationary models of magnetogenesis predicted a scale-invariant spectrum, corresponding to $n_B = -3$, although other values are possible in more complicated models [205]. The PMFs produced in phase transitions generically have $n_B = 2$ on large scales probed by CMB [206, 207, 208]. The damping scale depends on the amplitude of the PMF spectrum and the spectral index as [58, 59, 179]

$$\frac{k_D}{\text{Mpc}^{-1}} = \left[5.5 \times 10^4 h \left(\frac{B_\lambda}{\text{nG}} \right)^{-2} \left(\frac{2\pi}{\lambda/\text{Mpc}} \right)^{n_B+3} \frac{\Omega_b h^2}{0.022} \right]^{\frac{1}{n_B+5}}, \quad (5.3)$$

where h is the reduced Hubble constant, $H_0 = 100 h \text{ km}/(\text{s Mpc})$, and B_λ is obtained by smoothing the magnetic energy density over a comoving wavelength λ using a Gaussian filter:

$$B_\lambda^2 = \frac{1}{(2\pi)^3} \int_0^\infty d^3k e^{-k^2 \lambda^2} P_B(k) = \frac{2S_0}{(2\pi)^2} \frac{1}{\lambda^{n_B+3}} \Gamma\left(\frac{n_B+3}{2}\right). \quad (5.4)$$

It is common to take $\lambda = 1 \text{ Mpc}$, as it corresponds to the size of a typical region at the time of last scattering that later collapses to form a galactic halo. Another way to quantify the strength of the PMF is in terms of its contribution to the radiation energy density, namely,

$$\mathcal{E}_B = \frac{1}{(2\pi)^3} \int_0^{k_D} dk k^2 P_B(k), \quad (5.5)$$

and defining the effective PMF strength as $B_{\text{eff}} = \sqrt{8\pi\mathcal{E}_B}$. Correspondingly, one can define the fractional PMF density as $\Omega_{B\gamma} = \mathcal{E}_B/\rho_\gamma$ where ρ_γ is the total radiation energy density. The relation between B_{eff} , B_λ and $\Omega_{B\gamma}$ is given by [67, 179]

$$B_{\text{eff}} = \frac{B_\lambda (k_D \lambda)^{\frac{n_B+3}{2}}}{\sqrt{\Gamma((n_B+5)/2)}} = 3.3 \times 10^3 \sqrt{\Omega_{B\gamma}} \text{ nG}. \quad (5.6)$$

The stress-energy tensor associated with the PMF can be written as [183]

$$T_{B0}^0(\mathbf{x}, \tau) = -\frac{1}{8\pi a^4} B^2(\mathbf{x}) \equiv -\rho_\gamma \Delta_B, \quad (5.7)$$

$$T_{Bj}^i(\mathbf{x}, \tau) = \frac{1}{4\pi a^4} \left(\frac{1}{2} B^2(\mathbf{x}) \delta_j^i - B^i(\mathbf{x}) B_j(\mathbf{x}) \right) \equiv p_\gamma (\Delta_B \delta_j^i + \Pi_{Bj}^i), \quad (5.8)$$

where $B_i(\mathbf{x}) = B_i(\mathbf{x}, \tau_0)$, ρ_γ and $p_\gamma = \rho_\gamma/3$ are the photon density and pressure, Δ_B is the magnetic contribution to the radiation density contrast and Π_{Bj}^i is the dimensionless anisotropic stress. Since there is no magnetic field at the background level, the quantities Δ_B and Π_B^{ij} are gauge invariant, as mentioned in Chapter 2.

5.2 CMB anisotropies from metric perturbations sourced by the PMF

The PMF perturbations couple to the baryons through the Lorentz force, and to the metric perturbations, and thus affect the CMB anisotropies. At linear order in perturbation theory, the PMF can be treated as a stiff source with no back-reaction from the metric or matter fluctuations. The traceless anisotropic stress $\Pi_B^i{}_j$ in equation (5.8) can be decomposed in its scalar, vector and tensor contributions as we did in Chapter 2,

$$\Pi_{Bij} = \Pi_B^{(0)} Q_{ij}^{(0)} + \Pi_B^{(\pm 1)} Q_{ij}^{(\pm 1)} + \Pi_B^{(\pm 2)} Q_{ij}^{(\pm 2)}. \quad (5.9)$$

The Lorentz force felt by the baryons and sourced by the PMF has to be included in the equations for the baryon velocity. At very early times, when baryons and photons are tightly coupled, the baryons equation for the scalar mode reads,

$$\dot{v}_b^{(0)} = \frac{1}{1+R} \left[-\mathcal{H}v_b^{(0)} + c_s^2 k \delta_b + \frac{kR}{4} (\delta_\gamma - 2\Pi_\gamma^{(0)}) + \frac{R}{4} L^{(0)} \right], \quad (5.10)$$

where $L^{(0)} = k(\Delta_B - 2\Pi_B^{(0)})$ is the scalar component of the Lorentz force and $R \equiv 4\rho_\gamma/3\rho_b$. Likewise the same term is included in the baryons equations when the tight coupling approximation stop holding. Similarly for the vector component of the baryon velocity we have (still in the tight coupling limit),

$$\dot{v}_b^{(1)} = -\mathcal{H}v_b^{(1)} - \frac{\rho_\gamma}{\rho_b} \dot{\kappa} \left(\frac{4}{3} v_b^{(1)} - q_\gamma^{(1)} \right) - \frac{1}{2} \frac{\rho_\gamma}{\rho_b} L^{(1)}, \quad (5.11)$$

where $\dot{\kappa}$ is the differential optical depth, or *opacity*, introduced in Sect. 3.2.1, q_γ is the photons' heat flux defined through $4\rho_\gamma v_\gamma/3 = \rho_\gamma q_\gamma$ and $L^{(1)} = k\Pi_B^{(1)}$ is the vector component of the Lorentz force. Considering the PMF as a stiff source in the perturbation equations means that

$$\dot{\Delta}_B = \dot{\Pi}_B^{(0,\pm 1,\pm 2)} = 0. \quad (5.12)$$

In solving the system of Boltzmann and Einstein equations, one needs to set the initial conditions for the scalar, vector and tensor modes. In Boltzmann codes, such as CAMB, they are set on super-horizon scales, $k\tau \ll 1$, and well after the neutrino decoupling, *i.e.* at $\tau \gg \tau_\nu$. After neutrinos decouple from photons, which happens at energies below 1 MeV, they free stream and can develop a non-zero anisotropic stress that compensates the anisotropic stress of the PMF. However, at $\tau < \tau_\nu$, neutrinos are bound in a tightly coupled fluid with photons and baryons and are unable to compensate for the magnetic anisotropic stress, which then acts as a source of adiabatic scalar and tensor mode perturbations [180]. The latter are usually assumed to be uncorrelated with the adiabatic fluctuations generated by inflation and are treated as separate *passive* magnetic modes [180, 183]. After the

neutrino decoupling, PMFs generate isocurvature type perturbations, in which the neutrino anisotropic stress compensates the anisotropic stress of the PMF, known as the *compensated modes* [181, 209, 210]. It was also realized that, for PMFs generated during inflation, there is another adiabatic mode known as the magnetic inflationary mode [205]. However, its amplitude is strongly model-dependent and, in order to keep our approach as model-independent as possible, we restrict our analysis to PMFs generated after inflation, and consider the passive and compensated modes only.

The amplitude of the adiabatic scalar mode is set by the comoving curvature perturbation ζ which, in the absence of a PMF, is conserved on super-Hubble scales. However, as mentioned above, a PMF present before neutrino decoupling would source the growth of ζ [180]. When neutrinos decouple, their anisotropic stress rapidly grows to compensate the anisotropic stress of the PMF. When the compensation is effective, ζ stops growing, having reached the final value [180, 183]

$$\zeta = \zeta(\tau_B) - \frac{1}{3}R_\gamma\Pi_B^{(0)}\left[\ln(\tau_\nu/\tau_B) + \left(\frac{5}{8R_\nu} - 1\right)\right], \quad (5.13)$$

where $\zeta(\tau_B)$ is the comoving curvature perturbation at the time τ_B and where R_γ and R_ν are the photon and neutrino fractions of the total radiation density. What is commonly referred to as the scalar passive mode, is the part of the adiabatic mode associated with the growth of ζ , proportional to $\ln(\tau_\nu/\tau_B)$, and its power spectrum is proportional to $\langle\Pi_B^{(0)*}\Pi_B^{(0)}\rangle$ [180, 183].

The compensated scalar modes start being actively sourced by the PMF after neutrino-decoupling. There are two such modes, sourced by Δ_B and $\Pi_B^{(0)}$, with power spectra proportional to $\langle\Delta_B^*\Delta_B\rangle$ and $\langle\Pi_B^{(0)*}\Pi_B^{(0)}\rangle$ respectively. The two scalar compensated modes are not independent, as the correlation $\langle\Delta_B^*\Pi_B^{(0)}\rangle$ does not vanish.

Since vector perturbations rapidly decay if not continuously sourced, there are no passive vector modes. The only regular solution for the vector part of the Einstein-Boltzmann system, with a PMF as an active source, is a compensated mode for which the anisotropic stress $\Pi_B^{(\pm 1)}$ is compensated by $\Pi_\nu^{(\pm 1)}$.

Tensor modes, like scalar modes, have both passive and compensated modes. The compensated tensor mode has a negligibly small amplitude and can be ignored [180, 183]. However, by the time of neutrino decoupling, the PMF sources an adiabatic tensor mode of amplitude [183]

$$H^{(\pm 2)} \approx R_\gamma\Pi_B^{(\pm 2)}\left[\ln(\tau_\nu/\tau_B) + \left(\frac{5}{8R_\nu} - 1\right)\right]. \quad (5.14)$$

5.3 MagCAMB, a patch with PMFs for CAMB

In order to compute the PMF anisotropies sourced by PMF, we developed a patch² for the Boltzmann code CAMB [81]. We introduced the effects of the PMF into the Einstein and Boltzmann equations closely following the formalism of [183] and the associated code by Shaw and Lewis (SL). The PMF enters the Einstein equations according to

$$G_{\mu\nu} = \frac{1}{m_0^2} (T_{\mu\nu} + T_{\mu\nu}^B), \quad (5.15)$$

where $T_{\mu\nu}^B$ is given by equations (5.7), (5.8). As mentioned earlier, the quantities Δ_B and Π_B are gauge invariant and hence we do not need to worry about transforming our variables in synchronous gauge. The scalar and vector components of the baryon velocity is modified as explained in the previous section, equations (5.10), (5.11).

The magnetic modes initial conditions are set according to Appendix B in [183]. For this modes, the primordial power spectra have to be calculated from the magnetic field power spectrum (5.1). The magnetic modes power spectra are then defined from the PMF correlation functions. We summarize the correlation function calculation in the next subsection.

5.3.1 PMF Correlation functions

We begin with the Fourier transform of the PMF energy-momentum tensor, T_{Bj}^i in equation (5.8) given by

$$T_{Bj}^i(\mathbf{k}) = \frac{1}{4\pi a^4 (2\pi)^3} \int d^3q \left[\frac{1}{2} \delta_j^i B_l(\mathbf{q}) B^l(\mathbf{k} - \mathbf{q}) - B^i(\mathbf{k}) B_j(\mathbf{k} - \mathbf{q}) \right]. \quad (5.16)$$

Using the previous equation, the magnetic perturbations Δ_B and Π_{Bj}^i are given by

$$\Delta_B(\mathbf{k}) = \frac{1}{3 p_\gamma} T_{Bi}^i = \frac{1}{8\pi \rho_\gamma^0 (2\pi)^3} \int d^3q B_l(\mathbf{q}) B^l(\mathbf{k} - \mathbf{q}), \quad (5.17)$$

$$\Pi_{Bj}^i(\mathbf{k}) = \frac{1}{p_\gamma} \left(T_{Bj}^i - \frac{1}{3} \delta_j^i T_{Bn}^n \right) = \frac{3}{4\pi \rho_\gamma^0 (2\pi)^3} \int d^3q \left[\frac{1}{3} \delta_j^i B_l(\mathbf{q}) B^l(\mathbf{k} - \mathbf{q}) - B^i(\mathbf{q}) B_j(\mathbf{k} - \mathbf{q}) \right]. \quad (5.18)$$

²The patch is publicly available at <https://alexzucca90.github.io/MagCAMB/>

The scalar, vector and tensor components of Π_{Bj}^i are then obtained by the scalar products $\Pi_{Bj}^{ij} Q_{ij}^{(0,\pm 1,\pm 2)}$, and are respectively

$$\Pi_B^{(0)}(\mathbf{k}) = \frac{3}{2} Q_{ij}^{(0)}(\mathbf{k}) \Pi_B^{ij}(\mathbf{k}) = -\frac{3}{2} \frac{3}{4\pi\rho_\gamma^0(2\pi)^3} \int d^3q \left[\frac{1}{3} B_l(\mathbf{q}) B^l(\mathbf{k}-\mathbf{q}) - \hat{k}_i B^i(\mathbf{q}) \hat{k}_j B^j(\mathbf{k}-\mathbf{q}) \right], \quad (5.19)$$

$$\begin{aligned} \Pi_B^{(\pm 1)}(\mathbf{k}) &= 2Q_{ij}^{(\mp 1)}(\mathbf{k}) \Pi_B^{ij}(\mathbf{k}) \\ &= -\frac{3i}{4\pi\rho_\gamma^0(2\pi)^3} \int d^3q \left[\hat{k}_i B^i(\mathbf{q}) e_j^{(\mp)} B^j(\mathbf{k}-\mathbf{q}) + \hat{k}_i B^i(\mathbf{k}-\mathbf{q}) e_j^{(\mp)} B^j(\mathbf{q}) \right], \end{aligned} \quad (5.20)$$

$$\Pi_B^{(\pm 2)}(\mathbf{k}) = \frac{2}{3} Q_{ij}^{(\mp 2)}(\mathbf{k}) \Pi_B^{ij}(\mathbf{k}) = -\sqrt{\frac{2}{3}} \frac{3}{4\pi\rho_\gamma^0(2\pi)^3} \int d^3q e_i^{(\mp)} B^i(\mathbf{q}) e_j^{(\mp)} B^j(\mathbf{k}-\mathbf{q}). \quad (5.21)$$

We then use the equations above to compute the correlation functions of the magnetic perturbations. We define $\beta = \hat{\mathbf{k}} \cdot \widehat{(\mathbf{k}-\mathbf{q})}$, $\gamma = \hat{\mathbf{k}} \cdot \hat{\mathbf{q}}$ and $\mu = \hat{\mathbf{q}} \cdot \widehat{(\mathbf{k}-\mathbf{q})}$. In the scalar sector we have three correlation functions,

$$\langle \Delta_B(\mathbf{k}) \Delta_B^*(\mathbf{k}') \rangle = \frac{\delta^{(3)}(\mathbf{k}-\mathbf{k}')}{32\pi^2(\rho_\gamma^0)^2} \int d^3q (1+\mu^2) P_B(q) P_B(|\mathbf{k}-\mathbf{q}|), \quad (5.22)$$

$$\begin{aligned} \langle \Delta_B(\mathbf{k}) \Pi_B^{(0)*}(\mathbf{k}') \rangle &= \frac{3\delta^{(3)}(\mathbf{k}-\mathbf{k}')}{16\pi^2(\rho_\gamma^0)^2} \int d^3q P_B(q) P_B(|\mathbf{k}-\mathbf{q}|) \\ &\quad \times \left[1 - \frac{1}{2}\mu^2 - \frac{3}{2}(\beta^2 + \gamma^2) + \frac{3}{2}\mu\gamma\beta \right], \end{aligned} \quad (5.23)$$

$$\begin{aligned} \langle \Pi_B^{(0)}(\mathbf{k}) \Pi_B^{(0)*}(\mathbf{k}') \rangle &= \frac{9\delta^{(3)}(\mathbf{k}-\mathbf{k}')}{8\pi^2(\rho_\gamma^0)^2} \int d^3q P_B(q) P_B(|\mathbf{k}-\mathbf{q}|) \\ &\quad \times \left[1 + \frac{1}{4}\mu^2 - \frac{3}{4}(\gamma^2 + \beta^2) - \frac{3}{2}\mu\gamma\beta + \frac{9}{4}\gamma^2\beta^2 \right]. \end{aligned} \quad (5.24)$$

The vector two-point correlation function is

$$\langle \Pi_B^{(1)}(\mathbf{k}) \Pi_B^{(1)*}(\mathbf{k}') \rangle = \frac{9\delta^{(3)}(\mathbf{k}-\mathbf{k}')}{4\pi^2(\rho_\gamma^0)^2} \int d^3q P_B(q) P_B(|\mathbf{k}-\mathbf{q}|) \left[1 - 2\gamma^2\beta^2 + \gamma\beta\mu \right], \quad (5.25)$$

and, finally, the tensor two-point correlation function is

$$\langle \Pi_B^{(2)}(\mathbf{k}) \Pi_B^{(2)*}(\mathbf{k}') \rangle = \frac{3\delta^{(3)}(\mathbf{k}-\mathbf{k}')}{8\pi^2(\rho_\gamma^0)^2} \int d^3q P_B(q) P_B(|\mathbf{k}-\mathbf{q}|) (1+\beta^2)(1+\gamma^2). \quad (5.26)$$

In solving these integrals, we have to remember that we imposed a sharp cutoff on the magnetic field power spectra, that is $P_B(k) = 0$ if $k > k_D$. This translates in the condition

$$q < k_D, \quad |\mathbf{k}-\mathbf{q}| < k_D, \quad (5.27)$$

for the integrals above. The condition (5.27) is satisfied when $0 < k < 2k_D$, so the integrals can then be split into double integrals: one over $x \equiv \gamma$ and another over $z \equiv q/k$. Also, the condition $0 < k < 2k_D$ split the integrals in three different cases:

$$1) \int_{\frac{k_D}{k}-1}^{\frac{k_D}{k}} dz \int_{\gamma_0}^1 dx \cdots + \int_1^{\frac{k_D}{k}-1} dz \int_{-1}^1 dx \cdots + \int_0^1 dz \int_{-1}^1 dx \quad \text{when } \frac{k_D}{k} > 2, \quad (5.28)$$

$$2) \int_1^{\frac{k_D}{k}} dz \int_{\gamma_0}^1 dx \cdots + \int_{\frac{k_D}{k}-1}^1 dz \int_{\gamma_0}^1 dx \cdots + \int_0^{\frac{k_D}{k}-1} dz \int_{-1}^1 dx \quad \text{when } 2 > \frac{k_D}{k} > 1, \quad (5.29)$$

$$3) \int_{1-\frac{k_D}{k}}^{\frac{k_D}{k}} dz \int_{\gamma_0}^1 dx \cdots \quad \text{when } 1 > \frac{k_D}{k} > \frac{1}{2}, \quad (5.30)$$

where $\gamma_0 \equiv \frac{k^2+p^2-1}{2kp}$. The integral over x can then be solved analytically, while the integral over z is either solved with symbolic calculus packages such as MATLAB, or numerically.

5.3.2 Implementation of the PMF Power Spectra

The magnetic modes power spectra can be derived from the correlation functions above. From each correlation function we define the corresponding power spectrum defined as

$$\langle X(\mathbf{k})Y^*(\mathbf{k}') \rangle = (2\pi)^3 \frac{2\pi^2}{k^3} \delta^{(3)}(\mathbf{k} - \mathbf{k}') \mathcal{P}_{XY}(k), \quad (5.31)$$

where $X, Y = \Delta_B, \Pi_B^{(0,\pm 1,\pm 2)}$. In the code we write the power spectra as

$$\mathcal{P}_{XY}(k) = A^{(m)} \frac{S_0^2}{(2\pi)^6 (\rho_\gamma^0)^2} t^{2n_B+6} \mathcal{I}_{XY}(t, n_B). \quad (5.32)$$

where $t \equiv k/k_D$, $m = 0, 1, 2$, $A^{(0)} = 1/4$, $A^{(1)} = 2$ and $A^{(2)} = 2/3$. The term $\mathcal{I}_{XY}(t, n_B)$ includes the integrals in the correlation function. For $-3 < n_B < -1.5$ we confirm that the term $t^{2n_B+6} \mathcal{I}_{XY}(t, n_B)$ depends weakly on k_D/k , so we evaluate it at $k_D/k \rightarrow \infty$. To maximize the speed performance of our code we interpolate the results on a grid $-3 < n_B < -1.5$ with a cubic spline. For the range $n_B > -1.5$ however, the integrals do depend on t and we adopt the following method. In each of the two regions $-1.5 < t < 0$ and $t \geq 0$ we sampled the integrals numerically and used a fitting function which is polynomial in t or $\log t$, depending on the mode. We also choose whether to include the term t^{2n_B+6} or not for numerical stability.

5.3.3 Results

In Fig. 5.1 we show the CMB anisotropies sourced by the perturbations induced by the PMF. The results are obtained using a PMF amplitude of 4.5 nG, a almost scale-invariant index, $n_B = -2.9$ and, for passive modes, $\beta = \log_{10}(\tau_\nu/\tau_B) = 17$, corresponding to the PMF generation energy scale of 10^{14} GeV. We see that potentially powerful constraints can come

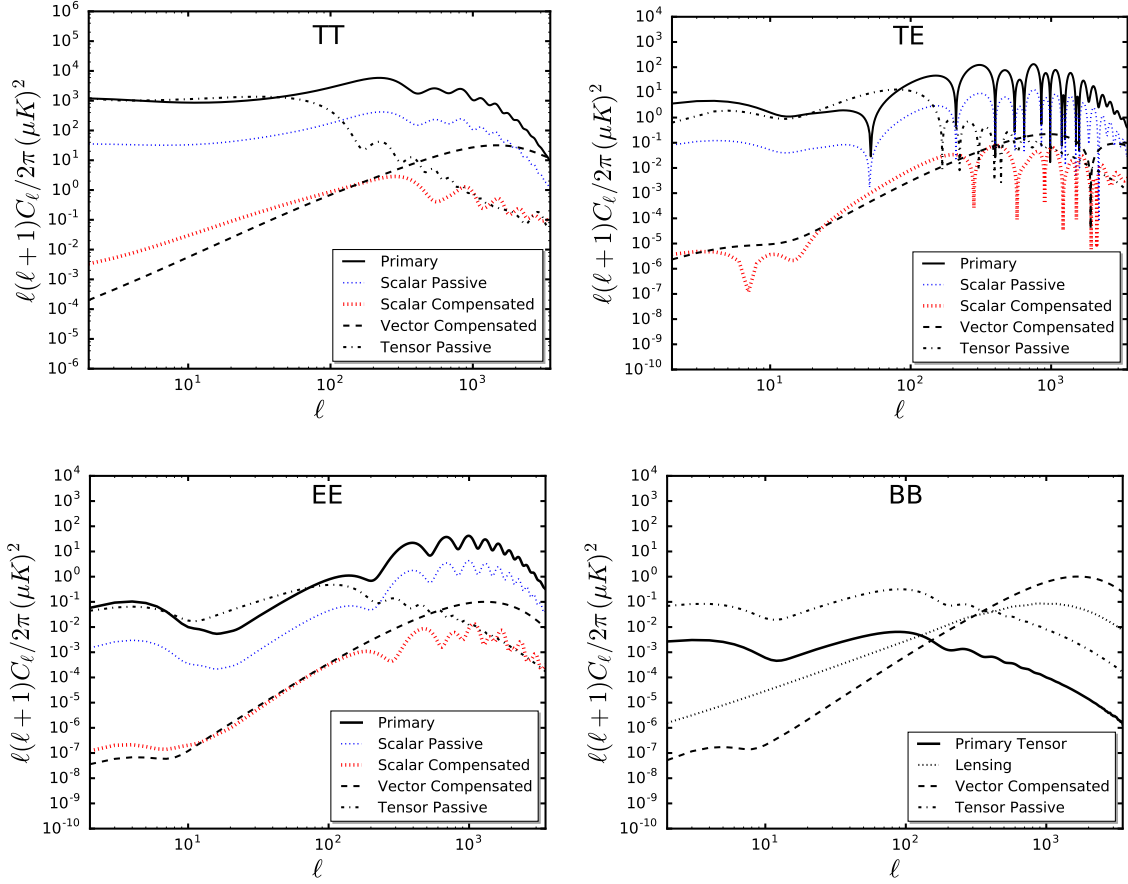


Figure 5.1: Contributions of relevant magnetic modes to the CMB temperature and polarization power spectra for a PMF with $B_{1\text{Mpc}} = 4.5$ nG and $n_B = 2.9$. For the passive modes, the time of the generation of the PMF is set at $\beta = \log_{10}(\tau_\nu/\tau_B) = 17$. The cosmological parameters are set to $\omega_b = 0.0226$, $\omega_c = 0.112$, $T_{\text{CMB}} = 2.7255$ K, $h = 0.7$, $A_s = 2.1 \times 10^{-9}$, $n_s = 0.96$, $r = 0.1$, $n_T = 1$.

from the B-mode polarization in the bottom right panel. In fact, on smaller scales $\ell \simeq 1000$, the magnetic vector compensated mode dominates the B-mode polarization patterns. In addition, in Fig. 5.2, we show the vector mode contribution to BB for different values of the spectral index, which is representative of the way all CMB spectra vary with n_B . Note the change in the dependence on n_B that occurs at $n_B = -1.5$. In the $-3 < n_B < -1.5$ range, the magnetic power spectrum is dominated by the power k^{2n_B+6} [183], and an increase in n_B causes a shift of power from lower to higher ℓ . This reduces the CMB anisotropy power on scales within the observational window. In contrast, for $n_B \geq -1.5$, the magnetic power spectrum is dominated by the power k^3 and the CMB power spectrum becomes independent on n_B . In that regime, larger values of n_B lead to more CMB power for the same PMF strength on 1 Mpc scale.

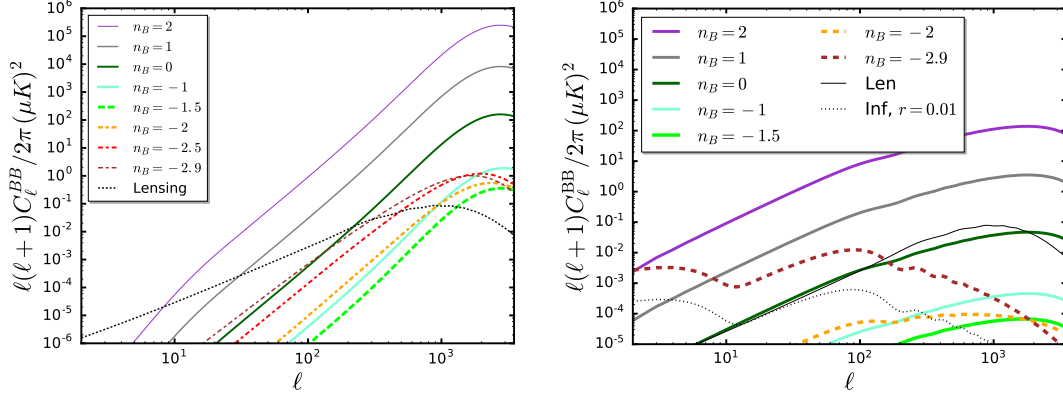


Figure 5.2: The B-mode spectrum from the PMF compensated vector mode (left panel) and tensor passive mode (right panel) with $B_{1\text{Mpc}} = 2\text{ nG}$ and different values of the spectral index n_B . The black thin line shows the lensing contribution.

The contribution of the magnetic vector mode to the B-mode polarization power spectrum, can be well constrained by the current and future CMB experiments capable of detecting the B-modes from weak lensing. We will focus on this in the next Section.

5.4 Constraining PMF with Planck and SPT data

In this Section we use the CMB power spectra by the Planck satellite [211] and the measurements of the CMB B-mode polarization by the SPT [64] to constrain the amplitude, the spectral index and the time of generation of the PMF.

We developed a patch for the popular Markov Chain Monte Carlo (MCMC) engine CosmoMC that uses the MagCAMB code presented in Sect. 5.3 as a theory module. The patch, dubbed MagCosmoMC³, assumes that the passive and compensated magnetic modes, as well as the standard inflationary modes are all uncorrelated and computes the overall theoretical predictions as

$$C_\ell^{\text{theor}} = C_\ell^{\text{infl}} + C_\ell^{\text{pass}} + C_\ell^{\text{comp}}, \quad (5.33)$$

where each term includes the scalar and tensor modes with the addition that compensated modes also include the vector modes.

For Planck, we use the joint TT, TE, EE and BB likelihood in the range $2 < \ell < 29$, denoted as lowTEB, together with the high- ℓ temperature likelihood in the range $30 < \ell < 2508$, simply denoted as TT. We also consider the case in which the TT likelihood is replaced with the joint TT, TE and EE polarization likelihood (denoted as TTTEEE). We also perform the analysis with and without using the likelihood from the BICEP2/Keck-Planck (BKP) cross correlation analysis [45].

³The code is publicly available at <https://github.com/alexzucca90/MagCosmoMC>.

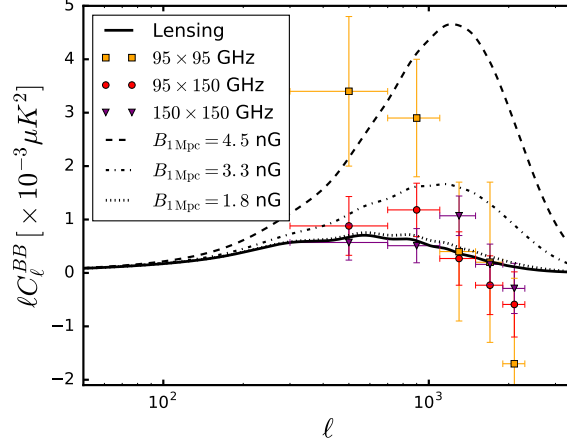


Figure 5.3: The B-mode spectrum from the PMF vector mode added to the lensing contribution (solid black line) for $B_{1\text{Mpc}} = 4.5$ nG (dashed line), $B_{1\text{Mpc}} = 3.3$ nG (dot-dashed line) and $B_{1\text{Mpc}} = 1.8$ nG (dotted line), with $n_B = -2.9$. The three SPT bandpowers are shown in orange, red and purple.

The SPT likelihood [64]⁴ is a multivariate Gaussian likelihood and uses three bandpowers from the 95GHz \times 95GHz, 95GHz \times 150GHz and 150GHz \times 150GHz spectra. It also takes into account the contributions to B-modes from the dust emission within our Galaxy and from the polarized emission from extragalactic sources. The dust emission is modelled according to Eq. (21) in [64] and is scaled by an overall dust emission amplitude A_{dust} [212]. The extragalactic sources are modelled through a constant C_ℓ term with different amplitudes for each bandpower, $A_{\text{PS},95}$, $A_{\text{PS},95 \times 150}$ and $A_{\text{PS},150}$. These nuisance parameters are marginalized over using priors shown in Tabel 5.1. We implemented the SPT likelihood in our MagCosmoMC code and we introduced the B-mode spectrum from PMFs.

Parameter	Prior	
A_{dust}	[0.0, 2.5]	Gaussian
$A_{\text{PS},95}$	[0.0, 4.0]	flat
$A_{\text{PS},95 \times 150}$	[0.0, 4.0]	flat
$A_{\text{PS},150}$	[0.04, 0]	flat

Table 5.1: Priors on the nuisance parameters used in the SPT likelihood described in Sect. 5.4.2.

We assume a flat universe and, as in [58], restrict our analysis to three massless neutrinos. We account for the effect of weak lensing by large scale structure on the primary mode only, and we marginalize over astrophysical residuals [58, 211].

⁴The SPT likelihood code is available at <http://pole.uchicago.edu/public/data/keisler15/>

The pivot Fourier number for the inflationary primordial spectrum is set to $k_* = 0.05\text{Mpc}^{-1}$, while the magnetic smoothing scale is set to $\lambda = 1\text{Mpc}$. We vary the baryon density $\omega_b = \Omega_b h^2$, the CDM density $\omega_c = \Omega_c h^2$, the reionization optical depth τ_{reion} , the ratio of the sound horizon to the angular diameter distance at decoupling θ , and the amplitude A_s and the spectral index n_s of the primary primordial spectrum of curvature perturbations. We also vary the additional magnetic parameters $B_{1\text{Mpc}}$, n_B and $\beta = \log_{10}(\tau_\nu/\tau_B)$. The priors assumed on the parameters are given in Table 5.2.

Parameter	Flat Prior
ω_b	[0.005, 0.1]
ω_c	[0.001, 0.99]
τ_{reion}	[0.01, 0.8]
θ	[0.5, 10]
$\ln(10^{10} A_s)$	[2, 4]
n_s	[0.8, 1.2]
r	[0, 2]
$B_{1\text{Mpc}}$	[0, 10]
$\log_{10}(B_{1\text{Mpc}}/\text{nG})$	[-5, 1]
$\beta = \log_{10}(\tau_\nu/\tau_B)$	[4, 17]
n_B	[-2.9, 3]

Table 5.2: Priors on the parameters varied in the MCMC analysis. We performed the analysis separately with the uniform and logarithmic priors on $B_{1\text{Mpc}}$.

As can be seen from Fig. 5.2, for nearly scale-invariant PMFs, the passive tensor magnetic mode is similar in shape to the primary (inflationary) tensor mode, with an amplitude that depends on the time of the generation of the PMF, $\beta = \log_{10}(\tau_\nu/\tau_B)$. To address a potential degeneracy between the tensor-to-scalar ratio $r = A_T/A_s$ and β , we consider the cases with a fixed $r = 0$, as well as with co-varying the two parameters.

5.4.1 Constraints from Planck data

To derive constraints on the PMF from Planck, we use the Planck likelihood code described in detail in [211]. A thorough analysis has already been conducted by the Planck collaboration in [58]. Since scalar passive modes are not supposed to contribute significantly to the magnetic signals in the CMB (as shown in the previous Chapter), the authors of [58] included them only in the special case of a nearly scale invariant PMF with $n_B = -2.9$. Conversely, we include scalar passive modes in all of our analysis for the sake of completeness.

Fig. 5.4 shows the marginalized probability distribution function (PDF) for $B_{1\text{Mpc}}$ derived from Planck data. The Figure only shows the case with $r = 0$, since the PDF in the case of co-varied r was essentially the same. The 95% CL bounds on $B_{1\text{Mpc}}$ are summarized in Tab. 5.3, including the case with co-varied r .

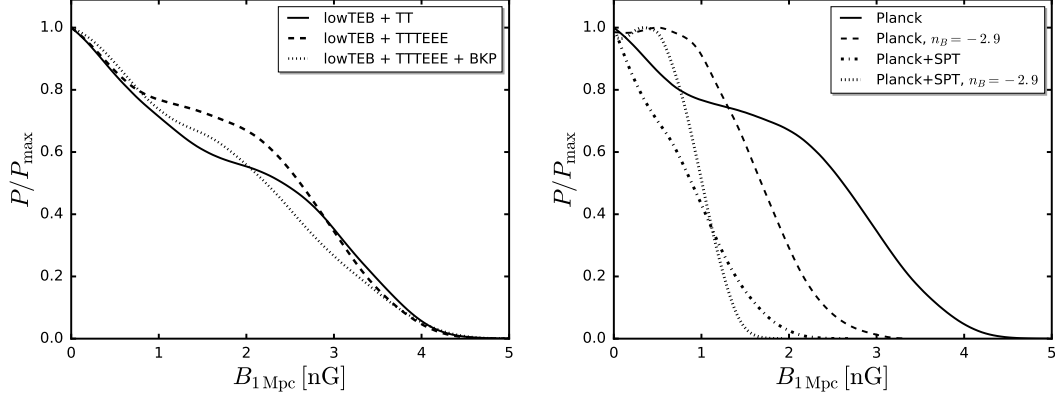


Figure 5.4: Left panel: the probability distribution function for the magnetic amplitude $B_{1\text{Mpc}}$ from the Planck data sets described in Sect. 5.4.1. We show only the case with $r = 0$ since varying r does not affect the results. Right panel: the marginalized PDFs for the magnetic amplitude $B_{1\text{Mpc}}$ from Planck and the combination of Planck and SPT. We only show the PDFs obtained with $r = 0$, as the case with co-varying r is essentially the same. We also show the PDFs for the nearly scale-invariant case, $n_B = -2.9$.

Data sets	$B_{1\text{Mpc}}/\text{nG}$
lowTEB + TT, $r = 0$	< 3.3
lowTEB + TT, r free	< 3.3
lowTEB + TTTEEE, $r = 0$	< 3.2
lowTEB + TTTEEE, r free	< 3.2
lowTEB + TTTEEE + BKP, $r = 0$	< 3.3
lowTEB + TTTEEE + BKP, r free	< 3.3

Table 5.3: Upper bounds (95% CL) for the PMF amplitude $B_{1\text{Mpc}}$ obtained from the combination of Planck data sets described in Sect. 5.4.1. The magnetic spectral index n_B and the PMF generation epoch parameter β are unconstrained.

The magnetic spectral index n_B and the PMF generation epoch parameter β are unconstrained. We discuss these parameters in more detail in the next subsection.

5.4.2 Constraints from Planck combined with SPT

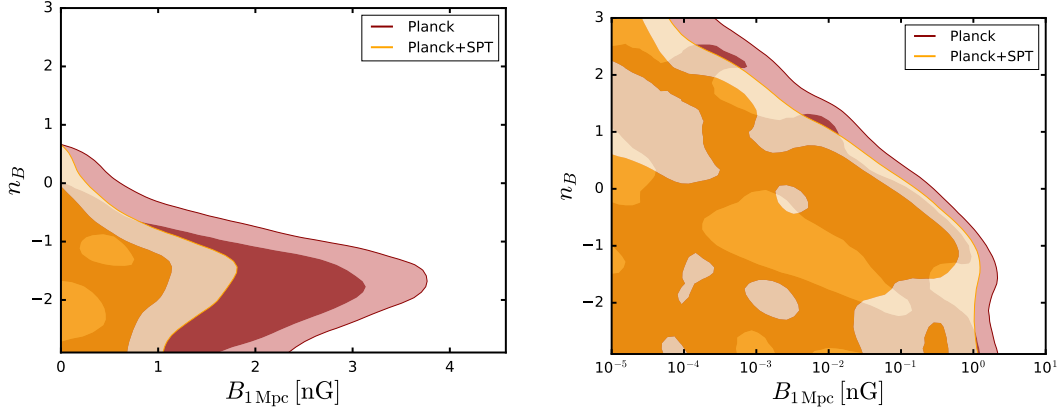


Figure 5.5: Left panel: the joint probability for the magnetic amplitude $B_{1\text{Mpc}}$ and the magnetic index n_B using uniform prior on $B_{1\text{Mpc}}$. Right panel: the joint probability for $B_{1\text{Mpc}}$ and n_B using uniform prior on $\log_{10}(B_{1\text{Mpc}}/\text{nG})$. The two shaded regions represent the 68% C.L. and 95% C.L. respectively. The apparent bound on n_B in the left panel disappears when using the logarithmic prior, as shown in the right panel. Note that the 68% C.L. “islands” appearing in both panels for $B_{1\text{Mpc}}$ are numerical artifacts due to the low sensitivity of the likelihood to small values of the PMF amplitude.

Combining Planck with the B-mode polarization spectrum from SPT significantly tightens the bounds on the PMF, because of the contribution of the PMF vector modes, as illustrated in Fig. 5.3. We perform the analysis using the SPT likelihood and the Planck lowTEB and TTEEE likelihoods, referring to the combination of them as Planck for simplicity. We do not include the BKP data, after the analysis in the previous subsection confirmed that it does not affect the bounds on the PMF.

In Fig. 5.5, we show the joint probability for the magnetic amplitude $B_{1\text{Mpc}}$ and the magnetic index n_B from Planck alone and after combining Planck with SPT. The two parameters are correlated, with the bound on $B_{1\text{Mpc}}$ becoming weaker with increasing n_B in the $-3 < n_B < -1.5$ range, and stronger for $n_B > -1.5$. This is due to the qualitative change in the dependence of the CMB spectra on the magnetic power spectrum that occurs at $n_B = -1.5$. Namely, as illustrated in Fig. 5.2, an increase in n_B results in a shift of power from lower to higher ℓ , reducing the CMB power on scales inside the observational window and thus allowing for larger PMF strengths. In contrast, for $n_B > -1.5$, the shapes of the CMB spectra are cutoff dominated, with larger n_B resulting in more CMB power for the same PMF strength on 1 Mpc scale, leading to tighter constraints on $B_{1\text{Mpc}}$.

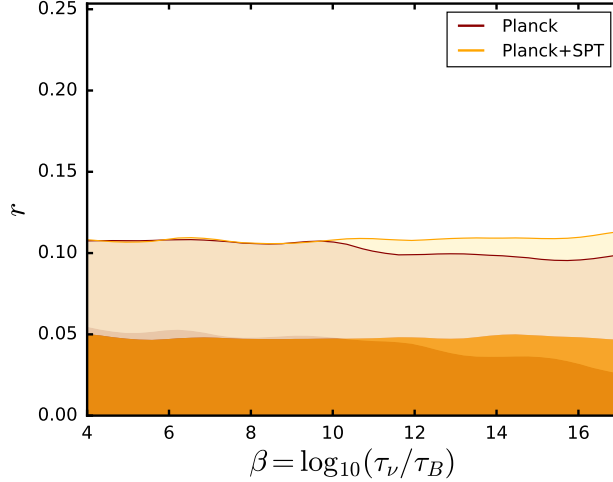


Figure 5.6: The joint probability for the scalar to tensor ratio r and the time of generation of the PMF $\log_{10}(\tau_\nu/\tau_B)$. The two shaded regions represent the 68%CL and 95% CL, respectively.

Fig. 5.5 separately shows the cases with a uniform (left panel) and the logarithmic (right panel) priors on $B_{1\text{Mpc}}$. As expected, the apparent upper bound on n_B , present in the case of the uniform prior and also observed in [58], is not physical and disappears in the case of the logarithmic prior. Indeed, there cannot be a bound on the spectral index of the PMF spectrum without a positive detection of the amplitude. The PDFs for the amplitude $B_{1\text{Mpc}}$, after marginalizing over n_B , are shown in the right panel of Fig. 5.4.

	$B_{1\text{Mpc}}/\text{nG}$	B_{eff}/nG	$\Omega_{B\gamma}$
n_B marginalized	< 1.5	n/a	n/a
$n_B = -2.9$	< 1.2	< 1.2	$< 1.4 \times 10^{-7}$
$n_B = 2$	< 0.002	< 100	$< 10^{-3}$

Table 5.4: Upper bounds (95% CL) on the PMF amplitude $B_{1\text{Mpc}}$, the effective PMF strength B_{eff} and the magnetic density fraction $\Omega_{B\gamma}$ obtained from Planck and SPT.

Two values of n_B are of particular theoretical interest. The first and simplest models of inflationary magnetogenesis [54, 55] predict a nearly scale-invariant PMF with $n_B \approx -3$. The combined bound from Planck and SPT on the nearly scale-invariant PMF ($n_B = -2.9$)⁵ is $B_{1\text{Mpc}} \approx B_{\text{eff}} < 1.2$ nG at 95% CL. The corresponding bound from Planck alone is 2.0 nG, in agreement with [58].

The PMFs generated during preheating [56, 174] or in post-inflationary phase transitions [164] have small coherence lengths and are uncorrelated on cosmological scales. Causality

⁵To avoid divergent integrals, we restrict our analysis to $n_B \geq -2.9$. We also note that the dependence on the smoothing scale disappears and $B_{1\text{Mpc}} = B_{\text{eff}}$ for scale-invariant fields.

forces the spectra of such fields to have $n_B = 2$ on scales of relevance to CMB anisotropies [57, 204, 206]. For such fields, we find $B_{1\text{Mpc}} < 0.002$ nG at 95% CL. However, since most of the power of the causally generated PMFs is concentrated near the cutoff scale $2\pi/k_D \ll 1\text{Mpc}$, using $B_{1\text{Mpc}}$ to quantify their amplitude can be misleading. Instead, it is more appropriate to use $\Omega_{B\gamma}$ or B_{eff} , which are representative of the total PMF energy density [67, 208, 213]. Using the conversion in Eq. (5.6), we derive $\Omega_{B\gamma} < 10^{-3}$ or $B_{\text{eff}} < 100$ nG at 95% CL. For reference, the Big Bang Nucleosynthesis constrains the magnetic fraction to be $\Omega_{B\gamma} \lesssim 0.1$ [170, 171, 172, 173].

Constraints on the PMF strength after marginalizing over n_B , as well as for the two special cases of theoretical interest, are summarized in Table 5.4.

The joint probabilities for r and $\beta = \log_{10}(\tau_\nu/\tau_B)$, after marginalizing over other parameters, are shown in Fig. 5.6. It is evident that there is no degeneracy between them and that the time of the generation of the PMF is not constrained by data. This is because the contribution of the passive scalar and tensor modes to TT, TE and EE are too small even for the maximum allowed value of $\beta = 17$. As one can see from Fig. 5.1, the passive tensor mode is comparable in amplitude to the primary TT at low ℓ when $B_{1\text{Mpc}} = 4.5$ nG and $\beta = 17$. For smaller values of β , even higher PMF strengths would be required for the passive tensor mode to be relevant. Such high values of PMF are not allowed because of the PMF vector mode contribution to TT at high ℓ . Any remaining weak sensitivity to β is further diluted by degeneracies with A_s , n_s and τ_{reion} . Thus, the passive tensor mode contribution to TT at low ℓ is irrelevant for the strengths of PMF allowed by TT at high ℓ . The scalar passive mode is even less irrelevant, as evident from Fig. 5.1. Note that adding the BPK B-mode data does not make a big difference because of large uncertainties at ℓ where the contribution from the passive tensor mode is prominent. Adding the SPT data does not help in constraining β either, because SPT only constrains the vector mode contribution to BB and does not add information on scales relevant to the passive tensor mode.

5.5 Summary

In this Chapter we derived the bound on the strength of the primordial magnetic field from the SPT CMB B-mode polarization measurements in combination with the CMB temperature and polarization data from Planck. Adding the SPT information significantly tightens the bound, as it constrains the PMF vector mode contribution to B-modes at $\ell \sim 1000$. Specifically, adding the SPT data reduces the 95% CL bound on $B_{1\text{Mpc}}$, after marginalizing over the magnetic spectral index n_B , from 3.3 nG to 1.5 nG. For a nearly scale-invariant PMF with $n_B = -2.9$, the bound is reduced from 2 nG to 1.2 nG. The effective strength of a PMF generated in post-inflationary phase transitions, with $n_B = 2$, is constrained to $B_{\text{eff}} < 100$ nG, corresponding to $\Omega_{B\gamma} < 10^{-3}$, or $B_{1\text{Mpc}} < 0.002$ nG, at 95% CL.

Our results, as well as those obtained by the POLARBEAR collaboration in [63], demonstrated that one can extract competitive information about PMFs even from the existing B-mode measurements. Future CMB experiments, in addition to significantly improving the measurement of the B-mode spectrum at high ℓ , will eventually provide reliable data on scales relevant for the inflationary tensor mode. Such data will help to constrain the passive tensor PMF mode and, thus, the time of the generation of the PMF. Future CMB experiments will also constrain the parity-odd TB and EB correlations, leading to meaningful bounds on the helical component of the PMF, which has been neglected in this work. They will also tightly constrain the mode-coupling correlations induced by the Faraday rotation of CMB polarizations. The Faraday rotation angle is linear in $B_{1\text{Mpc}}$, while CMB anisotropies scale as a square of the PMF strength (so that the CMB spectra scale as $B_{1\text{Mpc}}^4$), and, with the improved sensitivity and resolution of upcoming experiments, will reduce the upper bound on $B_{1\text{Mpc}}$ by an order of magnitude [196, 214, 215] as illustrated in Tab. 5.5 [197].

The pioneering work by the POLARBEAR [186], BICEP/KECK [187, 188] and SPT [64] collaborations has ushered cosmology into the era of precision B-mode science. In addition to searching for signatures of inflationary gravitational waves and primordial magnetic fields, B-modes will be used to probe the neutrino masses [216], modifications of gravity [217, 218], cosmic (super)strings [219, 220] and other fundamental physics [47].

		Current (nG)		SPT-3G (nG)		SO (nG)		CMB-S4 (nG)		Space Probe (nG)	
f_L	f_G	FR ^a	BB+ ^b	FR	BB ^c	FR	BB ^c	FR	BB ^c	FR	BB ^c
1	1	50	1	0.75	0.9	0.45	1	0.18	0.5	0.17	0.7
1	0	-	-	0.75	-	0.45	-	0.14	-	0.12	-
0	1	-	-	0.6	0.8	0.37	0.9	0.09	0.4	0.14	0.6
0	0	-	-	0.55	-	0.37	-	0.07	-	0.09	-

Table 5.5: Current and forecasted 68% CL bounds on the amplitude B_λ of a scale-invariant PMF for different choices of parameters f_L and f_G quantifying the fraction of the weak lensing contribution to BB and the fraction of the galactic rotation measure, respectively.

^aEstimated 68% CL bound based on the 95% CL bound of 93 nG derived by POLARBEAR. ^bThe 68% CL bound derived in this Chapter using TT, EE, TE spectra from Planck and BB from SPT. ^cBased on the B-mode spectrum alone, assuming fixed cosmological parameters.

Part III

Testing Fundamental Physics in the late time Universe

Chapter 6

Phenomenology of Scalar-Tensor Gravity

In this third part of the thesis we devote our efforts to the late time Cosmology. As we mentioned earlier in Chapter 1, one of the most intriguing problems in modern Cosmology is the nature of Dark Energy.

A possibility, already mentioned in the Introduction, is that the accelerated expansion of the Universe can be provided by a modification of the law of gravity on large scales. This can be achieved by breaking one, or more, of the hypothesis of Lovelock's theorem introduced in Chapter 2.

In particular, in this Chapter we focus on the class of scalar-tensor theories of gravity. These theories contain an extra degree of freedom in the gravitational sector of the action (2.2), and can lead to a dynamical effective dark energy when the range of the scalar interaction is cosmological. As a result, scalar-tensor models represent a well-motivated and versatile class of dark energy.

6.1 Horndeski Action

Adding a scalar degree of freedom to the gravitational sector of the action (2.2) requires particular care because of the possibility of *ghost*-like instabilities (fields with negative kinetic energy). According to Ostrogradsky's theorem [221], one can avoid them by keeping the equations of motion at second order in the derivatives of the metric $g_{\mu\nu}$ and the extra field φ . The most general scalar-tensor theory of gravity having second-order field equations was discovered by Horndeski in 1974 [26], and later resurrected by [28]. Its action is given by

$$S_H = \sum_{i=2}^5 \int d^4x \sqrt{-g} \mathcal{L}_i, \quad (6.1)$$

where the four Lagrangians are

$$\mathcal{L}_2 = K(\varphi, X), \quad (6.2)$$

$$\mathcal{L}_3 = -G_3(\varphi, X)\square\varphi, \quad (6.3)$$

$$\mathcal{L}_4 = G_4(\varphi, X)R + G_{4,X} \left[(\square\varphi)^2 - (\nabla_\mu\nabla_\nu\varphi)^2 \right], \quad (6.4)$$

$$\mathcal{L}_5 = G_5(\varphi, X)G_{\mu\nu}\nabla^\mu\nabla^\nu\varphi - \frac{G_{5,X}}{6} \left[(\square\varphi)^3 - 3(\square\varphi)(\nabla_\mu\nabla_\nu\varphi)^2 + 2(\nabla_\mu\nabla_\nu\varphi)^3 \right]. \quad (6.5)$$

Here K , G_3 , G_4 and G_5 are generic functions of the scalar field φ , $X \equiv -\partial_\mu\varphi\partial^\mu\varphi$ and the subscript X stands for ∂_X . The Horndeski action includes essentially all the commonly known models of dark energy: quintessence [222, 223], Brans-Dicke [224] models, k-essence [225, 226], kinetic gravity braiding [227, 228, 229] and galileons [27, 230]. Modified gravity models such as $f(R)$ and $f(G)$ gravity are also included in the Horndeski action. Models such as Dvali-Gabadadze-Porrati (DGP) gravity and the ghost free massive gravity lies outside the Horndeski action, although their covariantised decoupling limit does belong to the Horndeski class.

The Lagrangian (6.1) has been constructed to have second-order equation of motion, but other than that there are no symmetry properties which restrict the arbitrary functions K , G_3 , G_4 and G_5 . However, it is still possible to place restrictions to each term from their phenomenology. For example, one of the most recent constraints on the functions above comes from the observation of the gravitational wave GW170817 [231] and its electromagnetic counterpart [3, 4]. These observations constrained the difference between the speed of light to that of gravity waves to be¹

$$|c_T^2 - 1| < 10^{-15}, \quad (6.6)$$

where c_T^2 is the speed of gravitational waves. In Horndeski theories, the speed of gravitational waves is given by

$$c_T^2 = \frac{G_4 - XG_{5,\varphi} - XG_{5,X}\ddot{\varphi}}{G_4 - 2XG_{4,X} - X(G_{5,X}\dot{\varphi}H - G_{5,\varphi})}, \quad (6.7)$$

so that the terms $G_{5,X}$, $G_{5,\varphi}$ and $G_{4,X}$ are not relevant in the expression above. In a rather strong way one can hence assume that

$$G_4(X, \varphi) = G_4(\varphi), \quad G_5(X, \varphi) = 0. \quad (6.8)$$

¹It is worth mentioning that this constraint is performed at redshift $z = 0.1$. The speed of gravitational waves could in principle be different than the speed of light at higher redshifts.

Another phenomenological restriction on the Horndeski terms comes from the requirement of having a dynamical mechanism that screens the fifth force mediated by the scalar field inside the solar system, to satisfy the stringent local tests of gravity [232, 233].

6.2 Modified Gravity at cosmological scales

Although very general, the Horndeski action (6.1) is not suitable for model independent tests of gravity at cosmological scale due to the large freedom that one has in choosing in the functions in the action. Also, the cosmological phenomenology is not immediately apparent from the Horndeski Lagrangians. An effective field theory approach was developed in [33, 34], providing a framework for studying cosmological backgrounds and perturbations in single field MG/DE models. This formulation is usually referred to as *EFTofDE*. The advantage of the EFT approach is that the large freedom of the Horndeski functions can be compressed in a limited number of function that depends only on time. Furthermore, within the EFT approach it is also possible to consider higher order operators that correspond to the beyond Horndeski class as well as Lorentz violating theories. Equivalent formulations of the EFTofDE have also been developed in [234, 235, 236]. Here we focus on the one in [33, 34]. This has been fully implemented in the Einstein-Boltzmann solver EFTCAMB [237, 238] and we will use it in Chapter 8. The EFT action, written in Jordan frame (the frame in which matter is minimally coupled to the metric $g_{\mu\nu}$) and in the unitary gauge - where the field values is constant on the space-like hypersurfaces - is given by

$$S_{\text{EFT}} = \int d^4x \sqrt{-g} \left[\frac{m_0^2}{2} \Omega(t) R + \Lambda(t) - c(t) \delta g^{00} \right] + S_{\text{DE}}^{(2)} + S_m[g_{\mu\nu}], \quad (6.9)$$

where $\delta g^{00} = g^{00} + 1$ is the perturbation of the upper time-time component of the (Jordan frame) metric, and $\Omega(t)$, $\Lambda(t)$ and $c(t)$ are functions of the time coordinate t that control the background expansion. Only two of them are independent. The matter action S_m is a function of the Jordan frame metric $g_{\mu\nu}$ (hence this class of theories satisfy the weak equivalence principle). The term $S_{\text{DE}}^{(2)}$ includes second order terms in perturbations. For a general scalar-tensor theory this term includes six functions of time, while Horndeski theories only need three of them. Along with the three background functions $\Omega(t)$, $\Lambda(t)$ and $c(t)$, they are referred to as EFT functions. Constraining scalar-tensor theories of gravity on cosmological scales is then reduced to constraining the EFT functions. This can be done in a parametric way, by specifying each function's analytic form, or with non-parametric methods such as Gaussian processes or correlated prior methods [239, 240].

From the action above, one can obtain the modified Friedmann equations that generalize equations (2.22), (2.26), and the modified perturbed Einstein equations that generalize (2.115)-(2.118). Furthermore, because of the addition of an extra scalar degree of freedom, an extra equation evolving the perturbation of the scalar field, $\delta\varphi$ is also evolved. However,

the phenomenology of these models is still quite complex because of the large number of functions that enter the action (6.9).

There are other approaches that are able to capture most of the phenomenology of DE and MG models. While the EFTofDE aims to parametrize deviations from the Λ CDM model at the action level, it is possible to parametrize the deviations also at the level of equation of motion. Specifically, in MG models, the relations between the two potentials Φ and Ψ (in the conformal gauge (2.139)) and the matter perturbations δ are usually modified. This effect can be captured by modifying the Poisson and the slip equations (2.115), (2.118) as [37]

$$k^2\Psi = -\frac{\mu(a, k)}{2m_0^2}a^2\mu(a, k)\rho\Delta, \quad (6.10)$$

$$\frac{\Phi}{\Psi} = \gamma(a, k), \quad (6.11)$$

where in the equations above it is assumed that the radiation component is negligible and the two functions μ and γ are time and scale independent. The parametrization above, known as the (μ, γ) parametrization, has the advantage that it is fairly easy to understand the phenomenology. The function μ controls the effective Newton constant at cosmological scales, $G_{\text{eff}} = G_N\mu(a, k)$. When $\mu(a, k) > 1$, we expect a faster clustering of matter and an increase in the matter power spectrum. This effect is in principle detectable in the galaxy number counts reviewed in Sect. 3.2.2 as the correlation function depends on the matter power spectrum. Difficulties however can come from the fact that the galaxy-galaxy correlation function, especially at lower redshifts, is affected by nonlinear clustering. concern linear perturbations only and do not offer a framework for dealing with nonlinear effects. One is then forced to consider only the large scale Fourier modes, of which there are only few at low redshifts, reducing the constraining power of large scale structure probes.

The function $\gamma(a, k)$ is not directly observable [241, 242]. However it is possible to combine equation (6.10) and (6.11) and obtain

$$k^2(\Phi + \Psi) = -\frac{\Sigma(a, k)}{m_0^2}a^2\rho\Delta, \quad (6.12)$$

defining the function Σ , related to the μ and γ functions, through

$$\Sigma = \frac{\mu(1 + \gamma)}{2}. \quad (6.13)$$

Here again we have neglected the anisotropic stress from radiation and neutrinos. The function Σ affects the evolution of the Weyl potential $\Phi_+ \equiv (\Phi + \Psi)/2$ which enters the weak lensing correlation function. Thus, one can constrain μ and Σ by combining measurements of galaxy clustering and weak lensing distortions. Constraints on γ can then be derived from joint bounds on μ and Σ . Similarly to the case of the galaxy number count case, the

weak lensing correlation functions $\xi_{\pm}(\theta)$ introduced in Sect. 3.2.3 are affected by nonlinear effects. Restricting to the scales in the linear regime lowers their constraining power. Note that the same issue plagues the EFTofDE, as it only provides a framework for describing the background and the linear perturbations.

Nonetheless, ongoing and future surveys, such as DES, LSST and Euclid, will cover more of the sky at deeper redshifts, thus increasing the probed volume and, therefore, the number of linear modes. This makes the (mu, γ) parametrization a useful tool for cosmological tests of gravity with these surveys. Furthermore, the (mu, γ) parametrization has been implemented in the Einstein-Boltzmann patch MGCAMB [37, 243, 244]. We recently upgraded the MGCAMB code in [244] to accommodate massive neutrinos and dynamical DE, as described in the next Chapter.

The phenomenological parametrization, is able to the linear theory of known scalar-tensor models in the quasi-static limit, such as $f(R)$ gravity. In the quasi-static limit, one ignores the fast oscillations of the scalar field at large scales. Usually this approximation holds well within the sound horizon of the scalar field [245].

6.3 Screened Modified Gravity. The (m, β) parametrization

While the EFTofDwE and the (μ, γ) parametrization are suitable for studying the linear behaviour of modified gravity models, they do not take into account any of the *screening mechanisms* that hide the scalar interactions from detection in local and solar system tests.

In the remainder of this Chapter, we will focus on scalar-tensor models with screening mechanisms that are broadly classified to be of chameleon type [246, 247], *i.e.* where either the mass of the scalar and/or the coupling to matter has a dependence on the local matter density. We consider scalar-tensor theories defined by the action

$$S_{\text{ST}} = \int d^4x \sqrt{-g} \left[\frac{m_0^2}{2} R + \mathcal{L}_{\varphi} + \mathcal{L}_m[\psi, A^2(\varphi)g_{\mu\nu}] \right], \quad (6.14)$$

where $g_{\mu\nu}$ is the Einstein frame metri, ψ are the matter fields that follow the geodesics of the Jordan metric $\tilde{g}_{\mu\nu} \equiv A^2(\varphi)g_{\mu\nu}$, and \mathcal{L}_{φ} is the scalar field Lagrangian given by

$$\mathcal{L}_{\varphi} = -\frac{(\partial\varphi)^2}{2} - V(\phi). \quad (6.15)$$

The action in equation (6.14) is a Generalized Brans-Dicke (GBD) theory [224] that includes a potential for the scalar field. In all GBD theories, the scalar field mediates an additional gravitational interaction between massive particles. The net force on a test mass is given by

$$\vec{f} = -\vec{\nabla}\Psi - \frac{d \ln A(\phi)}{d\phi} \vec{\nabla}\phi, \quad (6.16)$$

where Ψ is the Newtonian potential. Since solar system and laboratory tests severely constrain the presence of the scalar force, GBD can only be viable if either the coupling of the scalar field to matter is always negligible, or if there is a dynamical screening mechanism that suppresses the force in dense environments. The latter can be accomplished with appropriately chosen functional forms of $A(\phi)$ and $V(\phi)$. Because of its coupling to matter, the scalar field dynamics are determined by an effective potential which takes into account the presence of the conserved matter density ρ of the environment

$$V_{\text{eff}}(\phi) = V(\phi) + (A(\phi) - 1)\rho. \quad (6.17)$$

For some forms of $V(\phi)$ and $A(\phi)$, the effective potential can have a density dependent minimum, $\phi(\rho)$. The scalar force will be screened if either the mass of the field happens to be extremely large or the coupling happens to be negligibly small at the minimum of $V_{\text{eff}}(\phi)$. Such models can be broadly classified as ‘‘Generalized Chameleons’’ (GC), and include the original chameleon model [246], $f(R)$, dilatons [248] and symmetrons [249].

The GC scalar-tensor theories considered here are viable only if the field stays at the minimum of the effective potential $V_{\text{eff}}(\phi)$ [250]. In this case, the effective dark energy equation of state is indistinguishable from -1 and the expansion history is practically the same as in the Λ CDM model. Furthermore, as long as the scalar field is at its density dependent minimum, $\phi(\rho)$, the theory can be described parametrically from the sole knowledge of the mass function $m(\rho)$ and the coupling $\beta(\rho)$ at the minimum of the potential [250, 251]

$$\frac{\phi(\rho) - \phi_c}{m_{\text{Pl}}} = \frac{1}{m_{\text{Pl}}^2} \int_{\rho}^{\rho_c} d\rho \frac{\beta(\rho)}{m^2(\rho)}, \quad (6.18)$$

where the mass is defined as

$$m^2(\rho) = \left. \frac{d^2 V_{\text{eff}}}{d\phi^2} \right|_{\phi=\phi(\rho)} \quad (6.19)$$

and the coupling is

$$\beta(\rho) = m_{\text{Pl}} \left. \frac{d \ln A}{d\phi} \right|_{\phi=\phi(\rho)}. \quad (6.20)$$

It is often simpler to characterize the functions $m(\rho)$ and $\beta(\rho)$ using the time evolution of the matter density of the Universe

$$\rho(a) = \frac{\rho_0}{a^3} \quad (6.21)$$

where a is the scale factor whose value now is $a_0 = 1$. This allows one to describe characteristic models in a simple way and the full dynamics can be recovered from the time evolution of the mass and coupling functions, $m(a), \beta(a)$. We refer to this parametrization as the (m, β) parametrization.

6.3.1 Evolution of linear perturbations

While the GC scalar-tensor theories predict the same expansion history as Λ CDM, the existence of the additional scalar interaction gives them distinguishing features in the evolution of linear matter and metric perturbations. More specifically, the attractive force mediated by the scalar enhances the overall growth of inhomogeneities. In addition, the relation between the curvature perturbation Φ and the Newtonian potential Ψ is modified. Both of these effects can be captured by the (μ, γ) parametrization of Sect. 6.2. In the quasi-static approximation, whose validity is discussed below, functions $\mu(k, a)$ and $\gamma(k, a)$ can be expressed in terms of $m(a)$ and $\beta(a)$ as [250].

$$\mu(a, k) = A^2(\phi)(1 + \epsilon(k, a)), \quad (6.22)$$

$$\gamma(a, k) = \frac{1 - \epsilon(k, a)}{1 + \epsilon(k, a)}, \quad (6.23)$$

where

$$\epsilon(k, a) = \frac{2\beta^2(a)}{1 + m^2(a)a^2/k^2}. \quad (6.24)$$

The conformal factor $A^2(\phi)$ that appears in equation (6.22) is indistinguishable from unity for viable models within the class of scalar-tensor theories considered in this Chapter, and can be safely ignored. Λ CDM is recovered when $\epsilon \rightarrow 0$ and $\mu = \gamma = 1$.

In the quasi-static approximation, the gravitational collapse equation, governing the evolution of matter density contrast δ reads

$$\ddot{\delta} + \mathcal{H}\dot{\delta} - \frac{3}{2}\Omega_m\mathcal{H}^2\mu(k, a)\delta = 0 \quad (6.25)$$

where dots represent derivatives with respect to conformal time. Two regimes can be distinguished. When the mode k is outside the Compton wavelength of the scalar field, i.e. $k/a \ll m(a)$, $\epsilon \ll 1$ and the growth is not modified. Inside the Compton wavelength, $k/a \gg m(a)$, gravity is enhanced by $1 + 2\beta^2(a)$, implying more growth. In addition, in the symmetron and dilaton models, the coupling $\beta(a)$ depends on the matter density and controls the transition to the enhanced growth.

Since ϵ is a manifestly non-negative number, the growth is generically enhanced, $\mu \geq 1$, while $\gamma < 1$ in these models. At the same time, the relation between the lensing potential $\Phi + \Psi$ and the matter density is effectively unchanged. Namely, the quantity $\Sigma(k, a)$ defined in equation (6.13) reads

$$\Sigma = A^2(\phi) \quad (6.26)$$

and is effectively unity for all viable modes. Thus, a clear detection of $\Sigma \neq 1$ would not only signal a breakdown of Λ CDM but would rule out the entire class of GBD models considered here. We note that, even though Σ is constrained to be very close to unity in viable GBD

models, its time derivative, $\dot{\Sigma}$, can, in principle, be non-negligible and affect the observables via the Integrated Sachs-Wolfe (ISW) effect (3.66).

When the functions $m(a)$ and $\beta(a)$ are regular, which is the case for chameleon models such as $f(R)$, and for dilatons, the error introduced by working in the quasi-static approximation scales as H/k [252]. For models such as the symmetron, in which the functions $m(a)$ and $\beta(a)$ vanish with a power $n < 1$ for $a > a_*$ and are zero for $a < a_*$ (and thus have a diverging derivative at a_*), the accuracy is reduced to $(H/k)^n$ [252, 253].

6.4 (m, β) parametrization for specific models

In what follows, we briefly give the specific functional forms of $m(a)$ and $\beta(a)$ adopted for the analysis in Sections 6.5 and 6.6. In order to compute the cosmological observables, we implemented the (m, β) parametrization in MGCAMB² using the mapping (6.22),(6.23).

6.4.1 $f(R)$ gravity

Among theories exhibiting chameleon screening are the $f(R)$ class of models [254, 255] described by the action

$$S = \int d^4x \sqrt{-g} \left[\frac{m_0^2}{2} f(R) + L_m[\psi, g_{\mu\nu}] \right] \quad (6.27)$$

where the function $f(R)$ is designed to depart from the Einstein-Hilbert form (2.2) at smaller values of the curvature R . As a specific example, we take the form proposed by Hu and Sawicki (HS) [256],

$$f(R) = R - 2\Lambda + \frac{f_{R_0}}{n} \frac{R_0^{n+1}}{R^n}, \quad (6.28)$$

where Λ is the cosmological constant term, R_0 is the value of the curvature today and $f_{R_0} \equiv (1 - df/dR)_{R=R_0}$. As argued in [256, 257, 258], all viable $f(R)$ models should be of such “disappearing cosmological constant” type [258], and models similar to HS were proposed in [257, 258].

For all $f(R)$ models, $\beta(a) = 1/\sqrt{6}$, while the mass function is model dependent. In the HS model, we have

$$m(a) = \tilde{m}_0 \left(\frac{4\Omega_\Lambda + \Omega_m a^{-3}}{4\Omega_\Lambda + \Omega_m} \right)^{(n+2)/2} \quad (6.29)$$

²This analysis was performed with the previous version of MGCAMB. In that version, observables computed in models with massive neutrinos could have up to 4% systematics. This has been fixed in the latest version of MGCAMB, that we describe in Chapter 7.

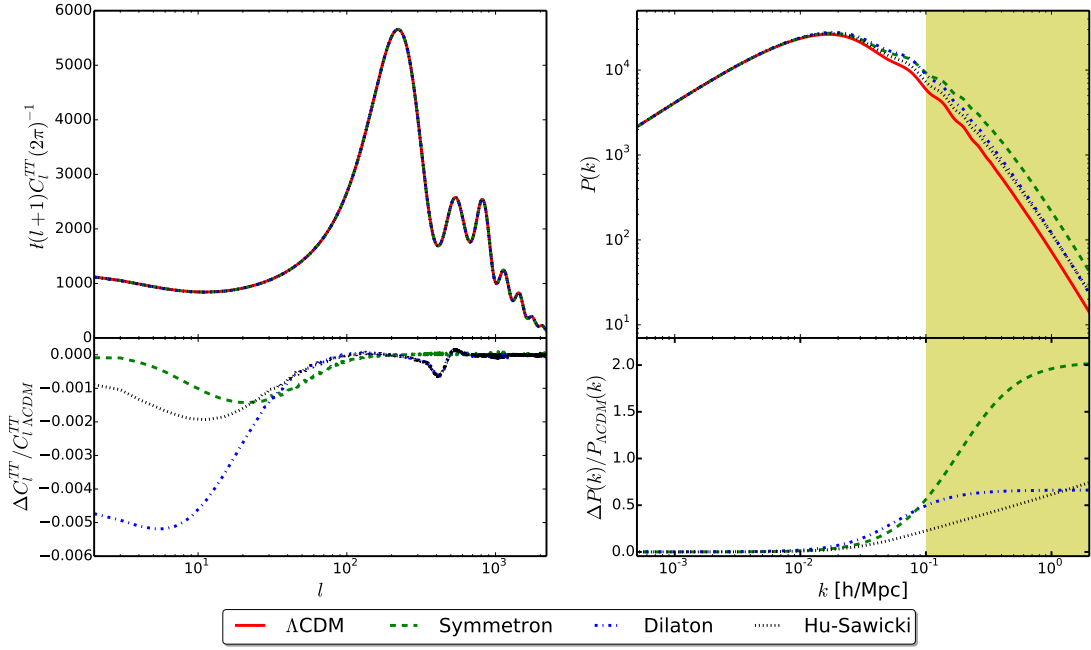


Figure 6.1: Plots of CMB temperature anisotropy C_l^{TT} (left) and the matter power spectrum $P(k)$ (right) for the models studied in this paper. The parameters used for the symmetron model are: $a_\star = 0.25$, $\beta_\star = 1$ and $\xi_\star = 10^{-3}$. The parameters used for the dilaton model are: $\beta_0 = 3$ and $\xi_0 = 6 \times 10^{-3}$. The parameters used for Hu-Sawicki $f(R)$ model are $f_{R_0} = 10^{-4}$ and $n = 1$. The yellow shaded region shows the scales that are not taken into account in the data analysis.

where Ω_Λ and Ω_m are the dark energy and matter density fractions today, and \tilde{m}_0 is a mass scale that can be expressed in terms of f_{R_0} as [250]

$$\tilde{m}_0 = H_0 \sqrt{\frac{4\Omega_\Lambda + \Omega_m}{(n+1)f_{R_0}}}. \quad (6.30)$$

Local tests of gravity require $f_{R_0} \lesssim 10^{-6}$ [259], while astrophysical constraints from dwarf galaxies imply that $f_{R_0} \lesssim 10^{-7}$ [260]. These bounds depend on accurate modelling of non-linear physics. In what follows, we will derive the constraint on f_{R_0} from current cosmological data using only information from linear scales, and also forecast constraints expected from future surveys like LSST.

Representative CMB and matter power spectra for $f(R)$ are shown in Fig. 6.1. A notable effect on the CMB spectrum is the suppression of power at small multipoles, which is due to the reduced Integrated Sachs-Wolfe (ISW) effect. The magnitude of the ISW effect is proportional to the net change in the gravitational potential along the line of sight. In Λ CDM, the change in the potential is a reduction caused by the onset of cosmic acceleration. In $f(R)$, the additional scalar force enhances the potential which, combined with the decay due to acceleration, leads to a smaller net change and, thus, a smaller ISW effect. The other notable impact of $f(R)$ on the CMB spectrum is the enhanced lensing, which has the effect of slightly dumping the peaks. The enhanced growth is more evident in the plot of $P(k)$. Qualitatively, these features are common to all GBD models.

6.4.2 Dilaton model

Another relevant example is the environmentally dependent dilaton [248], where the screening mechanism is of the Damour-Polyakov type [261]. This model, inspired by string theory in the large string coupling limit, has an exponentially runaway potential

$$V(\phi) = V_0 e^{-\phi/m_0}, \quad (6.31)$$

with the value of V_0 set to generate the current acceleration of the Universe, while the coupling function is

$$A(\phi) = 1 + \frac{A_2}{2m_0^2} (\phi - \phi_\star)^2. \quad (6.32)$$

In dense environments, the minimum of the effective potential approaches $\phi = \phi_\star$, and the coupling function $\beta(a)$ vanishes. The coefficient A_2 has to be large to satisfy local tests of gravity; typically $A_2 \gtrsim 10^6$. These models can be described by a mass function given by

$$m^2(a) = 3A_2 H^2(a) \quad (6.33)$$

and, assuming matter domination, a coupling function

$$\beta(a) = \beta_0 a^3, \quad (6.34)$$

where $\beta_0 = \Omega_\Lambda/\Omega_m \sim 2.7$ is related to V_0 , and is determined by requiring that ϕ plays the role of dark energy. We will present our constraints on the mass in terms of a scalar-force range parameter ξ_0 , defined as

$$\xi_0 = \frac{H_0}{c \tilde{m}_0} = \frac{1}{\sqrt{3}A_2}, \quad (6.35)$$

where $\tilde{m}_0 = m(a = 1)$. We show representative CMB and matter power spectra for the dilaton model in Fig. 6.1, with parameter values being large on purpose to exaggerate the qualitative features of the model.

6.4.3 Symmetrons

Another example of a GBD model with the Damour-Polyakov screening mechanism is the symmetron [249], where the scalar field has a quartic potential,

$$V(\phi) = V_0 + \frac{m_\star^2 \phi_\star^2}{2} \left[-\frac{1}{2} \left(\frac{\phi}{2\phi_\star} \right)^2 + \frac{1}{4} \left(\frac{\phi}{\phi_\star} \right)^4 \right] \quad (6.36)$$

and a coupling function,

$$A(\phi) = 1 + \frac{\beta_\star}{2\phi_\star} \phi^2. \quad (6.37)$$

When matter density is large, the effective potential has a minimum at $\phi = 0$ and $A(\phi) \rightarrow 1$, thus decoupling the scalar from matter. At lower densities, the effective potential acquires a non-zero minimum, activating the scalar force. For cosmological densities, the transition occurs at

$$\rho_\star = \frac{\rho_m}{a_\star^3} = \frac{m_0 m_\star^2 \phi_\star^2}{2\beta_\star}, \quad (6.38)$$

where ρ_m is the matter density today. Thus, one can work with a_\star , along with m_\star and β_\star , as the three free parameters of the theory. At $a > a_\star$, the model can be described by

$$m(a) = m_\star \sqrt{1 - \left(\frac{a_\star}{a} \right)^3} \quad (6.39)$$

and

$$\beta(a) = \beta_\star \sqrt{1 - \left(\frac{a_\star}{a} \right)^3}, \quad (6.40)$$

while $\beta(a) = 0$ for $a < a_\star$. As in the case of dilatons, we represent our bounds in terms of a range parameter ξ_\star , defined as

$$\xi_\star = \frac{H_0}{c} \frac{1}{m_\star}. \quad (6.41)$$

Representative CMB and matter power spectra for this model are shown in Fig. 6.1.

6.4.4 Generalized Chameleon models

In our forecasts, we will also consider generalized models of chameleon type [262] defined by

$$m(a) = \tilde{m}_0 a^{-r}, \quad \beta(a) = \beta_0 a^{-s} . \quad (6.42)$$

In practically all viable chameleon models, the coupling function is expected to vary extremely slowly at redshifts probed by large scale structure surveys. Thus, for all practical purposes, it can be taken to be a constant of order unity.

6.4.5 Binned Model

As discussed so far, for any of the aforementioned models, each with its own theoretical motivation, one can determine the functional forms of $m(a)$ and $\beta(a)$. This effectively reduces the two free functions $m(a)$ and $\beta(a)$ to a handful of parameters. However, one might be interested in knowing how well the two functions are constrained in general, without regard for any specific model. One can then proceed by discretizing either of the two functions in bins of redshift space and treating the amplitude in each bin as a free parameter to be constrained.

Varying both, the coupling and the mass functions, simultaneously would be redundant, since their effect is largely degenerate. Since it is the mass parameter that affects the shape of the matter power spectrum, we fix $\beta(a)$ to a constant value of order unity and bin $m(a)$ in redshift. If a non-zero $m^{-1}(a)$ were detected, it would signal the presence of a scalar interaction and further investigation would be required to determine if the variation occurs in $\beta(a)$, $m(a)$ or both.

While a binning scheme gives a model independent (rather a far less model dependent) treatment of $m(a)$, the larger number of parameters (values of m in each bin) results in weaker constraints on the individual parameters. To extract useful information, we apply the Principal Components Analysis (PCA) technique (reviewed in Section 6.6.7). The resulting Principal Components (PCs) are linear combinations of the original bin values and the propagated uncertainty (from original errors on the bins) in their values can inform us about those PCs that are best constrained by data and the number of degrees of freedom they can potentially be constrained.

6.5 Constraints from current data

In this Section, we use a combination of currently available CMB, lensing and Baryonic Acoustic Oscillation (BAO) data, as well as measurements of the matter power spectrum, to derive constraints on the GBD parameters. To compute the observables, we implemented

the parametrizations described in the previous Section in MGCAMB. We then use it with an appropriately modified version of CosmoMC [145] to obtain the posterior distributions for the model parameters. Since current data is unable to simultaneously constrain multiple GBD parameters, we will only consider models from the previous Section for which meaningful constraints are possible.

6.5.1 The datasets used in the analysis

We use the measurements of CMB temperature anisotropy from the second data release of the *Planck* survey [10] in the form of the full *Planck* TT high- ℓ likelihood ($30 < \ell < 2500$) along with the low- ℓ polarization ($\ell < 30$). We refer to the above datasets as PLC. We also consider the *Planck* 2015 lensing potential spectrum [263] extracted from mode-coupling correlations, and refer to this dataset as CMBLens.

In addition to inducing higher order correlations, lensing by large scale structures affects the TT spectrum at higher ℓ , slightly damping the oscillatory features. In [264], and subsequently in [10], the lensing contribution to TT was quantified via an amplitude A_L multiplying the lensing power spectrum in the calculation of the theoretical prediction for TT. The parameter A_L was used to quantify the significance of detection of the lensing contribution to TT. However, instead of measuring the expected value of $A_L = 1$, since the lensing contribution to TT is calculated from the same model as the rest of the spectrum, the best fit value obtained for LCDM from the PLC dataset in [10] was $A_L = 1.22 \pm 0.10$, or two standard deviations away from the expectation. As discussed in [264] (see also [265]) this is due to an apparent tension between the higher- ℓ and lower- ℓ data when trying to fit LCDM to Planck TT data. To negate the effect of this tension, the parameter A_L was sometimes co-varied with other parameters when deriving constraints on LCDM in [10]. In what follows, we take the view that A_L is not a physical parameter and should be held fixed to 1 when deriving constraints on cosmological models. However, we also investigate and discuss the effect of co-varying A_L in the case of $f(R)$.

For BAO measurements, we used data from the 6dF survey [96] and from SDSS, specifically the MGS [97] and BOSS data releases (LOWZ and CMASS) [266].

We also use the matter power spectrum (referred to as MPK) from SDSS LRG DR4 [267], but only on linear scales, $k \leq 0.1 h/\text{Mpc}$. We are aware of the fact that non-linear corrections can play a role even at $k \lesssim 0.1 \text{ Mpc}$ and that a proper treatment of the bias and the redshift space distortions (RSD) must take them into account. This was studied at length in [268] for the SDSS DR9 power spectrum and it was found that the differences in the upper bounds on neutrino masses obtained using four different RSD models were under 20%. Based on this, we expect that bounds on the GBD parameters (such as f_{R_0}) obtained from MPK are accurate to within 30%, which is sufficient given that constraints from current data are relatively weak.

Finally, we consider the weak lensing data from the Canada France Hawaii Telescope Lensing Survey 2DCFHTLenS [269], referred to as WL. To avoid dealing with non-linear scales, we adopt a conservative cut and exclude $\theta < 30'$ from the measurements of the correlation function ξ_{\pm} , which corresponds to $k < 0.1 h/\text{Mpc}$ scales.

6.5.2 Constraints on $f(R)$

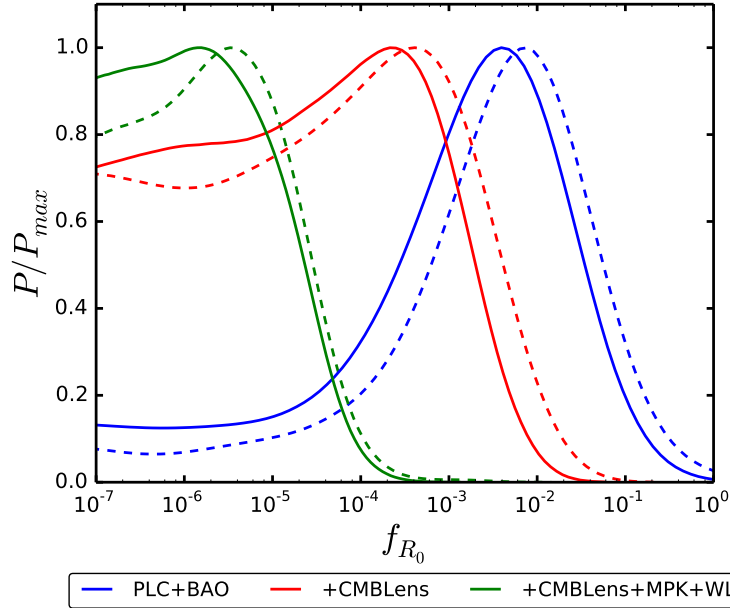


Figure 6.2: The marginalized posterior distribution for the f_{R_0} parameter in the Hu-Sawicki model ($n = 1$) for different combinations of datasets. The solid lines show the PDF in case of massive neutrinos with a fixed mass $\sum m_\nu = 0.06 \text{ eV}$, while the dashed lines show the PDF for the case when the neutrino mass was varying. Due to the degeneracy between f_{R_0} and $\sum m_\nu$, we see that the constraint on f_{R_0} become weaker when the neutrino mass is varied. The datasets are labeled according to the notation introduced in Sec. 6.5.1. The symbol + means that we add data on top of the PLC+BAO dataset. For example, +lensing means PLC+BAO+lensing.

The Hu-Sawicki $f(R)$ model has two parameters, f_{R_0} and n . In what follows, we fix $n = 1$ because that is a common choice in the literature, and also because the two parameters are highly correlated and the current data cannot simultaneously constrain both. We chose a flat prior on $\log_{10} f_{R_0}$ within the $[-7, 0]$ range. We have checked that changing the range of the flat prior does not affect our results.

Fig. 6.2 shows the constraints on f_{R_0} for different combinations of datasets described in Sect. 6.5.1, after marginalizing over all the other cosmological parameters. We considered the case in which the total neutrino mass is fixed at $\sum m_\nu = 0.06 \text{ eV}$ (solid lines), and the case where it can vary within $0 \leq \sum m_\nu \leq 1 \text{ eV}$ (dashed lines). The results from Fig. 6.2 are summarized in Table 6.1.

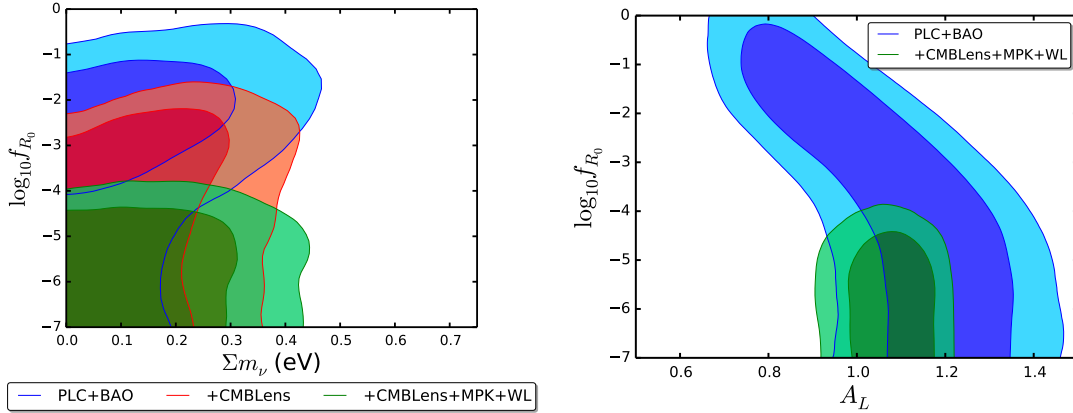


Figure 6.3: Left panel: joint contours for f_{R_0} and Σm_ν in the Hu-Sawicki model ($n = 1$) after marginalizing over all other cosmological parameters. The darker and lighter shades correspond respectively to the 68% C.L. and the 95% C.L. Right panel: joint contours for f_{R_0} and A_L in the Hu-Sawicki model. The darker and lighter shades correspond respectively to the 68% C.L. and the 95% C.L. Using PLC+BAO data sets only it is possible to detect high values of f_{R_0} that can cure the tension in lensing amplitude A_L . However such high values are ruled out once we add lensing and LSS data sets.

Data sets	Fixed Σm_ν	Varying Σm_ν	
	f_{R_0}	f_{R_0}	Σm_ν (eV)
PLC+BAO	0.05 (0.14)	0.08 (0.23)	0.24(0.35)
+CMBLens	$3(8) \times 10^{-3}$	$0.6(1.6) \times 10^{-2}$	0.22(0.31)
+MPK	$0.6(1.6) \times 10^{-4}$	$0.7(1.7) \times 10^{-4}$	0.24(0.34)
+WL	$3(7) \times 10^{-5}$	$4(9) \times 10^{-5}$	0.23(0.33)

Table 6.1: The 68% (95%) CL upper limits of f_{R_0} and the sum of neutrino masses using different combinations of data sets shown in the table.

We can see that the combination of PLC and BAO datasets (blue lines) only weakly constrains the model. Modified gravity affects the CMB temperature anisotropy spectrum in two ways: it affects the low- ℓ power spectrum through the ISW effect and enhances the damping at high- ℓ due to the enhancement in clustering and, as a consequence, the lensing potential. Thus, the observed lack of power at low- ℓ multipoles and the apparent preference of enhanced lensing in CMB TT, when compared to the Λ CDM prediction, can be reconciled by a non-zero f_{R_0} . This is the reason for the peak in the PLC+BAO likelihood. Adding the CMBLens data (red lines) tightens the constraint substantially. The enhancement of growth due to the extra scalar interaction affects the lensing potential measured by *Planck*, which is known to be in excellent agreement with the Λ CDM prediction [10]. Thus, the weak preference for larger f_{R_0} coming from PLC+BAO is overwhelmed by the stronger CMBLens data that is consistent with $f_{R_0} = 0$. The constraint becomes even tighter after adding the MPK and WL datasets (green lines).

$f(R)+A_L$, fixed $\sum m_\nu$		$f(R)+A_L$, varying $\sum m_\nu$		
f_{R_0}	A_L	f_{R_0}	A_L	$\sum m_\nu$
$3(8) \times 10^{-5}$	$1.08^{+0.07(0.12)}_{-0.05(0.13)}$	$0.4(1.0) \times 10^{-4}$	$1.11^{+0.10(0.16)}_{-0.06(0.15)}$	$0.30(0.38)$

Table 6.2: 68% (95%) CL bounds on f_{R_0} , A_L and $\sum m_\nu$ using all the data sets: PLC+BAO+CMB lens+MPK+WL

The dashed lines in Fig. 6.2 show the impact of co-varying the combined mass of neutrinos, $\sum m_\nu$, along with f_{R_0} . Massive neutrinos suppress the growth and can partially compensate for the enhanced clustering in $f(R)$, slightly weakening the bounds on f_{R_0} . The extent of the degeneracy can be inferred from the left panel of Fig. 6.3 which shows the joint confidence contours for the two parameters. We see that, although the constraint on f_{R_0} becomes tighter as we add the LSS data, the constraint on $\sum m_\nu$ remains roughly the same. This is because we are restricting our analysis to linear scales, while the effect of massive neutrinos becomes more relevant on smaller scales and, hence, causes only a small degradation of f_{R_0} constraints.

Up to this point, we kept the unphysical lensing amplitude parameter A_L fixed at its expected value of 1. However, one may wonder if the discrepancy in A_L observed in the Λ CDM model also persists in $f(R)$, and what effect co-varying A_L has on the bounds on f_{R_0} . The results for two different combinations of data are shown in the right panel of Fig. 6.3. Although it seems that, in the case of PLC+BAO, the lensing amplitude tension has been reconciled, we argue that this is not due to a genuine signal of modified gravity. As discussed previously, the PLC+BAO data yields a peak in the likelihood of f_{R_0} because the preference for enhanced lensing and the lack of power at low ℓ in C_ℓ^{TT} can be reconciled with a non-zero f_{R_0} . The enhanced lensing appears to cure the A_L problem and this is depicted in Fig. 6.3, where we see that there is a strong degeneracy between A_L and f_{R_0} for large values of the latter (blue contours). However such large values of f_{R_0} are ruled out once we add the datasets that probe clustering (green contours). Still, the value of A_L when co-fit with f_{R_0} is in better agreement with the prediction. For the combination of all data we find

$$A_L = 1.11^{+0.20}_{-0.14} \quad 68 \% \text{ C.L., all datasets.} \quad (6.43)$$

The results of the analysis with varying A_L are summarized in Table 6.2.

6.5.3 Constraints on the symmetron model

Here we derive constraints on the inverse mass parameter, ξ_\star , defined in equation (6.41), which represents the Compton wavelength of the scalar interaction. We fix the other two symmetron parameters, taking $a_\star = 0.25$ and $\beta_\star = 1$, since current data is unable to constrain them simultaneously with ξ_\star .

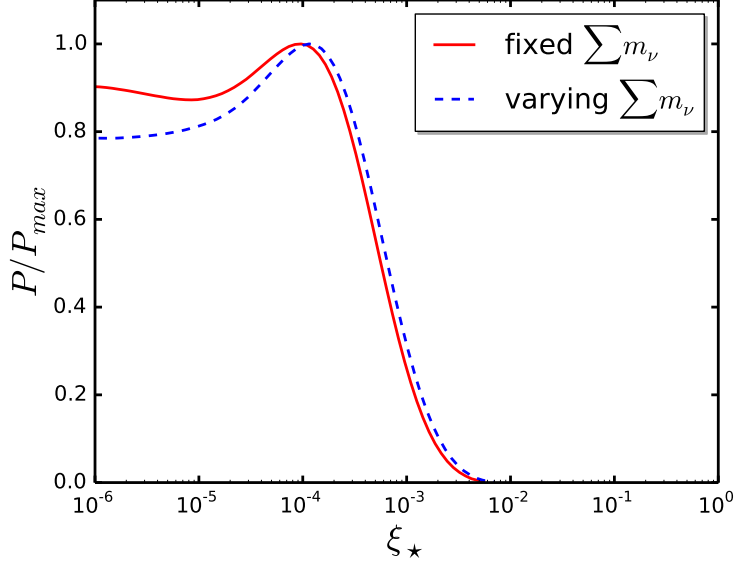


Figure 6.4: The marginalized posterior distribution for ξ_* in symmetron model with $\beta_* = 1$ and $a_* = 0.25$ considering neutrinos with $\sum m_\nu = 0.06$ eV (red solid line) and marginalizing over a varying $\sum m_\nu$ (blue dashed line). The data sets used in this analysis are PLC+BAO+lensing+MPK+WL as described in section 6.5.1.

Fig. 6.4 shows the posterior probability distribution for the ξ_* parameter with a fixed $\sum m_\nu = 0.06$ eV (red solid line) as well as after marginalizing over a varying $\sum m_\nu$ (blue dashed line). We find an upper bound of $\xi_* < 1.5 \times 10^{-3}$ at 95 % C.L, which corresponds to a Compton wavelength of \sim a few Mpc. Our bounds are summarized in Table 6.3.

As mentioned above, current data is unable to simultaneously constrain all the model parameters because they are highly correlated. We also note that one cannot derive meaningful constraints for smaller values of coupling constant β_* as the modification of growth is relatively small for the scales and redshifts currently probed. Further, since a_* sets the onset of modified growth, we would see tighter constraints on ξ_* for smaller a_* values. Nevertheless, as we will show in Sect. 6.6, future surveys with larger sky and deeper redshift coverage will be able to constrain ξ_* along with the other two parameters.

6.5.4 Constraints on the dilaton model

	Fixed $\sum m_\nu$	Varying $\sum m_\nu$	
symmetron	ξ_*	ξ_*	$\sum m_\nu$
	$0.8 (1.5) \times 10^{-3}$	$0.9 (1.8) \times 10^{-3}$	$0.16 (0.27)$
dilaton	ξ_0	ξ_0	$\sum m_\nu$
	$2.1 (3) \times 10^{-3}$	$2.3 (3) \times 10^{-3}$	$0.15 (0.25)$

Table 6.3: Summary of the 95% CL upper limits of the MG parameters and the sum of neutrino masses (in unit of eV) derived from current observations described in Sec. 6.5.1.

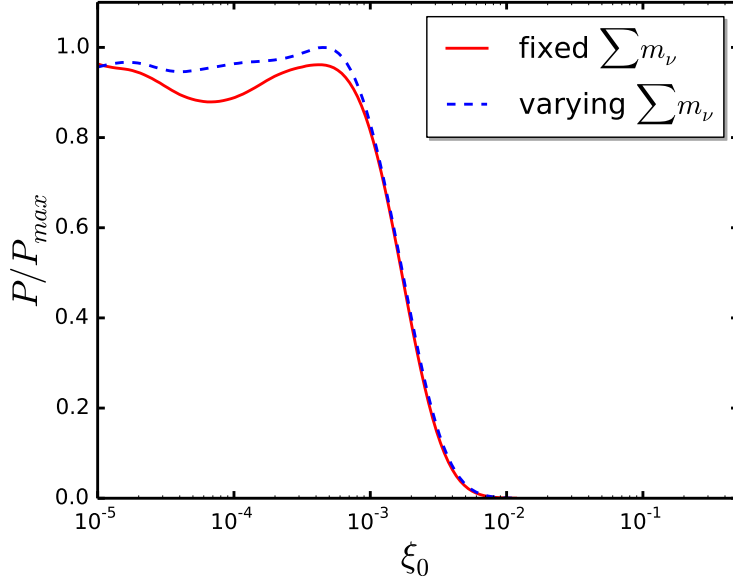


Figure 6.5: Marginalized posterior distribution for ξ_0 in the dilaton model with $\beta_0 = 5$. The datasets used in the analysis are PLC+BAO+lensing+MPK+WL as described in section 6.5.1. The red solid line shows the case with massive neutrinos with a fixed mass of $\sum m_\nu = 0.06\text{eV}$, while the blue solid lines shows the PDF after marginalizing over a varying $\sum m_\nu$.

Analogously to the symmetron model, we constrain the inverse mass parameter ξ_0 defined by equation. (6.35), and fix β_0 to a constant. Fig. 6.5 shows the posterior distribution for ξ_0 with the current value of the coupling parameter fixed at $\beta_0 = 5$. We find an upper bound of $\xi_0 < 3 \times 10^{-3}$ (95 % C.L.). As for symmetrons, the sensitivity to the coupling is weak due to the lack of data on linear scales. However, as we will see in Sec. 6.6, constraints will improve significantly with future surveys. Our results for the dilaton model are summarized in Table 6.3.

6.6 Forecasts

Constraints on scalar gravitational interactions derived in the previous Section, using current information available on linear scales, are relatively weak when compared to bounds available from astrophysical tests. With improved redshift resolution, depth and sky coverage that future surveys will provide, the number of modes in the linear regime will dramatically increase. Thus, it is interesting to know if future constraints from linear scales can become compatible with astrophysical bounds.

In what follows, we perform a series of Fisher forecasts for the model parameters described in the previous Section, using, where possible, the current bounds on model parameters as fiducial values in the forecast. Where there was no upper bound, we use fiducial values motivated by a combination of theoretical considerations and existing constraints

from non-linear scales. We also perform a principal component analysis (PCA) of $m(a)$ for a fixed order unity coupling β , to see how well future datasets can constrain an evolving mass parameter.

6.6.1 The data assumed in the forecast

The data we consider in our forecast include CMB temperature anisotropy (T) and polarization (E) power spectra with characteristics of the Planck survey, weak lensing shear (WL) and galaxy number count (GC) from an LSST-like survey³, with the survey parameters adopted from [270], and their cross-correlations. In some cases, we compare this to constraints expected from the Dark Energy Survey (DES)⁴.

Theoretical power spectra are calculated assuming the LSST (DES) GC data is partitioned into 10 (4) tomographic redshift bins, while the WL shear field is split into 6 (4) tomographic redshift bins. In addition, we assume a flat FRW geometry and vary h , $\Omega_c h^2$, $\Omega_b h^2$, τ , n_s , w and A_s , together with the modified gravity parameters. The fiducial values of the cosmological parameters are taken to be the Planck 2015 best fit results. To calculate the WL and GC auto- and cross-correlation spectra in our scalar-tensor models, we have applied the MGCAMB patch to CAMBSources [113, 272]⁵. The details of the implementation are described in [37, 273].

6.6.2 Fisher analysis

For a given model, one can calculate the Fisher matrix [274] to determine how well future surveys can constrain its parameters. The inverse of the Fisher matrix provides a lower bound on the covariance matrix of the model parameters via the Cramér-Rao inequality, $\mathbf{C} \geq \mathbf{F}^{-1}$. For zero-mean Gaussian-distributed observables, such as the angular correlations C_ℓ^{XY} , the Fisher matrix is given by

$$F_{ab} = f_{\text{sky}} \sum_{\ell=\ell_{\text{min}}}^{\ell_{\text{max}}} \frac{2\ell+1}{2} \text{Tr} \left(\frac{\partial C_\ell}{\partial p_a} \tilde{C}_\ell^{-1} \frac{\partial C_\ell}{\partial p_b} \tilde{C}_\ell^{-1} \right), \quad (6.44)$$

where p_a is the a^{th} parameter of our model and $\tilde{\mathbf{C}}_\ell$ is the “observed” covariance matrix with elements \tilde{C}_ℓ^{XY} that include contributions from noise:

$$\tilde{C}_\ell^{XY} = C_\ell^{XY} + N_\ell^{XY}. \quad (6.45)$$

³<http://www.lsst.org>

⁴<http://www.darkenergysurvey.org/>. The analysis presented in this Chapter has been performed in [271], before the DES survey released the 1YR data.

⁵CAMB sources has been integrated in CAMB in the 2019 version.

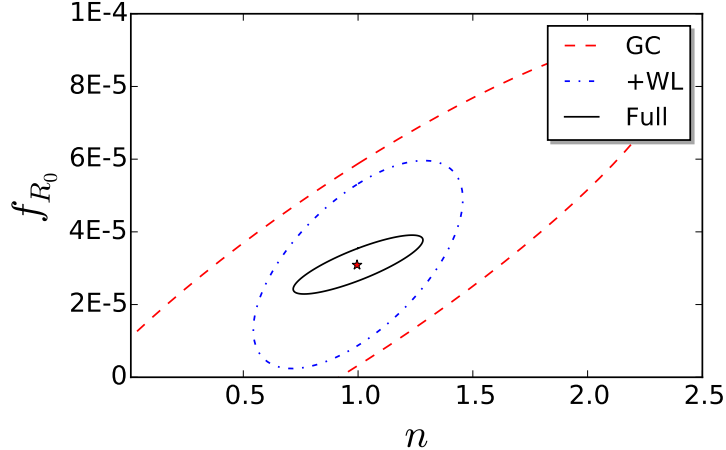


Figure 6.6: Expected 1σ bounds on the parameters of the Hu-Sawicki model. The assumed fiducial model is marked with a star. The importance of using the “Full” set of observables (WL, GC and their cross-correlation) is clearly demonstrated. The Planck CMB data is included in all cases and is important for constraining the standard cosmological parameters.

Equation (6.44) assumes that all fields $X(\hat{\mathbf{n}})$ are measured over contiguous regions covering a fraction f_{sky} of the sky. The value of the lowest multipole can be approximately inferred from $\ell_{\text{min}} \approx \pi/(2f_{\text{sky}})$. The noise matrix N_{ℓ}^{XY} includes the statistical noise as well as the expected systematic errors. We refer the reader to [37, 273] for the details of the Fisher matrix calculations for the individual experiments considered in our analysis.

6.6.3 The $f(R)$ forecast

In Fig. 6.6 we show 1σ constraints on parameters of the Hu-Sawicki $f(R)$ model, as expected from LSST+ (LSST WL + LSST GC + Planck CMB). Recall that current data is unable to constrain f_{R_0} unless one assumes a fixed value for n , since the two parameters are highly degenerate. Thus, the forecast in Fig. 6.6 depends strongly on the assumed fiducial value, indicated with a \star on the plot. What we see is that for $n \sim 1$ or smaller, future data will be able to constrain both parameters simultaneously.

Fig. 6.6 also shows the importance of including the cross-correlation between WL and GC. The information from GC alone is largely diluted by the unknown galaxy bias. Weak lensing, while not sensitive to the bias, is plagued by degeneracies coming from projection effects. Combining them helps determine the bias and break the degeneracies coming from projections.

Fig. 6.7 compares joint 1σ constraints on f_{R_0} and the combined mass of neutrinos, $\sum m_\nu$, as expected from LSST+ vs those expected from DES+. We see that LSST+ can reduce uncertainties in both parameters by a factor of 3. The plot shows the effect of marginalizing over n , however the outcome depends on the assumed fiducial value of n (which is $n = 1$).

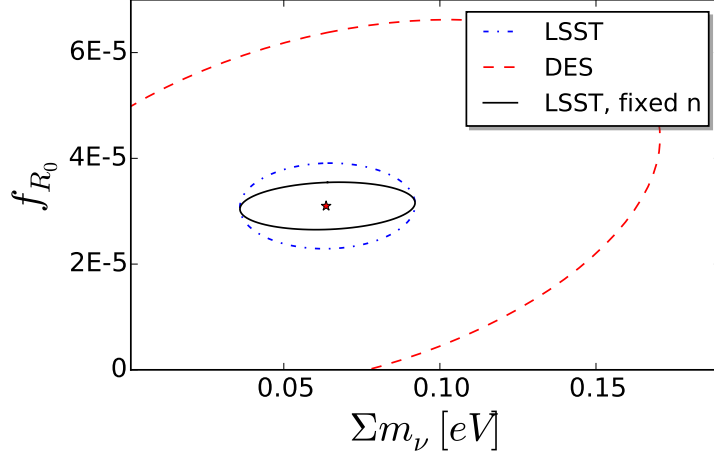


Figure 6.7: Comparison of the uncertainties expected from LSST+ vs those from DES+ for the f_{R_0} parameter of the $n = 1$ Hu-Sawicki model and the total mass of neutrinos. The assumed fiducial model is marked with a star. The effect of fixing n , as opposed to marginalizing over it, is also shown.

6.6.4 The symmetron forecast

Fig. 6.8 shows the bounds on the parameters of the symmetron parameters expected from LSST+. As a fiducial model, we assume $\beta_\star = 1$ and a mass scale of $\xi_\star = 10^{-3}$, which corresponds to a range of a few Mpc. Current data is unable to constrain ξ_\star if $a_\star = 0.5$ or larger. For this reason, the bound on ξ_\star in Sect. 6.5 was derived for a fixed $a_\star = 0.25$. We perform a forecast using two different fiducial values: $a_\star = 0.25$ and 0.5 . In the former case, LSST+ clearly improves on the bound in Sect. 6.5, even after marginalizing over a_\star and β_\star . It will also be able to provide a non-trivial bound on ξ_\star for $a_\star = 0.5$, which is the value assumed in much of the previous literature. The current and expected bounds are summarized in Tab. 6.4.

It is interesting to examine the possible degeneracy between the symmetron parameters and the total mass of neutrinos. Fig. 6.9 shows the joint uncertainties in ξ_\star and Σm_ν expected from LSST+ assuming a fiducial model with $\beta_\star = 1$, $\xi_\star = 10^{-3}$, $a_\star = 0.5$ and $\Sigma m_\nu = 0.06\text{eV}$. It is clear from the figure that there is practically no degeneracy between ξ_\star and m_ν which is because they affect the growth on different scales. Fixing the other MG parameters in this model, as opposed to marginalizing over them, does not change the degree of degeneracy, neither it improves the constraints.

6.6.5 The dilaton forecast

Fig. 6.10 shows expected bounds on the dilaton model parameters, with $\beta_0 = 1$ and $\xi_0 = 10^{-3}$ as the fiducial values. Similar to the symmetron case, we find that an LSST-like survey can constrain the inverse mass parameter ξ_0 to a percent level accuracy which is a significant

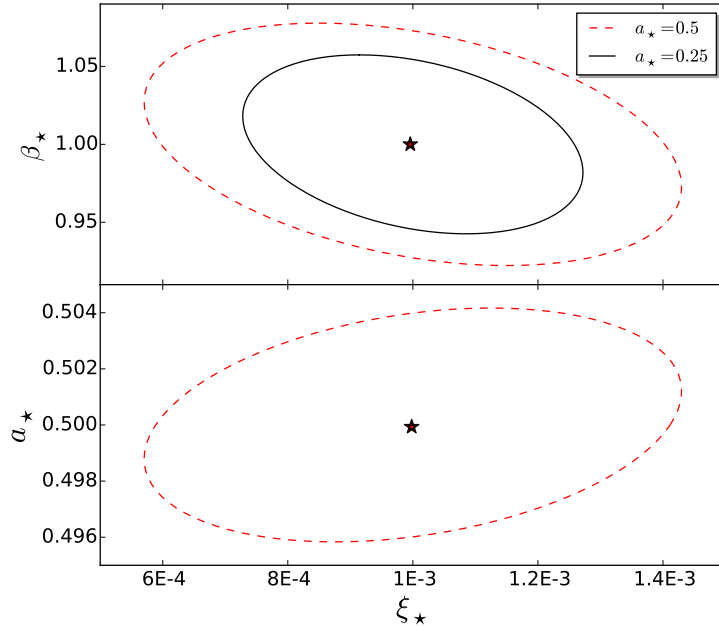


Figure 6.8: Expected 1σ constraints from LSST+ on the parameters of the symmetron model. The assumed fiducial models are marked with a star. Unlike current data, LSST+ can simultaneously constrain β_* and a_* to a few percent level, and will improve the current bounds on ξ_* . See Table 6.4 for a quantitative comparison.

improvement over current constraints. Constraints on the coupling constant β_0 , however, are not as tight as those on β_* in the symmetron case. This is due to a lesser impact of the dilaton on the linear matter power spectrum. One can see from Fig. 6.1 that for the chosen fiducial values, $P(k)$ would deviate from the Λ CDM prediction far less in the dilaton case compared to the symmetron. The bottom panel in Fig. 6.10 shows the expected joint constraints on the neutrino masses, which are tighter than those for the symmetron. Again, this is because dilatons have a much lesser impact on the growth on linear scales.

6.6.6 The Generalized Chameleon model

Forecasts for the Generalized Chameleon provide a general estimate of how well one could constrain the scalar gravitational interactions with a next generation WL survey such as LSST. In Fig. 6.11 we show forecasted uncertainties on the parameters of the generalized Chameleon model for two fiducial values of r , assuming that the coupling is constant ($s = 0$). For a slower evolution with time ($r = 1$), the scalaron mass decreases slower and modification to growth extends back to larger redshifts, leading to significantly tighter constraints. Thus, while LSST+ can constrain the coupling, the mass and the time-variation of the scalaron mass simultaneously, the strength of the bounds depends strongly on the assumed fiducial model.

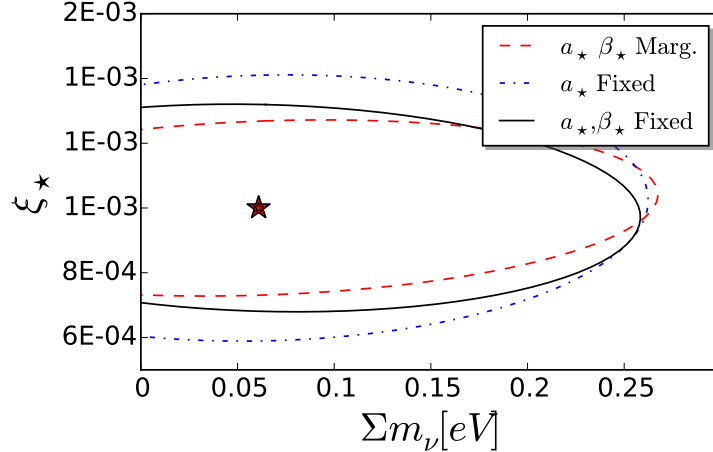


Figure 6.9: Expected 1σ bounds on the ξ_* parameter of the symmetron model and the mass of neutrinos, $\sum m_\nu$. The assumed fiducial model is marked with a star. Fixing the other MG parameters in this model, as opposed to marginalizing over them, does not change the degree of degeneracy, neither it improves the constraints.

6.6.7 Principal Component Analysis of $m(a)$

In addition to considering particular functional forms of $\beta(a)$ and $m(a)$ as motivated by the scalar-tensor models mentioned in preceding sections, it is also interesting to treat the coupling and the mass as two general functions and ask what features of these two functions can be constrained by the future data. In principle, one could discretize the functions $\beta(a)$ and $m(a)$ into N bins in a and treat the bins values as free parameters. However, we find that even future data will not be able to simultaneously constrain $m(a)$ and $\beta(a)$ in a completely model-independent way, since the two parameters are largely degenerate in their effect on the observables on linear scales, as they appear together in $\epsilon(a, k)$ (see equation. (6.24)). For this reason, we fix β at a constant value of order unity and discretize $m(a)$ into bins with $m(a_i), i = 1, \dots, N$.

As with earlier forecasts, we can calculate the Fisher matrix, and invert it to find the covariance matrix,

$$C_{ij} \equiv \langle (p_i - \bar{p}_i)(p_j - \bar{p}_j) \rangle, \quad (6.46)$$

where \bar{p}_i are the “fiducial” values, and parameters include the bins $m(a_i)$, as well as the rest of cosmological parameters. We then isolate the $N \times N$ block of the matrix, C^m corresponding to the covariance of $m(a_i)$ after marginalization over other parameters. Since the individual bins of $m(a_i)$ bins are highly correlated, the covariance matrix for these parameters will be non-diagonal, and the value of m in any particular bin will be practically unconstrained. The Principal Component Analysis (PCA) [240, 273, 275, 276, 277] is a way to decorrelate the parameters and find their linear combinations that are best constrained

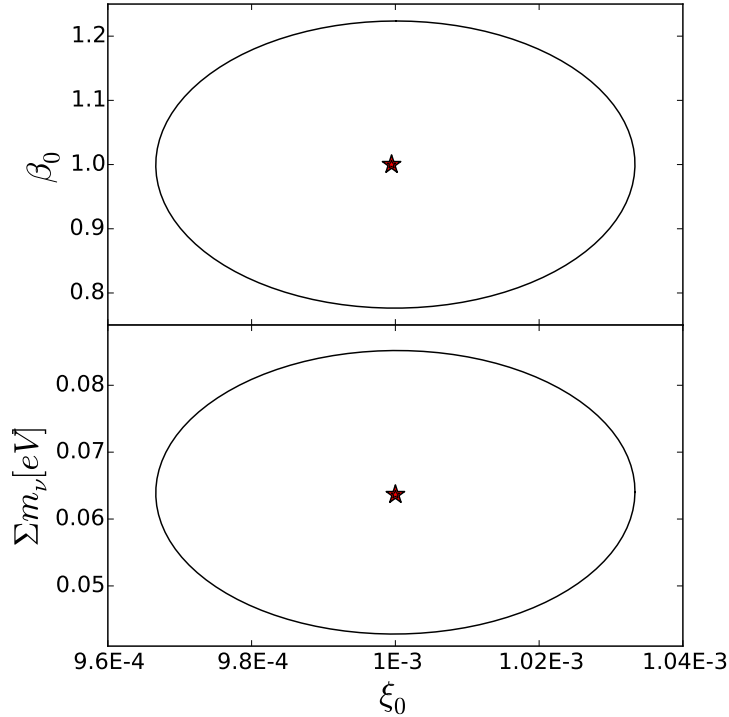


Figure 6.10: 1σ bounds on the neutrino masses and parameters of the dilaton model expected from LSST+. The fiducial values are marked with stars.

by data. Namely, we solve an eigenvalue problem to find a matrix W^m that diagonalizes C^m :

$$C^m = (W^m)^T \Lambda W^m ; \quad \Lambda_{ij} = \lambda_i \delta_{ij} , \quad (6.47)$$

where $W_{ij}^m \equiv \hat{e}_i(a_j)$ are the eigenvectors (or eigenmodes) and λ_i 's are the eigenvalues. In the limit of large N , one can write an arbitrary $m(a)$ as an expansion into $\hat{e}_i(a)$:

$$m(a) - \bar{m}(a) = \sum_{i=1}^N \alpha_i \hat{e}_i(a) \quad (6.48)$$

in which case λ_i can be interpreted as the variance of α_i ,

$$\lambda_i = \sigma_{\alpha_i}^2 . \quad (6.49)$$

It is customary to order the eigenmodes from the best constrained to the worst. Then the i^{th} eigenmode is referred to as the i^{th} principal component (PC). Typically, one finds that only the first few modes are well constrained by the data, while most of them are practically unconstrained.

For our forecast, we partition $m(a)$ into 11 bins, with 10 of them evenly spaced in redshift within $z \in [0, 3]$, and the 11th bin ranging from $z = 3$ to $z = 30$. The last bin

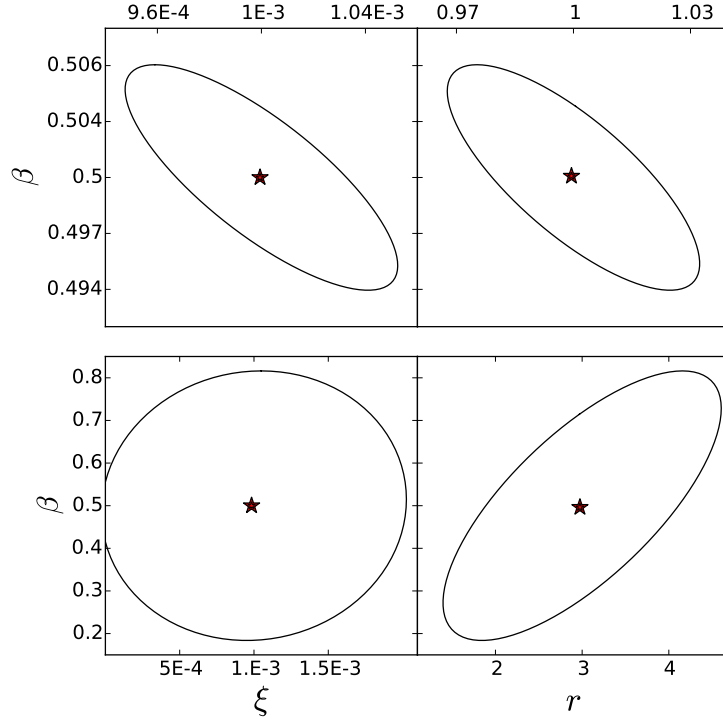


Figure 6.11: Expected 1σ constraints on the the Generalized Chameleon parameters for a fiducial model with $r = 3$ (top) and $r = 1$ (bottom) as a fiducial model. In each case, the value of r is varied and marginalized over.

can be taken to be wide because the observables we work with are weakly sensitive to modifications at high redshifts. In what follows, we marginalize over the 11th bin, since it is largely degenerate with some of the cosmological parameters, most prominently with Ω_m . We take the fiducial model to be $\beta = 0.4$ and $m(a_i) = m_0$ for all i , with $m_0 = H_0/\xi c$ and $\xi = 10^{-3}$, corresponding to $m_0 = 0.2$ h/Mpc.

The left panel in Fig. 6.12 shows the the forecasted uncertainties in the measurement of the eigenvectors for two cases: when β is fixed, and when β is marginalized over. In both cases, we marginalize over all cosmological parameters and the 11th m -bin. The right panel in Fig. 6.12 presents the first four best constrained eigenvectors of $m(a)$ after marginalizing over β . One can interpret the best constrained mode (PC1) as that corresponding to a weighted average value of $m(a)$. The second best constrained mode (PC2) has a single node and corresponds to the difference between the high- z and low- z values of $m(a)$. The third best mode (PC3) has 3 nodes, PC4 has 4 nodes, and so on.

The eigenvalue plot demonstrates that marginalizing over β affects the first eigenmode of $m(a)$, but not the others. This is because the main effect of a constant β is an overall rescaling of the strength of the 5th force. It is largely degenerate with the average value of $m(a)$, but has no impact on the detectability of time-variation of $m(a)$. After marginalizing

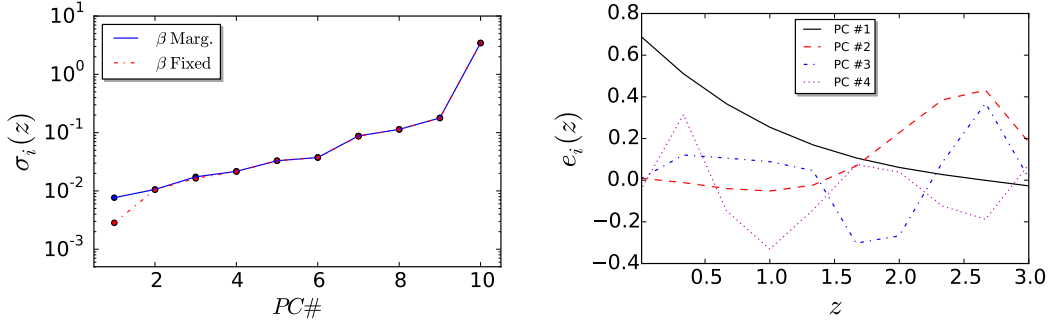


Figure 6.12: Left panel: the uncertainties (square roots of eigenvalues) associated with the eigenmodes of $m(a)$ for the case when the coupling is fixed at $\beta = 0.4$ (solid line), and when it is marginalized over (dashed line). Right panel: the first four best constrained eigenmodes of $m(a)$ after marginalizing over β .

over β , LSST+ can measure one mass parameters (the average $m(a)$) with an accuracy that is better than 0.01 h/Mpc, or about 5% of the fiducial m_0 , and another 3 parameters, describing more rapid evolution of the mass with time, with accuracy better than 0.02 h/Mpc, or 10% of the fiducial value.

The extrema of the eigenmodes indicate the “sweet spots” in redshift, or epochs at which variations in $m(a)$ are best constrained with LSST+. It is evident from the right panel in Fig. 6.12, for instance the shape of PC2, that LSST+ is more sensitive to time-variations at $z > 1.5$. This is because at higher redshifts there is a larger number of Fourier modes that are still in the linear regime.

6.7 Summary

Parameters	Hu-Sawicki $f(R)$		symmetron			dilaton	
	f_{R_0}	$n = 1$	ξ_*	$\beta_* = 1$	$a_* = 0.25$ (0.5)	ξ_0	$\beta_0 = 1$ (5)
Current 1σ	4×10^{-5}	-	10^{-3}	-	-	unconstrained (2.3×10^{-3})	-
LSST+ 1σ	6×10^{-6}	0.3	2 (2.9) $\times 10^{-4}$	0.05 (0.07)	0.001 (0.005)	2.7×10^{-5}	2.3×10^{-1}

Table 6.4: The current 68 % C.L. uncertainties and those expected from LSST+. The blocks with “-” mean the parameter was fixed at its fiducial value. The values in parenthesis indicate those obtained for an alternative fiducial value.

Modifications of gravity on cosmological scales can potentially explain the origin of cosmic acceleration. Scalar-tensor theories of gravity, in which an additional gravitational scalar degree of freedom mediates an extra force at cosmological ranges is a broad class of viable MG models. These can be encapsulated in the Horndeski action (6.1). However, due to its large freedom encoded in the arbitrary functions appearing in the 4 lagrangians (6.2)-(6.5), the Horndeski action is not suitable for cosmological tests of gravity. Several phenomenological approaches exists, the EFTofDE and other phenomenological parametrizations. In this

Chapter we focused on the Generalized Brans-Dicke theories that can be parametrized, in the quasi-static limit, with only two functions of time: $m(a)$ and $\beta(a)$. While the former expresses the mass of the scalar field and hence set the scale at which the fifth force acts, the latter express the strength with which the scalar is coupled to matter.

We have investigated the observational constraints on three MG models within the general framework of the GBD theory, namely, the $f(R)$, the symmetron and the dilaton models, using latest observations of CMB, BAO, weak lensing and galaxy clustering. In all cases, we used observables on linear scales to avoid the complexities of the modelling of nonlinearities and redshift-space distortions.

We find that the Λ CDM model is consistent with all observations. Specifically, we find the constraint on f_{R_0} , the model parameter in the Hu-Sawicki $f(R)$ model, to be $f_{R_0} < 8 \times 10^{-5}$ (95% CL) when the sum of neutrino masses is fixed to be 0.06 eV. Since both massive neutrinos and MG models studied in this paper can alter the structure growth in a scale-dependent way, a degeneracy is expected. Therefore we perform another analysis with the neutrino mass varying, and we find that the constraint is diluted to $f_{R_0} < 1.0 \times 10^{-4}$ (95% CL). For the symmetron model, the 95% CL upper limit is $\xi_\star < 1.8 \times 10^{-3}$ with β_\star and a_\star fixed at 1 and 0.25, respectively. For the dilaton model, we find $\xi_0 < 3 \times 10^{-3}$ at 95% CL when $\beta_0 = 5$. Tables 6.2 and 6.3 summarize the current bounds.

We have also performed a forecast for ongoing and upcoming imaging surveys including DES and LSST, and present the results in Sec. 6.6. A comparison between the current and future constraints on model parameters is shown in Table 6.4. As one can see, the improvement is significant and, despite the high level of degeneracy, more than one parameter can be constrained simultaneously. In the Hu-Sawicki model, the upper limit of f_{R_0} is reduced by a factor of 6.7 and n can be constrained with $\approx 25\%$ accuracy for $n = 1$. For the dilaton model, current data is unable to constrain ξ_0 if $\beta_0 = 1$. However, we find that LSST+ can simultaneously constrain ξ_0 at $\sim \text{few} \times 10^{-5}$ and measure $\beta_0 \sim 1$ with $\approx 20\%$ accuracy. In the symmetron model, the constraint on ξ_\star is improved by a factor of 3, while simultaneously constraining a_\star and β_\star within a few percent. This is compatible with current bounds derived from astrophysical tests, such as the cluster profile [278], galactic dynamics and so on, which requires high-resolution N-body or hydrodynamical simulations [262, 279] of the MG models. Additionally, to demonstrate the capabilities of an LSST-like survey, we have presented constraints on the Generalized Chameleon model in Fig. 6.11.

Given the power of future surveys, a model-independent analysis will become possible. In this work, we performed a PCA study of $m(a)$, to forecast the maximum number of parameters of the scalaron mass function that can be well determined. We find that an LSST-like survey will be able to measure the average mass parameter with an accuracy of 0.01 h/Mpc and another 3 parameters quantifying the time-variation of $m(a)$ with an accuracy that is better than 0.02 h/Mpc. Finally, we note that future spectroscopic and HI surveys, such as eBOSS and SKA [280, 281], will also provide powerful constraints on

MG parameters that will be highly complementary to those from a photometric survey like LSST [\[282\]](#).

Chapter 7

MGCAMB with massive neutrinos and dynamical DE

For the analysis performed in the previous Chapter we used the first update of the code MGCAMB, namely the one developed in [243] that was compatible with CosmoMC. That version, as well as the original one [37], was largely based on the assumption that modifications of gravity appear well after the radiation-matter equality, and that the role played by the anisotropic stress in relativistic particle species is negligible. This limited the accuracy of modelling the effects of massive neutrinos. On the other hand, the neutrino mass can no longer be neglected in cosmological predictions, as the upcoming surveys are expected to probe masses close to the measured difference of 0.05 eV between the masses of different neutrino flavours. Massive neutrinos contribute to the expansion rate as matter, but stream out of smaller gravitational potentials, suppressing the growth on small scales. This effect can be partially degenerate with those of modifications of gravity and, therefore, must be accounted for.

Another limitation of the prior versions of MGCAMB was the assumption of constant dark energy density. Generally, modified gravity (MG) theories predict modifications of the expansion history along with the modified growth of structures. The ability to study the covariance of the two can be important for ruling out broad classes of alternative gravity theories [283].

In this Chapter we present a major update of MGCAMB allowing for dynamical dark energy and accurate modelling of massive neutrinos.¹ This version is compatible with the latest CosmoMC and is restructured to make it easier to customize to work with different parameterizations of phenomenological functions. The modifications of gravity can now be introduced at arbitrarily high redshifts, as long as the phenomenological functions continuously approach their Λ CDM values in the past. Users wishing to study models that do not

¹This new patch is available at <https://github.com/sfu-cosmo/MGCAMB>

approach the GR limit in the past will need to introduce the corresponding changes in the initial conditions.

To demonstrate the capabilities of this new version, we present joint constraints on the modified growth, massive neutrinos and the dark energy equation of state from the latest cosmological observations, including the Planck 2015 CMB data [211], the Joint Light Curve analysis (JLA) supernovae [87], the BAO measurements from 6dF [96] and SDSS DR7 [97], the measurements of the Hubble parameter, the angular-diameter distance and the redshift space distortions from BOSS DR12 [98], and the recent galaxy clustering and weak lensing measurements from the Dark Energy Survey (DES) [121].

7.1 Modified Growth framework

When describing deviations from GR on large scales, we assume that the Universe is well described by a FRW metric with small perturbations. We adopt the conformal Newtonian gauge (2.139) and consider the perturbations of the energy momentum tensor as given in equations (2.85)-(2.88). Here we denote $v^{(0)} \equiv \theta$ to adapt to the notation in the literature. The energy momentum tensor components evolve according to the conservation equations (2.122), (2.123) that in Newtonian gauge read [284]

$$\dot{\delta} = -(1+w) \left(\theta - 3\dot{\Phi} \right) - 3\mathcal{H} \left(\frac{\delta P}{\delta \rho} - w \right) \delta, \quad (7.1)$$

$$\dot{\theta} = -\mathcal{H}(1-3w)\theta - \frac{\dot{w}}{1+w}\theta + \frac{\delta P/\delta \rho}{1+w}k^2\delta - k^2\sigma + k^2\Psi. \quad (7.2)$$

These equations hold for the combination of all cosmological fluids or for any decoupled subset of fluids such as CDM, the photon-baryon fluid and massive neutrinos after decoupling.

To close the system of equations for cosmological perturbations, one needs two additional equations relating the perturbed energy momentum tensor and the metric potentials Φ and Ψ . In Λ CDM, one can combine the 0_0 Einstein equation (2.115) with the divergence of the Einstein equation 0_i (2.116) to obtain

$$k^2\Phi = -4\pi G a^2 \rho \Delta, \quad (7.3)$$

where Δ is the gauge-invariant density contrast,

$$\rho \Delta \equiv \rho \delta + \frac{3\mathcal{H}}{k^2}(\rho + P)\theta. \quad (7.4)$$

One can also use the traceless part of the i_j Einstein equation (2.118), given in Newtonian gauge by

$$k^2(\Phi - \Psi) = 12\pi G a^2(\rho + P)\sigma, \quad (7.5)$$

and use this to write an equation relating Ψ and Δ :

$$k^2\Psi = -4\pi G a^2 [\rho\Delta + 3(\rho + P)\sigma]. \quad (7.6)$$

Eqs. (7.5) and (7.6), combined with the conservation equations (7.1) and (7.2), are the ones used in the Einstein-Boltzmann solvers such as CAMB and CLASS to compute the cosmological observables.

MGCAMB adopts the (μ, γ) parametrization introduced in Sect. 6.2. In order to have a well defined parametrization at earlier times, when the anisotropic stress from radiation and neutrinos is not negligible the equations (6.10), (6.11) are modified to include the anisotropic stress,

$$k^2\Psi = -4\pi G\mu(a, k)a^2 [\rho\Delta + 3(\rho + P)\sigma], \quad (7.7)$$

$$k^2[\Phi - \gamma(a, k)\Psi] = 12\pi G\mu(a, k)a^2(\rho + P)\sigma. \quad (7.8)$$

Given the form of $\mu(a, k)$ and $\gamma(a, k)$, equations (7.7) and (7.8), along with (7.1) and (7.2), can be used to evolve the system of equations and compute the cosmological observables of interest. Note that $\mu(a, k)$ is introduced as a modification of equation (7.6) that relates Ψ and Δ , instead of (7.3), because matter perturbations respond to the gradients of the Newtonian potential Ψ . This makes μ a parameter that directly controls the strength of the gravitational interaction.

The gravitational slip function γ is not directly related to cosmological observables [241, 242] and, therefore, is generally difficult to constrain without fixing μ or making additional assumptions. Instead, it is often more informative to work with μ paired with function Σ that modifies the relation between the lensing potential ($\Phi + \Psi$) and Δ via

$$k^2(\Phi + \Psi) = -4\pi G\Sigma(a, k)a^2 [2\rho\Delta + 3(\rho + P)\sigma]. \quad (7.9)$$

In the limit of negligible anisotropic stress, Σ is simply related to μ and γ through equation (6.13), $\Sigma = \mu(1 + \gamma)/2$. One can break the degeneracy between μ and Σ and constrain both of them independently by combining data from clustering surveys with measurements of weak lensing [285, 286]. While it might be obvious to many readers, we would still like to note that constraints on μ depend on whether one marginalizes over γ or Σ .

The above-mentioned framework is implemented in MGCAMB, which can be used for two purposes. One can adopt functional forms of μ and γ , or μ and Σ , and fit the function parameters to data to search for any departure from the Λ CDM values of $\mu = \gamma = \Sigma = 1$. One can go even further and reconstruct the functions from the data using the correlated prior approach [287, 288, 289, 290], or the Gaussian Process Reduction [291, 292]. Another way to use MGCAMB is to study predictions of specific theories for certain cosmological observables. This application is limited by the fact that deriving the analytical forms for μ, γ

and Σ in a given theory requires adopting the quasi-static approximation (QSA) [293]. The validity of the QSA depends on the observable and the strength of modifications introduced by the theory on near-horizon scales. As a rule, QSA tends to work in most viable models [245, 293] and thus MGCAMB can be a good starting point for looking at the characteristic observational signatures of a theory.

7.2 The new MGCAMB patch

The set of equations used in the new MGCAMB patch is based on and has a large overlap with the previous versions [37, 243]. However, there are several important differences and, for the sake of completeness, we present the entire formalism.

In CAMB, cosmological perturbations are evolved in synchronous gauge (2.140). The Newtonian gauge potentials Φ and Ψ are related to the synchronous gauge potentials η and h through

$$\Phi = \eta - \mathcal{H}\alpha, \quad (7.10)$$

$$\Psi = \dot{\alpha} + \mathcal{H}\alpha, \quad (7.11)$$

where $\alpha = (\dot{h} + 6\dot{\eta})/2k^2$. The synchronous gauge perturbations of the energy-momentum tensor evolve according to

$$\dot{\delta} = -(1+w) \left(\theta + \frac{\dot{h}}{2} \right) - 3\mathcal{H} \left(\frac{\delta P}{\delta \rho} - w \right) \delta, \quad (7.12)$$

$$\dot{\theta} = -\mathcal{H}(1-3w)\theta - \frac{\dot{w}}{1+w}\theta + \frac{\delta P/\delta \rho}{1+w}k^2\delta - k^2\sigma. \quad (7.13)$$

In order to evolve the perturbations, one needs to compute the quantity \dot{h} , or the quantity \mathcal{Z} defined in CAMB as $\mathcal{Z} \equiv \dot{h}/2k$. In CAMB, this is done using the 0_0 Einstein equation (2.115) in synchronous gauge

$$k^2\eta + k\mathcal{H}\mathcal{Z} = -4\pi G a^2 \rho \delta. \quad (7.14)$$

In MGCAMB, the Einstein equations are modified and, hence, one needs an alternative way to compute \mathcal{Z} . From the definition of α , we have

$$\mathcal{Z} = k\alpha - \frac{3\dot{\eta}}{k}. \quad (7.15)$$

To find α and $\dot{\eta}$, we start by substituting Eqs. (7.10) and (7.11) into the modified Einstein equations (7.7) and (7.8), and combine the resulting equations to write the following expression for α :

$$\alpha = \left\{ \eta + \frac{\mu a^2}{2k^2} [\gamma \rho \Delta + 3(\gamma - 1)(\rho + P)\sigma] \right\} \frac{1}{\mathcal{H}}, \quad (7.16)$$

where we now include the factor $8\pi G$ in the definition of density and pressure, e.g. $8\pi G\rho \rightarrow \rho$. To derive an equation for $\dot{\eta}$, we first rearrange the equation above to solve for η , obtaining

$$\begin{aligned}\eta &= \mathcal{H}\alpha - \frac{\mu a^2}{2k^2} \{\gamma\rho\Delta + 3(\gamma - 1)\rho(1 + w)\sigma\} \\ &= \mathcal{H}\alpha - \frac{\mu a^2}{2k^2} \Gamma,\end{aligned}\tag{7.17}$$

where we defined

$$\Gamma = \gamma\rho\Delta + 3(\gamma - 1)\rho(1 + w)\sigma.\tag{7.18}$$

Next, we would like to differentiate Eq. (7.17) with respect to τ . To compute $(\rho\Delta)'$, we combine the conservation equations (7.12) and (7.13) to obtain

$$(\rho\Delta)' = -3\mathcal{H}\rho\Delta - (1 + w)\rho\theta \left[1 + \frac{3}{k^2}(\mathcal{H}^2 - \dot{\mathcal{H}}) \right] - 3\mathcal{H}\rho(1 + w)\sigma - (1 + w)\rho k\mathcal{Z}.\tag{7.19}$$

Finally, taking the derivative of Eq. (7.17) and using Eqs. (7.15) and (7.19), leaves us with the equation for $\dot{\eta}$:

$$\begin{aligned}\dot{\eta} &= \frac{1}{2} \frac{a^2}{3\rho a^2 \mu \gamma (1 + w) / 2 + k^2} \left\{ \rho(1 + w)\mu\gamma\theta \left[1 + 3\frac{\mathcal{H}^2 - \dot{\mathcal{H}}}{k^2} \right] + 3\mu(1 - \gamma)\rho(1 + w)\dot{\sigma} \right. \\ &\quad + \rho\Delta [\mathcal{H}\mu(\gamma - 1) - \dot{\mu}\gamma - \mu\dot{\gamma}] + k^2\alpha \left[\rho\mu\gamma(1 + w) - 2\left(\frac{\mathcal{H}^2 - \dot{\mathcal{H}}}{a^2} \right) \right] \\ &\quad \left. + 3\mathcal{H}\mu(\gamma - 1)(1 + w)\rho\sigma(3w + 2) - 3(1 + w)\rho\sigma \left[\dot{\mu}(\gamma - 1) - \dot{\gamma}\mu + \mu(1 - \gamma)\frac{\dot{w}}{1 + w} \right] \right\},\end{aligned}\tag{7.20}$$

where we replaced $\dot{\alpha}$ with

$$\dot{\alpha} = \Phi + \Psi - \eta,\tag{7.21}$$

and used the modified Einstein equations to express Φ and Ψ in terms of the energy-momentum perturbations.

Following the notation in CAMB, we introduce fluxes q and the anisotropic stress Π related to the velocity divergence θ and the anisotropic stress σ through

$$(1 + w)\theta = kq, \quad \frac{3}{2}(1 + w)\sigma = \Pi,\tag{7.22}$$

to rewrite the equation for $\dot{\eta}$ as

$$\begin{aligned}
\dot{\eta} = & \frac{1}{2} \frac{a^2}{3\rho a^2 \mu \gamma (1+w)/2 + k^2} \left\{ \rho \mu \gamma k q \left[1 + 3 \frac{\mathcal{H}^2 - \dot{\mathcal{H}}}{k^2} \right] + \rho \Delta [\mathcal{H} \mu (\gamma - 1) - \dot{\mu} \gamma - \mu \dot{\gamma}] \right. \\
& + 2\mu(1-\gamma)\rho\dot{\Pi} + k^2 \alpha \left[\rho \mu \gamma (1+w) - 2 \left(\frac{\mathcal{H}^2 - \dot{\mathcal{H}}}{a^2} \right) \right] \\
& \left. + 2\rho\Pi [\mathcal{H}(\gamma-1)(3w+2)\mu - \dot{\mu}(\gamma-1) - \dot{\gamma}\mu] \right\}. \tag{7.23}
\end{aligned}$$

The background and perturbation variables of energy-momentum appearing in the above equations are sums over the uncoupled fluid components, e.g. $\rho = \rho_{\text{b}+\gamma} + \rho_{\text{CDM}} + \rho_{\nu}$, *etc.*

There are two notable differences between Eq. (7.23) and its counterpart in the previous MGCAMB patch. First, the factor $(3w+2)$ in the last line corrects a typo present in the previous version.² As this correction is proportional to Π , it has a negligible effect at late times when the anisotropic stress is small. More importantly, the pre-factors of α and q are now generalized to allow for an arbitrary expansion history. The expression for $\dot{\eta}$ in the previous version of MGCAMB assumed dark energy with the equation of state $w_{\text{DE}} = -1$.

As in previous versions, the present MGCAMB patch assumes that GR is recovered deep in the radiation era. The code starts with the same initial conditions as CAMB and evolves the original CAMB system of equations up to a certain value of the scale factor, a_{trans} , set by the parameter `GRtrans`. After that, the code evolves the alternative equations described above. Unlike the previous version, the present patch has no restriction on how early the switch can happen, as long as it happens after the time at which the initial conditions are set for the smallest values of k and the phenomenological functions are such that the GR limit is approached continuously.

Computing \mathcal{Z} requires knowing the quantities δ , q , Π and $\dot{\Pi}$, which can be a challenging problem depending on the epoch at which $\dot{\eta}$ is evaluated. For example, at late times, CAMB stops evolving the full set of Boltzmann equations for photons and neutrinos and uses the radiation streaming approximation (RSA) instead [83]. In the RSA, δ_{γ} and δ_{ν} are computed by using approximated versions of \mathcal{Z} and $\dot{\mathcal{Z}}$ that do not include radiation. However, the current CAMB implementation of RSA uses the $\dot{\mathcal{Z}}$ Einstein equation. Since we do not have all the modified Einstein equations, we opt to use the RSA implementation from an older version of CAMB, which did not depend on the $\dot{\mathcal{Z}}$ Einstein equation. For small values of `GRtrans`, in order to preserve the accuracy we had to increase the time at which the RSA is switched on, which slows down MGCAMB with respect to the default CAMB by a factor of two.

²This factor is $(3w)$ in the last term of Eq. (36) of [243].

Before last scattering, CAMB uses a second order tight coupling expansion in which the computation of q_γ and $q_b \equiv v_b$ requires the knowledge of \mathcal{Z} and $\sigma^* \equiv k\alpha$. We resolve this by using the values of these quantities computed at the previous time-step.

In addition to the (μ, γ) parameterization, MGCAMB offers options to work with (μ, Σ) introduced in Sec. 7.1 and the (Q, R) functions of [294]. More details on their implementation are given in Appendix 7.2.4.

7.2.1 Massive Neutrinos

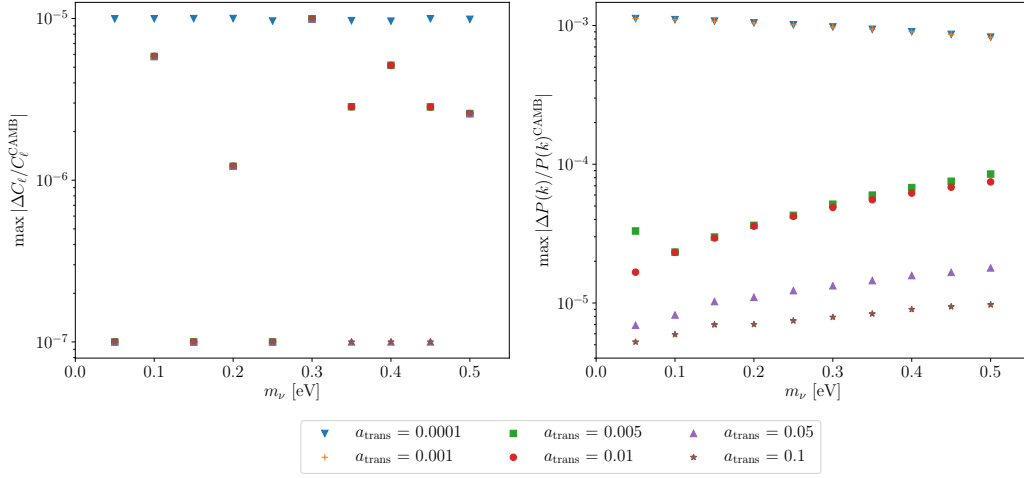


Figure 7.1: Maximum relative difference in C_ℓ^{TT} and $P(k)$ between the GR limit ($\mu = \gamma = 1$) of MGCAMB and standard CAMB for several values of the sum of the neutrino masses and different values of the scale factor at which the modified equations are turned on.

The default CAMB code calculates the quantities $\dot{\Pi}$ after computing \mathcal{Z} . In our case, $\dot{\Pi}$ is required to compute \mathcal{Z} . The computation of $\dot{\Pi}_\gamma$ and $\dot{\Pi}_r$ in the previous versions of MGCAMB ignored the contribution from massive neutrinos. In the current version, we compute $\dot{\Pi}_\nu$ by integrating the neutrinos equations before the computation of \mathcal{Z} . This is safe, since the equations for $\dot{\Pi}_\nu$ do not depend on \mathcal{Z} .

7.2.2 The CMB source function and the weak lensing transfer function

The CMB temperature integral solution (3.58) can be alternatively written as [295]

$$\Theta_\ell(k, \tau_0) = \int_0^{\tau_0} d\tau S_T(k, \tau) j_\ell(k\tau), \quad (7.24)$$

where $S_T(k, \tau)$ is the source term that differs from the three source functions (3.54) $S_{0,1,2}^{(0)}$ simply by integrating by parts and collecting the spherical Bessel function $j_\ell(k\tau)$. In syn-

chronous gauge, the source is

$$S_T(k, \tau) = g \left(\Theta_0 + 2\dot{\alpha} + \frac{\dot{v}_b}{k} + \frac{\Pi^{\text{pol}}}{4} + \frac{3\ddot{\Pi}^{\text{pol}}}{4k^2} \right) + e^{-\kappa}(\dot{\eta} + \ddot{\alpha}) + \dot{g} \left(\alpha + \frac{v_b}{k} + \frac{3\dot{\Pi}^{\text{pol}}}{2k^2} \right) + \frac{3\ddot{g}\Pi^{\text{pol}}}{4k^2}, \quad (7.25)$$

where κ is the optical depth, g is the visibility function and Π^{pol} is the polarization term (3.57). In CAMB, the calculation of the ISW term, $(\dot{\eta} + \ddot{\alpha})$, assumes GR and has to be replaced in MGCAMB. This was already done in the previous versions, but the contribution of massive neutrinos was neglected. We introduce massive neutrinos properly in the current version, using the following prescription. The ISW term can be written as

$$\ddot{\alpha} + \dot{\eta} = \dot{\Phi} + \dot{\Psi}, \quad (7.26)$$

where terms on the right hand side can be computed separately. The first term is determined by taking a derivative of Eq. (7.10), giving

$$\dot{\Phi} = \dot{\eta} - \mathcal{H}(\Psi - \mathcal{H}\alpha) - \dot{\mathcal{H}}\alpha. \quad (7.27)$$

Then, $\dot{\Psi}$ can be obtained by differentiating the modified Poisson equation (7.7),

$$\dot{\Psi} = -\frac{1}{2k^2}\dot{\mu}a^2[\rho\Delta + \rho\Pi] - \frac{1}{2k^2}\mu[(\rho a^2\Delta)^\cdot + 2(\rho a^2\Pi)^\cdot], \quad (7.28)$$

where $(\rho a^2\Delta)^\cdot$ is determined from Eq. (7.19) and

$$(\rho a^2\Pi)^\cdot = \rho a^2\dot{\Pi} - [2\mathcal{H}\rho a^2\Pi + (3P - \rho)a^2\Pi], \quad (7.29)$$

completing the set of required equations in a form suitable for implementation in CAMB.

The last modification concerns the implementation of the weak lensing transfer function, since CAMB assumes GR to calculate the Weyl potential $\Phi_+ \equiv (\Phi + \Psi)/2$. Instead, in MGCAMB, we compute Ψ and Φ from equations (7.7) and (7.8). The Weyl potential is used to compute the lensing correlation functions in the analysis presented in Sect. 7.3.

7.2.3 The GR limit of MGCAMB

We have checked the output of MGCAMB in the GR limit, when $\mu = \gamma = 1$, for a wide range of neutrino masses and values of the scale factor at which modifications are switched on. Fig. 7.1 shows the maximum relative difference in C_ℓ^{TT} and $P(k)$ between CAMB and MGCAMB for $0.05 \text{ eV} \leq \sum m_\nu \leq 0.5 \text{ eV}$ and $0.0001 \leq a_{\text{trans}} \leq 0.1$. In all cases the deviations are below 0.1%. In order to achieve this accuracy for $a_{\text{trans}} < 0.005$, we had to

delay the time at which the RSA in MGCAMB is switched on by a factor of 20, which doubles the running time of the code.

7.2.4 Other parameterizations

The μ, Σ parameterization

As mentioned in Sect. 7.1, rather than working with μ and γ , it can be beneficial to constrain μ and Σ , with the latter defined in Eq. (7.9). In this version of MGCAMB, we implement (μ, Σ) by mapping it onto (μ, γ) using $\gamma = 2\Sigma - \mu$, which agrees with Eq. (7.9) in the limit of negligible anisotropic stress ($\sigma \rightarrow 0$). In other words, we *define* Σ as

$$\Sigma = \frac{1}{2}\mu(1 + \gamma). \quad (7.30)$$

The circumstances in which the difference between this definition and the one in Eq. (7.9) can be important are not entirely clear to us. If necessary, it is relatively easy to add to MGCAMB a separate set of equations for the (μ, Σ) parameterization based on Eq. (7.9).

The Q, R parameterization

Another phenomenological parameterization was introduced in [294] in which modifications of gravity are encoded in functions Q and R defined through

$$k^2\Phi = -4\pi G a^2 Q \rho \Delta, \quad (7.31)$$

$$k^2(\Psi - R\Phi) = -12\pi G Q a^2(\rho + P)\sigma. \quad (7.32)$$

This parameterization is consistently implemented in MGCAMB. The corresponding equation for $\dot{\eta}$ is

$$\begin{aligned} \dot{\eta} = \frac{1}{2} \frac{1}{\frac{3}{2} Q a^2 \rho (1+w) + k^2} & \left\{ Q k \rho q \left(1 + \frac{3}{k^2} (\mathcal{H}^2 - \dot{\mathcal{H}}) \right) \right. \\ & \left. + \rho \Delta \left(\mathcal{H} Q (1-R) - \dot{Q} \right) + k^2 \alpha \left(Q \rho (1+w) - 2 \frac{\mathcal{H}^2 - \dot{\mathcal{H}}}{a^2} \right) \right\}, \end{aligned} \quad (7.33)$$

where the factor of $8\pi G$ is absorbed into ρ and P . For the ISW effect, we replace Eq. (7.28) with

$$\dot{\Psi} = R\dot{\Phi} + \dot{R}\Phi - \frac{\dot{Q}\rho a^2\Pi}{k^2} - \frac{Q(\rho a^2\Pi)}{k^2}. \quad (7.34)$$

7.3 Joint constraints on modified growth, massive neutrinos and the dark energy equation of state

The MGCAMB patch has been implemented in the Markov Chain Monte Carlo (MCMC) engine CosmoMC [145, 296], and is called MGCosmoMC.³ To demonstrate its use, we derive joint constraints of massive neutrinos, modified growth, and the DE equation of state from the datasets included in the current version of CosmoMC. We consider three models: Λ CDM with the sum of neutrino masses $\sum m_\nu$ as an additional parameter (hereafter referred to as Model 0), a model with μ and γ varied along with $\sum m_\nu$ and Λ playing the role of dark energy (Model 1), and a model with the DE equation of state varying in addition to $\sum m_\nu$, μ and γ (Model 2).

In Models 1 and 2, we adopt the (μ, γ) parameterization used by the Planck collaboration [11, 297], *i.e.*

$$\mu(a) = 1 + E_{11}\Omega_{\text{DE}}(a), \quad (7.35)$$

$$\gamma(a) = 1 + E_{21}\Omega_{\text{DE}}(a), \quad (7.36)$$

where $\Omega_{\text{DE}}(a) = \rho_{\text{DE}}/\rho_{\text{tot}}$. We present the results in terms of the derived quantities $\mu_0 \equiv \mu(a=1)$, $\gamma_0 \equiv \gamma(a=1)$ and $\Sigma_0 \equiv \mu_0(1 + \gamma_0)/2$. In Model 2, we adopt the CPL parameterization [298, 299] of the DE equation of state,

$$w_{\text{DE}}(a) = w_0 + (1 - a)w_a. \quad (7.37)$$

In all cases, we also varied the six “vanilla” Λ CDM parameters, running four parallel chains until the Gelman/Rubin convergence statistics reached $R < 0.01$.

7.3.1 The datasets

Our analysis made use of the Planck CMB temperature and polarization anisotropy spectra in combination with other datasets. Although the 2018 results were recently released [11], the latest Planck likelihood code was not available at the time of writing, so we used the 2015 version [211]. Specifically, we used the Planck 2015 TT, TE and EE likelihood for multipoles in the range $30 \leq \ell \leq 2508$ along with the lowTEB polarization likelihood for multipoles in the range $2 \leq \ell \leq 29$. We also used the Planck CMB lensing measurements from the minimum variance combination of temperature and polarization with the conservative cut of $40 \leq \ell < 400$.⁴

³Available at <https://github.com/sfu-cosmo/MGCosmoMC>

⁴We use the files `smicadx12_Dec5_ft1_mv2_ndclpp_p_teb_consext8`

We have combined CMB data with the Type Ia supernovae luminosity distance measurements from JLA [87], the BAO measurements from the 6dF galaxy survey [96] (at $z = 0.106$), the SDSS DR7 Main Galaxy Sample (MGS) [97] (at $z = 0.15$), the measurements of the Hubble parameter $H(z_i)$, the angular-diameter distance $d_A(z_i)$ and the redshift space distortion measurements of $f(z_i)\sigma_8(z_i)$ at $z_i = \{0.38, 0.51, 0.61\}$ provided by the BOSS DR12 [98]. As usually done in the literature, we assumed that the 6dF and MGS measurements are independent from BOSS DR12.

We have also used the recent galaxy clustering and weak lensing measurements from the DES Year 1 results [121]. This dataset consists of the measurements of the angular two-point correlation functions of galaxy clustering, cosmic shear and galaxy-galaxy lensing in a set of 20 logarithmic bins of angular separation in the range $2.5' - 250'$. Since the MG formalism has no nonlinear prescription for structure formation, the angular separations probing the nonlinear scales were properly removed. To do so, we adopted the same method as in [300] and used the “standard” data DES cutoff as described in Appendix A. Moreover, we modified the DES likelihood code in order to compute the theoretical predictions of the cosmic shear and the galaxy-galaxy lensing correlation functions using the Weyl potential $k^2\Phi_+$ instead of using the GR approximation $k^2\Phi_+ = k^2\Phi = -(3/2)\Omega_m H_0^2 a^{-1} \delta_m$, as described in Appendix B. Finally, the covariance between the DES data and the 6dF, MGS and BOSS measurements is ignored, as the observations are carried on different sky patches [300].

7.3.2 The GR limit consistency check

Parameter	CosmoMC	MG ($a_{\text{trans}} = 0.01$)	MG ($a_{\text{trans}} = 0.001$)
ω_b	0.02237 ± 0.00014	0.02237 ± 0.00014	0.02237 ± 0.00014
ω_c	0.1178 ± 0.0011	0.1178 ± 0.0011	0.1178 ± 0.0011
$100\theta_{\text{MC}}$	1.04095 ± 0.00030	1.0410 ± 0.0003	1.04095 ± 0.00030
τ	0.076 ± 0.015	0.075 ± 0.015	0.075 ± 0.015
$\sum m_\nu$ (95 % CL)	< 0.206 eV	< 0.198 eV	< 0.212 eV
n_s	0.9684 ± 0.0042	0.9684 ± 0.0042	0.9684 ± 0.0042
$\ln(10^{10} A_s)$	3.080 ± 0.028	3.079 ± 0.027	3.080 ± 0.029
Best fit: $-\log(\text{Like})$	7098.93	7098.90	7098.98

Table 7.1: The 68 % CL uncertainties and best fit values of parameters obtained using the original CosmoMC, compared to the results from the GR limit of MGCosmoMC for two different values of a_{trans} which sets the scale factor beyond which the modified set of equations is evolved. The bound on the net mass of neutrinos is at the 95% CL.

To assess the impact of the small systematic errors introduced by the approximations used in MGCAMB, we performed a consistency check of the GR limit of MGCosmoMC by comparing the results of three MCMC runs: 1) using the original CosmoMC code, 2) using MGCosmoMC with $\mu = \gamma = 1$ and $a_{\text{trans}} = 0.01$ and 3) using MGCosmoMC with $\mu = \gamma = 1$ and $a_{\text{trans}} = 0.001$. In all runs, we varied the six vanilla Λ CDM parameters and

the mass of neutrinos. The results are summarized in Table 7.1. We can see that the best fit values and the confidence intervals for cosmological parameters are practically the same in all cases and, hence, the results are consistent.

7.3.3 Results

Parameter	Model 0	Model 1	Model 2
ω_b	0.02237 ± 0.00014	0.02239 ± 0.00014	0.02231 ± 0.00016
ω_c	0.1178 ± 0.0011	0.1175 ± 0.0011	0.1183 ± 0.0013
$100 \theta_{\text{MC}}$	1.0409 ± 0.0003	1.0410 ± 0.0003	1.0408 ± 0.0003
τ	0.075 ± 0.015	0.067 ± 0.017	0.072 ± 0.018
n_s	0.969 ± 0.004	0.969 ± 0.004	0.967 ± 0.005
$\ln(10^{10} A_s)$	3.08 ± 0.03	3.06 ± 0.03	3.07 ± 0.03
$\sum m_\nu$ (95 % CL)	< 0.21 eV	< 0.24 eV	< 0.49 eV
$\mu_0 - 1$	0	-0.09 ± 0.30	-0.07 ± 0.29
$\gamma_0 - 1$	0	0.46 ± 0.79	0.43 ± 0.77
$\Sigma_0 - 1$	0	0.01 ± 0.06	0.02 ± 0.07
w_0	-1	-1	-0.84 ± 0.13
w_a	0	0	-0.48 ± 0.36
χ^2	7098.93	7097.62	7097.72
$\Delta\chi^2$	-	-1.31	-1.21

Table 7.2: The 68 % CL uncertainties and best fit values of parameters constrained using MGCosmoMC. The bound on the net mass of neutrinos is at the 95% CL. Model 0 corresponds to Λ CDM with massive neutrinos. Model 1, in addition, includes modified growth on the Λ CDM background, while Model 2 adds a varying DE equation of state using the CPL parameterization. We can see that the CPL parametrization does not improve the fit of the model.

The joint constraints derived on massive neutrinos, modified growth and the DE equation of state are summarized in Table 7.2 for Models 0, 1 and 2 defined at the beginning of this Section. For Models 1 and 2 we used $a_{\text{trans}} = 0.001$. Also, Fig. 7.2 shows the marginalized distributions of the relevant parameters, with their Λ CDM limits shown with dashed grey lines. We find the 95% CL bound on massive neutrinos to be

$$\begin{aligned} \sum m_\nu &< 0.21 \text{ eV}, & \text{Model 0,} \\ \sum m_\nu &< 0.24 \text{ eV}, & \text{Model 1,} \\ \sum m_\nu &< 0.49 \text{ eV}, & \text{Model 2.} \end{aligned}$$

Our bound on the neutrino mass for Model 0 is comparable to the DES Year 1 result of 0.29 eV at 95% CL [121]. The use of the CMB polarization data at high- ℓ in our analysis is the reason for the stronger constraint.

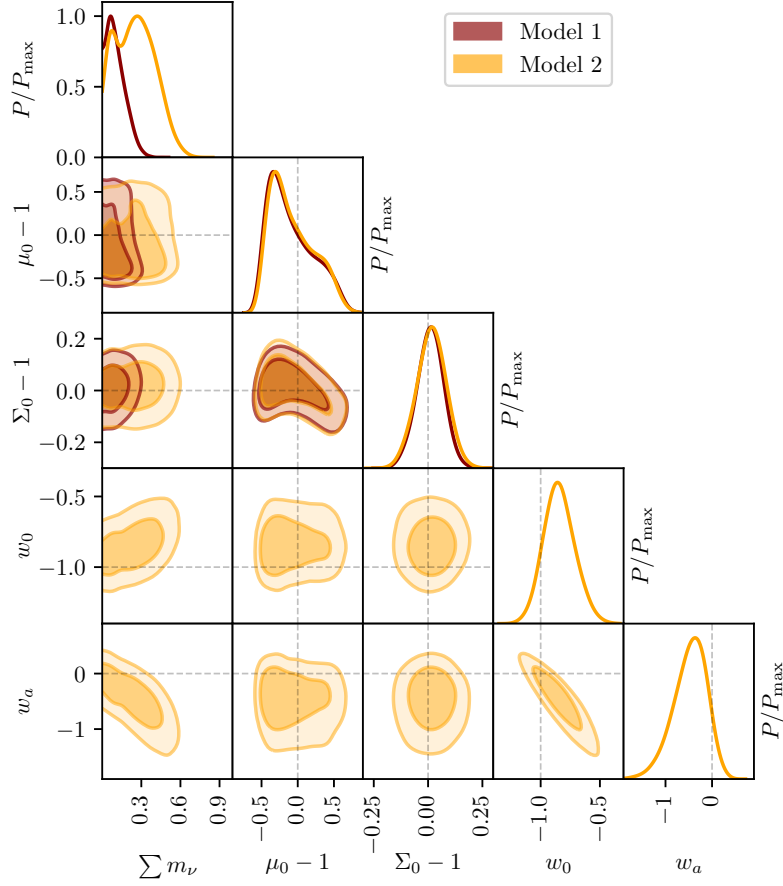


Figure 7.2: The marginalized joint posterior distribution of the Model 1 and Model 2 parameters. The plots along the diagonal show the marginalized posterior distribution of each parameter. The grey dashed lines indicate the Λ CDM limit values of the additional parameters. The darker and lighter shades correspond to the 68% and the 95% CL, respectively.

In Model 1, the effective (cosmological) Newton’s constant can vary at late times. Such variation can happen, for example, in scalar-tensor theories of gravity, where it would generally be scale-dependent. In such theories, the extra Yukawa force mediated by the scalar gravitational degree of freedom enhances the structure formation at scales below the Compton wavelength of the scalar field, which could negate the free streaming suppression of structure formation due to the non-zero neutrino mass. Since in our analysis we considered a scale-independent parameterization of μ, γ , this degeneracy between $\sum m_\nu$ and $\mu_0 - 1$ is not present and the constraint on $\sum m_\nu$ is comparable to the one in Model 0.

In Model 2, μ is also scale-independent, however the DE density is time-dependent and the degeneracy between the dynamics of DE and the neutrino mass weakens the constraints on $\sum m_\nu$. The degeneracy between the neutrino mass and the CPL parameters w_0 and w_a is evident from Fig. 7.2. The 95% C.L. bounds on the modified growth parameters are consistent with the Λ CDM limit and with the results obtained by DES [300]. Note that, as

expected, the bounds on γ_0 are generally weaker than those on μ_0 and Σ_0 , because there is no observable that can cleanly separate its effect from the latter two. Our constraints on the variation in the DE equation of state also indicate a good agreement with the Λ CDM model.

The analysis presented in this Section illustrates how the new MGCAMB patch allows one to derive simultaneous constraints on the neutrino mass, MG and the DE equation of state. The new patch also makes it easy to implement alternative parameterizations of the MG functions and the DE equation of state.

7.4 Discussion

In this Chapter we presented a significant update of MGCAMB that features a consistent implementation of massive neutrinos and dynamical dark energy, as well as a new structure that renders the implementation of custom models easier. The new version also has no restriction on the value of the transition time at which the modifications to the linearized Einstein equations are switched on.

MGCAMB was the first publicly released modified Boltzmann solver for cosmological tests of gravity. Since its introduction in 2008 [37], MGCAMB has been used in over 100 works. A number of other codes have been introduced since, most notably ISiTGR [301], EFTCAMB [237, 238] and hi_class [302]. Of them, ISiTGR is close to MGCAMB in its spirit, also introducing phenomenological modifications of equations of motion using the two functions Q and R defined in Sect. 7.2.4. EFTCAMB is based on the effective description of the background and perturbations solutions in general scalar-tensor theories [34, 235, 303] as described in Sect. 6.2, while hi_class uses an alternative effective description of perturbations in scalar-tensor theories on a fixed background [236].

MGCAMB is best suited for model-independent constraints on μ and Σ , sometimes referred to as G_{matter} and G_{light} , which are closely related to observables. The choice of the parameterized forms of μ and Σ can be informed by the QSA limit of particular types of modified gravity theories [304]. One can also perform non-parametric reconstructions of μ and Σ aided by a prior covariance derived from ensembles of modified gravity theories. Such priors can be obtained with the help of EFTCAMB as in Ref. [283].

With the present update, MGCAMB should remain a useful tool for cosmological tests of gravity, offering accuracy appropriate for data expected from the next generation surveys such as Euclid [305] and LSST [306].

Chapter 8

Dynamical DE and Scalar-Tensor Gravity

So far we have considered MG as a model of DE only for theoretical reasons. In Chapter 6 we analysed models with the same expansion history of the Λ CDM model, while in Chapter 7 we only used a simple dynamical DE model in the new MGCAMB patch to show the new feature. However, reasons to consider dynamical DE energy are not only appealing to theorists. With the recent data becoming more accurate, several 2-3 σ “tensions” began arising when interpreting observations within the Λ CDM model. For instance, the value of the Hubble constant H_0 inferred by the CMB measurements from the Planck satellite [10] differs from the value inferred by “local” measurements [307] by about 3.4 σ - a problem known as “the H_0 tension” - with the most recent measurements pushing this discrepancy to 4.4 σ [308]. Likewise, the value of σ_8 ¹ as inferred from local and cosmological measurements differs by about 2 σ [121].

Although these tensions might just be due to unaccounted systematics effects or perhaps to statistical fluctuations [309], it has been shown that they could be relieved if the DE density evolved with time [13]. Moreover, the data shows a preference for an *increasing* DE density, with an equation of state w_{DE} crossing the so-called phantom divide of -1 . Such dynamics cannot be explained by a minimally coupled quintessence field DE, but can happen in more general scalar-tensor theories of gravity. Also, within these extensions, using the effective DE equation of state as a parameter might not be ideal as these theories can effectively violate $\rho_{\text{DE}}^{\text{eff}} < 0$. This does not violate any energy conditions as DE in this context is just an effective quantity that enters the Friedmann equation.

In [310] we performed a non-parametric reconstruction of the effective DE density $\rho_{\text{DE}}^{\text{eff}} < 0$ and confirmed that there is a slight preference for an increasing DE over time. We summarize that work in Sect. 8.1. In principle the observed increasing DE should affect the

¹ σ_8 is defined as the variance of the (linear) density field, in randomly placed spheres of radii 8 Mpc, see e.g. [84]

ISW signal in the CMB temperature anisotropies (3.66), because the potentials Φ and Ψ would evolve differently w.r.t the Λ CDM model. However, modelling the ISW contribution requires a choice of a model in order to evolve the perturbations. In this Chapter we choose the class of Generalized Brans-Dicke models introduced in Chapter 6 and reconstruct their potential from the observed expansion history. Since the dynamics of GBD theories both at background and perturbed level is encoded in the background EFT functions², this allows us to properly evolve the perturbations equations and evaluate the viability of the reconstructed theories. By construction these theories fit the observed expansion history of the Universe but can still have alternative evolution of the perturbations.

8.1 The Reconstruction of the DE density

In [310] we performed a Bayesian, non-parametric reconstruction of the Dark Energy density, using only background observables. Here we summarize the correlated prior method for the DE density reconstruction procedure and the observables used in the analysis. The datasets included the CMB distance priors, the ‘‘Joint Light-curve Analysis’’ [87], the BAO distance measurements from i) the 6dF Galaxy Survey [96], ii) SDSS DR7 Main Galaxy Sample [97], iii) the tomographic BOSS DR12 [311, 312], (iv) eBOSS DR14 quasar sample [100], v) the Lyman- α forest of BOSS DR11 quasars [99, 313], the Hubble parameter H_0 from [307] and from the Observational Hubble parameters Data [314].

The effective DE energy density is modelled through the Friedmann equation

$$H^2 = H_0^2 (E_m + \Omega_\Lambda X(a)). \quad (8.1)$$

where $E_m \equiv \sum_i \rho_i(a)/\rho_{\text{crit}}^0$ includes all the matter fields, baryons, CDM, radiation and neutrinos and $X(a) \equiv \rho_{\text{DE}}^{\text{eff}}(a)/\rho_{\text{DE}}^{\text{eff}}(a=1)$ denotes the contributions to the standard Friedmann equation from any other terms than the usual matter and radiation. Since the impact of different DE/MG models differs at the perturbative level, using only the cosmological background observables allows us to obtain a model independent reconstruction of the DE density. The goal of the DE density reconstruction is to obtain the function $X(a)$ from the data. We assume that $X(a)$ is a Gaussian random variable whose distribution is determined by the correlation function

$$\langle [X(a) - X^{\text{fid}}(a)] [X(a') - X^{\text{fid}}(a')] \rangle = \xi_{\bar{X}}(|a - a'|), \quad (8.2)$$

where $X^{\text{fid}}(a)$ is a fiducial model, chosen to be the Λ CDM in our case, i.e. $X^{\text{fid}}(a) \equiv 1$. For the correlation function $\xi_{\bar{X}}(|a - a'|)$ we use the time-translation invariant CPZ form

²The second order EFT functions for GBD all vanish, $\gamma_i = 0$, $i = 1, \dots, 6$.

[239, 240],

$$\xi_{\bar{X}}(|a - a'|) = \frac{\xi(0)}{1 + (|a - a'|/a_c)^2}, \quad (8.3)$$

where a_c determines the correlation length and $\xi(0)$ sets the strength of the prior. $\xi(0)$ is related to the expected variance of the mean $\sigma_{\bar{X}}^2$ through $\sigma_{\bar{X}}^2 \simeq \pi\xi(0)a_c/(a_{\max} - a_{\min})$. The function $X(a)$ is then binned in a vector $\mathbf{X} \equiv (X_1, \dots, X_N)$ where $X_i = (1/\Delta) \int_{a_i}^{a_i+\Delta} da X(a)$. Here, a_i is the scale factor of the i -th bin and Δ is the width of the bin. In [310] $N = 40$ and the bins are uniformly distributed in the interval $a_i \in [0.001, 1]$. In absence of the correlation function $\xi_{\bar{X}}$, the 40 bins would be independent of each other and the uncertainties in the reconstruction would become so large as to make the reconstruction program useless. Moreover, a physical DE density at a time a would necessarily show a correlation with its previous values and enforcing equation (8.2) helps guaranteeing this physical condition. Furthermore, it suppresses the unavoidable oscillations induced by the statistical fluctuations in the data. This is similar to the approach often used by the machine learning community, a correlation function such as (8.2) is used to impose a regularization on the model to prevent overfitting. Then the cross validation (CV) is performed on the two parameters that control the ‘‘regularizer’’ $\xi_{\bar{X}}$ to improve the predictability of the model.

The Gaussian prior distribution assumes the form

$$\mathcal{P}_{\text{prior}}(\mathbf{X}) \propto \exp \left[-(\mathbf{X} - \mathbf{X}^{\text{fid}})^T \mathbf{C}^{-1} (\mathbf{X} - \mathbf{X}^{\text{fid}}) / 2 \right] \quad (8.4)$$

where \mathbf{C} is the correlation matrix to be calculated using the CPZ form. The reconstructed \mathbf{X} is the one that maximizes the posterior probability,

$$\mathcal{P}(\mathbf{X}|\mathbf{D}) \propto \mathcal{L}(\mathbf{D}|\mathbf{X}) \mathcal{P}_{\text{prior}}(\mathbf{X}), \quad (8.5)$$

where $\mathcal{L}(\mathbf{D}|\mathbf{X})$ is the likelihood function. The effect of the prior is to introduce another contribution on the total χ^2 , given by

$$\chi_{\text{tot}}^2 = \chi_{\text{data}}^2 + \chi_{\text{prior}}^2, \quad (8.6)$$

where

$$\chi_{\text{prior}}^2 = (\mathbf{X} - \mathbf{X}^{\text{fid}})^T \mathbf{C}^{-1} (\mathbf{X} - \mathbf{X}^{\text{fid}}). \quad (8.7)$$

A *weak* prior will have large $\xi(0)$ and a small a_c , effectively correlating values of $X(a)$ in a narrower interval, allowing for more oscillations/noise in the reconstructed $X(a)$. Conversely, a *strong* prior has smaller $\xi(0)$ and a larger a_c . Such a prior correlates $X(a)$ on larger time-scales and effectively smoothen the reconstructed dark energy density. In [310] the best-fit DE reconstruction reduced the χ -squared by 13.9 compared to the best-fit Λ CDM model. However, given the larger amount of parameters in the $X(a)$ reconstruction, a more fair model comparison involves the evaluation of the Bayes factor. In the best case, the Bayes

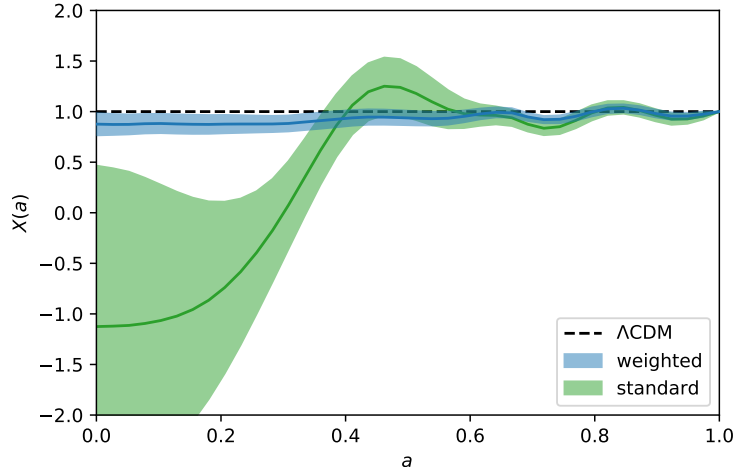


Figure 8.1: Reconstructions of the DE fractional density $X(a)$. The green line (and its shaded regions) denote our “standard” reconstruction using a prior $\sigma_{\bar{X}} = 0.04$ and a correlation scale $a_c = 0.06$. The blue reconstruction denote the evidence weighted reconstruction. In both cases the shaded regions denote the 1σ (68% C.L.) intervals. Finally, for comparison, we highlighted the Λ CDM scenario with the black dashed line.

factor - defined as the logarithm of the ratio of the Bayesian evidences - was 0.77 ± 0.28 , meaning a very weak evidence for dynamical DE.

In Fig. 8.1 we show the DE density reconstruction performed with our “standard” choice of prior, $\sigma_{\bar{X}} \equiv 0.04$, $a_c = 0.06$ (coloured in green) and the evidence weighted reconstruction (coloured in blue). The latter is obtained by linearly combining reconstructions with different Δ_X weighted by the Bayesian evidence. Here Δ_X denotes the width of the uniform prior of the bins X_i . The shaded regions denote the 1σ confidence level. It is important to notice how the model are still compatible with the Λ CDM model, denoted with the black dashed line, at 2σ level.

8.2 Dynamical DE and GBD theories

Although the evidence for dynamical DE is rather weak, incoming new data might strengthen this hypothesis. Non-trivial features in the DE density profile such as the ones present in the reconstruction shown in Fig. 8.1 motivate us to consider more complex gravity theories. In the remainder of this Chapter, we explore this possibility and focus on the class of the GBD theories of gravity. We already worked with GBD theories in Chapter 6, where we explored the parameter space of some specific models in the GBD class. In those models, we assumed that the background field φ was “sitting” at the minimum of the effective potential, so that the effective DE density was basically behaving like the cosmological constant. In this Chapter we adopt a different approach. We do not assume any specific form of the GBD potential, but rather we want to infer it from the observed expansion history of the

Universe. Such theories can “naturally” give rise to the observed ghostly behaviour of the effective DE density. It is important to stress the fact that such phantom DE dynamics is only apparent and no ghost instabilities are generated in GBD theories. For clarity, we rewrite the GBD action (6.14) here as [315, 316, 317]

$$S = \int d^4x \sqrt{-g} \left[\frac{m_0^2}{2} F(\phi) R - \frac{1}{2} K(\phi) (\partial\phi)^2 - U(\phi) \right] + S_m[g_{\mu\nu}, \psi_i], \quad (8.8)$$

where we now denote the extra scalar degree of freedom as ϕ and $K(\phi)$ is the kinetic coupling function. One can always set $K(\phi) \equiv 1$ by a redefinition of the scalar field ϕ , as we will do in what follows. The modified Einstein equations are obtained by varying the action w.r.t. the metric $g_{\mu\nu}$,

$$FG_{\mu\nu} = \frac{1}{m_0^2} (T_{\mu\nu}^m + T_{\mu\nu}^\phi) + \nabla_\mu \nabla_\nu F - g_{\mu\nu} \square F, \quad (8.9)$$

where ∇_μ denotes the covariant derivative w.r.t. the coordinate x^μ , $\square \equiv g^{\mu\nu} \nabla_\mu \nabla_\nu$, $T_{\mu\nu}^m$ is the matter energy-momentum tensor and

$$T_{\mu\nu}^\phi \equiv \partial_\mu \phi \partial_\nu \phi - g_{\mu\nu} \left[\frac{1}{2} \partial_\alpha \phi \partial^\alpha \phi + U(\phi) \right]. \quad (8.10)$$

The equation for the scalar field ϕ is then obtained by extremizing the action (8.8) w.r.t. the changes in the field ϕ ,

$$\square \phi = U_\phi - \frac{m_0^2}{2} F_\phi R, \quad (8.11)$$

where the subscript ϕ denotes a derivative w.r.t. ϕ . For convenience, we rescale field $\phi \rightarrow \phi/m_0$ to make it dimensionless, and the potential $U \rightarrow U/m_0^2$ to have it in CAMB units [81] of Mpc^{-2} .

The freedom in choosing the two functions $F(\phi)$ and $U(\phi)$ translates in the ability of GBD theories to reproduce any expansion history. This idea was explored in [318, 319, 320] where an attempt of reconstructing the scalar-tensor Lagrangian, *i.e.* the two functions F and U , was performed using the Hubble parameter $H(z)$ inferred from the supernovae dataset available at that time. In these works, the reason to consider scalar-tensor theories of gravity was similar to our motivations here, that the supernovae dataset at that time showed a preference for an effective phantom DE equation of state, $w_{\text{DE}} < -1$. The full Lagrangian reconstruction however required the knowledge of the growth of the density perturbation $\delta(z)$. An interesting example is given in $f(R)$ gravity where the only unknown function is the function f itself and the full reconstruction can be done with the sole knowledge of the expansion history $H(a)$ [321].

In the present work we adopt a slightly different approach. Since the growth of perturbations is rather complicated to parametrize due to observational and theoretical limitations (redshift-space distortions, scale dependence in the case of scalar-tensor gravity etc), we can

reconstruct only one of the two functions $U(\phi)$ and $F(\phi)$ from the expansion history, while the other function is chosen to have a preferred behaviour. Here we choose to parametrize the coupling function $F(\phi)$ since its functional form is usually suggested by some high-energy theory. Such a reconstruction, which we call “designer GBD”, can also be performed to find $F(\phi)$ for a given $U(\phi)$.

We will parametrize the coupling function $F(\phi)$ in two different ways: via its functional form, for example choosing $F(\phi) = \exp(\phi)$, and via its time dependence, $F(a)$. We consider the two cases separately.

8.3 Designer GBD from $F(\phi)$

We begin with the first option, *i.e.* assuming a functional form for $F(\phi)$. We use a coupling function

$$F(\phi) = \exp(\xi\phi), \quad (8.12)$$

where the dimensionless parameter ξ controls the coupling strength. As we will show later, Assuming a functional form for the coupling function $F(\phi)$ has the advantage that it allows to follow the dynamics of the background field $\phi(a)$ and guarantees that the reconstructed theory is free from ghost and gradient instabilities. That there are no ghost instabilities in this approach should be evident because the kinetic energy terms remain positive. We begin by writing the Friedmann equations in a FLRW background in such a way that they only include derivatives of the coupling function w.r.t the scalar field ϕ ,

$$\mathcal{H}^2 = \frac{1}{\mathcal{D}} \frac{\rho a^2}{3m_0^2} + \frac{1}{\mathcal{D}} \frac{U a^2}{3}, \quad (8.13)$$

$$\mathcal{G} \frac{\ddot{a}}{a} = 2\mathcal{D}\mathcal{H}^2 - \frac{a^2\mathcal{H}^2}{2} \left(\frac{1}{3} + F_{\phi\phi} \right) (\phi')^2 - \frac{1}{2} \frac{(\rho + P)a^2}{m_0^2} - \frac{1}{2} F_{\phi} a^2 \mathcal{H}^2 \phi'' \quad (8.14)$$

where

$$\mathcal{D} = F - \frac{1}{6} a^2 (\phi')^2 + a F_{\phi} \phi', \quad (8.15)$$

$$\mathcal{G} = F + \frac{1}{2} a F_{\phi} \phi', \quad (8.16)$$

and $' \equiv \partial_a$. The background equation for ϕ becomes

$$\phi'' = - \left(\frac{\ddot{a}}{a^2 \mathcal{H}^2} + \frac{2}{a} \right) \phi' - \frac{1}{\mathcal{H}^2} U_{\phi} + \frac{3\ddot{a}}{\mathcal{H}^2 a^3} F_{\phi}. \quad (8.17)$$

Comparing the Friedmann equation (8.13) with the equation (8.1) we obtain an expression for the effective DE in GBD theories,

$$\frac{\rho_{\text{DE}}^{\text{eff}} a^2}{3m_0^2} \equiv \left(\frac{1}{\mathcal{D}} - 1 \right) \frac{\rho a^2}{3m_0^2} + \frac{1}{\mathcal{D}} \frac{U a^2}{3}. \quad (8.18)$$

The potential U at each time can be reconstructed using the Friedmann equation (8.13). However, this requires the knowledge of the dynamics of the field ϕ in order to determine the denominator \mathcal{D} . Hence we seek an equation for the scalar ϕ that does not contain the potential U and its derivatives. The required equation can be obtained combining the two Friedmann equations (8.13) and (8.14) in order to eliminate the dependence on the unknown $U(\phi)$. Using the e -fold number $N = \ln a$ as a time variable we obtain

$$\begin{aligned} \phi'' = & -\frac{1 + F_{\phi\phi}(\phi')^2}{F_{\phi}} \\ & + \left(1 + \frac{1}{2} \frac{3E_m + 4E_r - E'_\nu - \Omega_\Lambda X'}{E_m + E_r + E_\nu + \Omega_\Lambda X}\right) \phi' \\ & + \frac{1}{F_{\phi}} \frac{(F - 1)(3E_m + 4E_r - E'_\nu) - F\Omega_\Lambda X'}{E_m + E_r + E_\nu + \Omega_\Lambda X}, \end{aligned} \quad (8.19)$$

where now $'$ denotes derivatives w.r.t. $\ln a$, $E_m \equiv \rho_m/\rho_{\text{crit}}^0$ includes CDM and baryons, $E_r \equiv \rho_r/\rho_{\text{crit}}^0$ includes photons and massless neutrinos and $E_\nu \equiv \rho_\nu/\rho_{\text{crit}}^0$ includes massive neutrinos species only. As stated above, this equation can be solved once we fix the functional form of $F(\phi)$ and the background dark energy density $X(a)$. In the following we will solve the equation (8.19) using the exponential coupling (8.12) and the reconstructed fractional dark energy densities $X(a)$ obtained in [310].

8.3.1 Parameter space

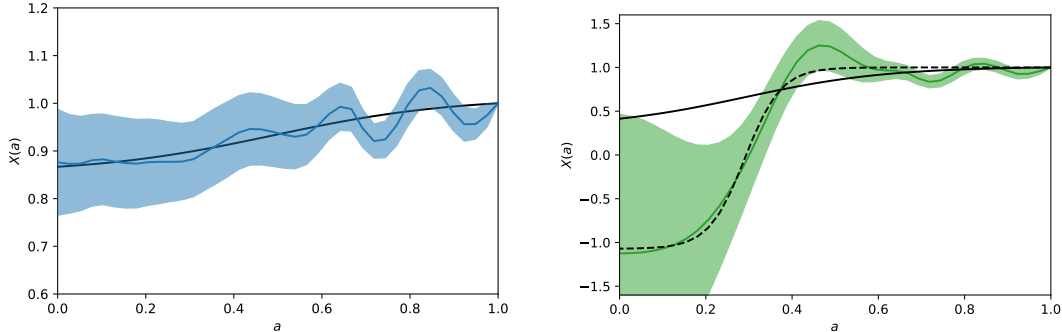


Figure 8.2: Hyperbolic tangent fits to the reconstructions of $X(a)$. On the left panel we show the weighted reconstruction with its 1σ confidence level and its tanh fitting function in black (hereafter X1). On the right panel we show the standard reconstruction with and in the dashed black line its tanh fitting function. The solid black line on the right panel denotes an alternative form of $X(a)$ (hereafter X2) used in the reconstruction of the GBD theories.

Solving equation (8.19) requires setting the initial value of the field, ϕ_{ini} and its derivative ϕ'_{ini} at an initial time a_{ini} . Along with the coupling constant ξ , the theory has four free parameters that have to be adjusted. However, if we assume that gravity on large scales

is close to GR at early times, say until a_{ini} , the coupling function must be equal to unity, $F(\phi) = 1$, until a_{ini} . For $F(\phi) = \exp(\xi\phi)$ this means that the parameter space is reduced at early times as we only consider $\phi_{\text{ini}} \equiv 0$. Moreover, if we wish to explain the features in the DE density reconstruction as arising from the dynamics of the field ϕ , then we need to require that the initial scale factor of the reconstruction is set at a time $a_{\text{ini}} \lesssim 0.1$.

We explore the remaining three-dimensional parameter space checking whether the equation (8.19) has a solution. We also impose additional constraints on the parameter space: first, in order to satisfy observational constraints from Big Bang Nucleo-synthesis (BBN) on the variation of the Newton's constant, $\Delta G_N \lesssim 10\%$, we have to restrict the variations of the coupling function $F(\phi)$ to be less than 10 % as well. Ghost and gradient instabilities, that are usually plaguing effective theories of gravity, are not triggered as the reconstruction described above follows the dynamic of a perfectly healthy theory. There is however an additional constraint that we have to impose on the parameter space and concerns the perturbations. Since in the following sections we will analyse the perturbations of the reconstructed GBD theories, we have to require the perturbations to be stable in the sense that we shall now describe. We consider small perturbations about the FRLW background, with φ denoting a Fourier mode of the perturbation about the background field ϕ . The equation for the mode φ has the following form

$$A\ddot{\varphi} + B\dot{\varphi} + (C + k^2D)\varphi + H_0E = 0, \quad (8.20)$$

where the coefficients A, \dots, E are time-dependent functions. The coefficients A, \dots, E , given by the equations (C.1) - (C.5), can be calculated from the background quantities ϕ , $F(\phi(a))$ and $U(\phi(a))$ ³. The potential $U(\phi)$ is obtained algebraically from the Friedmann equation (8.13),

$$Ua^2 = 3\mathcal{D}H_0^2a^2(E_m + E_r + E_\nu + \Omega_\Lambda X) - 3H_0^2a^2(E_m + E_r + E_\nu). \quad (8.21)$$

We first require a well defined equation for the perturbation φ , i.e. $A \neq 0$. We also require that there are no fast-growing modes for the scalar field perturbation φ . Since the perturbations φ couple to the other metric perturbations, having fast growing modes could give rise to catastrophic results (for example huge back-reaction on the background cosmology) or perturbations far from the observed ones.

For the ‘‘standard’’ and weighted best-fit reconstructions (the green and blue lines respectively in Fig. 8.1) the solution of the equation (8.19) triggers fast-growing modes instabilities. While the reasons for this are not fully understood (although they seem to be due to the non-monotonic behaviour of $X(a)$ while having a monotonic coupling function

³This also requires the mapping to the EFT framework developed in Sect. 8.3.2.

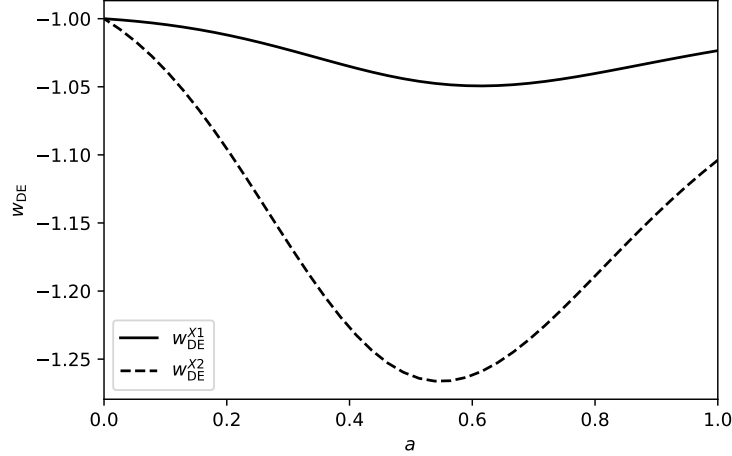


Figure 8.3: DE equation of state w_{DE} for the two fitting functions X1 and X2 introduced in Fig. 8.2.

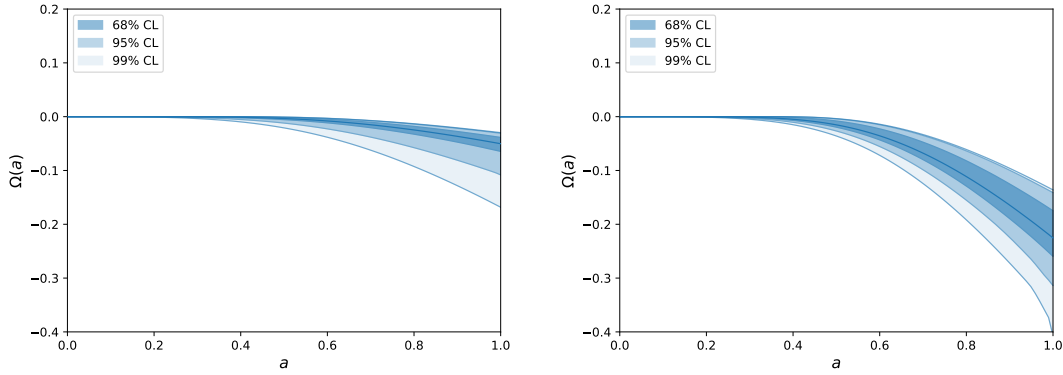


Figure 8.4: The EFT $\Omega = F(\phi) - 1$ function for the reconstructed GBD theories using an exponential $F(\phi)$. The “confidence levels” regions denote the prior distribution on the parameters ϕ'_{ini}, ξ and $\log_{10} a_{\text{ini}}$ projected on the Ω function.

$F(\phi) = \exp(\xi\phi)$, we considered a smooth fitting function of the $X(a)$ reconstruction of the form

$$X_{\text{fit}}(a) = A \tanh[B(a - C)] + D, \quad (8.22)$$

where the parameter D is chosen such that $X_{\text{fit}}(a = 1) = 1$.

In Fig. 8.4 we show the EFT Ω function from the reconstructed GBD theories from the fit (8.22) to the weighted reconstruction (left panel) and for a similar tanh function that allows a larger change in DE density (the black solid line on the right panel of Fig. 8.2). We refer to these two shapes of $X(a)$ as X1 and X2 respectively, and the corresponding equations on state are shown in Fig. 8.3. The GBD reconstructions are obtained by sampling from

the initial conditions space $(\phi'_{\text{ini}}, \log_{10} a_{\text{ini}}, \xi)$ with uniform prior on the intervals

$$\frac{\phi'_{\text{ini}}}{m_0} \in [-10^{-6}, 10^{-6}], \quad \log_{10} a_{\text{ini}} \in [-3, -1], \quad \xi \in [0.1, 10]. \quad (8.23)$$

The blue shaded regions denote the prior distribution projected onto the Ω function and the darker blue line denotes the mean Ω function from the reconstructed theories. We see that for all the theories that we probed, the increasing DE density drives the field to negative values, effectively reducing the coupling of the scalar with gravity. We then conclude that a larger increase of the DE density yields a larger change in the EFT Ω function.

8.3.2 Perturbations Evolution

One of our goals is to investigate the cosmological viability of the reconstructed theories. We focus on the signatures of GBD theories on the CMB anisotropies and the matter power spectrum $P(k)$, and the ISW effect through the cross correlation of the CMB temperature and the Galaxy Number Counts (GNC). The computation of the cosmological observables is performed solving the Einstein-Boltzmann system of equations with the EFTCAMB⁴ code which implements the EFTofDE presented in Sect. 6.2 in the Einstein-Boltzmann solver CAMB. GBD theories can be mapped onto the EFT formalism via the following equations

$$\Omega(a) = F(\phi(a)) - 1, \quad (8.24)$$

$$\frac{ca^2}{m_0^2} = \frac{1}{2} \mathcal{H}^2(\phi')^2, \quad (8.25)$$

$$\frac{\Lambda a^2}{m_0^2} = \frac{1}{2} \mathcal{H}^2(\phi')^2 - Ua^2, \quad (8.26)$$

with the second order perturbation functions all vanishing. The advantage of the GBD theories in the reconstruction program is that their perturbations depend only on the background EFT functions. As we saw earlier, these can be reconstructed by one assumption about their coupling function $F(\phi)$ and the knowledge of the expansion history.

We modified the EFTCAMB code and replaced the background parametrization in terms of the DE equation of state w_{DE} with the more general $X(a)$. We also introduced a new module that performs the numerical reconstruction of the GBD theory solving equation (8.19). The reconstructed GBD theory is then mapped onto the EFT formalism using the scheme above. The modifications are described in detail in App. D

⁴<https://github.com/EFTCAMB/EFTCAMB>

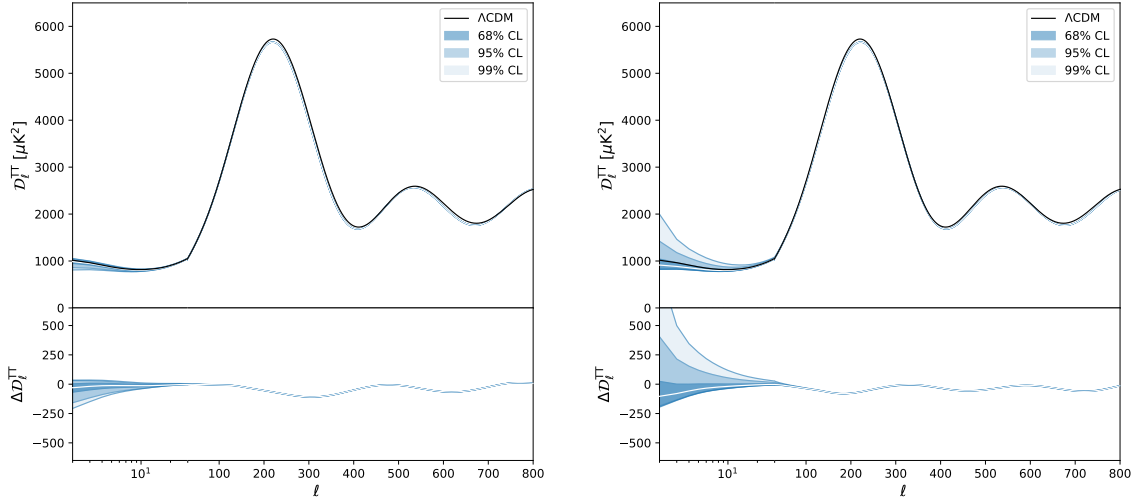


Figure 8.5: CMB anisotropies from the reconstructed GBD theories from the X1 (left panel) and X2 (right panel) DE densities. As expected the GBD theories affect mainly the ISW effect at low ℓ . The lower panels show the difference in power w.r.t. the Λ CDM best fit model.

8.3.3 CMB anisotropies and Matter Power Spectra

Here we investigate the signatures of the designed GBD theory in the CMB temperature anisotropies and in the matter power spectrum. We expect to see the low- ℓ part of the CMB power spectrum affected because of the ISW effect. In Fig. 8.5 we show the CMB temperature anisotropies power spectrum $\mathcal{D}_\ell \equiv \ell(\ell+1)(2\pi)^{-1}C_\ell$ of the reconstructed GBD theories from the X1 and X2 DE histories. As before, we sampled the parameter space uniformly and projected the parameter space onto the \mathcal{D}_ℓ 's. The shaded regions represent the sampled probability density and the white lines the probability means. In this sampling procedure we used the same cosmological parameters as obtained in the reconstruction of $X(a)$, except for the parameters n_s and A_s that were fixed to the best fit Λ CDM case.

As expected, we observe a modified ISW effect at small ℓ . Also, we see that a larger increase in DE density yields a larger ISW signal in the CMB. Clearly, with a different expansion history and a different theory of gravity, the time derivatives of the two potentials Φ and Ψ will differ from the Λ CDM scenario. In the latter, the two potentials start decaying when Dark Energy (the cosmological constant) begins to dominate the expansion history. In the designed GBD theories however, we have two competing effects: on one hand the different expansion history due to the reconstructed Dark Energy will drive a different decay of the potentials. Specifically, with the effective DE given by the hyperbolic tangent fit, the matter dominated era lasts longer than in the Λ CDM, delaying the decay of the two potentials. On the other hand, the fifth force on cosmological scales mediated by the

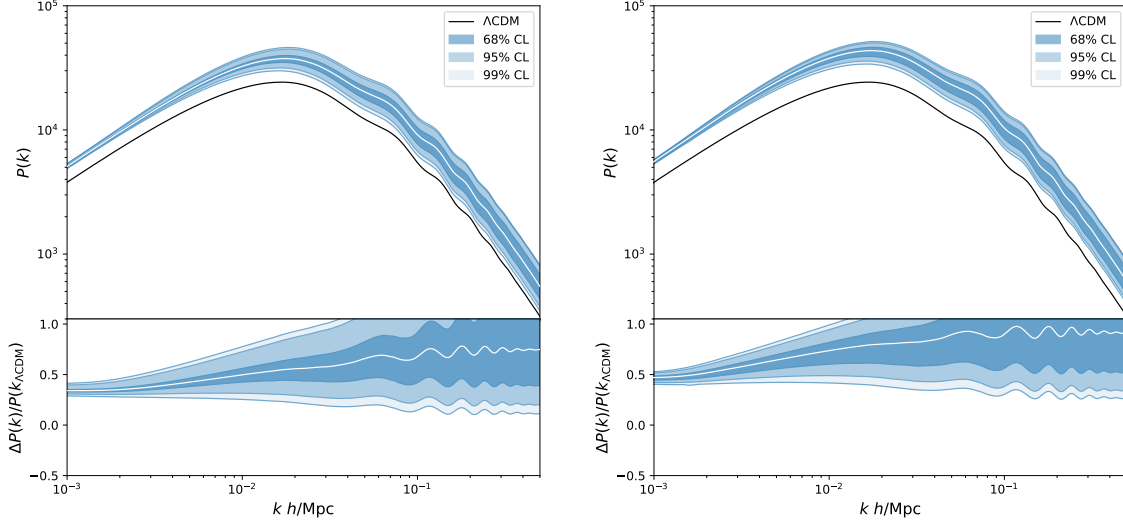


Figure 8.6: Linear matter power spectrum (at redshift $z = 0$) for the reconstructed GBD theories from X1 (left panel) and X2 (right panel). The lower panels show the relative differences w.r.t. the Λ CDM best fit model.

extra scalar ϕ will drive a growth of the two potentials. Which effect dominates depends on the details of the theory and its parameters. Whether the two potentials grow or decay is irrelevant for CMB temperature anisotropies as the latter are sensitive to the square of the ISW transfer function (3.66).

The differences in the high- ℓ part of the spectra are mainly due to the different distance to the last scattering surface (because of the different expansion history) which causes a shift in the peaks, and also due to different cosmological parameters ω_b and ω_c . These high- ℓ differences could be potentially eliminated by a MCMC parameter estimation, but this is beyond the scope of this work.

Fig. 8.6 shows the linear matter power spectra (upper plot) and the relative differences w.r.t. to the Λ CDM case (lower panels). First of all, we note an overall shift upwards for the GBD theories. At early times, before DE begins to dominate the background dynamics, the Planck best-fit Λ CDM model has more DE density than the GBD models with the reconstructed DE. This means that in the GBD models the matter dominated era (MDE) lasts slightly longer than in the Λ CDM model, allowing matter to cluster more, hence the overall shift upwards of the matter power spectrum. This is evident from comparing the reconstructed GBD theories from the two DE densities X1 and X2. X2 starts with a lower value of DE and the matter-DE equality is delayed to later times, allowing matter to cluster even further effectively shifting the matter power spectrum to larger values.

In addition to the change in the matter-DE equality, there is also the effect of the fifth force mediated by the scalar and the effect of the coupling $F(\phi)$. This is encoded in the way

the deviations from Λ CDM spread at smaller scales. Finally the oscillations that we note at $k \approx 0.1 h/\text{Mpc}$ are due to the different position of the BAO scale due to a slightly different expansion history of the GBD models.

8.3.4 Galaxy Number Counts and ISW effect

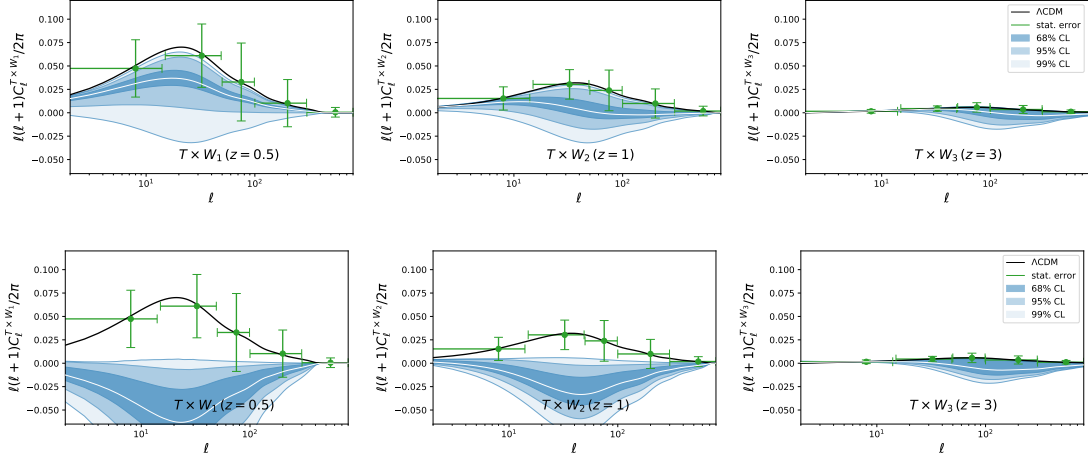


Figure 8.7: Comparison of the CMB temperature and Galaxy Number Counts cross correlation spectra between the Planck best-fit Λ CDM model and the designed GBD theory from the X1 (upper panels) and X2 (lower panels) DE densities. As we can see, the CMB temperature - GNC cross correlations for the GBD theories can be either positive or negative.

Here we present the theoretical predictions for the CMB temperature and GNC cross correlation power spectra. The angular power spectra are computed by implementing the GBD designer approach in the EFTCAMB patch for CAMB sources⁵ [113, 272]. The cross correlations are computed as in equation (3.31),

$$C_{\ell}^{Tg} = \frac{2}{\pi} \int dk k^2 I_{\ell}^{\text{ISW}}(k, \tau_0) I_{\ell}^{\text{GNC}}(k, \tau_0) \mathcal{P}_{\mathcal{R}}(k), \quad (8.27)$$

The ISW transfer function is given by eq. (3.66) and the GNC transfer function is given by

$$\Delta_{\ell}^{\text{GNC}}(k, \tau_0) = \int_0^{\tau_0} d\tau W(z) \frac{dz}{d\tau} b_g(\tau, k) \delta(\tau, k) j_{\ell}[k(\tau_0 - \tau)] + \text{corrections}, \quad (8.28)$$

where $\delta(k, \tau)$ is the matter density perturbation, $W(z)$ is the survey window function, b_g is the galaxy bias for the galaxies observed by the survey. The term ‘‘corrections’’ in

⁵The latest EFTCAMB patch is not compatible with the latest CAMB yet. In its last update, CAMB and CAMB sources have been merged, so we used the last available iteration of CAMB sources at https://github.com/cmbant/CAMB/tree/CAMB_sources.

eq. (8.28) denotes collectively the redshift-space-distorsion corrections, lensing terms, and other contributions suppressed by \mathcal{H}/k [113]. Since we are not interested in constraining the parameters of the GBD theories, but rather in investigating the sign of the ISW effect we choose three Gaussian window functions W_1 , W_2 and W_3 at the mean redshifts $z_1 = 0.2$, $z_2 = 0.5$ and $z_3 = 1$. The variances for the window functions are $\sigma_1 = \sigma_2 = 0.05$ and $\sigma_3 = 0.1$. The galaxy bias b_g is in general time and scale dependent. At the large scales observed in the surveys one expects the scale dependence to be weak, while the time dependence has usually a simple polynomial parametrization, see [322]. Since the bias is degenerate with the ISW amplitude one has to calibrate the bias parameters using other observables, such as GNC auto correlations, or cross correlations between GNC and galaxy lensing. However, as we are only interested in broad features of the ISW signal, we will fix the galaxy bias to $b_g \equiv 1$.

In Fig. 8.7 we show the theoretical prediction of the cross correlations for the two classes of reconstructed GBD theories from X1 (upper panels) and X2 (lower panels). With green error bars we show the statistical uncertainties of the Λ CDM model calculated from the theoretical signal-to-noise ratio

$$\left(\frac{S}{N}\right)_\ell^2 = \frac{f_{\text{sky}}(2\ell + 1)}{4\pi} \frac{(C_\ell^{Tg})^2}{C_\ell^{TT} C_\ell^{gg} + (C_\ell^{Tg})^2}, \quad (8.29)$$

where f_{sky} is the fraction of sky observed in the survey, and C_ℓ^{gg} is the angular power spectrum of the galaxy number counts. As we can see the two different DE densities yield different signs of the ISW effect. Especially in the case of DE with smaller values at early times such as X2, the ISW can be negative.

8.3.5 Physical Interpretation

Some of the GBD theories sampled previously are cosmologically viable, at least from the perspective of fitting the CMB and matter power spectra. Here we focus on the physical interpretation of such theories. To illustrate the reconstruction technique, we take one of the samples obtained above and reconstruct the corresponding potential using Eq. (8.21), which gives us $U(a)$. We then obtain the background field $\phi(a)$ by solving Eq. (8.19), thus we are able to reconstruct the potential shape $U(\phi)$ for the range of ϕ covered by its dynamics during the period of cosmic history under consideration. In Fig. 8.8 we show the reconstructed potential for four reconstructed GBD theory from the X1 DE density with $\phi'_{\text{ini}}/m_0 = 0$ and $a_{\text{ini}} = 10^{-2}$ and $\xi = 0.5, 1.5, 3$ and 10 respectively. We can see how in all four cases the potential is an unstable potential with a cusp at the origin. Stronger couplings leads to steeper potentials. The field ϕ starts at the top of the cusp and falls down the potential.

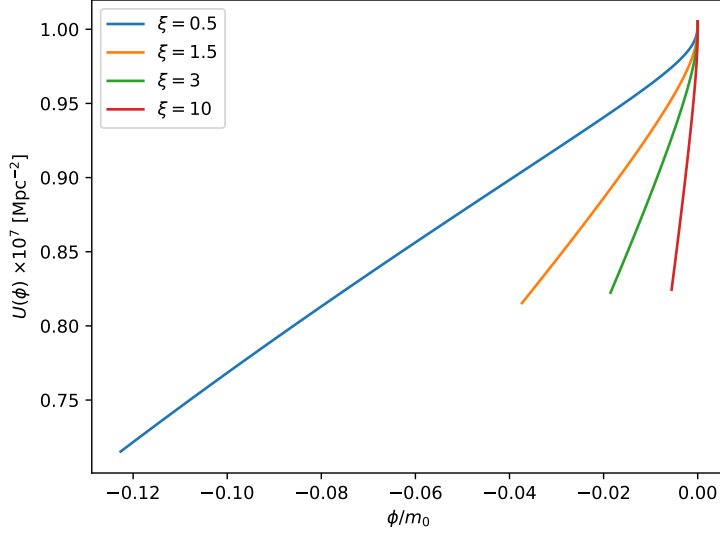


Figure 8.8: Reconstructed potential for four of the sampled GBD theories with coupling $\xi = 0.5$ 1.5, 3 and 10 respectively.

A few considerations about the reconstructed potentials. Their shape resembles the shape of chameleon-like models although reflected about the vertical axis. However, when the field runs down the potential, its coupling also decreases at the same time, while for chameleon models such as the one considered in [246, 247] the opposite happens. Another difference with the models considered in [246, 247] is that in the latter the scalar field usually sits at the minimum of the potential. In that case the field is trapped, and its dynamics cannot be reconstructed with an approach like the one proposed here.

In Fig. 8.9 we show the cosmological observables for the selected models. While the CMB anisotropies are almost the same for each model, they differ considerably in the clustering of matter and this is also noticeable in the cross correlations C_ℓ^{Tg} at the bottom panels.

In the higher redshift windows, the larger values of couplings constants ξ drive a growth of the gravitational potentials Ψ and Φ due to the fifth force mediated by the scalar field, causing a negative ISW effect. When DE eventually starts dominating the potentials stop growing and instead decay, turning the sign of the ISW effect.

8.4 Designer GBD from $F(a)$

We now change approach and we use a given $F(a)$ (as opposed to $F(\phi)$) to reconstruct $U(a)$. This method has already been used to reconstruct the GBD Lagrangian from the expansion history inferred from an early SN dataset [319, 320] and we shall briefly describe

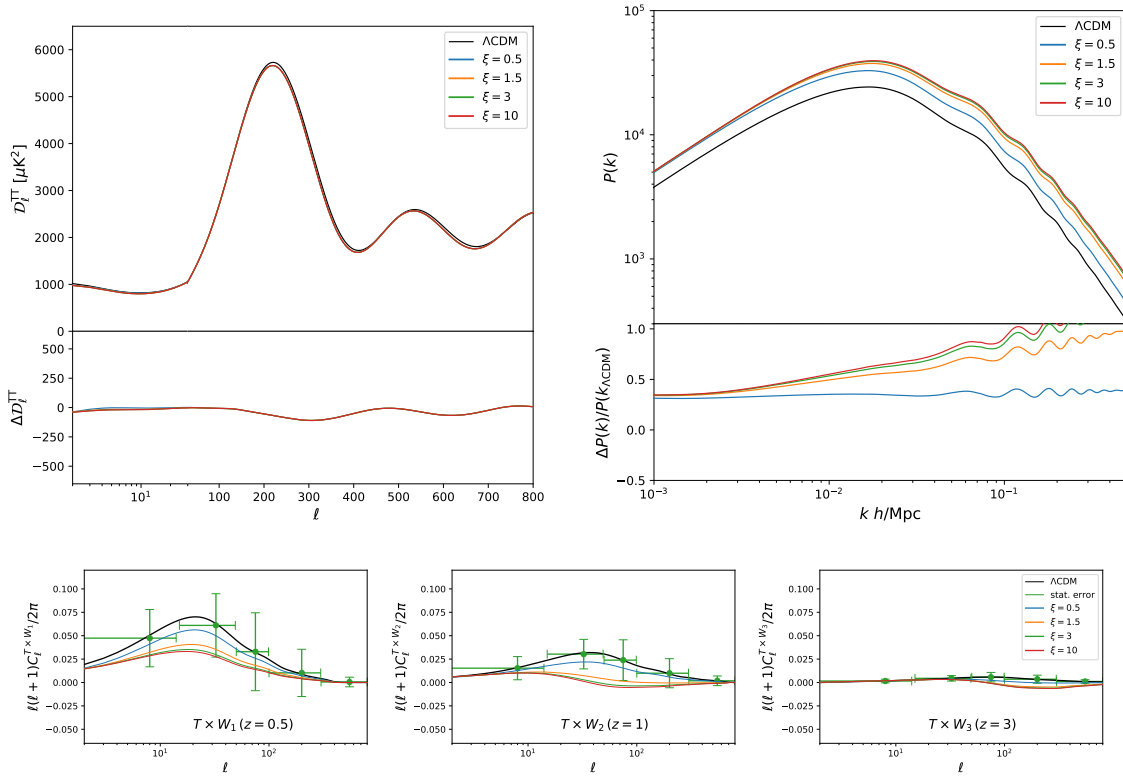


Figure 8.9: Cosmological observables for the models reconstructed in Fig. 8.8 compared to the best fit Λ CDM model.

it here. In this case we can write the modified Friedmann equations as,

$$\mathcal{H}^2 = \frac{1}{3m_0^2} \frac{1}{F + aF'} \left[\rho a^2 + \frac{1}{2} \dot{\phi}^2 + U a^2 \right], \quad (8.30)$$

$$\dot{\mathcal{H}} = \frac{1}{F + \frac{1}{2} aF'} \left\{ \left[F + 2aF' + a^2 F'' \right] \mathcal{H}^2 - \frac{1}{2m_0^2} \left[P a^2 + \frac{1}{2} \dot{\phi}^2 - U a^2 \right] \right\}, \quad (8.31)$$

where again, primes denote derivatives w.r.t. the scale factor. We can eliminate the dependence of the potential U in the second Friedmann equation, Eq. (8.31), using the Friedmann equation (8.30). We obtain

$$\dot{\mathcal{H}} = \frac{1}{F + \frac{1}{2} aF'} \left\{ \left[\frac{5}{2} F + \frac{7}{2} aF' + a^2 F'' \right] \mathcal{H}^2 - \frac{(\rho + P)a^2}{2m_0^2} - \frac{1}{2m_0^2} \dot{\phi}^2 \right\}. \quad (8.32)$$

Now one can reconstruct the potential $U(a)$ by eliminating $\dot{\phi}$ from the equation (8.30) using the equation (8.32). This yields

$$\frac{U a^2}{m_0^2} = \mathcal{H}^2 \left[\frac{1}{2} F - \frac{1}{2} aF' - a^2 F'' \right] + \frac{(P - \rho)a^2}{2m_0^2} + \dot{\mathcal{H}} \left[F + \frac{1}{2} aF' \right] \quad (8.33)$$

Then, knowing the potential $U(a)$ one can reconstruct the kinetic energy $\dot{\phi}^2$ again from the equation (8.30). This reconstruction procedure is an example of the pure EFT designer approach used in EFTCAMB [323] with the mapping

$$\frac{\Lambda a^2}{m_0^2} = \frac{1}{2m_0^2} \dot{\phi}^2 - \frac{U a^2}{m_0^2}, \quad (8.34)$$

$$\frac{c a^2}{m_0^2} = \frac{1}{2m_0^2} \dot{\phi}^2. \quad (8.35)$$

We can gain some useful information about the theory by solving the differential equation for $\dot{\phi}^2$. In fact, by having the field profile $\phi(a)$, the profile of $U(a)$ and the ansatz $F(a)$ one can reconstruct the functional forms $F(\phi)$ and $U(\phi)$, but only for the values of $\phi(a)$ assumed by the field.

8.4.1 Parameter Space

In this case the parameter space is, in principle, infinite dimensional as we are dealing with an arbitrary function. We can restrict the parameter space by assuming a functional form of the function $F(a)$. Here we use the following two examples,

$$F(a) = 1 + \Omega_0 a^s, \quad (8.36)$$

$$F(a) = 1 + \sum_{i=1}^5 \alpha_i a^i, \quad (8.37)$$

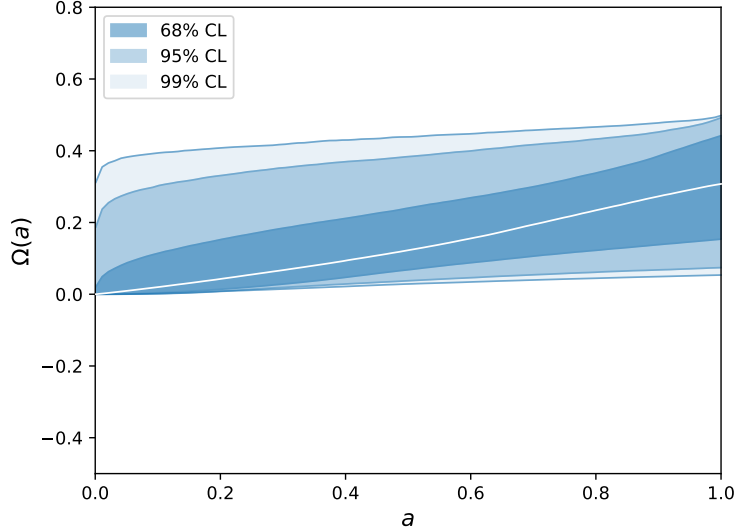


Figure 8.10: Power law EFT Ω functions reconstructed from the DE density X1.

and we sample the parameter space in the regions

$$\Omega_0 \in [-1, 1], \quad s \in [10^{-2}, 3], \quad (8.38)$$

$$\alpha_i \in [-1, 1], \quad (8.39)$$

with a uniform prior. For each form of $F(a)$ we performed the reconstruction from the two $X(a)$ shown in Fig. 8.1 and their hyperbolic tangent fit (8.22) as illustrated in Fig. 8.2. For the power law function we find no stable GBD theories for any of the considered $X(a)$, except the tanh fit X1, as in Sect. 8.3. In Fig. 8.10 we show the allowed distribution of EFT functions Ω with the power law time dependence.

For the polynomial $F(a)$, which is allowed to oscillate, we find that it is general enough to have reconstructions for each of the four DE densities considered. The stable EFT Ω functions sampled from the parameter space (8.39) are shown in Fig. 8.11.

8.4.2 Results

For the stable theories we computed the same cosmological observables as in Sections 8.3.3 and 8.3.4. In Fig. 8.12 we show the plots of the cosmological observables corresponding to the sampled parameter space (8.38) of the reconstruction of the power law $\Omega(a)$ from the X1 DE density. We can see that in the sampled region of the parameter space there is at least a region that yields viable observations. In the following subsection will reconstruct the Lagrangian of one these viable models.

In Fig. 8.13, we show the cosmological observables for the reconstructed GBD with a polynomial time dependence of the coupling function $F(a)$. We show only the results from

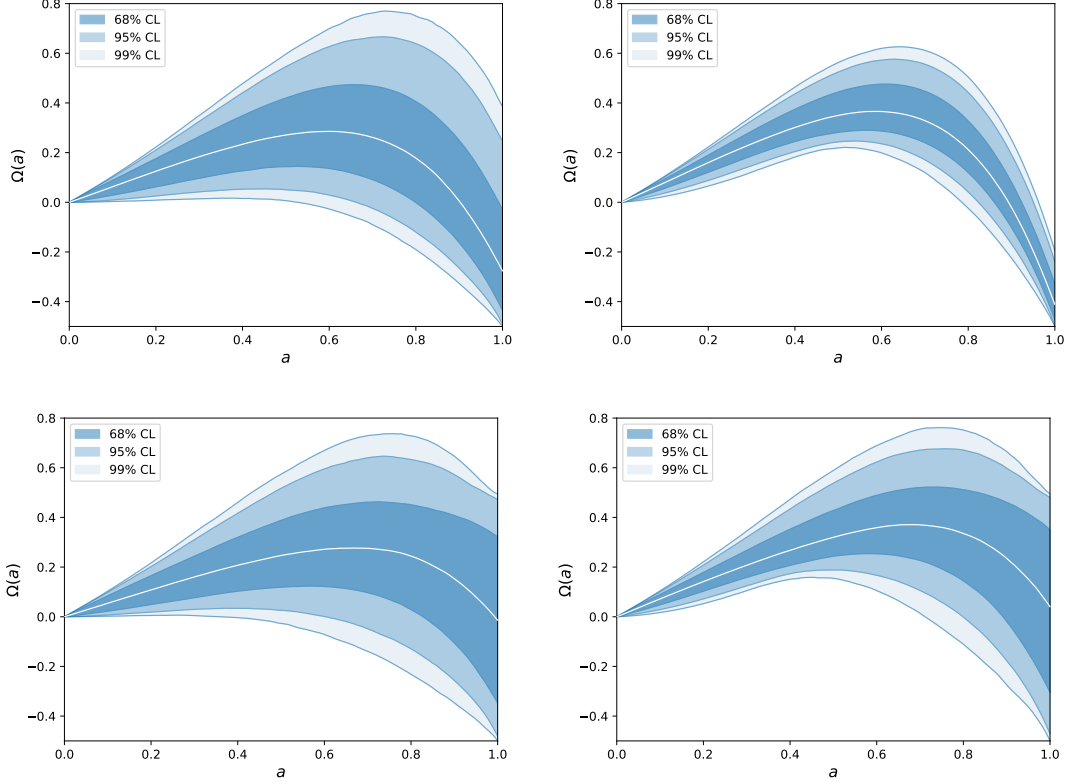


Figure 8.11: Polynomial EFT Ω functions reconstructed from the weighted $X(a)$ (upper left), standard $X(a)$ (upper right) and their respective tanh fits (lower panels).

the X1 as the other three cases show similar behaviours. The noticeable difference is in the ISW signal that is much larger for the “standard” reconstruction and can also yield negative ISW cross correlations in the lower redshift survey window.

8.4.3 Physical Interpretation

As the last step, we reconstruct the GBD Lagrangian for a viable theory obtained from the analysis above. We begin with the Lagrangian reconstructed from the power law $F(a)$ for one viable example. From the EFT c function, equation (8.35), we can obtain the kinetic energy $(\phi')^2$. We then integrate the kinetic energy providing an arbitrary initial condition for the field ϕ_0 . Changing ϕ_0 does not affect the reconstruction but only shifts the field values. The shape of the coupling function is then obtained by plotting $\Omega(a)$ against the solution $\phi(a)$. Similarly, the potential $U(\phi)$ can be obtained from the difference of the EFT functions c and Λ . We selected a viable model with an increase in Ω of 5% in order to satisfy the BBN constraints. The reconstructed coupling $\Omega(\phi)$ and the potential $U(\phi)$ are shown in Fig. 8.14, while the related cosmological observables are shown in Fig. 8.15a. We note that the potential has a shape similar to the ones in the most common chameleon models. Actually, the potential for larger field values start growing again, resembling a symmetron-

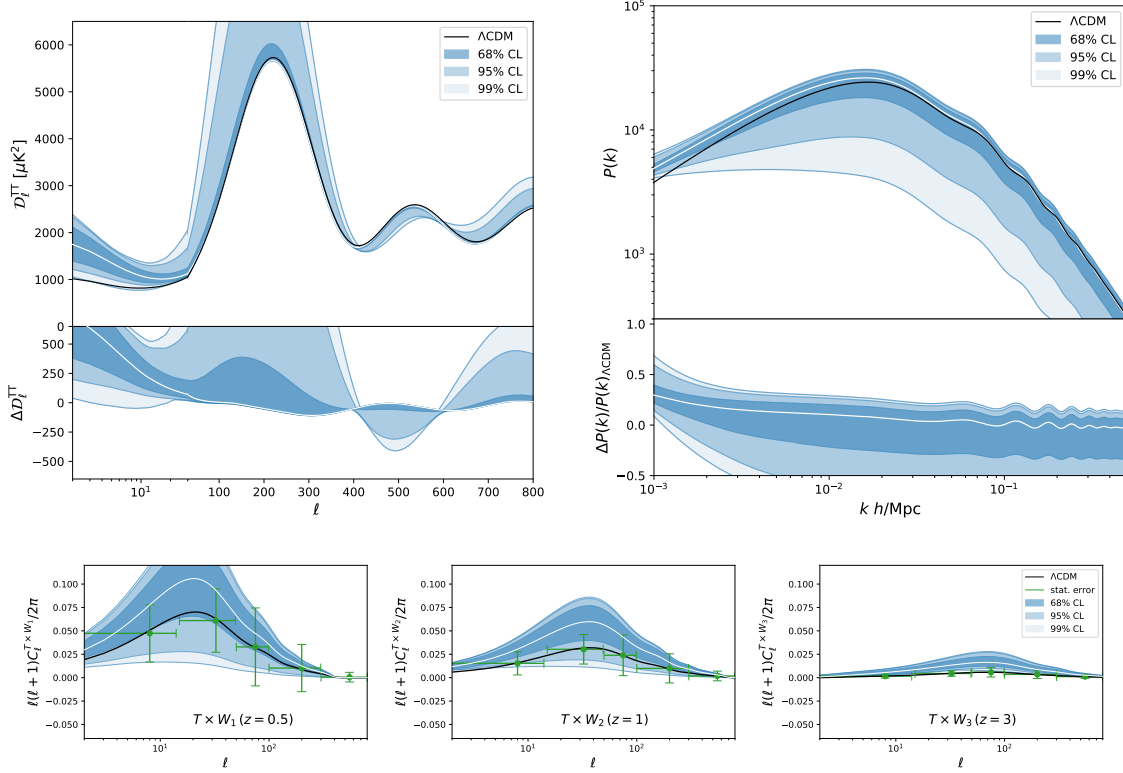


Figure 8.12: Cosmological observables from the reconstructed power law $\Omega(a)$ using the X1 DE density.

like shape after the phase transition. The coupling function is a monotonically increasing function of the field, and changes its slope at larger values of the field.

Similarly, Fig. 8.15b shows the reconstructed coupling $\Omega(\phi)$ and the potential $U(\phi)$ for the GBD theories with polynomial coupling $F(a)$, using the “standard” and weighted reconstructions (as well as their tanh fits). The corresponding cosmological observables are shown in Fig. 8.15c. The potentials have the characteristic runaway shape, with small features to accommodate the oscillations in the reconstructed $X(a)$, and seem to be unbounded from below for large values of the field. The couplings $\Omega(a)$ in this case are not monotonic.

8.5 Summary

In this Chapter we considered the latest reconstructions of the Dark Energy density as provided by our work in [310] and developed a method to reconstruct the Lagrangian a scalar-tensor theory for the background observations. These reconstructed theories agree with the observations of the expansion history by construction and hence should help relieving the “tensions” in the Λ CDM model. We found that the oscillatory behaviour of the cannot be explained by a GBD theory with monotonic coupling with gravity. However a

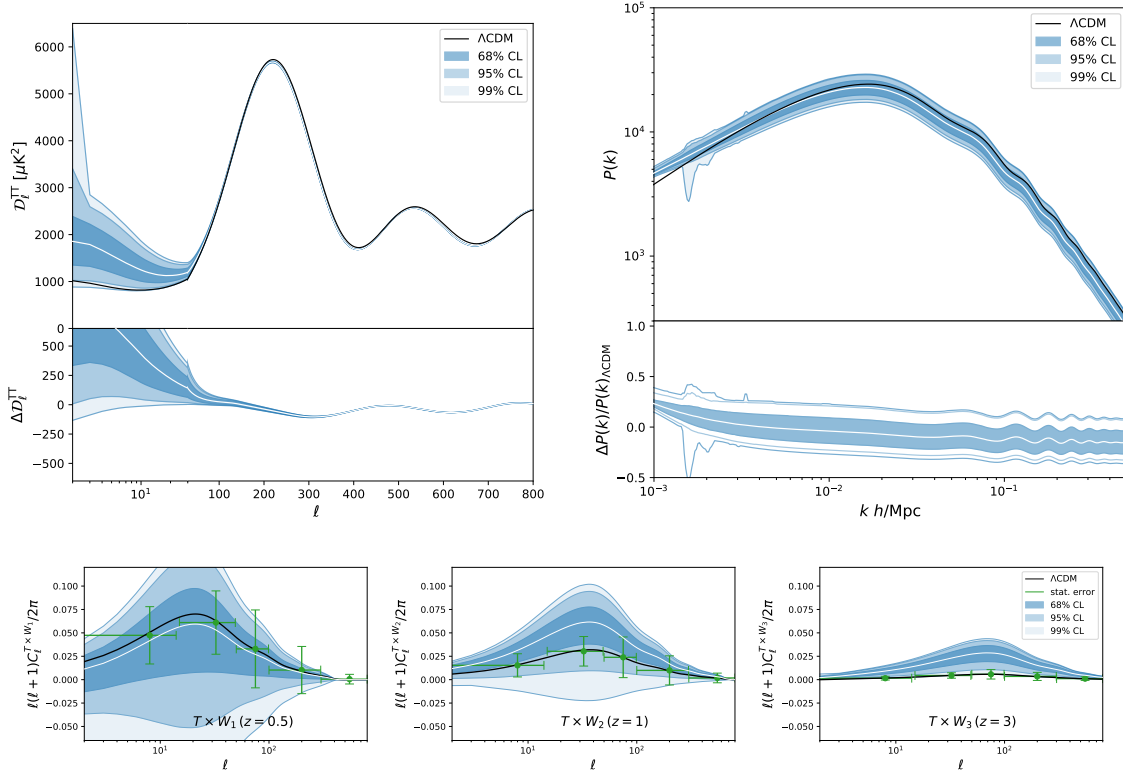


Figure 8.13: Cosmological observables from the reconstructed polynomial $\Omega(a)$.

phantom-like DE that increases in time can be explained by such theories, for which we also reconstructed the potential, at least for the values assumed by the field during its cosmological dynamics. While in the case of reconstructed theories from the knowledge of $F(\phi)$ and from the polynomial $F(a)$ we obtained unstable theories that seems to have a potential unbounded from below, in the case of the reconstruction from a power law $\Omega(a)$ we obtained chameleon-looking theories that have a potential bounded from below.

The method developed here would definitely benefit from the latest reconstruction of the EFT functions from cosmological observations performed in [35]. In that work, instead of using only observations of the expansion history, also perturbations observables were used, making the reconstructed theories cosmologically viable by construction. It would hence be very interesting to apply the method developed in this Chapter to reconstruct the Lagrangian of a fully viable GBD theory. This is left for future work.

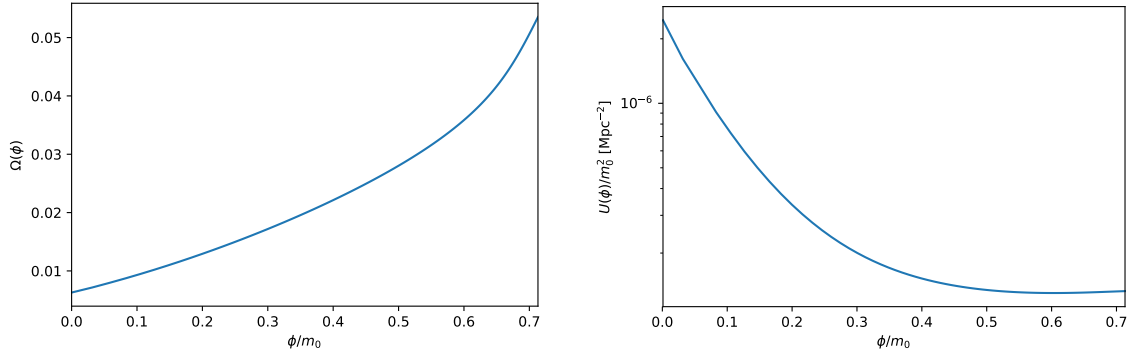


Figure 8.14: Reconstructed coupling and potential from the DE density X1 for the power law time dependence of $\Omega(a)$.

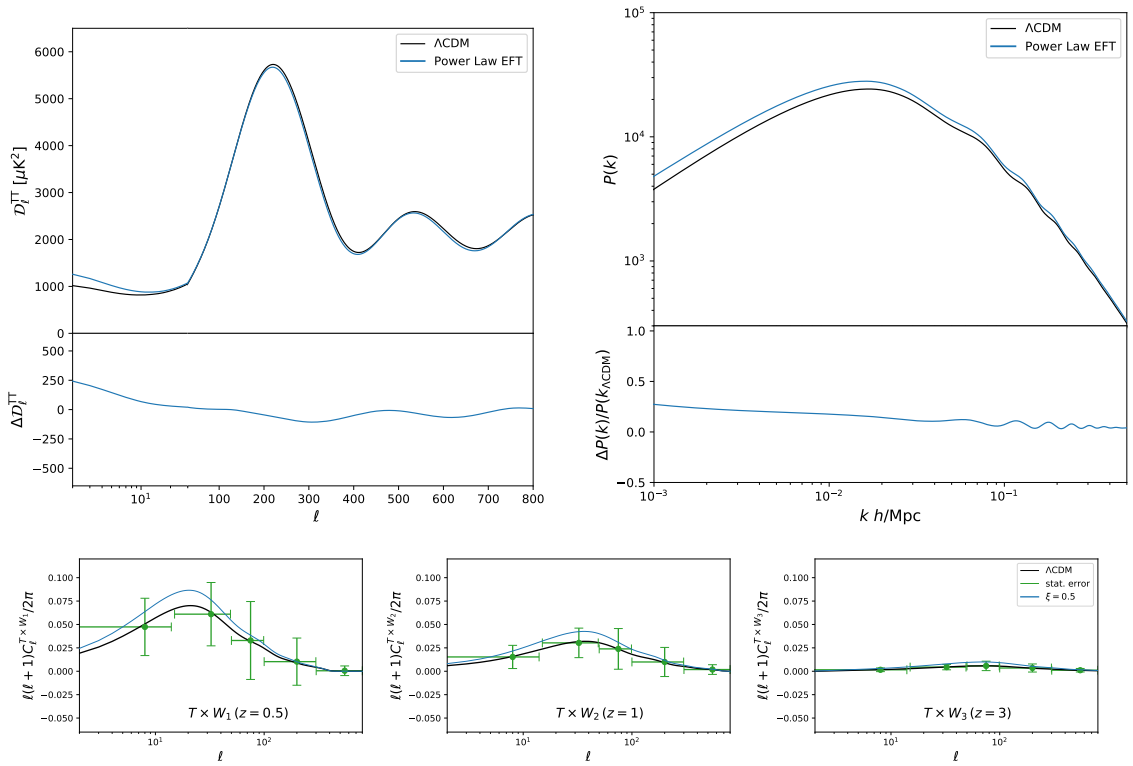


Figure 8.15a: Cosmological observables from the theory reconstructed in Fig. 8.14.

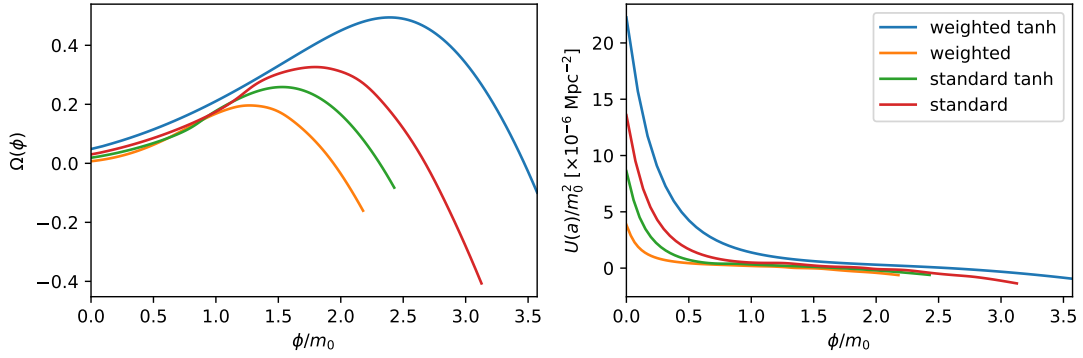


Figure 8.15b: Reconstructed coupling and potential from the standard and weighted DE density reconstructions (and their tanh fit) using a fifth order polynomial coupling $F(a)$.

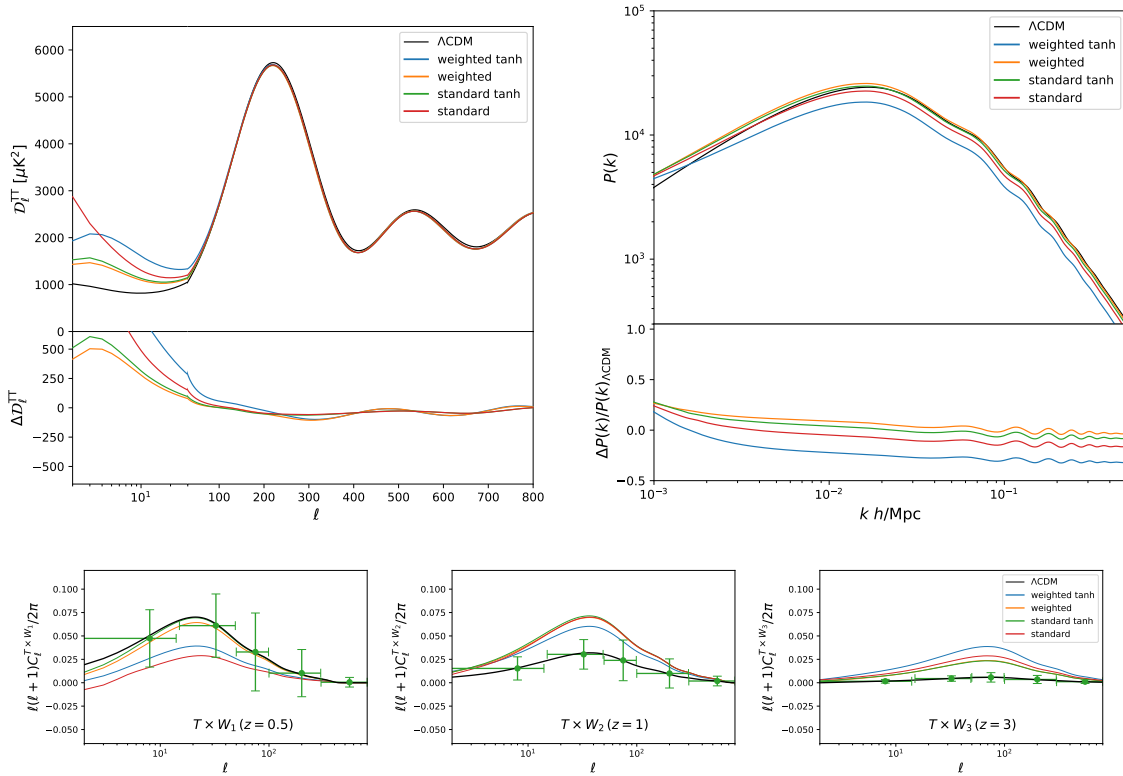


Figure 8.15c: Cosmological observables from GBD theories reconstructed from polynomial $\Omega(a)$.

Chapter 9

Summary and future directions

We began this thesis with an introduction of the main concepts that lay the basis for the standard model of cosmology. We first reviewed the background expansion of the Universe and subsequently built the linear perturbation theory, useful to describe the inhomogeneities that we observe at the larger cosmological scales. The hope is that this first part will serve as a reference for future students at the beginning of their journey in cosmology.

We then summarized the main cosmological observables used to test gravity and other fundamental physics with cosmological data. This was done with the idea that it should be a quick introduction for those interested in understanding the ideas behind the commonly used numerical codes in cosmology.

9.1 Early Universe

Part II was devoted to the investigation of two topics in the early Universe. First, in Chapter 4, we constrained the model of constant roll inflation using the latest CMB data. This model generalizes the commonly used slow-roll approximation for inflationary models by assuming that the inflaton field rolls down the potential at a constant rate, and hence can be used to test the slow roll condition. We found that, in general, the slow roll approximation is well satisfied. The main result of this Chapter was computing the primordial power spectra in this model of inflation using the efficient exact method developed in [135], and fitting it to the cosmological data. This method can be used for any model of inflation, including multi-field inflation models.

In Chapter 5 we considered the impact of a primordial magnetic field present in the primeval plasma prior to recombination on the CMB. We considered only a non-helical magnetic field yielding parity even modes in the CMB anisotropies. In particular, we have demonstrated the power of the CMB B-mode polarization measurements in constraining the amplitude $B_{1\text{Mpc}}$ of such a primordial magnetic field, and obtained the tightest bound to date on its amplitude, $B_{1\text{Mpc}} < 1.5$ nG, after marginalizing over the spectral index n_B . This was accompanied by the developed of the first publicly available code to compute

CMB anisotropies from PMF, `MagCAMB`¹. This code was based on an earlier version of the code developed by Shaw and Lewis in [183]. We extended the code to an arbitrary range of spectral indices and embedded it in the MCMC sampler CosmoMC. We then ported the SPT high- ℓ B-mode likelihood into CosmoMC and used the SPT data to constrain the PMF amplitude and spectral index. Future B-mode measurements will be able to provide even stronger constraints on the PMF amplitude and the `MagCAMB` will be very valuable in this task.

The `MagCAMB` code does not account for the helical component of the magnetic field and does not have the ability to compute parity odd cross correlations to the CMB anisotropies. Future CMB surveys will be also able to measure the parity odd TB and EB cross correlations. These will be introduced in the next version of the code.

9.2 Late time Universe - Dark Energy

In Part III we focused on the nature of Dark Energy as inferred from cosmological observations. The most common framework adopted in the literature are scalar-tensor theories of gravity. In Chapter 6, we briefly reviewed the Horndeski class of theories and three phenomenological parametrizations usually adopted when testing gravity on cosmological scales. We derived constraints on a set of models that exhibit the chameleon-type of screening mechanism, that hides the fifth-force mediated by the extra scalar from local observations. To do so we modified the previous version of the `MGCAMB` code. However, that version was based on the assumption that radiation is mostly negligible at later times and contributions of massive neutrinos were mostly ignored. Given the precision of the ongoing and future observations, the effects of massive neutrinos can no longer be neglected. For this reason, in Chapter 7, we developed the new version of the `MGCAMB` code. This version consistently implements massive neutrinos in the modified growth scenario and allowed for dynamical Dark Energy. The code is now hosted on Github at <https://github.com/sfu-cosmo/MGCAMB>. The code is widely used in the community and we expect the new update to be very useful for analyzing data from upcoming surveys.

Finally, in Chapter 8, we presented two types of Lagrangian reconstruction methods for Generalized Brans Dicke theories from the observations of the DE density. We were mostly interested in the qualitative features of the ISW effect and its potential for constraining these class of models. We find that, for viable theories that do not violate the BBN constraints on the variation of the Newton's constant, and are consistent with existing CMB and large scale structure observations, the ISW has a positive sign, although with slightly different patterns of growth of the gravitational potentials. For these type of theories we could also reconstruct the Lagrangian and found that, in one case, they look like symmetron type

¹The code can be downloaded at <https://github.com/alexzucca90/MagCAMB>

theories, yielding an increasing effective DE density. This work was accompanied by the creation of a GBD module for the code EFTCAMB that we have made publicly available at <https://github.com/alexzucca90/EFTCAMB-DErecon>. Future reconstructions of the EFT functions using new, more precise data, will be able to provide better reconstructions of the GBD Lagrangian, and, ultimately, help us converge to the theory that will explain the nature of Dark Energy.

Bibliography

- [1] LIGO SCIENTIFIC COLLABORATION AND VIRGO COLLABORATION collaboration, *Observation of gravitational waves from a binary black hole merger*, *Phys. Rev. Lett.* **116** (2016) 061102.
- [2] LIGO SCIENTIFIC COLLABORATION AND VIRGO COLLABORATION collaboration, *Gw170817: Observation of gravitational waves from a binary neutron star inspiral*, *Phys. Rev. Lett.* **119** (2017) 161101.
- [3] LIGO SCIENTIFIC, VIRGO, FERMI GBM, INTEGRAL, ICECUBE, ASTROSAT CADMIUM ZINC TELLURIDE IMAGER TEAM, IPN, INSIGHT-HXMT, ANTARES, SWIFT, AGILE TEAM, 1M2H TEAM, DARK ENERGY CAMERA GW-EM, DES, DLT40, GRAWITA, FERMI-LAT, ATCA, ASKAP, LAS CUMBRES OBSERVATORY GROUP, OzGRAV, DWF (DEEPER WIDER FASTER PROGRAM), AST3, CAASTRO, VINROUGE, MASTER, J-GEM, GROWTH, JAGWAR, CALTECHNRAO, TTU-NRAO, NUSTAR, PAN-STARRS, MAXI TEAM, TZAC CONSORTIUM, KU, NORDIC OPTICAL TELESCOPE, EPESSTO, GROND, TEXAS TECH UNIVERSITY, SALT GROUP, TOROS, BOOTES, MWA, CALET, IKI-GW FOLLOW-UP, H.E.S.S., LOFAR, LWA, HAWC, PIERRE AUGER, ALMA, EURO VLBI TEAM, PI OF SKY, CHANDRA TEAM AT MCGILL UNIVERSITY, DFN, ATLAS TELESCOPES, HIGH TIME RESOLUTION UNIVERSE SURVEY, RIMAS, RATIR, SKA SOUTH AFRICA/MEERKAT collaboration, *Multi-messenger Observations of a Binary Neutron Star Merger*, *Astrophys. J.* **848** (2017) L12 [1710.05833].
- [4] LIGO SCIENTIFIC, VIRGO, FERMI-GBM, INTEGRAL collaboration, *Gravitational Waves and Gamma-rays from a Binary Neutron Star Merger: GW170817 and GRB 170817A*, *Astrophys. J.* **848** (2017) L13 [1710.05834].
- [5] SUPERNOVA COSMOLOGY PROJECT collaboration, *Measurements of Omega and Lambda from 42 high redshift supernovae*, *Astrophys. J.* **517** (1999) 565 [astro-ph/9812133].
- [6] SUPERNOVA SEARCH TEAM collaboration, *Observational evidence from supernovae for an accelerating universe and a cosmological constant*, *Astron. J.* **116** (1998) 1009 [astro-ph/9805201].
- [7] WMAP collaboration, *First year Wilkinson Microwave Anisotropy Probe (WMAP) observations: Determination of cosmological parameters*, *Astrophys. J. Suppl.* **148** (2003) 175 [astro-ph/0302209].

- [8] WMAP collaboration, *Nine-Year Wilkinson Microwave Anisotropy Probe (WMAP) Observations: Cosmological Parameter Results*, *Astrophys. J. Suppl.* **208** (2013) 19 [[1212.5226](#)].
- [9] PLANCK collaboration, *Planck 2015 results. I. Overview of products and scientific results*, *Astron. Astrophys.* **594** (2016) A1 [[1502.01582](#)].
- [10] PLANCK collaboration, *Planck 2015 results. XIII. Cosmological parameters*, *Astron. Astrophys.* **594** (2016) A13 [[1502.01589](#)].
- [11] PLANCK collaboration, *Planck 2018 results. VI. Cosmological parameters*, [1807.06209](#).
- [12] C. P. Burgess, *Intro to Effective Field Theories and Inflation*, [1711.10592](#).
- [13] G.-B. Zhao et al., *Dynamical dark energy in light of the latest observations*, *Nat. Astron.* **1** (2017) 627 [[1701.08165](#)].
- [14] R. R. Caldwell, *A Phantom menace?*, *Phys. Lett.* **B545** (2002) 23 [[astro-ph/9908168](#)].
- [15] S. M. Carroll, M. Hoffman and M. Trodden, *Can the dark energy equation - of - state parameter w be less than -1 ?*, *Phys. Rev.* **D68** (2003) 023509 [[astro-ph/0301273](#)].
- [16] A. Vikman, *Can dark energy evolve to the phantom?*, *Phys. Rev.* **D71** (2005) 023515 [[astro-ph/0407107](#)].
- [17] A. Papapetrou, *Einstein's theory of gravitation and flat space*, *Proceedings of the Royal Irish Academy. Section A: Mathematical and Physical Sciences* **52** (1948) 11.
- [18] S. N. Gupta, *Quantization of einsteins gravitational field: General treatment*, *Proceedings of the Physical Society. Section A* **65** (1952) 608.
- [19] R. H. Kraichnan, *Special-relativistic derivation of generally covariant gravitation theory*, *Phys. Rev.* **98** (1955) 1118.
- [20] S. Weinberg, *Photons and gravitons in perturbation theory: Derivation of maxwell's and einstein's equations*, *Phys. Rev.* **138** (1965) B988.
- [21] S. Deser, *Selfinteraction and gauge invariance*, *Gen. Rel. Grav.* **1** (1970) 9 [[gr-qc/0411023](#)].
- [22] B. Bertotti, L. Iess and P. Tortora, *A test of general relativity using radio links with the Cassini spacecraft*, *Nature* **425** (2003) 374.
- [23] S. S. Shapiro, J. L. Davis, D. E. Lebach and J. S. Gregory, *Measurement of the Solar Gravitational Deflection of Radio Waves using Geodetic Very-Long-Baseline Interferometry Data, 1979-1999*, *Phys. Rev. Lett.* **92** (2004) 121101.
- [24] I. I. Shapiro, *Solar system tests of general relativity: recent results and present plans*, in *General Relativity and Gravitation, 1989*, N. Ashby, D. F. Bartlett and W. Wyss, eds., p. 313, 1990.

- [25] A. Joyce, B. Jain, J. Khoury and M. Trodden, *Beyond the Cosmological Standard Model*, *Phys. Rept.* **568** (2015) 1 [1407.0059].
- [26] G. W. Horndeski, *Second-order scalar-tensor field equations in a four-dimensional space*, *International Journal of Theoretical Physics* **10** (1974) 363.
- [27] A. Nicolis, R. Rattazzi and E. Trincherini, *The Galileon as a local modification of gravity*, *Phys. Rev.* **D79** (2009) 064036 [0811.2197].
- [28] C. Deffayet, X. Gao, D. A. Steer and G. Zahariade, *From k-essence to generalised Galileons*, *Phys. Rev.* **D84** (2011) 064039 [1103.3260].
- [29] T. Kobayashi, M. Yamaguchi and J. Yokoyama, *Generalized G-inflation: Inflation with the most general second-order field equations*, *Prog. Theor. Phys.* **126** (2011) 511 [1105.5723].
- [30] C. D. Hoyle, U. Schmidt, B. R. Heckel, E. G. Adelberger, J. H. Gundlach, D. J. Kapner et al., *Submillimeter tests of the gravitational inverse square law: a search for 'large' extra dimensions*, *Phys. Rev. Lett.* **86** (2001) 1418 [hep-ph/0011014].
- [31] EOT-WASH GROUP collaboration, *Sub-millimeter tests of the gravitational inverse square law*, in *CPT and Lorentz symmetry. Proceedings: 2nd Meeting, Bloomington, USA, Aug 15-18, 2001*, pp. 9–15, 2002, hep-ex/0202008, DOI.
- [32] D. J. Kapner, T. S. Cook, E. G. Adelberger, J. H. Gundlach, B. R. Heckel, C. D. Hoyle et al., *Tests of the gravitational inverse-square law below the dark-energy length scale*, *Phys. Rev. Lett.* **98** (2007) 021101 [hep-ph/0611184].
- [33] G. Gubitosi, F. Piazza and F. Vernizzi, *The Effective Field Theory of Dark Energy*, *JCAP* **1302** (2013) 032 [1210.0201].
- [34] J. K. Bloomfield, É. É. Flanagan, M. Park and S. Watson, *Dark energy or modified gravity? An effective field theory approach*, *JCAP* **1308** (2013) 010 [1211.7054].
- [35] M. Raveri, *Reconstructing Gravity on Cosmological Scales*, 1902.01366.
- [36] E. Bertschinger and P. Zukin, *Distinguishing Modified Gravity from Dark Energy*, *Phys. Rev.* **D78** (2008) 024015 [0801.2431].
- [37] G.-B. Zhao, L. Pogosian, A. Silvestri and J. Zylberberg, *Searching for modified growth patterns with tomographic surveys*, *Phys. Rev.* **D79** (2009) 083513 [0809.3791].
- [38] A. A. Starobinsky, *A New Type of Isotropic Cosmological Models Without Singularity*, *Phys. Lett.* **B91** (1980) 99.
- [39] K. Sato, *First-order phase transition of a vacuum and the expansion of the Universe*, *Mon. Not. Roy. Astron. Soc.* **195** (1981) 467.
- [40] A. H. Guth, *Inflationary universe: A possible solution to the horizon and flatness problems*, *Phys. Rev. D* **23** (1981) 347.

- [41] A. Albrecht and P. J. Steinhardt, *Cosmology for grand unified theories with radiatively induced symmetry breaking*, *Phys. Rev. Lett.* **48** (1982) 1220.
- [42] A. D. Linde, *A new inflationary universe scenario: A possible solution of the horizon, flatness, homogeneity, isotropy and primordial monopole problems*, *Phys. Lett. B* **108** (1982) 389.
- [43] PLANCK collaboration, *Planck 2015 results. XX. Constraints on inflation*, *Astron. Astrophys.* **594** (2016) A20 [[1502.02114](#)].
- [44] PLANCK collaboration, *Planck 2018 results. X. Constraints on inflation*, [1807.06211](#).
- [45] BICEP2, PLANCK collaboration, *Joint Analysis of BICEP2/KeckArray and Planck Data*, *Phys. Rev. Lett.* **114** (2015) 101301 [[1502.00612](#)].
- [46] SIMONS OBSERVATORY collaboration, *The Simons Observatory: Science goals and forecasts*, *JCAP* **1902** (2019) 056 [[1808.07445](#)].
- [47] CMB-S4 collaboration, *CMB-S4 Science Book, First Edition*, [1610.02743](#).
- [48] J. Lesgourgues, G. Mangano, G. Miele and S. Pastor, *Neutrino Cosmology*. Cambridge University Press, 2013, [10.1017/CBO9781139012874](#).
- [49] L. M. Widrow, *Origin of galactic and extragalactic magnetic fields*, *Rev. Mod. Phys.* **74** (2002) 775 [[astro-ph/0207240](#)].
- [50] R. M. Athreya, V. K. Kapahi, P. J. McCarthy and W. van Breugel, *Large rotation measures in radio galaxies at $Z > 2$* , *Astron. Astrophys.* **329** (1998) 809.
- [51] L. M. Widrow, D. Ryu, D. R. G. Schleicher, K. Subramanian, C. G. Tsagas and R. A. Treumann, *The First Magnetic Fields*, *Space Sci. Rev.* **166** (2012) 37 [[1109.4052](#)].
- [52] A. Neronov and I. Vovk, *Evidence for strong extragalactic magnetic fields from Fermi observations of TeV blazars*, *Science* **328** (2010) 73 [[1006.3504](#)].
- [53] H. Tashiro, W. Chen, F. Ferrer and T. Vachaspati, *Search for CP Violating Signature of Intergalactic Magnetic Helicity in the Gamma Ray Sky*, *Mon. Not. Roy. Astron. Soc.* **445** (2014) L41 [[1310.4826](#)].
- [54] M. S. Turner and L. M. Widrow, *Inflation Produced, Large Scale Magnetic Fields*, *Phys. Rev.* **D37** (1988) 2743.
- [55] B. Ratra, *Cosmological 'seed' magnetic field from inflation*, *Astrophys. J.* **391** (1992) L1.
- [56] A. Diaz-Gil, J. Garcia-Bellido, M. Garcia Perez and A. Gonzalez-Arroyo, *Magnetic field production during preheating at the electroweak scale*, *Phys. Rev. Lett.* **100** (2008) 241301 [[0712.4263](#)].
- [57] K. Jedamzik and G. Sigl, *The Evolution of the Large-Scale Tail of Primordial Magnetic Fields*, *Phys. Rev.* **D83** (2011) 103005 [[1012.4794](#)].

- [58] PLANCK collaboration, *Planck 2015 results. XIX. Constraints on primordial magnetic fields*, *Astron. Astrophys.* **594** (2016) A19 [1502.01594].
- [59] K. Subramanian and J. D. Barrow, *Magnetohydrodynamics in the early universe and the damping of nonlinear Alfvén waves*, *Phys. Rev.* **D58** (1998) 083502 [astro-ph/9712083].
- [60] K. Subramanian and J. D. Barrow, *Microwave background signals from tangled magnetic fields*, *Phys. Rev. Lett.* **81** (1998) 3575 [astro-ph/9803261].
- [61] T. R. Seshadri and K. Subramanian, *CMBR polarization signals from tangled magnetic fields*, *Phys. Rev. Lett.* **87** (2001) 101301 [astro-ph/0012056].
- [62] R. Keisler, C. L. Reichardt, K. A. Aird, B. A. Benson, L. E. Bleem, J. E. Carlstrom et al., *A Measurement of the Damping Tail of the Cosmic Microwave Background Power Spectrum with the South Pole Telescope*, *Astrophys. J.* **743** (2011) 28 [1105.3182].
- [63] POLARBEAR collaboration, *POLARBEAR Constraints on Cosmic Birefringence and Primordial Magnetic Fields*, *Phys. Rev.* **D92** (2015) 123509 [1509.02461].
- [64] SPT collaboration, *Measurements of Sub-degree B-mode Polarization in the Cosmic Microwave Background from 100 Square Degrees of SPTpol Data*, *Astrophys. J.* **807** (2015) 151 [1503.02315].
- [65] A. Kosowsky and A. Loeb, *Faraday rotation of microwave background polarization by a primordial magnetic field*, *Astrophys. J.* **469** (1996) 1 [astro-ph/9601055].
- [66] A. Kosowsky, T. Kahniashvili, G. Lavrelashvili and B. Ratra, *Faraday rotation of the Cosmic Microwave Background polarization by a stochastic magnetic field*, *Phys. Rev.* **D71** (2005) 043006 [astro-ph/0409767].
- [67] L. Pogosian, A. P. S. Yadav, Y.-F. Ng and T. Vachaspati, *Primordial Magnetism in the CMB: Exact Treatment of Faraday Rotation and WMAP7 Bounds*, *Phys. Rev.* **D84** (2011) 043530 [1106.1438].
- [68] A. Einstein, *Erklärung der Perihelbewegung des Merkur aus der allgemeinen Relativitätstheorie. (German) [Explanation of the perihelical motion of Mercury from the General Theory of Relativity]*, .
- [69] A. Einstein, *Über das Relativitätsprinzip und die aus demselben gezogenen Folgerungen. (German) [On the Relativity Principle and the conclusions drawn from it]*, *Jahrbuch der Radioaktivität und Elektronik* **4** (1907) 411.
- [70] A. Einstein, *Die formale Grundlage der allgemeinen Relativitätstheorie. (German) [The formal basis of the Theory of General Relativity]*, .
- [71] D. Hilbert, *Grundlagen der Physik, Erste Mitteilung, vorgelegt in der Sitzung vom 20. November 1915*, *Gott. Nach.* **1915** (1915) 395.
- [72] P. Coles, *Einstein, Eddington and the 1919 eclipse*, *ASP Conf. Ser.* **252** (2001) 21 [astro-ph/0102462].

- [73] D. Lovelock, *The Einstein tensor and its generalizations*, *J. Math. Phys.* **12** (1971) 498.
- [74] G. R. Dvali, G. Gabadadze and M. Porrati, *4-D gravity on a brane in 5-D Minkowski space*, *Phys. Lett.* **B485** (2000) 208 [[hep-th/0005016](#)].
- [75] J. C. Mather et al., *Measurement of the Cosmic Microwave Background spectrum by the COBE FIRAS instrument*, *Astrophys. J.* **420** (1994) 439.
- [76] R. Maartens, *Is the Universe homogeneous?*, *Phil. Trans. Roy. Soc. Lond.* **A369** (2011) 5115 [[1104.1300](#)].
- [77] R. Jimenez, R. Maartens, A. R. Khalifeh, R. R. Caldwell, A. F. Heavens and L. Verde, *Measuring the Homogeneity of the Universe*, **1902.11298**.
- [78] E. Hubble, *A Relation between Distance and Radial Velocity among Extra-Galactic Nebulae*, *Proceedings of the National Academy of Science* **15** (1929) 168.
- [79] J. M. Bardeen, *Gauge-invariant cosmological perturbations*, *Phys. Rev. D* **22** (1980) 1882.
- [80] R. Durrer, *Gauge Invariant Cosmological Perturbation Theory: A General Study and It's Application to the Texture Scenario of Structure Formation*, *Fundamentals of Cosmic Physics* **3** (1994) 209 [[astro-ph/9311041](#)].
- [81] A. Lewis, A. Challinor and A. Lasenby, *Efficient computation of CMB anisotropies in closed FRW models*, *Astrophys. J.* **538** (2000) 473 [[astro-ph/9911177](#)].
- [82] J. Lesgourgues, *The Cosmic Linear Anisotropy Solving System (CLASS) I: Overview*, *arXiv e-prints* (2011) arXiv:1104.2932 [[1104.2932](#)].
- [83] D. Blas, J. Lesgourgues and T. Tram, *The Cosmic Linear Anisotropy Solving System (CLASS). Part II: Approximation schemes*, *Journal of Cosmology and Astro-Particle Physics* **2011** (2011) 034 [[1104.2933](#)].
- [84] S. Dodelson, *Modern cosmology*. Academic Press, San Diego, CA, 2003.
- [85] SNLS collaboration, *SALT: A Spectral adaptive Light curve Template for Type Ia supernovae*, *Astron. Astrophys.* **443** (2005) 781 [[astro-ph/0506583](#)].
- [86] SNLS collaboration, *SALT2: Using distant supernovae to improve the use of Type Ia supernovae as distance indicators*, *Astron. Astrophys.* **466** (2007) 11 [[astro-ph/0701828](#)].
- [87] SDSS collaboration, *Improved cosmological constraints from a joint analysis of the SDSS-II and SNLS supernova samples*, *Astron. Astrophys.* **568** (2014) A22 [[1401.4064](#)].
- [88] J. T. Nielsen, A. Guffanti and S. Sarkar, *Marginal evidence for cosmic acceleration from Type Ia supernovae*, *Sci. Rep.* **6** (2016) 35596 [[1506.01354](#)].
- [89] M. Hicken, W. M. Wood-Vasey, S. Blondin, P. Challis, S. Jha, P. L. Kelly et al., *Improved Dark Energy Constraints from ~100 New CfA Supernova Type Ia Light Curves*, *Astrophys. J.* **700** (2009) 1097 [[0901.4804](#)].

- [90] C. Contreras, M. Hamuy, M. M. Phillips, G. Folatelli, N. B. Suntzeff, S. E. Persson et al., *The Carnegie Supernova Project: First Photometry Data Release of Low-Redshift Type Ia Supernovae*, **139** (2010) 519 [[0910.3330](#)].
- [91] M. Ganeshalingam, W. Li and A. V. Filippenko, *Constraints on dark energy with the LOSS SN Ia sample*, *Mon. Not. Roy. Astron. Soc.* **433** (2013) 2240 [[1307.0824](#)].
- [92] G. Aldering, G. Adam, P. Antilogus, P. Astier, R. Bacon, S. Bongard et al., *Overview of the Nearby Supernova Factory*, in *Survey and Other Telescope Technologies and Discoveries*, J. A. Tyson and S. Wolff, eds., vol. 4836 of , pp. 61–72, Dec., 2002, [DOI](#).
- [93] W. Hu and N. Sugiyama, *Small scale cosmological perturbations: An Analytic approach*, *Astrophys. J.* **471** (1996) 542 [[astro-ph/9510117](#)].
- [94] D. J. Eisenstein and W. Hu, *Baryonic Features in the Matter Transfer Function*, *Astrophys. J.* **496** (1998) 605 [[astro-ph/9709112](#)].
- [95] D. H. Weinberg, M. J. Mortonson, D. J. Eisenstein, C. Hirata, A. G. Riess and E. Rozo, *Observational probes of cosmic acceleration*, *Phys. Rep.* **530** (2013) 87 [[1201.2434](#)].
- [96] F. Beutler, C. Blake, M. Colless, D. H. Jones, L. Staveley-Smith, L. Campbell et al., *The 6dF Galaxy Survey: baryon acoustic oscillations and the local Hubble constant*, *Mon. Not. Roy. Astron. Soc.* **416** (2011) 3017 [[1106.3366](#)].
- [97] A. J. Ross, L. Samushia, C. Howlett, W. J. Percival, A. Burden and M. Manera, *The clustering of the SDSS DR7 main Galaxy sample – I. A 4 per cent distance measure at $z = 0.15$* , *Mon. Not. Roy. Astron. Soc.* **449** (2015) 835 [[1409.3242](#)].
- [98] BOSS collaboration, *The clustering of galaxies in the completed SDSS-III Baryon Oscillation Spectroscopic Survey: cosmological analysis of the DR12 galaxy sample*, *Mon. Not. Roy. Astron. Soc.* **470** (2017) 2617 [[1607.03155](#)].
- [99] BOSS collaboration, *Quasar-Lyman α Forest Cross-Correlation from BOSS DR11 : Baryon Acoustic Oscillations*, *JCAP* **1405** (2014) 027 [[1311.1767](#)].
- [100] M. Ata et al., *The clustering of the SDSS-IV extended Baryon Oscillation Spectroscopic Survey DR14 quasar sample: first measurement of baryon acoustic oscillations between redshift 0.8 and 2.2*, *Mon. Not. Roy. Astron. Soc.* **473** (2018) 4773 [[1705.06373](#)].
- [101] U. Seljak and M. Zaldarriaga, *A Line of sight integration approach to cosmic microwave background anisotropies*, *Astrophys. J.* **469** (1996) 437 [[astro-ph/9603033](#)].
- [102] J. R. Bond and G. Efstathiou, *Cosmic background radiation anisotropies in universes dominated by nonbaryonic dark matter*, *Astrophys. J.* **285** (1984) L45.
- [103] J. R. Bond and G. Efstathiou, *The statistics of cosmic background radiation fluctuations*, *Mon. Not. Roy. Astron. Soc.* **226** (1987) 655.
- [104] W. Hu and M. J. White, *CMB anisotropies: Total angular momentum method*, *Phys. Rev.* **D56** (1997) 596 [[astro-ph/9702170](#)].

- [105] L. Pogosian, P. S. Corasaniti, C. Stephan-Otto, R. Crittenden and R. Nichol, *Tracking dark energy with the ISW effect: Short and long-term predictions*, *Phys. Rev. D* **72** (2005) 103519 [[astro-ph/0506396](#)].
- [106] A. Lewis and A. Challinor, *Weak gravitational lensing of the CMB*, *Phys. Rept.* **429** (2006) 1 [[astro-ph/0601594](#)].
- [107] R. A. Sunyaev and Y. B. Zeldovich, *The Observations of Relic Radiation as a Test of the Nature of X-Ray Radiation from the Clusters of Galaxies*, *Comments on Astrophysics and Space Physics* **4** (1972) 173.
- [108] J. P. Ostriker and E. T. Vishniac, *Generation of microwave background fluctuations from nonlinear perturbations at the ERA of galaxy formation*, *Astrophys. J. Lett.* **306** (1986) L51.
- [109] J. E. Carlstrom, P. A. R. Ade, K. A. Aird, B. A. Benson, L. E. Bleem, S. Busetti et al., *The 10 Meter South Pole Telescope*, *Publ. Astron. Soc. Pac.* **123** (2011) 568 [[0907.4445](#)].
- [110] K. T. Story, C. L. Reichardt, Z. Hou, R. Keisler, K. A. Aird, B. A. Benson et al., *A Measurement of the Cosmic Microwave Background Damping Tail from the 2500-Square-Degree SPT-SZ Survey*, *Astrophys. J.* **779** (2013) 86 [[1210.7231](#)].
- [111] D. S. Swetz, P. A. R. Ade, M. Amiri, J. W. Appel, E. S. Battistelli, B. Burger et al., *Overview of the Atacama Cosmology Telescope: Receiver, Instrumentation, and Telescope Systems*, *Astrophys. J., Suppl. Ser.* **194** (2011) 41 [[1007.0290](#)].
- [112] S. Das, B. D. Sherwin, P. Aguirre, J. W. Appel, J. R. Bond, C. S. Carvalho et al., *Detection of the Power Spectrum of Cosmic Microwave Background Lensing by the Atacama Cosmology Telescope*, *Physical Review Letters* **107** (2011) 021301 [[1103.2124](#)].
- [113] A. Challinor and A. Lewis, *Linear power spectrum of observed source number counts*, *Phys. Rev. D* **84** (2011) 043516 [[1105.5292](#)].
- [114] M. LoVerde and N. Afshordi, *Extended Limber Approximation*, *Phys. Rev. D* **78** (2008) 123506 [[0809.5112](#)].
- [115] J. A. Peacock and R. E. Smith, *Halo occupation numbers and galaxy bias*, *Mon. Not. Roy. Astron. Soc.* **318** (2000) 1144 [[astro-ph/0005010](#)].
- [116] U. Seljak, *Analytic model for galaxy and dark matter clustering*, *Mon. Not. Roy. Astron. Soc.* **318** (2000) 203 [[astro-ph/0001493](#)].
- [117] A. Cooray and R. K. Sheth, *Halo Models of Large Scale Structure*, *Phys. Rept.* **372** (2002) 1 [[astro-ph/0206508](#)].
- [118] R. Takahashi, M. Sato, T. Nishimichi, A. Taruya and M. Oguri, *Revising the Halofit Model for the Nonlinear Matter Power Spectrum*, *Astrophys. J.* **761** (2012) 152 [[1208.2701](#)].

- [119] A. Mead, J. Peacock, C. Heymans, S. Joudaki and A. Heavens, *An accurate halo model for fitting non-linear cosmological power spectra and baryonic feedback models*, *Mon. Not. Roy. Astron. Soc.* **454** (2015) 1958 [[1505.07833](#)].
- [120] A. Mead, C. Heymans, L. Lombriser, J. Peacock, O. Steele and H. Winther, *Accurate halo-model matter power spectra with dark energy, massive neutrinos and modified gravitational forces*, *Mon. Not. Roy. Astron. Soc.* **459** (2016) 1468 [[1602.02154](#)].
- [121] DES collaboration, *Dark Energy Survey year 1 results: Cosmological constraints from galaxy clustering and weak lensing*, *Phys. Rev.* **D98** (2018) 043526 [[1708.01530](#)].
- [122] K.-W. Ng and G.-C. Liu, *Correlation functions of CMB anisotropy and polarization*, *Int. J. Mod. Phys.* **D8** (1999) 61 [[astro-ph/9710012](#)].
- [123] G. Chon, A. Challinor, S. Prunet, E. Hivon and I. Szapudi, *Fast estimation of polarization power spectra using correlation functions*, *Mon. Not. Roy. Astron. Soc.* **350** (2004) 914 [[astro-ph/0303414](#)].
- [124] R. G. Crittenden and N. Turok, *Looking for a cosmological constant with the rees-sciama effect*, *Phys. Rev. Lett.* **76** (1996) 575.
- [125] T. Giannantonio, R. Scranton, R. G. Crittenden, R. C. Nichol, S. P. Boughn, A. D. Myers et al., *Combined analysis of the integrated Sachs-Wolfe effect and cosmological implications*, *Phys. Rev.* **D77** (2008) 123520 [[0801.4380](#)].
- [126] T. Giannantonio, R. Crittenden, R. Nichol and A. J. Ross, *The significance of the integrated Sachs-Wolfe effect revisited*, *Mon. Not. Roy. Astron. Soc.* **426** (2012) 2581 [[1209.2125](#)].
- [127] B. Stölzner, A. Cuoco, J. Lesgourgues and M. Bilicki, *Updated tomographic analysis of the integrated Sachs-Wolfe effect and implications for dark energy*, *Phys. Rev.* **D97** (2018) 063506 [[1710.03238](#)].
- [128] A. J. Shajib and E. L. Wright, *Measurement of the integrated Sachs-Wolfe effect using the AllWISE data release*, *Astrophys. J.* **827** (2016) 116 [[1604.03939](#)].
- [129] S. Ferraro, B. D. Sherwin and D. N. Spergel, *WISE measurement of the integrated Sachs-Wolfe effect*, *Phys. Rev.* **D91** (2015) 083533 [[1401.1193](#)].
- [130] H. Motohashi, A. A. Starobinsky and J. Yokoyama, *Inflation with a constant rate of roll*, *JCAP* **1509** (2015) 018 [[1411.5021](#)].
- [131] H. Motohashi and A. A. Starobinsky, *Constant-roll inflation: confrontation with recent observational data*, *EPL* **117** (2017) 39001 [[1702.05847](#)].
- [132] K. Freese, J. A. Frieman and A. V. Olinto, *Natural inflation with pseudo nambu-goldstone bosons*, *Phys. Rev. Lett.* **65** (1990) 3233.
- [133] A. R. Liddle, P. Parsons and J. D. Barrow, *Formalizing the slow roll approximation in inflation*, *Phys. Rev.* **D50** (1994) 7222 [[astro-ph/9408015](#)].

- [134] J.-O. Gong and E. D. Stewart, *The Density perturbation power spectrum to second order corrections in the slow roll expansion*, *Phys. Lett.* **B510** (2001) 1 [[astro-ph/0101225](#)].
- [135] J. T. G. Ghersi and A. V. Frolov, *Two-point correlators revisited: Fast and slow scales in multifield models of inflation*, *JCAP* **1705** (2017) 047 [[1609.04770](#)].
- [136] J. Martin, H. Motohashi and T. Suyama, *Ultra Slow-Roll Inflation and the non-Gaussianity Consistency Relation*, *Phys. Rev.* **D87** (2013) 023514 [[1211.0083](#)].
- [137] V. F. Mukhanov, *Gravitational Instability of the Universe Filled with a Scalar Field*, *JETP Lett.* **41** (1985) 493.
- [138] M. Sasaki, *Large Scale Quantum Fluctuations in the Inflationary Universe*, *Prog. Theor. Phys.* **76** (1986) 1036.
- [139] V. F. Mukhanov, *Quantum theory of gauge-invariant cosmological perturbations*, *Zh. Eksp. Teor. Fiz.* **94** (1988) 1.
- [140] V. P. Ermakov, *Second order differential equations. Conditions of complete integrability*, *Univ. Izv. Kiev* **III** (1880) .
- [141] E. Pinney, *The nonlinear differential equation $y'' + p(x)y' + cy^{>3} = 0$* , *Proceedings of the American Mathematical Society* **1** (1950) 681.
- [142] A. Kamenshchik and G. Venturi, *Remarks on the method of comparison equations (generalized WKB method) and the generalized Ermakov-Pinney equation*, *Russ. Phys. J.* **52** (2009) 1339 [[math-ph/0506017](#)].
- [143] K. Freese and W. H. Kinney, *Natural Inflation: Consistency with Cosmic Microwave Background Observations of Planck and BICEP2*, *JCAP* **1503** (2015) 044 [[1403.5277](#)].
- [144] A. Karam, L. Marzola, T. Pappas, A. Racioppi and K. Tamvakis, *Constant-Roll (Quasi-)Linear Inflation*, *JCAP* **1805** (2018) 011 [[1711.09861](#)].
- [145] A. Lewis and S. Bridle, *Cosmological parameters from CMB and other data: A Monte Carlo approach*, *Phys. Rev.* **D66** (2002) 103511 [[astro-ph/0205436](#)].
- [146] B. Audren, J. Lesgourgues, K. Benabed and S. Prunet, *Conservative constraints on early cosmology with MONTE PYTHON*, *JCAP* **2** (2013) 001 [[1210.7183](#)].
- [147] D. Blas, J. Lesgourgues and T. Tram, *The Cosmic Linear Anisotropy Solving System (CLASS). Part II: Approximation schemes*, *JCAP* **7** (2011) 034 [[1104.2933](#)].
- [148] K. Tzirakis and W. H. Kinney, *Inflation over the hill*, *Phys. Rev.* **D75** (2007) 123510 [[astro-ph/0701432](#)].
- [149] J. Gilbert, *Power-law density fluctuations from inflation*, *Phys. Rev. D* **52** (1995) 5486.
- [150] L. Anguelova, P. Suranyi and L. C. R. Wijewardhana, *Systematics of Constant Roll Inflation*, *JCAP* **1802** (2018) 004 [[1710.06989](#)].

- [151] Y.-F. Cai, X. Chen, M. H. Namjoo, M. Sasaki, D.-G. Wang and Z. Wang, *Revisiting non-Gaussianity from non-attractor inflation models*, *JCAP* **1805** (2018) 012 [[1712.09998](#)].
- [152] Z. Yi and Y. Gong, *On the constant-roll inflation*, *JCAP* **1803** (2018) 052 [[1712.07478](#)].
- [153] S. Nojiri, S. D. Odintsov and V. K. Oikonomou, *Constant-roll Inflation in $F(R)$ Gravity*, *Class. Quant. Grav.* **34** (2017) 245012 [[1704.05945](#)].
- [154] H. Motohashi and A. A. Starobinsky, *$f(R)$ constant-roll inflation*, *Eur. Phys. J.* **C77** (2017) 538 [[1704.08188](#)].
- [155] M. J. P. Morse and W. H. Kinney, *Large- η constant-roll inflation is never an attractor*, *Phys. Rev.* **D97** (2018) 123519 [[1804.01927](#)].
- [156] D. Grasso and H. R. Rubinstein, *Magnetic fields in the early universe*, *Phys. Rept.* **348** (2001) 163 [[astro-ph/0009061](#)].
- [157] D. Ryu, H. Kang, J. Cho and S. Das, *Turbulence and Magnetic Fields in the Large Scale Structure of the Universe*, *Science* **320** (2008) 909 [[0805.2466](#)].
- [158] D. Ryu, D. R. G. Schleicher, R. A. Treumann, C. G. Tsagas and L. M. Widrow, *Magnetic Fields in the Large-Scale Structure of the Universe*, *Space Sci. Rev.* **166** (2012) 1 [[1109.4055](#)].
- [159] D. R. G. Schleicher, M. Latif, J. Schober, W. Schmidt, S. Bovino, C. Federrath et al., *Magnetic fields during high redshift structure formation*, *Astronomische Nachrichten* **334** (2013) 531 [[1211.4356](#)].
- [160] M. A. Latif, D. R. G. Schleicher, W. Schmidt and J. Niemeyer, *The small-scale dynamo and the amplification of magnetic fields in massive primordial haloes*, *Mon. Not. Roy. Astron. Soc.* **432** (2013) 668 [[1212.1619](#)].
- [161] J. M. Wagstaff, R. Banerjee, D. Schleicher and G. Sigl, *Magnetic field amplification by the small-scale dynamo in the early Universe*, *Phys. Rev.* **D89** (2014) 103001 [[1304.4723](#)].
- [162] A. M. Beck, K. Dolag, H. Lesch and P. P. Kronberg, *Strong magnetic fields and large rotation measures in protogalaxies by supernova seeding*, *Mon. Not. Roy. Astron. Soc.* **435** (2013) 3575 [[1308.3440](#)].
- [163] D. Seifried, R. Banerjee and D. Schleicher, *Supernova explosions in magnetized, primordial dark matter haloes*, *Mon. Not. Roy. Astron. Soc.* **440** (2014) 24 [[1311.4991](#)].
- [164] T. Vachaspati, *Magnetic fields from cosmological phase transitions*, *Phys. Lett.* **B265** (1991) 258.
- [165] A. Brandenburg, T. Kahniashvili and A. G. Tevzadze, *Nonhelical inverse transfer of a decaying turbulent magnetic field*, *Phys. Rev. Lett.* **114** (2015) 075001 [[1404.2238](#)].

- [166] A. Brandenburg and T. Kahniashvili, *Classes of hydrodynamic and magnetohydrodynamic turbulent decay*, *Phys. Rev. Lett.* **118** (2017) 055102 [[1607.01360](#)].
- [167] J. Reppin and R. Banerjee, *Nonhelical turbulence and the inverse transfer of energy: A parameter study*, *Phys. Rev.* **E96** (2017) 053105 [[1708.07717](#)].
- [168] A. Brandenburg, T. Kahniashvili, S. Mandal, A. R. Pol, A. G. Tevzadze and T. Vachaspati, *Evolution of hydromagnetic turbulence from the electroweak phase transition*, *Phys. Rev.* **D96** (2017) 123528 [[1711.03804](#)].
- [169] A. Brandenburg, R. Durrer, T. Kahniashvili, S. Mandal and W. W. Yin, *Statistical Properties of Scale-Invariant Helical Magnetic Fields and Applications to Cosmology*, *JCAP* **1808** (2018) 034 [[1804.01177](#)].
- [170] P. J. Kernan, G. D. Starkman and T. Vachaspati, *Big bang nucleosynthesis constraints on primordial magnetic fields*, *Phys. Rev.* **D54** (1996) 7207 [[astro-ph/9509126](#)].
- [171] D. Grasso and H. R. Rubinstein, *Revisiting nucleosynthesis constraints on primordial magnetic fields*, *Phys. Lett.* **B379** (1996) 73 [[astro-ph/9602055](#)].
- [172] B.-l. Cheng, A. V. Olinto, D. N. Schramm and J. W. Truran, *Constraints on the strength of primordial magnetic fields from big bang nucleosynthesis revisited*, *Phys. Rev.* **D54** (1996) 4714 [[astro-ph/9606163](#)].
- [173] D. G. Yamazaki and M. Kusakabe, *Effects of power law primordial magnetic field on big bang nucleosynthesis*, *Phys. Rev.* **D86** (2012) 123006 [[1212.2968](#)].
- [174] A. Diaz-Gil, J. Garcia-Bellido, M. Garcia Perez and A. Gonzalez-Arroyo, *Primordial magnetic fields from preheating at the electroweak scale*, *JHEP* **07** (2008) 043 [[0805.4159](#)].
- [175] P. Adshead, J. T. Giblin, T. R. Scully and E. I. Sfakianakis, *Magnetogenesis from axion inflation*, *JCAP* **1610** (2016) 039 [[1606.08474](#)].
- [176] R. Durrer and A. Neronov, *Cosmological Magnetic Fields: Their Generation, Evolution and Observation*, *Astron. Astrophys. Rev.* **21** (2013) 62 [[1303.7121](#)].
- [177] N. Barnaby, R. Namba and M. Peloso, *Observable non-gaussianity from gauge field production in slow roll inflation, and a challenging connection with magnetogenesis*, *Phys. Rev.* **D85** (2012) 123523 [[1202.1469](#)].
- [178] A. J. Long, E. Sabancilar and T. Vachaspati, *Leptogenesis and Primordial Magnetic Fields*, *JCAP* **1402** (2014) 036 [[1309.2315](#)].
- [179] A. Mack, T. Kahniashvili and A. Kosowsky, *Microwave background signatures of a primordial stochastic magnetic field*, *Phys. Rev.* **D65** (2002) 123004 [[astro-ph/0105504](#)].
- [180] A. Lewis, *CMB anisotropies from primordial inhomogeneous magnetic fields*, *Phys. Rev.* **D70** (2004) 043011 [[astro-ph/0406096](#)].

- [181] F. Finelli, F. Paci and D. Paoletti, *The Impact of Stochastic Primordial Magnetic Fields on the Scalar Contribution to Cosmic Microwave Background Anisotropies*, *Phys. Rev.* **D78** (2008) 023510 [[0803.1246](#)].
- [182] D. Paoletti, F. Finelli and F. Paci, *The full contribution of a stochastic background of magnetic fields to CMB anisotropies*, *Mon. Not. Roy. Astron. Soc.* **396** (2009) 523 [[0811.0230](#)].
- [183] J. R. Shaw and A. Lewis, *Massive neutrinos and magnetic fields in the early universe*, *Phys. Rev. D* **81** (2010) 043517 [[0911.2714](#)].
- [184] K. Subramanian and J. D. Barrow, *Small-scale microwave background anisotropies due to tangled primordial magnetic fields*, *Mon. Not. Roy. Astron. Soc.* **335** (2002) L57 [[astro-ph/0205312](#)].
- [185] K. Subramanian, T. R. Seshadri and J. Barrow, *Small - scale CMB polarization anisotropies due to tangled primordial magnetic fields*, *Mon. Not. Roy. Astron. Soc.* **344** (2003) L31 [[astro-ph/0303014](#)].
- [186] POLARBEAR collaboration, *A Measurement of the Cosmic Microwave Background B-Mode Polarization Power Spectrum at Sub-Degree Scales with POLARBEAR*, *Astrophys. J.* **794** (2014) 171 [[1403.2369](#)].
- [187] BICEP2 collaboration, *Detection of B-Mode Polarization at Degree Angular Scales by BICEP2*, *Phys. Rev. Lett.* **112** (2014) 241101 [[1403.3985](#)].
- [188] BICEP2, KECK ARRAY collaboration, *Improved Constraints on Cosmology and Foregrounds from BICEP2 and Keck Array Cosmic Microwave Background Data with Inclusion of 95 GHz Band*, *Phys. Rev. Lett.* **116** (2016) 031302 [[1510.09217](#)].
- [189] C. Bonvin, R. Durrer and R. Maartens, *Can primordial magnetic fields be the origin of the BICEP2 data?*, *Phys. Rev. Lett.* **112** (2014) 191303 [[1403.6768](#)].
- [190] D. Paoletti and F. Finelli, *Constraints on a stochastic background of primordial magnetic fields with WMAP and South Pole Telescope data*, *Physics Letters B* **726** (2013) 45 [[1208.2625](#)].
- [191] D. Larson, J. Dunkley, G. Hinshaw, E. Komatsu, M. R.olta, C. L. Bennett et al., *Seven-year Wilkinson Microwave Anisotropy Probe (WMAP) Observations: Power Spectra and WMAP-derived Parameters*, *Astrophys. J. Suppl.* **192** (2011) 16 [[1001.4635](#)].
- [192] SPT-3G collaboration, *SPT-3G: A Next-Generation Cosmic Microwave Background Polarization Experiment on the South Pole Telescope*, *Proc. SPIE Int. Soc. Opt. Eng.* **9153** (2014) 91531P [[1407.2973](#)].
- [193] POLARBEAR collaboration, *The POLARBEAR-2 and the Simons Array Experiment*, *J. Low. Temp. Phys.* **184** (2016) 805 [[1512.07299](#)].
- [194] D. R. Sutton, C. Feng and C. L. Reichardt, *Current and Future Constraints on Primordial Magnetic Fields*, *Astrophys. J.* **846** (2017) 164 [[1702.01871](#)].

- [195] D. D. Harari, J. D. Hayward and M. Zaldarriaga, *Depolarization of the cosmic microwave background by a primordial magnetic field and its effect upon temperature anisotropy*, *Phys. Rev.* **D55** (1997) 1841 [[astro-ph/9608098](#)].
- [196] S. De, L. Pogosian and T. Vachaspati, *CMB Faraday rotation as seen through the Milky Way*, *Phys. Rev.* **D88** (2013) 063527 [[1305.7225](#)].
- [197] L. Pogosian and A. Zucca, *Searching for Primordial Magnetic Fields with CMB B-modes*, *Class. Quant. Grav.* **35** (2018) 124004 [[1801.08936](#)].
- [198] K. Subramanian, *The origin, evolution and signatures of primordial magnetic fields*, *Rept. Prog. Phys.* **79** (2016) 076901 [[1504.02311](#)].
- [199] J. D. Barrow, P. G. Ferreira and J. Silk, *Constraints on a primordial magnetic field*, *Phys. Rev. Lett.* **78** (1997) 3610 [[astro-ph/9701063](#)].
- [200] J. D. Barrow, *Cosmological limits on slightly skew stresses*, *Phys. Rev.* **D55** (1997) 7451 [[gr-qc/9701038](#)].
- [201] T. Kahniashvili and B. Ratra, *Effects of Cosmological Magnetic Helicity on the Cosmic Microwave Background*, *Phys. Rev.* **D71** (2005) 103006 [[astro-ph/0503709](#)].
- [202] K. E. Kunze, *Effects of helical magnetic fields on the cosmic microwave background*, *Phys. Rev. D* **85** (2012) 083004 [[1112.4797](#)].
- [203] M. Ballardini, F. Finelli and D. Paoletti, *CMB anisotropies generated by a stochastic background of primordial magnetic fields with non-zero helicity*, *JCAP* **1510** (2015) 031 [[1412.1836](#)].
- [204] K. Jedamzik, V. Katalinic and A. V. Olinto, *Damping of cosmic magnetic fields*, *Phys. Rev.* **D57** (1998) 3264 [[astro-ph/9606080](#)].
- [205] C. Bonvin, C. Caprini and R. Durrer, *Magnetic fields from inflation: The CMB temperature anisotropies*, *Phys. Rev.* **D88** (2013) 083515 [[1308.3348](#)].
- [206] R. Durrer and C. Caprini, *Primordial magnetic fields and causality*, *JCAP* **0311** (2003) 010 [[astro-ph/0305059](#)].
- [207] K. Jedamzik and G. Sigl, *Evolution of the large-scale tail of primordial magnetic fields*, *Phys. Rev. D* **83** (2011) 103005 [[1012.4794](#)].
- [208] T. Kahniashvili, A. G. Tevzadze and B. Ratra, *Phase Transition Generated Cosmological Magnetic Field at Large Scales*, *Astrophys. J.* **726** (2011) 78 [[0907.0197](#)].
- [209] M. Giovannini, *Magnetized initial conditions for CMB anisotropies*, *Phys. Rev.* **D70** (2004) 123507 [[astro-ph/0409594](#)].
- [210] M. Giovannini, *Tight coupling expansion and fully inhomogeneous magnetic fields*, *Phys. Rev.* **D74** (2006) 063002 [[astro-ph/0606759](#)].
- [211] PLANCK collaboration, *Planck 2015 results. XI. CMB power spectra, likelihoods, and robustness of parameters*, *Astron. Astrophys.* **594** (2016) A11 [[1507.02704](#)].

- [212] PLANCK collaboration, *Planck intermediate results. XXX. The angular power spectrum of polarized dust emission at intermediate and high Galactic latitudes*, *Astron. Astrophys.* **586** (2016) A133 [[1409.5738](#)].
- [213] T. Kahniashvili, A. G. Tevzadze, S. K. Sethi, K. Pandey and B. Ratra, *Primordial magnetic field limits from cosmological data*, *Phys. Rev. D* **82** (2010) 083005 [[1009.2094](#)].
- [214] A. Yadav, L. Pogosian and T. Vachaspati, *Probing primordial magnetism with off-diagonal correlators of CMB polarization*, *Phys. Rev. D* **86** (2012) 123009 [[1207.3356](#)].
- [215] L. Pogosian, *Searching for primordial magnetism with multifrequency cosmic microwave background experiments*, *Mon. Not. Roy. Astron. Soc.* **438** (2014) 2508 [[1311.2926](#)].
- [216] TOPICAL CONVENERNERS: K.N. ABAZAJIAN, J.E. CARLSTROM, A.T. LEE collaboration, *Neutrino Physics from the Cosmic Microwave Background and Large Scale Structure*, *Astropart. Phys.* **63** (2015) 66 [[1309.5383](#)].
- [217] L. Amendola, G. Ballesteros and V. Pettorino, *Effects of modified gravity on B-mode polarization*, *Phys. Rev. D* **90** (2014) 043009 [[1405.7004](#)].
- [218] M. Raveri, C. Baccigalupi, A. Silvestri and S.-Y. Zhou, *Measuring the speed of cosmological gravitational waves*, *Phys. Rev. D* **91** (2015) 061501 [[1405.7974](#)].
- [219] A. Moss and L. Pogosian, *Did BICEP2 see vector modes? First B-mode constraints on cosmic defects*, *Phys. Rev. Lett.* **112** (2014) 171302 [[1403.6105](#)].
- [220] A. Avgoustidis, E. J. Copeland, A. Moss, L. Pogosian, A. Pourtsidou and D. A. Steer, *Constraints on the fundamental string coupling from B-mode experiments*, *Phys. Rev. Lett.* **107** (2011) 121301 [[1105.6198](#)].
- [221] M. Ostrogradsky, *Mémoires sur les équations différentielles, relatives au problème des isopérimètres*, *Mem. Acad. St. Petersburg* **6** (1850) 385.
- [222] B. Ratra and P. J. E. Peebles, *Cosmological consequences of a rolling homogeneous scalar field*, *Phys. Rev. D* **37** (1988) 3406.
- [223] C. Wetterich, *Cosmology and the fate of dilatation symmetry*, *Nuclear Physics B* **302** (1988) 668 .
- [224] C. Brans and R. H. Dicke, *Mach's principle and a relativistic theory of gravitation*, *Phys. Rev.* **124** (1961) 925.
- [225] C. Armendariz-Picon, T. Damour and V. F. Mukhanov, *k - inflation*, *Phys. Lett.* **B458** (1999) 209 [[hep-th/9904075](#)].
- [226] C. Armendariz-Picon, V. F. Mukhanov and P. J. Steinhardt, *Essentials of k essence*, *Phys. Rev. D* **63** (2001) 103510 [[astro-ph/0006373](#)].
- [227] C. Deffayet, O. Pujolas, I. Sawicki and A. Vikman, *Imperfect Dark Energy from Kinetic Gravity Braiding*, *JCAP* **1010** (2010) 026 [[1008.0048](#)].

- [228] T. Kobayashi, M. Yamaguchi and J. Yokoyama, *G-inflation: Inflation driven by the Galileon field*, *Phys. Rev. Lett.* **105** (2010) 231302 [[1008.0603](#)].
- [229] O. Pujolas, I. Sawicki and A. Vikman, *The Imperfect Fluid behind Kinetic Gravity Braiding*, *JHEP* **11** (2011) 156 [[1103.5360](#)].
- [230] A. Nicolis, R. Rattazzi and E. Trincherini, *Energy's and amplitudes' positivity*, *JHEP* **05** (2010) 095 [[0912.4258](#)].
- [231] LIGO SCIENTIFIC, VIRGO collaboration, *GW170817: Observation of Gravitational Waves from a Binary Neutron Star Inspiral*, *Phys. Rev. Lett.* **119** (2017) 161101 [[1710.05832](#)].
- [232] A. De Felice, R. Kase and S. Tsujikawa, *Vainshtein mechanism in second-order scalar-tensor theories*, *Phys. Rev.* **D85** (2012) 044059 [[1111.5090](#)].
- [233] K. Koyama, G. Niz and G. Tasinato, *Effective theory for the Vainshtein mechanism from the Horndeski action*, *Phys. Rev.* **D88** (2013) 021502 [[1305.0279](#)].
- [234] F. Piazza and F. Vernizzi, *Effective Field Theory of Cosmological Perturbations*, *Class. Quant. Grav.* **30** (2013) 214007 [[1307.4350](#)].
- [235] J. Gleyzes, D. Langlois, F. Piazza and F. Vernizzi, *Essential Building Blocks of Dark Energy*, *JCAP* **1308** (2013) 025 [[1304.4840](#)].
- [236] E. Bellini and I. Sawicki, *Maximal freedom at minimum cost: linear large-scale structure in general modifications of gravity*, *JCAP* **1407** (2014) 050 [[1404.3713](#)].
- [237] B. Hu, M. Raveri, N. Frusciante and A. Silvestri, *Effective Field Theory of Cosmic Acceleration: an implementation in CAMB*, *Phys. Rev.* **D89** (2014) 103530 [[1312.5742](#)].
- [238] M. Raveri, B. Hu, N. Frusciante and A. Silvestri, *Effective Field Theory of Cosmic Acceleration: constraining dark energy with CMB data*, *Phys. Rev.* **D90** (2014) 043513 [[1405.1022](#)].
- [239] R. G. Crittenden, G.-B. Zhao, L. Pogosian, L. Samushia and X. Zhang, *Fables of reconstruction: controlling bias in the dark energy equation of state*, *Journal of Cosmology and Astro-Particle Physics* **2012** (2012) 048 [[1112.1693](#)].
- [240] R. G. Crittenden, L. Pogosian and G.-B. Zhao, *Investigating dark energy experiments with principal components*, *JCAP* **0912** (2009) 025 [[astro-ph/0510293](#)].
- [241] L. Amendola, M. Kunz and D. Sapone, *Measuring the dark side (with weak lensing)*, *JCAP* **0804** (2008) 013 [[0704.2421](#)].
- [242] L. Amendola, M. Kunz, M. Motta, I. D. Saltas and I. Sawicki, *Observables and unobservables in dark energy cosmologies*, *Phys. Rev.* **D87** (2013) 023501 [[1210.0439](#)].
- [243] A. Hojjati, L. Pogosian and G.-B. Zhao, *Testing gravity with CAMB and CosmoMC*, *JCAP* **1108** (2011) 005 [[1106.4543](#)].

- [244] A. Zucca, L. Pogosian, A. Silvestri and G.-B. Zhao, *MGCAMB with massive neutrinos and dynamical dark energy*, [1901.05956](#).
- [245] I. Sawicki and E. Bellini, *Limits of quasistatic approximation in modified-gravity cosmologies*, *Phys. Rev.* **D92** (2015) 084061 [[1503.06831](#)].
- [246] J. Khoury and A. Weltman, *Chameleon cosmology*, *Phys. Rev.* **D69** (2004) 044026 [[astro-ph/0309411](#)].
- [247] P. Brax, C. van de Bruck, A.-C. Davis, J. Khoury and A. Weltman, *Detecting dark energy in orbit - The Cosmological chameleon*, *Phys. Rev.* **D70** (2004) 123518 [[astro-ph/0408415](#)].
- [248] P. Brax, C. van de Bruck, A.-C. Davis and D. Shaw, *The Dilaton and Modified Gravity*, *Phys. Rev.* **D82** (2010) 063519 [[1005.3735](#)].
- [249] K. Hinterbichler and J. Khoury, *Symmetron Fields: Screening Long-Range Forces Through Local Symmetry Restoration*, *Phys. Rev. Lett.* **104** (2010) 231301 [[1001.4525](#)].
- [250] P. Brax, A.-C. Davis, B. Li and H. A. Winther, *A Unified Description of Screened Modified Gravity*, *Phys. Rev.* **D86** (2012) 044015 [[1203.4812](#)].
- [251] P. Brax, A.-C. Davis and B. Li, *Modified Gravity Tomography*, *Phys. Lett.* **B715** (2012) 38 [[1111.6613](#)].
- [252] P. Brax and P. Valageas, *Impact on the power spectrum of Screening in Modified Gravity Scenarios*, *Phys. Rev.* **D88** (2013) 023527 [[1305.5647](#)].
- [253] C. Llinares and D. Mota, *Releasing scalar fields: cosmological simulations of scalar-tensor theories for gravity beyond the static approximation*, *Phys. Rev. Lett.* **110** (2013) 161101 [[1302.1774](#)].
- [254] S. Capozziello, S. Carloni and A. Troisi, *Quintessence without scalar fields*, *Recent Res. Dev. Astron. Astrophys.* **1** (2003) 625 [[astro-ph/0303041](#)].
- [255] S. M. Carroll, V. Duvvuri, M. Trodden and M. S. Turner, *Is cosmic speed - up due to new gravitational physics?*, *Phys. Rev.* **D70** (2004) 043528 [[astro-ph/0306438](#)].
- [256] W. Hu and I. Sawicki, *Models of $f(R)$ Cosmic Acceleration that Evade Solar-System Tests*, *Phys. Rev.* **D76** (2007) 064004 [[0705.1158](#)].
- [257] S. A. Appleby and R. A. Battye, *Do consistent $F(R)$ models mimic General Relativity plus Λ ?*, *Phys. Lett.* **B654** (2007) 7 [[0705.3199](#)].
- [258] A. A. Starobinsky, *Disappearing cosmological constant in $f(R)$ gravity*, *JETP Lett.* **86** (2007) 157 [[0706.2041](#)].
- [259] P. Brax, *Environmental variation of constants in screened modified theories of gravity*, *Phys. Rev.* **D90** (2014) 023505 [[1310.2562](#)].
- [260] J. Sakstein, B. Jain and V. Vikram, *Detecting modified gravity in the stars*, *Int. J. Mod. Phys.* **D23** (2014) 1442002 [[1409.3708](#)].

- [261] T. Damour and A. M. Polyakov, *The String dilaton and a least coupling principle*, *Nucl. Phys.* **B423** (1994) 532 [[hep-th/9401069](#)].
- [262] P. Brax, A.-C. Davis, B. Li, H. A. Winther and G.-B. Zhao, *Systematic simulations of modified gravity: chameleon models*, *JCAP* **1304** (2013) 029 [[1303.0007](#)].
- [263] PLANCK collaboration, *Planck 2015 results. XV. Gravitational lensing*, *Astron. Astrophys.* **594** (2016) A15 [[1502.01591](#)].
- [264] PLANCK collaboration, *Planck 2013 results. XVI. Cosmological parameters*, *Astron. Astrophys.* **571** (2014) A16 [[1303.5076](#)].
- [265] G. E. Addison, Y. Huang, D. J. Watts, C. L. Bennett, M. Halpern, G. Hinshaw et al., *Quantifying discordance in the 2015 Planck CMB spectrum*, *Astrophys. J.* **818** (2016) 132 [[1511.00055](#)].
- [266] BOSS collaboration, *The clustering of galaxies in the SDSS-III Baryon Oscillation Spectroscopic Survey: baryon acoustic oscillations in the Data Releases 10 and 11 Galaxy samples*, *Mon. Not. Roy. Astron. Soc.* **441** (2014) 24 [[1312.4877](#)].
- [267] SDSS collaboration, *Cosmological Constraints from the SDSS Luminous Red Galaxies*, *Phys. Rev.* **D74** (2006) 123507 [[astro-ph/0608632](#)].
- [268] G.-B. Zhao, S. Saito, W. J. Percival, A. J. Ross, F. Montesano, M. Viel et al., *The clustering of galaxies in the SDSS-III Baryon Oscillation Spectroscopic Survey: weighing the neutrino mass using the galaxy power spectrum of the CMASS sample*, *Mon. Not. Roy. Astron. Soc.* **436** (2013) 2038 [[1211.3741](#)].
- [269] M. Kilbinger, L. Fu, C. Heymans, F. Simpson, J. Benjamin, T. Erben et al., *CFHTLenS: combined probe cosmological model comparison using 2D weak gravitational lensing*, *Mon. Not. Roy. Astron. Soc.* **430** (2013) 2200 [[1212.3338](#)].
- [270] LSST collaboration, *LSST: from Science Drivers to Reference Design and Anticipated Data Products*, *Astrophys. J.* **873** (2019) 111 [[0805.2366](#)].
- [271] A. Hojjati, A. Plahn, A. Zucca, L. Pogosian, P. Brax, A.-C. Davis et al., *Searching for scalar gravitational interactions in current and future cosmological data*, *Phys. Rev.* **D93** (2016) 043531 [[1511.05962](#)].
- [272] A. Lewis and A. Challinor, *The 21cm angular-power spectrum from the dark ages*, *Phys. Rev. D* **76** (2007) 083005 [[astro-ph/0702600](#)].
- [273] A. Hojjati, G.-B. Zhao, L. Pogosian, A. Silvestri, R. Crittenden and K. Koyama, *Cosmological tests of General Relativity: a principal component analysis*, *Phys. Rev.* **D85** (2012) 043508 [[1111.3960](#)].
- [274] M. Tegmark, A. Taylor and A. Heavens, *Karhunen-Loeve eigenvalue problems in cosmology: How should we tackle large data sets?*, *Astrophys. J.* **480** (1997) 22 [[astro-ph/9603021](#)].
- [275] D. Huterer and G. Starkman, *Parameterization of dark-energy properties: A Principal-component approach*, *Phys. Rev. Lett.* **90** (2003) 031301 [[astro-ph/0207517](#)].

- [276] G.-B. Zhao, L. Pogosian, A. Silvestri and J. Zylberberg, *Cosmological Tests of General Relativity with Future Tomographic Surveys*, *Phys. Rev. Lett.* **103** (2009) 241301 [0905.1326].
- [277] A. Hojjati, *Degeneracies in parametrized modified gravity models*, *JCAP* **1301** (2013) 009 [1210.3903].
- [278] H. Wilcox et al., *The XMM Cluster Survey: Testing chameleon gravity using the profiles of clusters*, *Mon. Not. Roy. Astron. Soc.* **452** (2015) 1171 [1504.03937].
- [279] P. Brax, A.-C. Davis, B. Li, H. A. Winther and G.-B. Zhao, *Systematic simulations of modified gravity: symmetron and dilaton models*, *Journal of Cosmology and Astro-Particle Physics* **2012** (2012) 002 [1206.3568].
- [280] G.-B. Zhao et al., *The extended Baryon Oscillation Spectroscopic Survey: a cosmological forecast*, *Mon. Not. Roy. Astron. Soc.* **457** (2016) 2377 [1510.08216].
- [281] G.-B. Zhao, D. Bacon, R. Maartens, M. Santos and A. Raccanelli, *Model-independent constraints on dark energy and modified gravity with the SKA*, [1501.03840](#).
- [282] D. Bacon et al., *Synergy between the Large Synoptic Survey Telescope and the Square Kilometre Array*, *PoS AASKA14* (2015) 145 [1501.03977].
- [283] J. Espejo, S. Peirone, M. Raveri, K. Koyama, L. Pogosian and A. Silvestri, *Phenomenology of Large Scale Structure in scalar-tensor theories: joint prior covariance of w_{DE} , Σ and μ in Horndeski*, [1809.01121](#).
- [284] E. Bertschinger, *On the Growth of Perturbations as a Test of Dark Energy*, *Astrophys. J.* **648** (2006) 797 [astro-ph/0604485].
- [285] Y.-S. Song, G.-B. Zhao, D. Bacon, K. Koyama, R. C. Nichol and L. Pogosian, *Complementarity of weak lensing and peculiar velocity measurements in testing general relativity*, *Phys. Rev.D* **84** (2011) 083523 [1011.2106].
- [286] F. Simpson, C. Heymans, D. Parkinson, C. Blake, M. Kilbinger, J. Benjamin et al., *CFHTLenS: testing the laws of gravity with tomographic weak lensing and redshift-space distortions*, *Mon. Not. Roy. Astron. Soc.* **429** (2013) 2249 [1212.3339].
- [287] R. G. Crittenden, L. Pogosian and G.-B. Zhao, *Investigating dark energy experiments with principal components*, *JCAP* **12** (2009) 025 [astro-ph/0510293].
- [288] R. G. Crittenden, G.-B. Zhao, L. Pogosian, L. Samushia and X. Zhang, *Fables of reconstruction: controlling bias in the dark energy equation of state*, *JCAP* **2** (2012) 048 [1112.1693].
- [289] G.-B. Zhao, M. Raveri, L. Pogosian, Y. Wang, R. G. Crittenden, W. J. Handley et al., *Dynamical dark energy in light of the latest observations*, *Nature Astronomy* **1** (2017) 627 [1701.08165].
- [290] Y. Wang, L. Pogosian, G.-B. Zhao and A. Zucca, *Evolution of Dark Energy Reconstructed from the Latest Observations*, *ApJL* **869** (2018) L8 [1807.03772].

- [291] T. Holsclaw, U. Alam, B. Sansó, H. Lee, K. Heitmann, S. Habib et al., *Nonparametric reconstruction of the dark energy equation of state*, *Phys. Rev.D* **82** (2010) 103502 [[1009.5443](#)].
- [292] T. Holsclaw, U. Alam, B. Sansó, H. Lee, K. Heitmann, S. Habib et al., *Nonparametric Dark Energy Reconstruction from Supernova Data*, *Physical Review Letters* **105** (2010) 241302 [[1011.3079](#)].
- [293] A. Silvestri, L. Pogosian and R. V. Buniy, *Practical approach to cosmological perturbations in modified gravity*, *Phys. Rev.* **D87** (2013) 104015 [[1302.1193](#)].
- [294] R. Bean and M. Tangmatitham, *Current constraints on the cosmic growth history*, *Phys. Rev. D* **81** (2010) 083534 [[1002.4197](#)].
- [295] M. Zaldarriaga and U. Seljak, *An all sky analysis of polarization in the microwave background*, *Phys. Rev.* **D55** (1997) 1830 [[astro-ph/9609170](#)].
- [296] A. Lewis, *Efficient sampling of fast and slow cosmological parameters*, *Phys. Rev. D* **87** (2013) 103529 [[1304.4473](#)].
- [297] PLANCK collaboration, *Planck 2015 results. XIV. Dark energy and modified gravity*, *Astron. Astrophys.* **594** (2016) A14 [[1502.01590](#)].
- [298] M. Chevallier and D. Polarski, *Accelerating universes with scaling dark matter*, *Int. J. Mod. Phys.* **D10** (2001) 213 [[gr-qc/0009008](#)].
- [299] E. V. Linder, *Exploring the expansion history of the universe*, *Phys. Rev. Lett.* **90** (2003) 091301 [[astro-ph/0208512](#)].
- [300] DES collaboration, *Dark Energy Survey Year 1 Results: Constraints on Extended Cosmological Models from Galaxy Clustering and Weak Lensing*, [1810.02499](#).
- [301] J. N. Dossett, M. Ishak and J. Moldenhauer, *Testing General Relativity at Cosmological Scales: Implementation and Parameter Correlations*, *Phys. Rev.* **D84** (2011) 123001 [[1109.4583](#)].
- [302] M. Zumalacrregui, E. Bellini, I. Sawicki and J. Lesgourgues, *hi class: Horndeski in the Cosmic Linear Anisotropy Solving System*, [1605.06102](#).
- [303] J. Bloomfield, *A Simplified Approach to General Scalar-Tensor Theories*, *JCAP* **1312** (2013) 044 [[1304.6712](#)].
- [304] L. Pogosian and A. Silvestri, *What can cosmology tell us about gravity? Constraining Horndeski gravity with Σ and μ* , *Phys. Rev.* **D94** (2016) 104014 [[1606.05339](#)].
- [305] EUCLID collaboration, *Euclid Definition Study Report*, *arXiv e-prints* (2011) [arXiv:1110.3193](#) [[1110.3193](#)].
- [306] LSST SCIENCE COLLABORATION collaboration, *LSST Science Book, Version 2.0*, *arXiv e-prints* (2009) [arXiv:0912.0201](#) [[0912.0201](#)].
- [307] A. G. Riess et al., *A 2.4% Determination of the Local Value of the Hubble Constant*, *Astrophys. J.* **826** (2016) 56 [[1604.01424](#)].

- [308] A. G. Riess, S. Casertano, W. Yuan, L. M. Macri and D. Scolnic, *Large Magellanic Cloud Cepheid Standards Provide a 1% Foundation for the Determination of the Hubble Constant and Stronger Evidence for Physics Beyond LambdaCDM*, [1903.07603](#).
- [309] D. Scott, *The Standard Model of Cosmology: A Skeptic's Guide*, 2018, [1804.01318](#), <https://inspirehep.net/record/1665882/files/1804.01318.pdf>.
- [310] Y. Wang, L. Pogosian, G.-B. Zhao and A. Zucca, *Evolution of dark energy reconstructed from the latest observations*, *Astrophys. J.* **869** (2018) L8 [[1807.03772](#)].
- [311] BOSS collaboration, *The clustering of galaxies in the completed SDSS-III Baryon Oscillation Spectroscopic Survey: tomographic BAO analysis of DR12 combined sample in Fourier space*, *Mon. Not. Roy. Astron. Soc.* **466** (2017) 762 [[1607.03153](#)].
- [312] BOSS collaboration, *The clustering of galaxies in the completed SDSS-III Baryon Oscillation Spectroscopic Survey: tomographic BAO analysis of DR12 combined sample in configuration space*, *Mon. Not. Roy. Astron. Soc.* **469** (2017) 3762 [[1607.03154](#)].
- [313] BOSS collaboration, *Baryon acoustic oscillations in the Ly-alpha forest of BOSS DR11 quasars*, *Astron. Astrophys.* **574** (2015) A59 [[1404.1801](#)].
- [314] M. Moresco, L. Pozzetti, A. Cimatti, R. Jimenez, C. Maraston, L. Verde et al., *A 6% measurement of the Hubble parameter at $z \sim 0.45$: direct evidence of the epoch of cosmic re-acceleration*, *JCAP* **1605** (2016) 014 [[1601.01701](#)].
- [315] P. G. Bergmann, *Comments on the scalar-tensor theory*, *Int. J. Theor. Phys.* **1** (1968) 25.
- [316] K. Nordtvedt, Jr., *Post-Newtonian Metric for a General Class of Scalar-Tensor Gravitational Theories and Observational Consequences.*, *Astrophys. J.* **161** (1970) 1059.
- [317] R. V. Wagoner, *Scalar-tensor theory and gravitational waves*, *Phys. Rev. D* **1** (1970) 3209.
- [318] B. Boisseau, G. Esposito-Farese, D. Polarski and A. A. Starobinsky, *Reconstruction of a scalar tensor theory of gravity in an accelerating universe*, *Phys. Rev. Lett.* **85** (2000) 2236 [[gr-qc/0001066](#)].
- [319] G. Esposito-Farese and D. Polarski, *Scalar tensor gravity in an accelerating universe*, *Phys. Rev.* **D63** (2001) 063504 [[gr-qc/0009034](#)].
- [320] L. Perivolaropoulos, *Crossing the phantom divide barrier with scalar tensor theories*, *JCAP* **0510** (2005) 001 [[astro-ph/0504582](#)].
- [321] L. Pogosian and A. Silvestri, *The pattern of growth in viable $f(R)$ cosmologies*, *Phys. Rev.* **D77** (2008) 023503 [[0709.0296](#)].
- [322] PLANCK collaboration, *Planck 2015 results. XXI. The integrated Sachs-Wolfe effect*, *Astron. Astrophys.* **594** (2016) A21 [[1502.01595](#)].

- [323] B. Hu, M. Raveri, N. Frusciante and A. Silvestri, *EFTCAMB/EFTCosmoMC: Numerical Notes v3.0*, [1405.3590](#).
- [324] Y.-S. Song, W. Hu and I. Sawicki, *The Large Scale Structure of $f(R)$ Gravity*, *Phys. Rev. D* **75** (2007) 044004 [[astro-ph/0610532](#)].

Appendix A

Linear DES 1YR data

Since the phenomenological parameterization implemented in MGCAMB has no prescription for nonlinear structure formation, in order to use the DES data, we remove the nonlinear data in the same way as was done in [297, 300]. We define

$$\Delta\chi^2 \equiv (\mathbf{t}_{\text{NL}} - \mathbf{t}_{\text{L}})^T \mathbf{C}^{-1} (\mathbf{t}_{\text{NL}} - \mathbf{t}_{\text{L}}), \quad (\text{A.1})$$

where \mathbf{t}_{NL} and \mathbf{t}_{L} represent the data vector containing the nonlinear and linear theory predictions, respectively, in the Λ CDM best-fit model and \mathbf{C} is the DES Year 1 full covariance matrix. The nonlinear predictions are obtained using the Halofit model present in the default CAMB. We then find the data point that contributes the most to $\Delta\chi^2$ and remove it. We then repeat the procedure until $\Delta\chi^2$ is less than a threshold. We arbitrarily define three set of cuts on the data: a “soft” cut where the $\Delta\chi^2$ threshold is 10, a “standard” cut with the threshold set to 5 and finally an “aggressive” cut with $\Delta\chi^2 < 1$. The number of data points removed are 88, 118 and 178, respectively. As an example, in Figs. 3.7, 3.8, 3.9 and 3.10 we show the “soft” cut applied to the DES galaxy-galaxy angular correlation function $w_{ii}(\theta)$, the cosmic shear ξ_{\pm}^{ij} and the tangential shear γ_t^{ij} , where i, j label the redshift bins. The blue and orange lines represent the nonlinear and linear theoretical predictions and the grey shaded lines show the data which is excluded by the above method.

The code used to produce the data cuts is also available at https://github.com/alexzucca90/DES_linear_data and can be used for any value of $\Delta\chi^2$ desired by the user.

Appendix B

Galaxy Clustering - Weak lensing theory with Weyl potential.

Here we describe the modifications to the DES likelihood required for evaluating the weak lensing observables ξ_+ , ξ_- and γ_t . The standard DES likelihood in CosmoMC assumes $\Phi + \Psi = 2\Phi$ and then relates the potential Φ to the density perturbation δ using the Poisson equation,

$$k^2\Phi = -\frac{3}{2a} \left(\frac{H_0}{c}\right)^2 \Omega_m \delta. \quad (\text{B.1})$$

In MGCAMB, the Poisson equation is modified and $\Phi = \Psi$ does not hold. Hence, we compute the Weyl potential power spectrum directly,

$$P_{\text{Weyl}}(k, z) = 2\pi^2 k \left(k^2 \frac{\tilde{\Phi}(z) + \tilde{\Psi}(z)}{2} \right)^2 P_{\mathcal{R}}(k), \quad (\text{B.2})$$

where the tilde quantities are the transfer functions at redshift z and $P_{\mathcal{R}}(k)$ is the primordial power spectrum. The cosmic shear correlations ξ_{\pm} are then given by

$$\xi_{\pm}^{ij}(\theta) = \frac{1}{2\pi} \int d\ell \ell J_{0/4}(\theta\ell) P_{\kappa}^{ij}(\ell), \quad (\text{B.3})$$

where $J_{0/4}(x)$ is the Bessel function of the first kind of order zero for ξ_+ and order four for ξ_- . Here, P_{κ} (in the Limber approximation) is given by

$$P_{\kappa}^{ij}(\ell) = \int_0^{\chi_H} d\chi \frac{q^i(\chi)q^j(\chi)}{\chi^2} P_{\text{Weyl}}\left(\frac{\ell + 1/2}{\chi}, \chi\right), \quad (\text{B.4})$$

where $q^i(\chi)$ is the lensing efficiency function,

$$q^i(\chi) = \chi \int_{\chi}^{\chi_H} d\chi' n^i(\chi') \frac{\chi' - \chi}{\chi'}, \quad (\text{B.5})$$

n^i denotes the effective number density of galaxies normalized to one and the Weyl power spectrum is evaluated using the linear theory only. The nonlinear data is removed according to the procedure explained in App. A.

Similarly, to calculate the tangential shear of background galaxies around foreground galaxies, we define the Weyl-matter power spectrum as

$$P_{\text{W/m}} = 2\pi^2 k \left(k^2 \frac{\tilde{\Phi}(z) + \tilde{\Psi}(z)}{2} \right) \tilde{\delta}_m(k, z) P_{\mathcal{R}}(k). \quad (\text{B.6})$$

The tangential shear is then given by

$$\gamma_t(\theta) = b \int \frac{d\ell}{2\pi} \ell J_2(\theta\ell) \int dz \frac{g(z)n(z)}{\chi(z)} P_{\text{W/m}} \left(\frac{\ell}{\chi}, \chi \right). \quad (\text{B.7})$$

Appendix C

EFT formalism for GBD

Here we collect the EFT mapping for the Generalised Brans-Dicke Theories, The coefficients for the equation for the perturbation (8.20) are given by [323]

$$A = \frac{ca^2}{m_0^2} + \frac{3}{4}a^2 \frac{(\mathcal{H}\Omega')^2}{1+\Omega}, \quad (\text{C.1})$$

$$B = \frac{\dot{c}a^2}{m_0^2} + 4\mathcal{H} \frac{ca^2}{m_0^2} + a \frac{\mathcal{H}\Omega'}{4(1+\Omega)} \left[3 \frac{(\rho_Q + P_Q)a^2}{m_0^2} + 3\mathcal{H}^2 a \Omega' \left(4 + \frac{\dot{\mathcal{H}}}{\mathcal{H}^2} + a \frac{\Omega''}{\Omega'} \right) \right] \\ + \frac{a\mathcal{H}\Omega'}{2(1+\Omega)} \left[\frac{3}{2} a \mathcal{H}^2 \Omega' - \frac{ca^2}{m_0^2} \right], \quad (\text{C.2})$$

$$C = \mathcal{H} \frac{\dot{c}a^2}{m_0^2} + (6\mathcal{H}^2 - 2\dot{\mathcal{H}}) \frac{ca^2}{m_0^2} + \frac{3}{2} a \mathcal{H}\Omega' (\ddot{\mathcal{H}} - 2\mathcal{H}^3) \\ - a \frac{\mathcal{H}\Omega'}{4(1+\Omega)} \left[-3 \frac{\dot{P}_Q a^2}{m_0^2} - 3\mathcal{H}^2 \frac{(\rho_Q + P_Q)a^2}{m_0^2} - 3a\mathcal{H}^3 \left(a\Omega'' + 6\Omega' + 2 \frac{\dot{\mathcal{H}}}{\mathcal{H}^2} \Omega' \right) \right] \\ + \frac{a\mathcal{H}\Omega'}{2(1+\Omega)} \left[-\frac{1}{2} \frac{\dot{\rho}_Q a^2}{m_0^2} - \mathcal{H} \frac{ca^2}{m_0^2} + \frac{3}{2} a \mathcal{H}\Omega' (3\mathcal{H}^2 - \dot{\mathcal{H}}) \right], \quad (\text{C.3})$$

$$D = \frac{ca^2}{m_0^2} + \frac{3(a\mathcal{H}\Omega')^2}{4(1+\Omega)} \quad (\text{C.4})$$

$$E = \left\{ \frac{ca^2}{m_0^2} + \frac{3(a\mathcal{H}\Omega')^2}{4(1+\Omega)} \right\} \dot{h} + \frac{a\mathcal{H}\Omega'}{4(1+\Omega)} \frac{(3\delta P_{m,\nu} - \delta\rho_{m,\nu})a^2}{m_0^2}, \quad (\text{C.5})$$

where h in the last equation is the usual metric perturbation in synchronous gauge as in CAMB.

Appendix D

Modifications to EFTCAMB

In this Appendix we describe the modifications to the EFTCAMB code that we performed in Chapter 8¹

D.1 The new structure of the code

The structure of this EFTCAMB mod is illustrated in Fig. 8.15a. It extends the structure of the original EFTCAMB code explained in [323]. The red lines represent the new modules and flags added in the code.

D.2 Implementation of the modified equations

D.2.1 Designer Background

As was already done in the original EFTCAMB, the background cosmological dynamics is studied with a designer approach. Defining the dark energy fractional density as $X(a) \equiv \rho_{\text{DE}}(a)/\rho_{\text{DE}}(a=1)$, the background equations are

$$\mathcal{H}^2 = \frac{a^2}{3m_0^2}(\rho_m + \rho_\nu) + H_0^2\Omega_\Lambda X a^2, \quad (\text{D.1})$$

$$\dot{\mathcal{H}} = -\frac{1}{2}\mathcal{H}^2 - \frac{a^2}{2m_0^2}(P_m + P_\nu) + \Omega_\Lambda H_0^2 a^2(aX' + 3X), \quad (\text{D.2})$$

$$\ddot{\mathcal{H}} = \frac{a^2}{m_0^2}\mathcal{H}\rho_m \left(\frac{1}{6} + w_m + \frac{3}{2}w_m^2\right) + \frac{a^2}{m_0^2} \left(\frac{\mathcal{H}}{6}\rho_\nu - \frac{\mathcal{H}}{2}P_\nu - \frac{1}{2}\dot{P}_\nu\right) \quad (\text{D.3})$$

$$+ \mathcal{H}a^2\Omega_\Lambda H_0^2 \left(2X + \frac{5}{2}aX' + \frac{1}{2}a^2X''\right), \quad (\text{D.4})$$

¹The code is available at <https://github.com/alexzucca90/EFTCAMB-DErecon>.

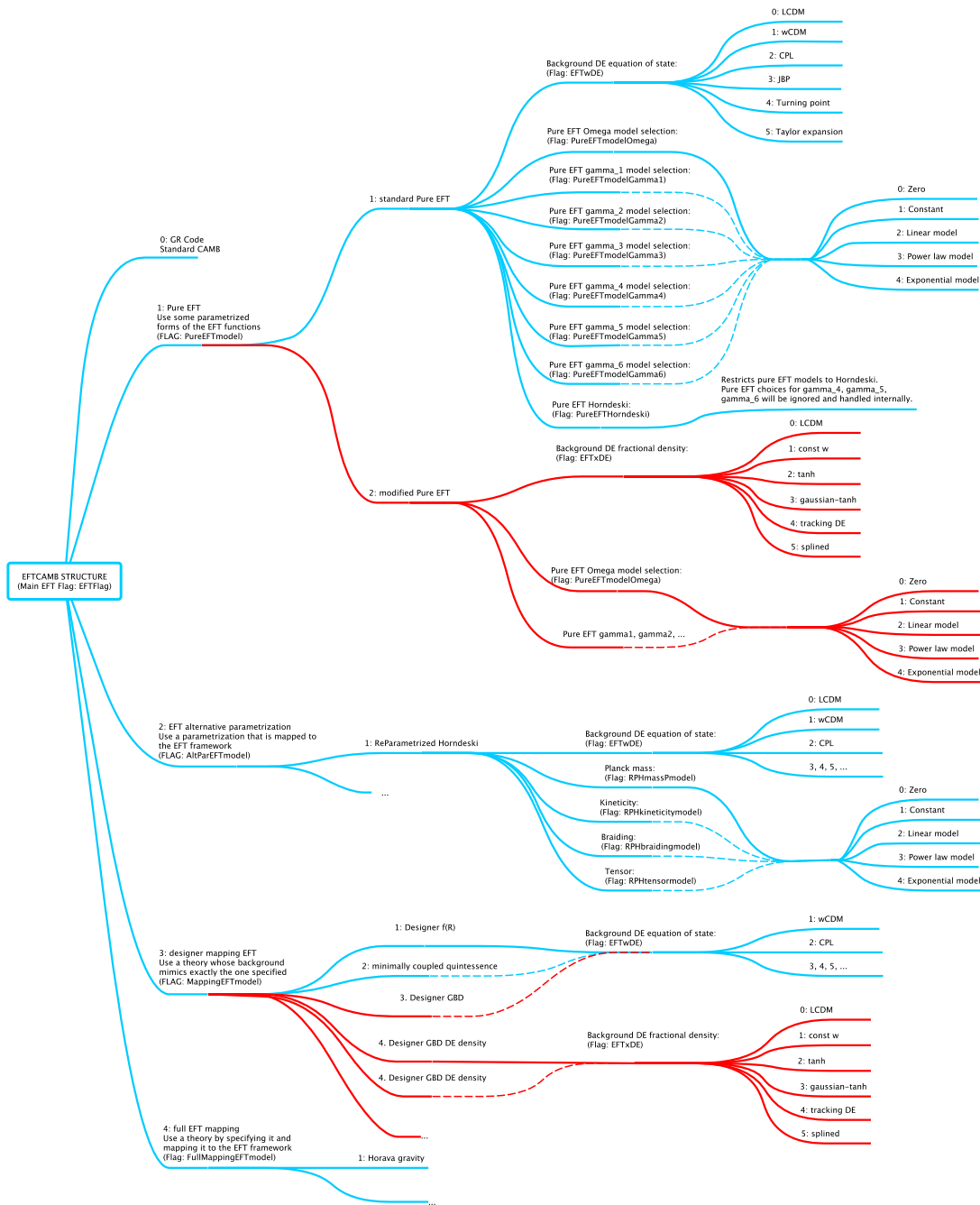


Figure 8.15a: Flowchart of the new EFTCAMB mod used in Chapter 8. The red regions are the new modules introduced in the code.

where the prime stands for derivative w.r.t. the scale factor a and the dot stands for derivative w.r.t. the conformal time η . Here, ρ_m and P_m are the energy density and pressure for the matter fields (baryons, dark matter, radiation and massless neutrinos) and ρ_ν and P_ν the energy density and the pressure of massive neutrinos. The massive neutrinos contributions are shown separately to stress the fact that in EFTCAMB, as well as in the original CAMB code, the massive neutrinos interactions are taken into account in a slightly different way (although the approach is the same for CAMB and EFTCAMB) due to the complicated time evolution of massive neutrinos. As defined above, X is the fractional dark energy density. The matter fields obey the continuity equation

$$\dot{\rho}_m + 3\mathcal{H}(\rho_m + P_m) = 0, \quad (\text{D.5})$$

while from the dark energy density one can reconstruct the effective dark energy equation of state according to

$$w_{\text{DE}} = -\frac{1}{3}a\frac{X'}{X} - 1. \quad (\text{D.6})$$

With the setup above, the background expansion history of the Universe is fixed by specifying a form for $X_{\text{DE}}(a)$. Then, once the background is chosen, one can determine the other EFT functions, Λ , c and their derivatives in terms of the expansion history $\mathcal{H}(a)$ and $\Omega(a)$. One has

$$\frac{ca^2}{m_0^2} = \left(\mathcal{H}^2 - \dot{\mathcal{H}}\right) \left(\Omega + \frac{a\Omega'}{2}\right) - \frac{a^2\mathcal{H}^2}{2}\Omega'' - \frac{1}{2}H_0^2a^3\Omega_\Lambda X', \quad (\text{D.7})$$

$$\frac{\Lambda a^2}{m_0^2} = -\Omega \left(2\dot{\mathcal{H}} + \mathcal{H}^2\right) - a\Omega' \left(2\mathcal{H}^2 + \dot{\mathcal{H}}\right) - a^2\mathcal{H}^2\Omega'' - \Omega_\Lambda H_0^2 a^3 X' - 3\Omega_\Lambda H_0^2 X a^2, \quad (\text{D.8})$$

$$\frac{\dot{c}a^2}{m_0^2} = \frac{\mathcal{H}}{2} \left(-aX'' - X'\right) \Omega_\Lambda H_0^2 a^3 - \Omega \left(\ddot{\mathcal{H}} - 4\dot{\mathcal{H}}\mathcal{H} + 2\mathcal{H}^3\right) \quad (\text{D.9})$$

$$+ \frac{a\Omega'}{2} \left(-\ddot{\mathcal{H}} + \dot{\mathcal{H}}\mathcal{H} + \mathcal{H}^3\right) + \frac{1}{2}a^2\mathcal{H}\Omega'' \left(\mathcal{H}^2 - 3\dot{\mathcal{H}}\right) - \frac{1}{2}a^3\mathcal{H}^3\Omega''',$$

$$\frac{\dot{\Lambda}a^2}{m_0^2} = -2\Omega \left(\ddot{\mathcal{H}} - \dot{\mathcal{H}}\mathcal{H} - \mathcal{H}^3\right) - a\Omega' \left(\ddot{\mathcal{H}} + 5\dot{\mathcal{H}}\mathcal{H} - \mathcal{H}^3\right) - a^2\Omega''\mathcal{H} \left(2\mathcal{H}^2 + 3\dot{\mathcal{H}}\right) - a^3\mathcal{H}^3\Omega''' \quad (\text{D.10})$$

$$- \mathcal{H}\Omega_\Lambda H_0^2 a^3 (aX'' + X').$$

Effective Dark Energy density parametrizations

We implemented several models for the background expansion history, motivated by the recent work presented in [310].

-The Λ CDM expansion history given by a constant $X(a)$. This can be chosen by setting $\text{EFTxDE} = 0$.

-The w CDM model:

$$X(a) = a^{-3(1+w_{\text{DE}})}, \quad (\text{D.11})$$

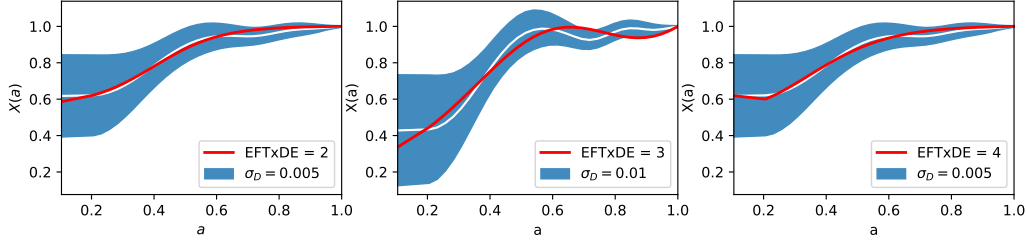


Figure 8.15b: The three types of parametrizations of $X(a)$ plotted over three Dark Energy density reconstructions form. The white lines correspond to the reconstructed best-fit $X(a)$ and the blue shaded regions represent the 68% C.L.. The red lines represent the parametrized $X(a)$ given by the equations (D.12) (left panel), (D.13) (center panel) and (D.14) (right panel).

where w_{DE} is chosen through the flag `EFTxDE_wDE`. This model can be chosen by setting `EFTxDE = 1`

- Hyperbolic tangent shape:

$$X(a) = A \tanh [B(a - C)] + 1 - A \tanh [B(1 - C)], \quad (\text{D.12})$$

where in the code notation we have $A = \text{EFTxDE_A}$, $B = \text{EFTxDE_B}$, etc. This model can be chosen by setting `EFTxDE = 2`. An example of this function can be seen in the left panel of Fig. 8.15b.

- Hyperbolic tangent normalized with a gaussian shape,,

$$X(a) = \left(A + B e^{-C(a-C)^2} \right) \tanh[E(a-D)] + 1 - \left(A + B e^{-C(1-C)^2} \right) \tanh[E(1-D)]. \quad (\text{D.13})$$

This model can be chosen by setting `EFTxDE = 3` and an example can be seen in the center panel of Fig. 8.15b.

- Hyperbolic tangent with tracking behaviour at earlier times,

$$A \tanh [B(a - C)] + D a^{-3} + 1 - A \tanh [B(1 - C)] - D. \quad (\text{D.14})$$

This model can be chosen by setting `EFTxDE = 4` and an example can be seen in Fig. 8.15b.

- The user can also introduce an interpolated dark energy density, by setting `EFTxDE = 5` and providing a table with a , $X(a)$, dX/da , and reading that file through `xDE_filename`.

D.3 Designer mapping EFT models

EFTCAMB allows the user to study the cosmology of specific single field DE/MG models by mapping them into the EFT language. The current version of EFTCAMB implements the designer $f(R)$ model, that we review in Sect. D.3.1 with the new $X(a)$ formalism,

and a minimally coupled quintessence model (with canonical kinetic term). Since the latter cannot reproduce an effective dark energy equation of state that crosses the phantom barrier $w_{\text{DE}} < -1$, we did not modify this class of models. Instead we choose to work with the generalized Brans-Dicke (GBD) theories for which we introduced the designer approach described in Chapter 8.

D.3.1 Designer $f(R)$

The designer approach to $f(R)$ gravity is described in detail in [321, 324] as well as in the original EFTCAMB notes [323]. Here we review the main ideas behind it using the notation introduced in our code. Although we do not use this branch in our analysis in Chapter 8, we report the implementation here for the interested users.

The action of $f(R)$ gravity in Jordan frame is

$$S = \int d^4x \sqrt{-g} \frac{m_0^2}{2} (R + f(R)) + S_m[g_{\mu\nu}], \quad (\text{D.15})$$

where f is a function of the Ricci scalar and S_m is the action of the matter fields minimally coupled to the Jordan frame metric $g_{\mu\nu}$. Such theories have 4th-order equation of motion and hence have enough freedom to reproduce any expansion history. It is worth mentioning that despite the fourth-order equations of motion, these theories (can be?) are free from ghost instabilities (Ostrogradski instability) but they propagate an additional scalar degree of freedom usually referred to as the *scalaron*.

The designer approach to $f(R)$ consists of fixing a background FRW model and solve a second order equation of motion for the function $f[(R(a))]$, eq. (D.19) below. The solutions of this equation belong to a one-parameter family labelled by the mass scale of the scalaron evaluated at the present time,

$$B \equiv \frac{f_{RR}}{1 + f_R} \frac{\mathcal{H}\dot{R}}{\dot{\mathcal{H}} - \mathcal{H}^2}, \quad (\text{D.16})$$

where the subscript R denotes a derivative w.r.t the Ricci scalar. We also define the following quantities

$$y \equiv \frac{f(R)}{H_0^2}, \quad E \equiv \frac{H^2}{H_0^2}, \quad \frac{R}{H_0^2} \equiv 3(4E + E'), \quad E_{m,r} \equiv \frac{\rho_{m,r}}{\rho_{\text{crit}}^0}, \quad (\text{D.17})$$

where primes denote derivatives w.r.t. $\ln a$ and ρ_{crit}^0 is the critical density evaluated at present time. In the equation above, the quantity E satisfies

$$E \equiv E_m + E_r + \Omega_\Lambda X. \quad (\text{D.18})$$

Then fixing the background expansion history by choosing the function X , one needs to solve the following equation for y ,

$$y'' - \left(1 + \frac{E'}{2E} + \frac{R''}{R'}\right) y' + \frac{R'}{6H_0^2 E} y = -\frac{R'}{H_0^2 E} \Omega_\Lambda X. \quad (\text{D.19})$$

In order to implement the equation (D.19), the original EFTCAMB code needs to compute the dark energy contribution in the function E and its derivatives. That is done using the

function $w_{\text{DE}}(a)$, its derivatives and the integral

$$g(x) = \int_1^{e^x} d\tilde{a} \frac{1 + w_{\text{DE}}(\tilde{a})}{\tilde{a}}, \quad \text{such that } X \equiv e^{-3g(x)}. \quad (\text{D.20})$$

In our code we just replace the function w_{DE} with the dark energy fractional density X ,

$$E' = -3\Omega_m e^{-3x} - 4\Omega_r e^{-4x} + \Omega_\Lambda X', \quad (\text{D.21})$$

$$E'' = 9\Omega_m e^{-3x} + 16\Omega_r e^{-4x} + \Omega_\Lambda X'', \quad (\text{D.22})$$

$$E''' = -27\Omega_m e^{-3x} - 64\Omega_r e^{-4x} + \Omega_\Lambda X''', \quad (\text{D.23})$$

where X' and successive derivatives are obtained from $X(a)$ using the chain rule. Then the designer procedure goes as already described in the original EFTCAMB notes: the equation (D.19) is solved provided the initial conditions and obtain the EFT functions Ω and Λ (c is identically zero in this model).

As a last note about our code, we mention the fact that the initial conditions for the designer $f(R)$ are introduced by calculating the dark energy equation of state at an initial time a_{ini} using the equation (D.6).

The user can select the designer- $f(R)$ model using the dark energy density $X(a)$ by setting `mappingEFTmodel=5` in the designer flag (`EFTflag=3`).

D.3.2 Designer GBD theories

Here we briefly describe the designer approach to the GBD theories. For a more detailed discussion we refer the reader to Sect. 8.3. The user can select the designer-GBD by setting `mappingEFTmodel=4` in the designer flag (`EFTflag=3`). The Friedmann equations and the equation for ϕ read

$$\mathcal{H}^2 = \frac{1}{3\Omega - a^2(\phi')^2/2 + 3a\Omega_\phi\phi'} \left(\frac{\rho a^2}{m_0^2} + U a^2 \right), \quad (\text{D.24})$$

$$(2\Omega + a\Omega_\phi\phi') \frac{\ddot{a}}{a} = \frac{\rho_m a^2}{3m_0^2} (1 - 3w_m) - a^2 \mathcal{H}^2 \left(\frac{1}{3} + \Omega_{\phi\phi} \right) (\phi')^2 - \Omega_\phi a^2 \mathcal{H}^2 \phi'' + \frac{4}{3} U a^2, \quad (\text{D.25})$$

$$\phi'' = -\frac{1}{a} \left(2 + \frac{\ddot{a}}{a\mathcal{H}^2} \right) \phi' - \frac{U_\phi}{\mathcal{H}^2} + \frac{\Omega_\phi}{a^2} \frac{3\ddot{a}}{a\mathcal{H}^2}, \quad (\text{D.26})$$

where primes denote derivatives w.r.t. the scale factor a and the subscript ϕ denotes a derivative w.r.t. the field ϕ . Compared to the $f(R)$ gravity case described in Sect. D.3.1, the designer approach for GBD theories is a little bit more complicated. In fact, fixing a background is not enough to fix the behaviour of the two functions Ω and U . For this reason, we fix a functional form of the coupling function $\Omega(\phi)$. Combining the equations (D.24), (D.25) and (D.26) and eliminating the dependence of the potential and its derivatives one

obtains a second order equation for ϕ ,

$$\begin{aligned} \phi'' = & -\frac{1 + \Omega_{\phi\phi}(\phi')^2}{\Omega_{\phi}} + \left(1 + \frac{1}{2} \frac{3E_m + 4E_r - E'_\nu - \Omega_{\Lambda} X'}{E_m + E_r + E_\nu + \Omega_{\Lambda} X}\right) \phi' \\ & + \frac{1}{\Omega_{\phi}} \frac{(\Omega - 1)(3E_m + 4E_r - E'_\nu) - \Omega \Omega_{\Lambda} X'}{E_m + E_r + E_\nu + \Omega_{\Lambda} X}, \end{aligned} \quad (\text{D.27})$$

where now primes denote derivatives w.r.t. $\ln a$, $E_m \equiv \rho_m/\rho_{\text{crit}}^0$ and we introduced the radiation density $E_r \equiv \rho_r/\rho_{\text{crit}}^0$ and the massive neutrinos density $E_\nu \equiv \rho_\nu/\rho_{\text{crit}}^0$. to be consistent with the code implementation. The equation above can be solved by fixing the background expansion history, by choosing the function $X(a)$, and the functional form of the coupling function $\Omega(\phi)$, and the initial conditions for the field ϕ . The user can select among several coupling functions with the flag `GBD_coupling_type` (see Sect. D.3.2 below for a description), and set the initial conditions through the flags `GBD_phi_ini` and `GBD_dphi_ini` at an initial time a_{ini} , `GBD_a_initial` in code notation.

Once the equation (D.27) is solved, the theory can be mapped into the EFT framework according to

$$\frac{ca^2}{m_0^2} = \frac{1}{2} \mathcal{H}^2(\phi')^2, \quad (\text{D.28})$$

$$\frac{\dot{c}a^2}{m_0^2} = -2\mathcal{H}^3(\phi')^2 + \mathcal{H}^3\phi'\phi'' + \mathcal{H}\frac{\ddot{a}}{a}(\phi')^2, \quad (\text{D.29})$$

$$\frac{\Lambda a^2}{m_0^2} = \frac{1}{2} \mathcal{H}^2(\phi')^2 - Ua^2, \quad (\text{D.30})$$

$$\frac{\dot{\Lambda}a^2}{m_0^2} = \frac{\dot{c}a^2}{m_0^2} - \dot{U}a^2, \quad (\text{D.31})$$

where the potential U and its derivative U_ϕ are obtained through

$$Ua^2 = 3\mathcal{F}H_0^2a^2(E_m + E_r + E_\nu + \Omega_{\Lambda}X) - 3H_0^2a^2(E_m + E_r + E_\nu), \quad (\text{D.32})$$

$$\mathcal{F} = \Omega - \frac{1}{6}(\phi')^2 + \Omega_{\phi}\phi', \quad (\text{D.33})$$

$$\dot{U}a^2 = U_{\phi}\phi'\mathcal{H}a^2, \quad (\text{D.34})$$

$$U_{\phi}a^2 = 3\Omega_{\phi}\frac{\ddot{a}}{a} - \mathcal{H}^2\phi'' - \left(\mathcal{H}^2 + \frac{\ddot{a}}{a}\right)\phi'. \quad (\text{D.35})$$

The EFT function Ω is easily obtained from the coupling function $\Omega(\phi)$ according to

$$\Omega(a) = \Omega(\phi(a)), \quad (\text{D.36})$$

$$\frac{d\Omega}{da} = \Omega_{\phi}\phi'\frac{1}{a}, \quad (\text{D.37})$$

$$\frac{d^2\Omega}{da^2} = \frac{1}{a^2} \left(\Omega_{\phi\phi}(\phi')^2 + \Omega_{\phi}\phi'' - \Omega_{\phi}\phi' \right), \quad (\text{D.38})$$

$$\frac{d^3\Omega}{da^3} = \frac{1}{a^3} \left(\Omega_{\phi\phi\phi}(\phi')^3 + 3\Omega_{\phi\phi}\phi'\phi'' - 3\Omega_{\phi\phi}(\phi')^2 - 3\Omega_{\phi}\phi' + \Omega_{\phi}\phi''' + 2\Omega_{\phi}\phi' \right), \quad (\text{D.39})$$

where the triple derivative ϕ''' is obtained from a derivative w.r.t. $\ln a$ of the equation (D.27).

Moreover, we also provide a designer-GBD module that uses the w_{DE} parametrization as in the original EFTCAMB code. This model can be chosen by setting `mappingEFTmodel=3` in the designer flag (`EFTflag=3`).

Functional forms of the coupling $\Omega(\phi)$

As mentioned above, the user can select several functional forms of the coupling function $\Omega(\phi)$.

- Linear coupling function:

$$\Omega(\phi) = 1 + \xi\phi, \quad (\text{D.40})$$

where ξ (`GBD_xi` in code notation) is a dimensionless coupling constant. This is chosen by setting `GBD_coupling_type = 1`.

- Quadratic coupling function:

$$\Omega(\phi) = 1 + \xi\phi^2, \quad (\text{D.41})$$

chosen by setting `GBD_coupling_type = 2`.

- Exponential coupling function:

$$\Omega(\phi) = \exp(\xi\phi), \quad (\text{D.42})$$

chosen by setting `GBD_coupling_type = 3`.

- Exponential coupling function (with negative exponent):

$$\Omega(\phi) = \exp(-\xi\phi), \quad (\text{D.43})$$

chosen by setting `GBD_coupling_type = 4`.

The user can also introduce a customized coupling function by modifying the subroutine `EFTCAMBDesignerGBD2Coupling` in the file `09p4_Designer_GBD_mod.f90`.